ABSTRACT

Title of Document: ELECTRONIC TRANSPORT IN LOW DIMENSIONS: CARBON NANOTUBES AND MESOSCOPIC SILVER WIRES

Tarek Khairy Ghanem, Doctor of Philosophy, 2008

Directed By: Associate Professor, Michael S. Fuhrer and Professor Ellen D. Williams, Department of Physics

This thesis explores the physics of low-dimensional electronic conductors using two materials systems, carbon nanotubes (CNTs) and lithographically-defined silver nanowires.

In order to understand the intrinsic electronic properties of CNTs, it is important to eliminate the contact effects from the measurements. Here, this is accomplished by using a conductive-tip atomic force microscope cantilever as a local electrode in order to obtain length dependent transport properties. The CNT-movable electrode contact is fully characterized, and is largely independent of voltage bias conditions, and independent of the contact force beyond a certain threshold. The contact is affected by the fine positioning of the cantilever relative to the CNT due to parasitic lateral motion of the cantilever during the loading cycle, which, if not controlled, can lead to non-monotonic behavior of contact resistance vs. force.

Length dependent transport measurements are reported for several metallic and semiconducting CNTs. The resistance versus length $R(L)$ of semiconducting CNTs is linear in the on state. For the depleted state $R(L)$ is linear for long channel lengths, but non-linear for short channel lengths due to the long depletion lengths in one-dimensional semiconductors. Transport remains diffusive under all depletion conditions, due to both low disorder and high temperature.

The study of quantum corrections to classical conductivity in mesoscopic conductors is an essential tool for understanding phase coherence in these systems. A long standing discrepancy between theory and experiment regards the phase coherence time, which is expected theoretically to grow as a power law at low temperatures, but is experimentally found to saturate. The origins of this saturation have been debated for the last decade, with the main contenders being intrinsic decoherence by zero-point fluctuations of the electrons, and decoherence by dilute magnetic impurities.

Here, the phase coherence time in quasi-one-dimensional silver wires is measured. The phase coherence times obtained from the weak localization correction to the conductivity at low magnetic field show saturation, while those obtained from universal conductance fluctuations at high field do not. This indicates that, for these samples, the origin of phase coherence time saturation obtained from weak localization is extrinsic, due to the presence of dilute magnetic impurities.

ELECTRONIC TRANSPORT IN LOW DIMENSIONS: CARBON NANOTUBES AND MESOSCOPIC SILVER WIRES

By

Tarek Khairy Ghanem

Dissertation submitted to the Faculty of the Graduate School of the
University of Maryland, College Park, in partial fulfillment
of the requirements for the degree of
Doctor of Philosophy
2008

Advisory Committee:
Associate Professor Michael S. Fuhrer, Chair/Advisor
Professor Ellen D. Williams, Advisor
Professor Richard L. Greene
Assistant Professor Min Ouyang
Professor Neil Goldsman

© Copyright by
Tarek Khairy Ghanem
2008

Dedication

To my mother Suhair Morsy Muhammed Youssef

Acknowledgements

In the name of Allah, the most gracious, the most merciful. All the praise and thanks be to Allah the lord of all that exists, who gave me the strength and patience through this long endeavor “And be patient, for surely Allah does not waste the reward of the good-doers” Quran 11:115, and peace and blessings of Allah be upon Muhammad, his last prophet and messenger who –as narrated in *Sahih Attermithi*- said “That who does not thank people (who help him), is indeed not truly thankful to Allah”, therefore I hereby offer my gratitude to all those who made this work possible, to those who went beyond the call of duty to make my life easier, and to those who kept my good company or put a smile on my face during difficult times.

I would like to first thank my advisors Dr. Michael Fuhrer and Dr. Ellen Williams for their support, patience, and encouragement. Michael always made himself available to discuss and comment on my work. He allowed me to explore my ideas, even the ones with no clear rewards, thus gaining experience and vision in doing independent research. He was also patient with my erratic schedule and sporadic attendance at the group meetings, both being direct results of my night owl life style. Ellen’s diligent feedback on my work was important, especially for understanding how to present results in a clear and accessible way. Both Michael and Ellen have a calm and friendly attitude, along with sharp, physics-oriented minds. It was a remarkable experience working with them.

Before that, I had another remarkable experience working with Dr. Richard Webb. He was a warm, kind advisor despite a fiery mode sometimes, along with a unique vision of physics. I owe him a great deal in my understanding of experimental

methods. I am grateful for his support, and for the ample time he spent teaching me even the smallest lab tricks. Dr. Webb moved to University of South Carolina in the middle of 2004. He kindly granted me to include the experiments I have done under his supervision as part of my thesis. These constitute the last chapter of this work.

Even before that, I spent a brief period working with Dr. Raymond Phaneuf. I am grateful to Ray for his support and for offering me my first glimpses into the world of experimental physics.

During my long affiliation with the Center for Superconductivity Research, I had the pleasure of dealing with Dr. Richard Greene. He was always kind, supportive, and accommodative of any requests I had. I am particularly grateful for all the feedback I got from him on my presentation skills during the CSR seminars. I also thank him for serving on my defense committee.

During my studies I enjoyed the company of many graduate students and postdocs. Enrique Cobas, Adrian Southard, Chaun Jang, Tobias Dürkop, Jainhao Chen, Shudong Xiao, Gokhan Esen, Todd Brintlinger, Yung-Fu Chen, Atif Imtiaz, Sudeep Datta, Joshua Higgins, Masa Ishigami, Samir Garzon, Yuanzhen Chen, Hamza Balci, David Tobias, Alexandra Curtin, Daniel Lenski, Sungjae Cho, and Stephanie Getty. I am thankful to everybody for all the good times or useful discussions we had, and for the occasional assistance with my work by many of them. I also would like to thank Jay Vaishnav, who at one point early on, gave me an advice which has fatefully set my wondrous journey through graduate school.

From the many professors I took courses with, I would like to offer special thanks to Dr. Thomas Antonsen for kindly deferring my final classical mechanics

exam as I fell ill and until I fully recovered. I would like also to mention Dr. Theodore Jacobson, a great teacher who made learning quantum mechanics fun. I reserve my greatest gratitude and respect to Dr. Michael Coplan whose unparalleled patience and kindness shall always remain a heart-warming memory.

I am grateful to the staff of the physics department for their extraordinary assistance and kindness. I am particularly indebted to Jane Hessing, Lorraine DeSalvo, Pauline Rirskopa, Linda Ohara, Alvaro Godinez (Amigo), and Russell Wood.

I would like to thank Jody Heckman-Bose of the IES for her kindness and invaluable advice. I also would like to thank Dr. Min Ouyang, and Dr. Neil Goldsman for serving on my defense committee.

College Park and many areas around are the home of a vibrant multicultural Muslim community which was my sanctuary over the years. I'm grateful to the staff of Darusalaam in College Park, Prince George Muslim Association in Lanham, and the Muslim Student Association chapter of UMD for all the efforts they do to keep these establishments up and running.

My life in College Park was made easier by the deep, warm friendship of many people, Tamer El-Sharnouby, Khaled Arisha (Uncle) and his wife Nesreen, Ashraf El-Masry , his wife Suzanne and their son - my little buddy- Bilal, and Tamer Nadeem. They were like my second family. I'm also grateful to Yasser Jaradat, Wael Akl, Ahmet Farouk Aysan, Hisham Abd-Allah, Abd-Elhameed Badawy, Ahmad Abd-Elhafez (Mawlana), Tamer Abu-Elfadl, Tarek Masood, and Amr El-Sherief. I

apologize for my many other friends whose names do not appear here, memories of their good company will always have a special place in my heart.

The kindness and support of my family was always a beacon of light and a nourishment to my spirit during all the times. My mother Suhair Morsy Youssef, my father Khairy Morsy Ghanem, my sisters Maha, Sahar, and Samar, and my brother Sameh, and my aunt Wahibah Morsy Youssef. No words can describe my love and appreciation to all of them.

College Park
Dhu Al-Qi'dah 1429 AH
November 2008 CE

طارق خيري مرسي غانم
Tarek Khairy Morsy Ghanem

Table of Contents

Dedication ii
Acknowledgements iii
Table of Contents vii
List of Tables ix
List of Figures x
Chapter 1: Background 1
1.1 The band structure of carbon nanotubes 2
1.2 Some concepts of electrical transport in one dimension 10
1.2.1 Quantization of conductance and the Landauer formula 12
1.2.2 Ohm's law versus localization 15
1.2.3 Coulomb blockade 19
1.3 Basics of atomic force microscopy 22
1.4 Review of previous experimental work 29
Chapter 2: Sample preparation and setup for performing local transport measurements on carbon nanotubes 37
2.1 Sample preparation 37
2.1.1 Chemical vapor deposition (CVD) of carbon nanotubes 37
2.1.2 Evaporation of fixed electrode 40
2.2 Cantilever preparation 44
2.3 Measurement setup 45
2.3.1 Variables of the problem 45
2.3.2 Instrumentation 46
2.3.3 Measurement procedure 47
Chapter 3: Characterization of the electrical contact between a conductive AFM cantilever and a carbon nanotube 57
3.1 Parameters of the contact 57
3.2 Conductance vs. load behavior 59
3.3 Conductance vs. both load and lateral position 65
3.4 Discussion 77
3.5 Temporal stability of the contact 92
3.6 Conclusions 98
Chapter 4: Length dependent transport measurements of carbon nanotubes 99
4.1 Experimental procedure 99
4.2 Results 106
4.2.1 Nanotube D7 106
4.2.2 Nanotube D1 111
4.2.3 Nanotube D5 115
4.2.4 Nanotube D3 120
4.3 Discussion 125
4.3.1 Contact resistance and contact type: Ohmic vs. Schottky 125
4.3.2 The effect of the islands band 130
4.3.3 Electrostatic effects 131

4.3.4 Depletion and charge transfer ... 133
4.3.5 Mean free path ... 138
4.3.6 Mobility ... 147
4.3.7 Comments on nanotube D7 ... 148
4.3.8 The D3 junction ... 150
4.4 Conclusion ... 152
Chapter 5: Transport measurements in mesoscopic silver wires at low temperatures ... 153
5.1 Background ... 153
5.2 The problem of τ_ϕ saturation ... 155
5.2.1 Intrinsic decoherence ... 156
5.2.2 Decoherence by dilute magnetic impurities ... 158
5.2.3 Dephasing by coupling to two-level systems (TLS) ... 165
5.2.4 Dephasing by external microwave noise ... 166
5.2.5 Other explanations ... 166
5.3 Experimental procedure ... 167
5.4 Results ... 178
5.4.1 Weak localization ... 178
5.4.2 Electron-electron interaction ... 184
5.4.3 Universal conductance fluctuations (UCF) ... 186
5.5 Conclusion ... 195
Appendix A: Measurements of other carbon nanotubes ... 197
A.1 Nanotube D2 ... 197
A.2 Nanotube D4 ... 199
A.3 Nanotube D6 ... 200
Bibliography ... 202

List of Tables

Table (2-1): Brief description of the nanotubes measured in Chapters 3 and 4 56
Table (4-1): Comparison of charge transfer and thermal doping fractions 137
Table (5-1): Parameters of the samples in Figure 5-1 and Figure 5-2 160
Table (5-2): Samples properties 172
Table (5-3): Theoretical coefficients for samples S-1 through S-4 181
Table (5-4): Experimentally measured τ_{ϕ} at about 10 mK for samples S-1 to S-4... 183
Table (5-5): Coefficients of $(\Delta R/R)_{\text{e-e}}=C_3T^{-1/2}$ for samples S-1 to S-4 185
Table (5-6): Theoretical coefficients for $(L_{\phi})_{\text{UCF}}=C_2T^{-1/3}$ from the correlation field and RMS data 190
Table (5-7): Coefficients for $\Delta G_{\text{RMS}}[(L_{\phi})_{\text{CorrField}}]^{-1/2}=C_5T^{-1/2}$ for samples S-3 and S-4 193

List of Figures

Figure 1-1: Structure of graphene sheet 3
Figure 1-2: Electronic band structure of graphene 4
Figure 1-3: Derivation of nanotubes from graphene sheet 6
Figure 1-4: Deduction of the 1-D nanotube band structure from the band structure of graphene 7
Figure 1-5: Density of states for a (11,0) semiconducting and a (12,0) metallic CNTs 9
Figure 1-6: Drain current versus gate voltage for metallic and semiconducting carbon nanotubes 10
Figure 1-7: A schematic of a ballistic conductor sandwiched between two reflectionless contacts 12
Figure 1-8: Two resistors connected in series 15
Figure 1-9: Schematic of a confined region (island) connected through tunnel barriers to leads, and equivalent circuit 20
Figure 1-10: Basic components of an atomic force microscope 23
Figure 1-11: Tip-surface interaction force as a function of tip-sample distance 24
Figure 1-12: Force curve in the absence of adhesion 27
Figure 1-13: Force curve in the presence of a meniscus layer 28
Figure 1-14: Conductance map and the corresponding conductance versus length data obtained using the AC current injection method 30
Figure 1-15: Resistance versus length data obtained from different length devices all patterned on one long nanotube 32
Figure 1-16: EFM image 33
Figure 1-17: Profile of voltage drop along a nanotube device at two different gate voltages obtained using the three-terminal method 34
Figure 1-18: Resistance versus length along a carbon nanotube device obtained using the two-terminal method 35
Figure 2-1: Details of the quartz tube furnace used for CVD growth of carbon nanotubes 39
Figure 2-2: Illustrations of sample preparation steps 42
Figure 2-3: Comparison of shadow-evaporated edges and an edge defined by e-beam lithography 43
Figure 2-4: Schematic of the measurement system 46
Figure 2-5: Photographs of the measurement setup 48
Figure 2-6: Constant current contour map of I_d as a function of both V_d and V_g on nanotube D2 55
Figure 3-1: Illustration of the two measurement geometries 60
Figure 3-2: Current-force curves of Types I, II, III, IV 61
Figure 3-3: Current response and deflection response, for force curves of Type I measured on nanotube D2 63
Figure 3-4: Current response and deflection response for force curves of Type I measured on nanotube D3 64
Figure 3-5: Current-force curves of Type I measured on seven different nanotubes 65

Figure 3-6: Two-dimensional plots of current vs. both horizontal position ΔX and loading ΔZ taken in the "horizontal profile" configuration using soft cantilevers 67
Figure 3-7: Two-dimensional plots of current vs. both horizontal position ΔX and loading ΔZ taken in the "horizontal profile" configuration using hard cantilevers.... 69
Figure 3-8: Two-dimensional plots of current vs. both vertical position ΔY and loading ΔZ taken in the "vertical profile" configuration using two different hard cantilevers 71
Figure 3-9: Constant drain current contours as a function of both V_g and ΔZ for metallic nanotube D7 74
Figure 3-10: Constant drain current contours as a function of both V_g and ΔZ for semiconducting nanotube D5........ 75
Figure 3-11: Constant drain current contours as a function of both V_d and displacement ΔZ for semiconducting nanotube D3 76
Figure 3-12: Constant drain current contours as a function of both V_d and displacement ΔZ for metallic nanotube D7 77
Figure 3-13: $dI(\Delta Z)/I(\Delta Z)$ calculated from force curves of Type I for five different nanotubes during loading........ 81
Figure 3-14: SEM images of a cantilever at different magnifications........ 85
Figure 3-15: Schematic of the pinned cantilever model 88
Figure 3-16: Schematic of the sliding cantilever model 90
Figure 3-17: Current and deflection versus time for tip-nanotube contacts 94
Figure 3-18: Current, deflection , and deflection fluctuations........ 94
Figure 3-19: Normalized noise power versus frequency of current measured in nanotube D2 at three gate voltages 96
Figure 3-20: Noise power versus frequency of deflection with the cantilever bound to the surface of the substrate........ 97
Figure 4-1: The full set of resistance values obtained for channel lengths between 65 and 85 μm on nanotube D5........ 103
Figure 4-2: Two time series of the drain current of nanotube D3 at fixed gate and drain voltages directly after a gate sweep 104
Figure 4-3: Effects of trapped charge and contact resistance on the measured drain current 105
Figure 4-4: An AFM topography scan of nanotube D7........ 107
Figure 4-5: Resistance versus channel length of nanotube D7 at various gate voltages between -10 V and 10 V 108
Figure 4-6: Drain current versus gate voltage sweeps at various lengths of nanotube D7........ 110
Figure 4-7: Current saturation in nanotube D7 111
Figure 4-8: An AFM topography scan of nanotube D1 111
Figure 4-9: Resistance versus length of nanotube D1 at various gate voltages between 9 V and -10 V........ 113
Figure 4-10: Drain current versus gate voltage sweeps at various lengths of nanotube D1........ 114
Figure 4-11: An AFM phase scan of nanotube D5 115

Figure 4-12: Resistance versus length of nanotube D5 at various gate voltages between 9 V and -10 V 117
Figure 4-13: Drain current versus gate voltage sweeps at various lengths of nanotube D5.. 119
Figure 4-14: An AFM topography scan of nanotube D3 120
Figure 4-15: Resistance versus length for nanotube D3 at a gate voltage of -10 V . 121
Figure 4-16: Change in behavior of nanotube D3 at 34 μm 122
Figure 4-17: Resistance versus length of nanotube D3 at various gate voltages between 9 V and -10 V 123
Figure 4-18: Drain current versus gate voltage sweeps at various lengths of nanotube D3.. 124
Figure 4-19: Determination of the threshold voltage V_{th} and the subthreshold swing S 127
Figure 4-20: Subthreshold swing S versus channel length L for nanotubes D5, D1, and D3.. 129
Figure 4-21: Resistivity and mean free path l as a function of V_g for the three semiconducting nanotubes D5, D1, and D3.. 140
Figure 4-22: Field effect mobility for nanotubes D5, D1, and D3 148
Figure 4-23: Resistivity and the corresponding mean free path as a function of gate voltage for the metallic nanotube D7.. 150
Figure 4-24: The transmission coefficient of the junction between the two segments of D3 151
Figure 5-1: Temperature dependence of τ_ϕ for four gold wires.............................. 157
Figure 5-2: Phase coherence time versus temperature for samples made of 5N Ag, 6N Ag, and 6N Au 159
Figure 5-3: Resistivity of a silver nanowire exposed to air at room temperature as a function of time.. 170
Figure 5-4: An example of a quasi 1-D metallic sample 172
Figure 5-5: Resistance of Ruthenium oxide thermometer as a function of temperature 173
Figure 5-6: The two measurement configurations used.. 176
Figure 5-7: L_ϕ for samples S-5 and S-6 as a function of excitation current at 7 mK. 178
Figure 5-8: Low field magnetoresistance for samples S-1 to S-4............................ 180
Figure 5-9: Experimentally measured τ_ϕ as a function of temperature for samples S-1 to S-4.. 182
Figure 5-10: Electron-electron interaction data for samples S-1 to S-4 186
Figure 5-11: UCF traces for samples S-3 and S-4 at 99 mK 189
Figure 5-12: $(L_\phi)_{UCF}$ for samples S-3 and S-4 as a function of temperature............. 191
Figure 5-13: ΔG_{RMS} as a function of temperature for samples S-3 and S-4 192
Figure 5-14: Residual scattering rate versus temperature for samples S-1 to S-4.... 194
Figure A-1: An AFM topography scan of nanotube D2.. 198
Figure A-2: Typical V_g and V_d sweeps on nanotube D2 198
Figure A-3: An AFM topography scan of nanotube D4.. 199
Figure A-4: Typical V_g and V_d sweeps on nanotube D4 200
Figure A-5: An AFM phase scan of nanotube D6 201

Figure A-6: Typical V_g and V_d sweeps on nanotube D6 201

Chapter 1: Background

Carbon nanotubes are tubular forms of carbon discovered nearly two decades ago by Iijima [1] which have attracted a great deal of attention ever since. The interest in carbon nanotubes is two-fold. On one hand, their nature as one-dimensional conductors and semiconductors makes them a test bed for exploring electrical, thermal, optical, and other physical properties in such reduced dimensionality. On the other hand, their unique combination of good electrical, thermal, and mechanical properties made them candidates for many applications.

Electronic transport properties of carbon nanotube devices, which are the main topic in this thesis, have attracted a lot of theoretical and experimental attention over the last decade. Various works have studied the contributions from contacts [2-7], defects and impurities [8-10], electron-phonon interaction [5, 11-14], and electron-electron interaction [15, 16].

A usual problem in interpreting transport data in carbon nanotube devices is separating the intrinsic response of the nanotube channel from the contact effects. Obtaining the intrinsic response of the nanotube channel is important in revealing the scattering mechanisms in nanotube devices, and in studying physical phenomena associated with the nanotube channel, such as localization in one dimension.

Carbon nanotubes can be thought of as strips of single sheets of graphite (graphene) which are rolled and connected seamlessly thus forming a tubular structure. A carbon nanotube can have either single or multiple walls, as is revealed by high resolution transmission electron microscopy (TEM). Single walled carbon

nanotubes, which are the main concern in this thesis, can be metallic, or semiconducting (with small or large bandgap), depending on their band structure. In the next section I will review the band structure of carbon nanotubes.

1.1 The band structure of carbon nanotubes

The starting point for understanding the band structure of carbon nanotubes is that the band structure of graphene, first studied by Wallace in 1947 [17], and revisited in many recent reviews [18-21]. The electronic configuration of the carbon atom is $1s^2 2s^2 2p^2$. The *s* orbital may hybridize with the three *p* orbitals to form four sp^3 orbitals pointing to the heads of a tetrahedron like in diamond or methane. It may also hybridize with only two of the *p* orbitals to form three sp^2 orbitals. These orbitals are oriented in one plane at 120° from each other (i.e. they are pointing to the heads of an equilateral triangle), while the remaining *p* orbital (conventionally designated as p_z) is normal to that plane, this is the situation in graphene, which consequently has a hexagonal lattice, as is schematically shown in Fig. 1-1 below.

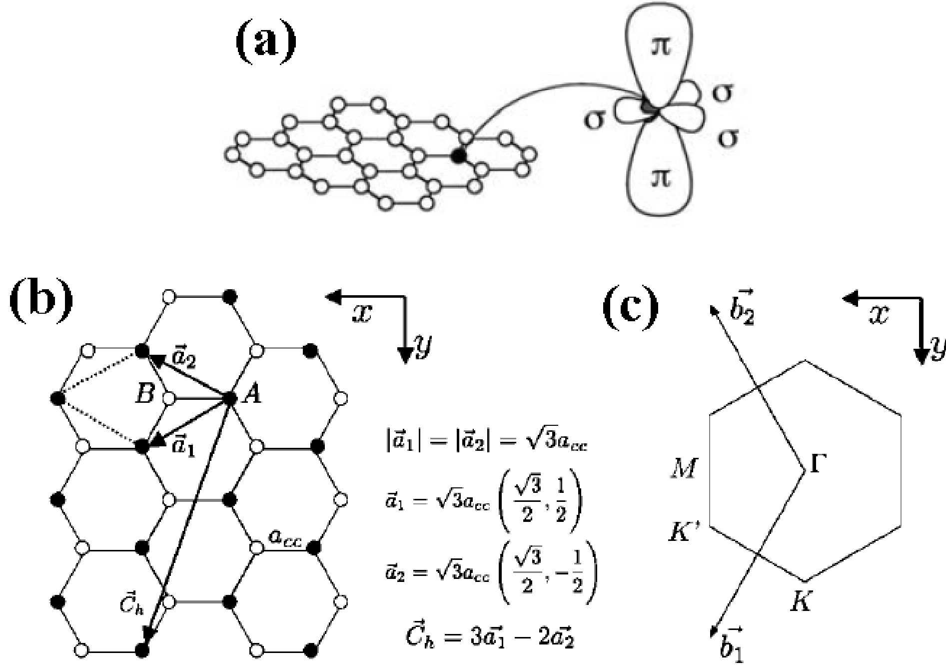

Figure 1-1: Structure of graphene sheet. (a) Illustration of the bonds in graphene sheet, the in-plane sp^2 orbitals form σ bonds, while the p_z orbitals perpendicular to the sheet form π bonds. (b) Basis vectors of the lattice of graphene. (c) Reciprocal lattice basis vectors, $\mathbf{b}_1 = b(1/2, \sqrt{3}/2)$ and $\mathbf{b}_2 = b(1/2, -\sqrt{3}/2)$, where $b = 4\pi / 3a_{C-C}$. (a) is from Reference [21], (b) and (c) are from Reference [20].

As can be seen, the three hybridized sp^2 orbitals form in-plane 'head on' σ bonds, while the p_z orbitals normal to the plane form 'side by side' π bonds. The energy spectrum corresponding to the bonding σ and antibonding σ^* states has a wide gap ~8 eV, while that of the π and π^* states forms a continuous energy band with a vanishing gap (see below). Therefore, the low energy electronic properties (< 4 eV) around the Fermi level, which exists in the gap of the $\sigma\sigma^*$ states, are rather governed by the $\pi\pi^*$ states. The σ bonds however, are the ones responsible for cohesive properties, and result in the high mechanical strength of carbon nanotubes. Considering only π electrons, the tight binding model yields a dispersion relation:

$$E(\mathbf{k}) = E_F \pm \gamma_0 \sqrt{1 + 4\cos\left(\frac{\sqrt{3}k_x a}{2}\right)\cos\left(\frac{k_y a}{2}\right) + 4\cos^2\left(\frac{k_y a}{2}\right)} \quad (1\text{-}1)$$

where **k** is a reciprocal lattice vector, $\gamma_0 \approx 3$ eV is the nearest neighbor overlap integral, $a = \sqrt{3}a_{C-C}$ is the lattice constant of the hexagonal lattice, where $a_{\text{C-C}} = 0.142$ is the carbon-carbon inter-atomic distance in graphene. The electronic band structure of graphene, and dispersion relation (1-1) are shown in Fig. 1-2 below.

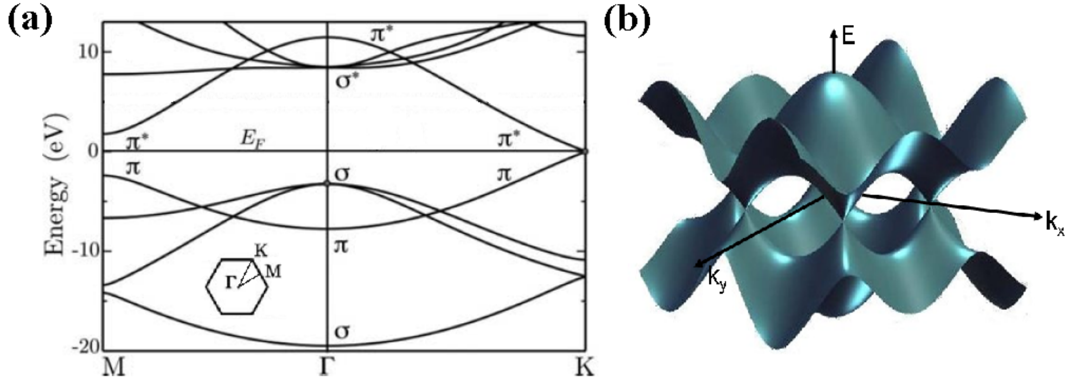

Figure 1-2: Electronic band structure of graphene. (a) Both σ and π bands along the symmetry directions M-Γ-K, notice the large gap between the σ and σ^* bands, and the crossing of the π and π^* bands at the K point. (b) Tight binding dispersion relation (Equation. (1-1)), notice the conical shape of the dispersion relation near the six K points. (a) is from Reference [21], and (b) is courtesy of M. S. Fuhrer.

The π and π^* bands touch at the corners of the Brillouin zone, these are usually labeled by their momentum vector as 'K points'. Therefore, graphene is a metal with vanishing density of states, or a zero-gap semiconductor. Near these high symmetry points, the dispersion relation takes the shape of a cone, and can be approximated as linear.

In order for a graphene sheet to be rolled seamlessly, the circumference of the resulting nanotube must correspond to a lattice vector, usually called the chiral vector $\mathbf{C}_h$. If the basis vectors of the hexagonal lattice are $\mathbf{a}_1$ and $\mathbf{a}_2$, then $\mathbf{C}_h = n\mathbf{a}_1 + m\mathbf{a}_2$, where n, m are integers, and the convention $0 \le |m| \le n$ ensures $\mathbf{C}_h$ is unique. As a shorthand, the nanotube specified by a chiral vector $\mathbf{C}_h = n\mathbf{a}_1 + m\mathbf{a}_2$ is called an '(n,m) nanotube'. The diameter for an (n,m) nanotube is given by:

$$d = \frac{|C_h|}{\pi} = \frac{a}{\pi}\sqrt{n^2 + m^2 + nm} \qquad (1\text{-}2)$$

Nanotubes whose two indices are equal (n,n) are called armchair nanotubes, while those whose second index is zero (n,0) are called zigzag nanotubes, the rest are called chiral nanotubes. An example of this rolling process is shown below in Fig. 1-3 for the case of a (5,3) nanotube.

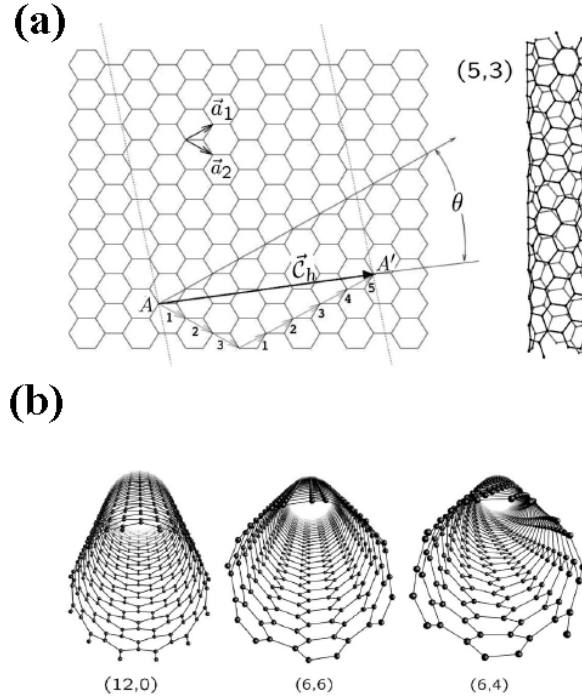

Figure 1-3: Derivation of nanotubes from graphene sheet. (a) An illustration for the case of a (5,3) nanotube, showing the chiral vector $\mathbf{C}_h=5\mathbf{a}_1+3\mathbf{a}_2$, the nanotube axis is normal to $\mathbf{C}_h$, the resulting nanotube is shown on the right. (b) An illustration of (12,0) zigzag, (6,6) armchair, and (6,4) chiral nanotubes. (a) and (b) are from Reference [20].

The continuity of the wavefunction around the circumference of the nanotube imposes the periodic boundary condition:

$$\mathbf{k}\cdot\mathbf{C}_h = 2\pi q \qquad (1\text{-}3)$$

where q is an integer. This defines a set of allowed $\mathbf{k}$ vectors which are parallel to $\mathbf{C}_h$. Each one of these vectors defines a vertical plane in the $E(k_x,k_y)$ space perpendicular to $\mathbf{C}_h$ (i.e. parallel to the axis of the nanotube), and the intersection of each plane with the 2-D dispersion relation shown in Fig. 1-2 above yields a 1-D dispersion relation for one of the nanotube subbands.

As mentioned before, the dispersion relation near the K points takes the form of a cone. Generally, a plane that is parallel to the axis of a cone would intersect it in a hyperbola. Thus all the dispersion relations for the second subband and up take a hyperbolic shape. For the first subband, if the allowed **k** vector does not pass through a K point (i.e. the head of the cone), then it will be hyperbolic too, and a gap exists between the conduction and valence bands, and the resulting nanotube would be semiconducting. However, in the special case when an allowed **k** vector passes through the K point, the dispersion relation becomes linear, with the conduction and valence bands meeting at the Fermi point at the head of the cone, thus creating a zero gap band structure, and the resulting nanotube would be metallic. These cases are schematically shown schematically in Fig. 1-4 below.

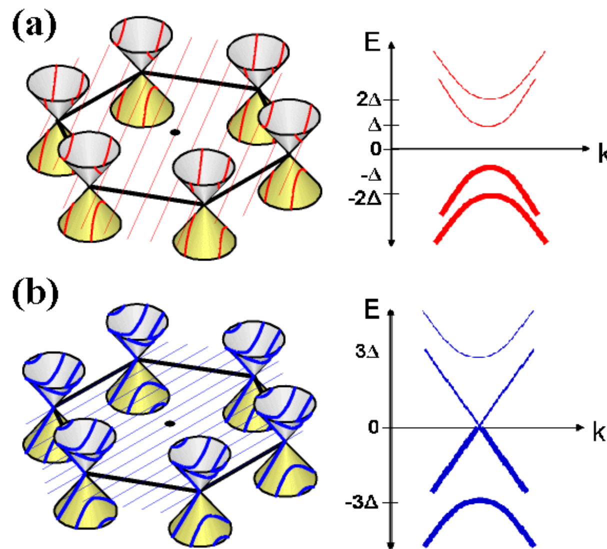

Figure 1-4: Deduction of the 1-D nanotube band structure from the band structure of graphene by application of the quantization condition (1-2) above. (a) The allowed k vectors do not pass by any K point, the slices through the cones are all hyperbolic, and the resulting nanotube is semiconducting. (b) One allowed k vector passes by a K point, the first subband is linear, and the nanotube is metallic. Δ is one half the bandgap defined in Equation (1-4) below. Courtesy of M. S. Fuhrer

The condition for an allowed **k** vector to pass by a K point is, from Equation. (1-3), $\mathbf{K}\cdot\mathbf{C}_h = 2\pi q$. This can be reduced to $n - m = 3p$, where p is an integer, all other nanotubes not satisfying that condition are semiconducting. However, because of the curvature of the nanotube upon rolling, a small gap opens in nanotubes satisfying the above condition except for $p = 0$, i.e. except for nanotubes where $n = m$. These (n,n) nanotubes are the only truly metallic nanotubes. Therefore, single walled carbon nanotubes can be classified into three types, metallic nanotubes, semiconducting nanotubes, and small gap semiconducting nanotubes (i.e. nominally metallic nanotubes with , in which curvature induces a gap). The gap in the latter is very small though, therefore they still act as essentially metallic at room temperature. For a semiconducting nanotube, the band gap is given by:

$$E_g = \frac{2\gamma_0 a_{C-C}}{d} \approx \frac{0.7\ eV.nm}{d} \qquad (1\text{-}4)$$

thus the bandgap is inversely proportional to the diameter. For small bandgap semiconductors, the gap is $\propto 1/d^2$, and is in the order of a few meV.

Within the tight binding model, it can be shown that the density of states exhibits Van Hove singularities at the onset of each subband, which is generally expected for a one dimensional conductor. In metallic nanotubes, the density of states is finite and constant between the top valence subband, and the bottom conduction subband. In semiconducting nanotubes, that density of states is zero as should be expected in the bandgap. This was also verified experimentally using scanning tunneling spectroscopy (STS). Fig. 1-5 below shows the calculated density of states

for an (11,0) semiconducting nanotube, and (12,0) metallic nanotube, which display Van Hove singularities.

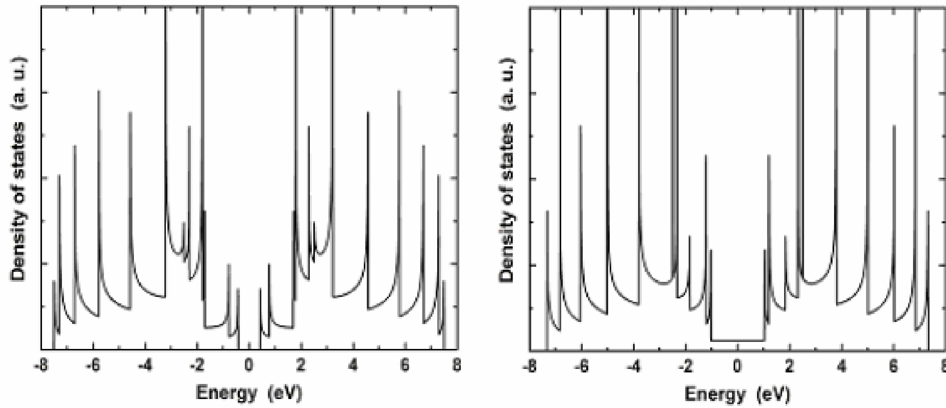

Figure 1-5: Density of states for a (11,0) semiconducting and a (12,0) metallic CNTs computed from tight binding show van Hove singularities. From Reference [22].

Typically, electrical transport in carbon nanotube devices is tested in a field effect transistor (FET) configuration, with two electrical contacts (the source and the drain) defining the channel, and a third terminal (the gate) which capacitively couples to it. The two types of carbon nanotubes can be differentiated easily in these transport measurements by the response of the current passing though the device to the gate voltage. Typically, semiconducting nanotubes show a FET like behavior, turning off completely at some gate voltage. Metallic nanotubes might show some mild gate modulation, but never turn off completely. Examples for both types of behavior are shown in Fig. 1-6 below.

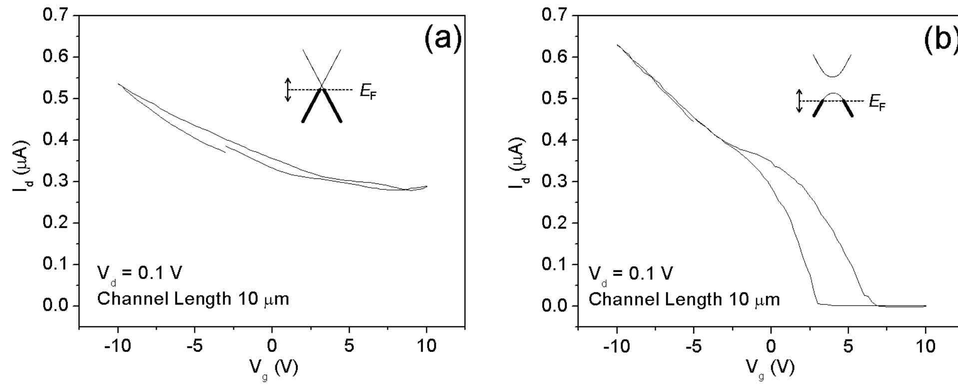

Figure 1-6: Drain current versus gate voltage for (a) metallic and (b) semiconducting carbon nanotubes.

In the next section, I will briefly review some aspects of electrical transport in one-dimensional conductors.

1.2 Some concepts of electrical transport in one dimension

As seen in the previous section, carbon nanotubes are essentially described as one-dimensional electrical conductors, which makes them a suitable test bed for exploring electrical transport in one dimension. However, the experimentally measured properties of a carbon nanotube device will depend on the properties of both the contacts and the channel.

An ideal carbon nanotube device consists of a disorder-free nanotube channel with reflectionless contacts, and low voltage applied across the contacts (source-drain voltage) at low temperatures. The conductance of such a device would simply be $4e^2/h \approx 155$ μS, corresponding to the contact resistance of a ballistic conductor with two conductance channels (see below). This picture closely corresponds with the

experimental measurements for short channel (~ 1 μm) devices, with ohmic contacts, and metallic carbon nanotube channels, or semiconducting nanotube channels in their on state, even at room temperature.

However, this picture significantly changes upon deviation from the conditions above. For example, Schottky barriers [2-4, 7] can exist for contacts to semiconducting nanotubes. Long nanotube channels are diffusive rather than ballistic conductors [23, 24]. A high bias across the contacts can induce current saturation in metallic carbon nanotubes [14], or velocity saturation in semiconducting nanotubes [25, 26]. Contacts can cause long range charge transfer doping in semiconducting nanotube channels under depletion conditions [27-29]. Disorder in the nanotube channel can cause phenomena like Coulomb blockade [10, 30-32], or localization [24, 33].

The above effects can mostly be divided into 'contact effects' and 'channel effects'. It is important to separate these two in order to obtain the true intrinsic response of the nanotube channel. Achieving this separation constitutes a significant portion of this thesis. The previous experimental efforts attempting to separate these effects would be the subject of the next section, and contact phenomena will be discussed further in Chapter 4.

The channel response depends on several factors, mainly the type of the nanotube (semiconducting or metallic), presence of disorder (structural defects or charged impurities from the substrate), temperature, and bias conditions (the latter two determine the electron-phonon interaction).

For the rest of this section, I will briefly review the basic concepts of electronic transport in a one dimensional channel within the Landauer formalism. The treatment below mostly follows References [18, 34-37].

1.2.1 Quantization of conductance and the Landauer formula

The basic model here is that of a ballistic conductor of length L with reflectionless contacts (reservoirs) on both sides which are kept at two different chemical potentials μ_1 and μ_2 , and both at zero temperature. The current in the conductor is carried by different transverse modes (subbands), each mode has a dispersion relation $E(N, k)$ with a cutoff energy $\varepsilon_N = E(N, k = 0)$, as sketched in Fig. 1-7 below.

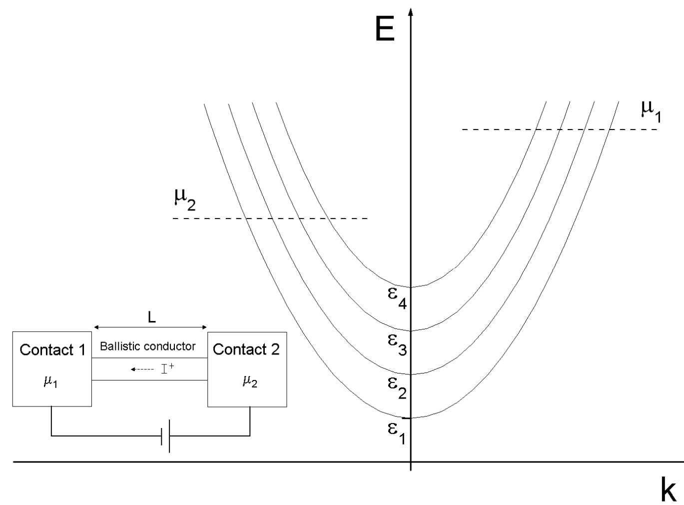

Figure 1-7: A schematic of a ballistic conductor sandwiched between two reflectionless contacts, and dispersion relations of the different transverse modes in the conductor. The reflectionless contacts (reservoirs) have quasi-Fermi levels of μ_1 and μ_2 . Adapted from Reference [34].

First, considering only a single mode, and assuming the $+k$ states are occupied according to a distribution function $f^+(E)$. For a uniform electron gas with electron density of n electrons per unit length, moving with velocity v, the current is env. Each k state has an electron density of 1/L, and $v = \hbar^{-1}\partial E / \partial k$, therefore the current becomes

$$I^+ = \frac{e}{L}\sum_k \frac{1}{\hbar}\frac{\partial E}{\partial k} f^+(E) \qquad (1\text{-}5)$$

the sum over k states can be converted into an integral using $\sum_k \rightarrow 2\times\frac{L}{2\pi}\int dk$, where the factor 2 accounts for spin degeneracy, thus the current becomes:

$$I^+ = \frac{2e}{h}\int_{\varepsilon}^{\infty} f^+(E) \quad dE \qquad (1\text{-}6)$$

where ε is the cutoff energy for the mode. Because the contacts are reflectionless, then the $+k$ states are occupied only by electrons originating at contact 1, and the $-k$ states are occupied only by electrons originating at contact 2. However, since all the states below μ_2 in contact 1 are occupied, the $-k$ states will not carry a current at zero temperature, and the current is entirely carried by the $+k$ states. In the case of a multi-mode wire Equation (1-6) can be generalized to the form:

$$I^+ = \frac{2e}{h}\int_{-\infty}^{\infty} f^+(E)M(E) \quad dE \qquad (1\text{-}7)$$

where $M(E)$ is the number of modes at an energy E (the number of modes for which $\varepsilon_N < E$). If we assume $M(E)$ is constant over the energy range $\mu_1 > E > \mu_2$, then Equation (1-7) can be written as:

$$I = \frac{2e^2}{h} M \frac{(\mu_1 - \mu_2)}{e} \qquad (1\text{-}8)$$

thus the conductance can now be identified as:

$$G_C = \frac{2e^2}{h} M \qquad (1\text{-}9)$$

therefore the conductance of a ballistic wire having *M* transverse modes is quantized in the amount of $2e^2 / h$. This corresponds to a contact resistance of:

$$R_C = (2e^2 / h)^{-1} \frac{1}{M} \qquad (1\text{-}10)$$

For single walled carbon nanotubes with only the 1st subband occupied, $M = 2$, leading to an ideal contact resistance of about 6.5 KΩ

The treatment above considers no scattering in the channel i.e. the probability that an electron transmitted at contact 1 reaches contact 2 is unity. If this probability is $T < 1$, then this causes part of the current I^+ to be reflected back into contact 1. This current is $I^- = (2e/h)M(1-T)(\mu_1 - \mu_2)$, and the net current becomes $I = (2e/h)MT(\mu_1 - \mu_2)$, thus the conductance now becomes:

$$G = \frac{2e^2}{h} MT \qquad (1\text{-}11)$$

which is the Landauer formula. This can be written as a sum of two resistances, a contact resistance, and a channel resistance, which are in series, as is shown below:

$$G^{-1} = (2e^2 / h)^{-1} \frac{1}{M} + (2e^2 / h)^{-1} \frac{1}{M} \frac{1-T}{T} \qquad (1\text{-}12)$$

where the first term can now be identified as the contact resistance given by Equation (1-10), and the second term is the actual channel resistance $G^{-1} = (2e^2/h)^{-1} \frac{1}{M}\frac{1-T}{T}$.

1.2.2 Ohm's law versus localization

An important question regards the situation when one or more conductors are joined in series. As will be shown below, their behavior depends on whether they are added incoherently or coherently i.e. whether phase information of the wave function propagating between them is destroyed or preserved (phase coherence will be discussed in detail in Chapter 5).

Consider two conductors with transmission probabilities T_1 and T_2 which are joined in series, as is shown in Fig. 1-8 below.

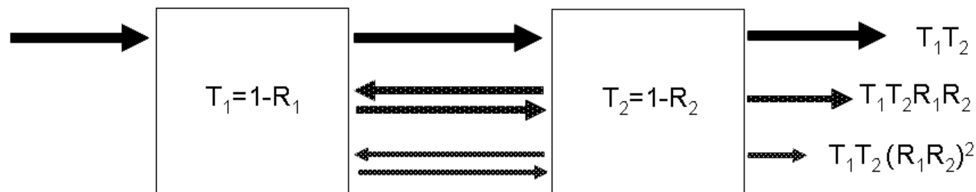

Figure 1-8: Two resistors connected in series having transmission probabilities T_1 and T_2 . If phase coherence is lost during the round trip, the overall transmission can be calculated as the sum of the probabilities of transmission with no reflection, with two reflections, with four reflections etc. Adapted from Reference [34].

In order to get the total transmission probability T_{12} across these two conductors, one needs not only to consider the directly transmitted portion of the wave function T_1T_2 , but also the multiply reflected portions between the conductors.

If the reflected portions do not have definite phase relationships, then the wave functions add incoherently, and the interference terms can be neglected. Thus T_{12} would be given by:

$$T_{12} = T_1 T_2 + T_1 T_2 R_1 R_2 + T_1 T_2 R_1^2 R_2^2 + ... = \frac{T_1 T_2}{1 - R_1 R_2} \qquad (1\text{-}13)$$

where R=(1-T) is the reflection coefficient. This can be written as:

$$\frac{1 - T_{12}}{T_{12}} = \frac{1 - T_1}{T_1} + \frac{1 - T_2}{T_2} \qquad (1\text{-}14)$$

Since the quantity (1-T)/T was found to define the resistance of a conductor with a transmission coefficient T, $G^{-1} = (2e^2 / h)^{-1} \frac{1}{M} \frac{1-T}{T}$ in Equation (1-12), then Equation (1-14) can now be interpreted as equivalent to a series addition of two resistors. To illustrate that Equation (1-14) leads to Ohm's law, consider the simple case of N identical scatterers with transmission coefficient T, equally distributed over a length of L, the total resistance can be written as (assuming M=1):

$$G_N^{-1} = (2e^2 / h)^{-1} \frac{1 - T_N}{T_N} = (2e^2 / h)^{-1} N \frac{1 - T}{T} \qquad (1\text{-}15)$$

and using $N = L / l$, where l is the distance between scatterers, then Equation (1-15) can be written as:

$$G^{-1}(L) = (2e^2/h)^{-1}\left(\frac{1-T}{T}\frac{1}{l}\right)L \tag{1-16}$$

which can be seen to be the 1-D version of Ohm's law $R(L) = \lambda L$, where λ is the 1-D resistivity, i.e. the resistance per unit length. Defining $l_0 = lT/(1-T)$, we can write Equation (1-16) as:

$$G^{-1}(L) = (2e^2/h)^{-1}\frac{L}{l_0} \tag{1-17}$$

Now considering the case where quantum interference effects are taken into account in the problem above (Fig. 1-8), in this case the transmission coefficient T_{12} becomes:

$$T_{12} = \frac{T_1 T_2}{1 - 2\sqrt{R_1 R_2}\cos\theta + R_1 R_2} \tag{1-18}$$

where θ is the phase shift acquired in one round trip between the scatterers. To obtain the scaling behavior, we need to obtain the ensemble average the resistance for all the possible arrangements of the two scatterers, i.e. for all the values of θ, defining the dimensionless resistance $\rho = (2e^2/h)G^{-1}$, we get:

$$\langle \rho_{12} \rangle = \left\langle \frac{1-T_{12}}{T_{12}} \right\rangle = \frac{1}{2\pi}\int \frac{1-T_{12}}{T_{12}} d\theta = \frac{1 + R_1 R_2 - T_1 T_2}{T_1 T_2} \tag{1-19}$$

where T_{12} is given by Equation (1-18), this can be seen to be different from Equation (1-13). This can be understood if Equation (1-19) is written as:

$$\rho_{12} = \rho_1 + \rho_2 + 2\rho_1\rho_2 \qquad (1\text{-}20)$$

we can see the presence of an extra term in addition to the classical sum of the two resistors, this is the interference term. Now considering a conductor of length L, where a small segment ΔL is added to it, and letting $\rho_2 \equiv \Delta\rho << \rho_1 \equiv \rho$, and assuming the small segment ΔL can be treated classically thus from Equation (1-17) $\Delta\rho = \Delta L / l_0$, then Equation (1-20) yields:

$$\frac{d\rho}{dL} \approx \frac{\rho(L+\Delta L) - \rho(L)}{\Delta L} = \frac{1+2\rho}{l_0} \qquad (1\text{-}21)$$

and for $\rho >> 1$ the solution would be:

$$\rho(L) = \frac{1}{2}\left[e^{2L/l_0} - 1\right] \qquad (1\text{-}22)$$

therefore, a single mode conductor with $R >> (2e^2/h)^{-1}$ has an exponential dependence on length that scales by $2/l_0$, which is the localized regime. This result applies to multimode conductors as well.

Thus whether one obtains $R(L)$ that is linear (Ohmic), or exponential (localized), depends on the preservation of phase coherence between scattering events. This will be discussed again in Chapter 4 in the context of my experimental results in carbon nanotubes.

1.2.3 Coulomb blockade

Coulomb blockade oscillations of conductance is a single electron charging phenomenon that happens when a small volume of a conductor or semiconductor (usually called 'island') is confined between two low transmittance tunnel junctions. This situation often happens in nanotube devices at low temperature, where a pair of defects might cause such confinement for a small segment of the nanotube channel or even for the whole nanotube channel if it is confined between low transmittance electrodes. A schematic for such a structure is shown in Fig. 1-9 below.

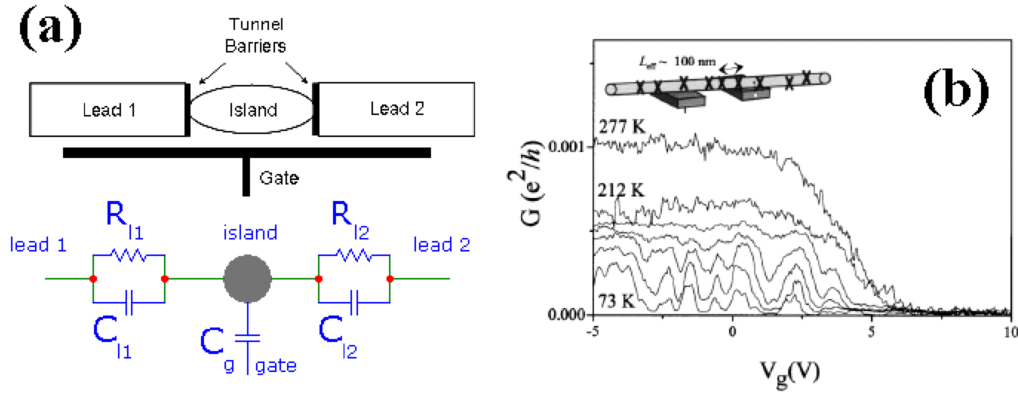

Figure 1-9: (a) Schematic of a confined region (island) connected through tunnel barriers to leads, and equivalent circuit. (b) Coulomb blockade oscillations observed in a semiconducting nanotube device at low temperature (from Reference [10]).

Since number of electrons N on the island can change only by discrete amounts, then for current to flow across the structure, the number of electrons must fluctuate between N and $N+1$. However, adding an electron to the island requires a charging energy

$$E(N+1) - E(N) = (N+1/2)e^2 / C_I \qquad \text{(1-23)}$$

where C_I is the capacitance between the island and the rest of the structure (leads and gate). If both temperature and bias voltage are smaller than the typical charging energy $E_C = e^2 / 2C_I$, then tunneling of that additional electron is energetically forbidden and no current flows. Thus one conditions to observe Coulomb blockade is $K_B T << E_C$. Another condition comes from the requirement that the time for the electron to tunnel off the island be large enough, such that its energy uncertainty is much smaller than the charging energy, i.e. $E_C > \delta E > h/\delta t$. The time scale δt for tunneling off the island could be estimated as the time constant RC_I where R is the

smaller of the resistances of the two tunnel barriers between the island and the leads. From that we get the condition $R > 2h/e^2$.

If the potential on the gate electrode is V_g, there would also be a change in the potential energy of the island due to the additional electron, which is given by:

$$\Delta U = -e(N+1)\frac{C_g}{C_I}V_g - (-eN)\frac{C_g}{C_I}V_g = -e\frac{C_g}{C_I}V_g \qquad (1\text{-}24)$$

where C_g is the capacitance between the island and gate only. This contribution is negative, i.e. the island with N+1 electrons has a lower potential energy than when it has N electrons. Therefore, the two contributions might balance out, equating (1-23) with (1-24), then the V_g values at which this occurs are:

$$V_g = \frac{e}{C_g}(N + \frac{1}{2}) \qquad (1\text{-}25)$$

at these V_g values, the N and N+1 situations are degenerate, and tunneling is permitted. Thus Coulomb blockade appears as periodic oscillations of conductance as a function of gate voltage, with a period of e/C_g.

The above ‘classical’ Coulomb blockade picture mainly applies to metallic islands where the energy level separation ΔE is much lower than $K_B T$ and can be considered a continuum. However, in cases where the density of states is low, as in a 2-D electron gas or carbon nanotubes, ΔE might exceed $K_B T$ and can be comparable to E_C. This adds an additional constraint on tunneling since now it has to happen

through single levels. Therefore the energy levels in the island need to be aligned with the Fermi level in the leads. In this case, the energy for adding an electron becomes the sum of ΔE and E_C .

1.3 Basics of atomic force microscopy

Since its introduction in 1986 by Binnig, Quate, and Gerber [38], the atomic force microscope (AFM) have been extensively used for imaging and characterizing surfaces. An AFM has five essential elements: (1) the force sensor which usually consists of a sharp tip (with typical tip size between 10-40 nm), this is attached to the end of a micro-cantilever (with typical force constant of 1-50 N/m), the force between the surface and tip is reflected as a deflection of the cantilever; (2) a method to detect the deflection of the cantilever, the most popular method being the optical lever configuration [39], in which a position sensitive photodetector (PSPD) is used to monitor the reflection of a laser beam off the end of the cantilever; (3) a feedback loop, to keep the selected control parameter (which depends on the operation mode, see below) constant; (4) positioning elements, these are used to change the lateral (XY) sample position in order to scan a specific area, or change the vertical (Z) position in response to the feedback loop such that the feedback control parameter is kept constant, these elements are usually constructed from piezoelectric materials; (5) a data acquisition and signal processing unit, in order to reconstruct the surface image. These units are schematically shown in Fig. 1-10 below.

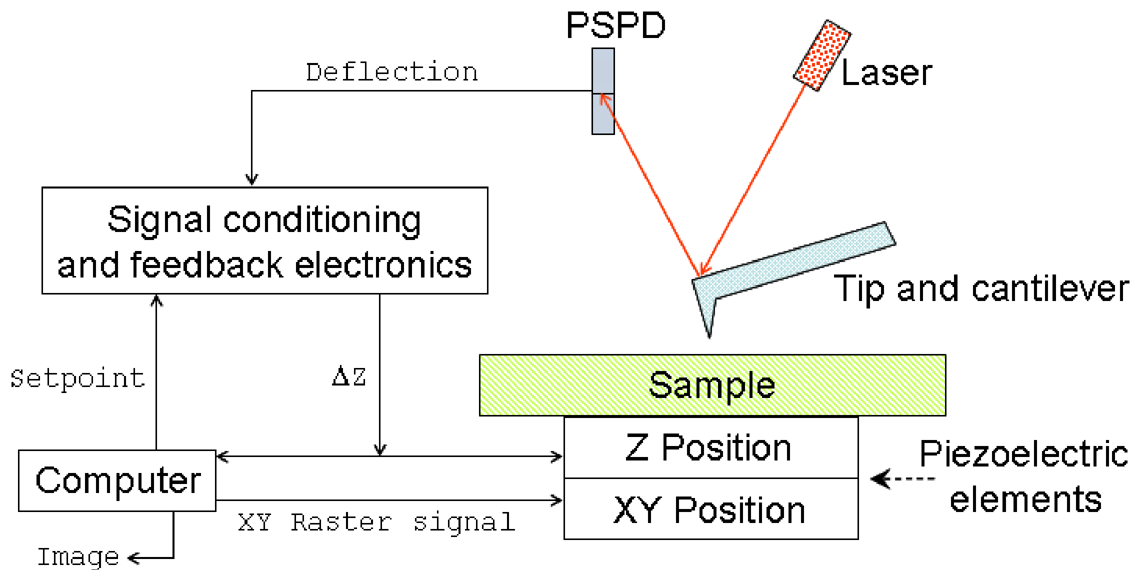

Figure 1-10: Basic components of an atomic force microscope (see text). ΔZ is the change in tip-surface distance needed to keep the control parameter equal to the setpoint. The image is constructed from $\Delta Z(X,Y)$.

In the absence of external electric or magnetic fields, and if the sample surface has no adsorbed meniscus layer, the tip-surface interaction force is dominated by the attractive Van der Waals force for small tip-surface distances, and by the repulsive contact force as the tip begins to touch the surface. The tip-surface interaction force as a function of the tip-surface distance is sketched in Fig. 1-11 below. This allows for three modes of operation.

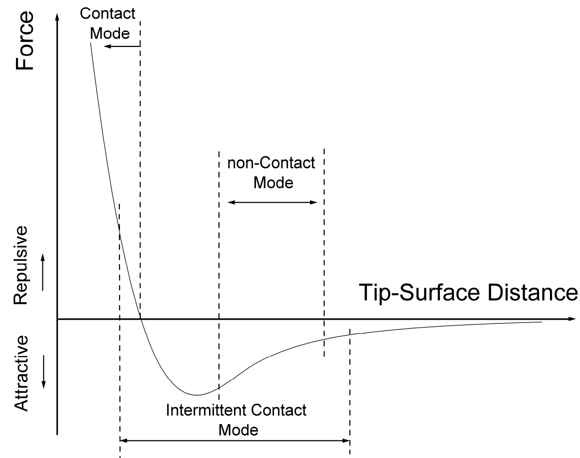

Figure 1-11: Tip-surface interaction force as a function of tip-sample distance. The operation regions for the three basic AFM modes are indicated (see below).

In contact mode, the tip is always touching the surface i.e. operation is always in the repulsive regime. The feedback control parameter is usually taken to be the deflection of the cantilever. As the tip encounters changes in the topography, the deflection consequently changes, and the feedback loop changes the Z position of the sample such that the deflection is kept at a predetermined setpoint. Contact mode enables the measurement of parameters that require an intimate contact between the tip and the surface, like local friction or conductivity. However it has the disadvantage of applying a large force to the surface which could result in damage to the tip or sample.

In non-contact mode the tip is vibrated with a small amplitude near its resonant frequency (usually at the first harmonic) while hovering above the surface, therefore this mode works exclusively in the attractive Van der Waals regime. The feedback control parameter is usually taken to be either the amplitude of the vibrations or the resonant frequency of the cantilever. The presence of the force gradient changes the effective force constant of the cantilever and therefore its

resonant frequency, amplitude, and phase. As the tip encounters changes in topography, these parameters consequently change, and the feedback loop changes the Z position of the sample such that either the amplitude or resonant frequency are kept at a predetermined setpoint. Non-contact mode has the advantage of applying a very small force to the sample surface, and its high resolution. However, it is hard to implement under ambient conditions due to the effects of the adsorbed water meniscus (which I will discuss shortly), it also works best only for relatively flat samples.

The last mode is the intermittent contact mode (also called AC mode or tapping mode). This mode is generally similar in implementation to non-contact mode. However, here the amplitude of cantilever vibrations is large, such that the tip actually contacts the surface in each vibration cycle, and the force gradient affecting the cantilever is mainly due to the repulsive part of the tip-sample force. This is the most versatile of the three modes. It can be readily operated under ambient conditions, and can be used to scan large area samples with diverse topography, while still applying a small force to the surface of the sample.

Under ambient conditions, an adsorbed film consisting of several monolayers of water is usually present on hydrophilic surfaces like quartz or SiO_2. Due to capillary effects, this meniscus layer causes an adhesion force between the tip and the surface. The magnitude of this adhesion force mainly depends on the ambient humidity [40]. In contact mode, this adhesion force increases the tip-surface force during scanning, thus increasing the possibility of wear or damage to the tip or surface. In non-contact mode, the meniscus layer can create blurriness and imaging

artifacts [41], since now the tip mainly interacts with the surface of the meniscus rather the real surface of the sample. AC mode however is not affected much by the meniscus layer as long as the amplitude of the cantilever is large enough to penetrate the layer and break free off it [42].

Other than scanning, some local properties like elasticity, adhesion, or hardness, might be explored at a specific point using force-distance curves (often called 'force curves'). In this procedure the deflection of the cantilever is monitored while it is moved in the direction normal to the surface (Z direction).

In the absence of a meniscus layer or any long range attractive force like electrostatic forces, the behavior is simple. Assuming the tip starts from a position where it is not in touch with the surface and is gradually lowered, the force curve behaves according to the following steps: (1) the deflection remains almost zero (it experiences the attractive Van der Waals force, however this is usually very small for distances beyond ~0.5 nm); (2) The tip contacts the surface (assumed to be a hard surface), it experiences a large repulsive contact force, the force is related to distance ΔZ by $F = k\Delta Z$, where k is the cantilever force constant, and ΔZ is measured from the contact point (since the deflection is proportional to force as is known from beam bending theory, the deflection too would be proportional to distance); (3) upon retraction of the tip during unloading, the deflection gradually decreases; (4) the deflection becomes constant again as the tip no longer contacts the surface. These steps are shown in Fig. 1-12 below.

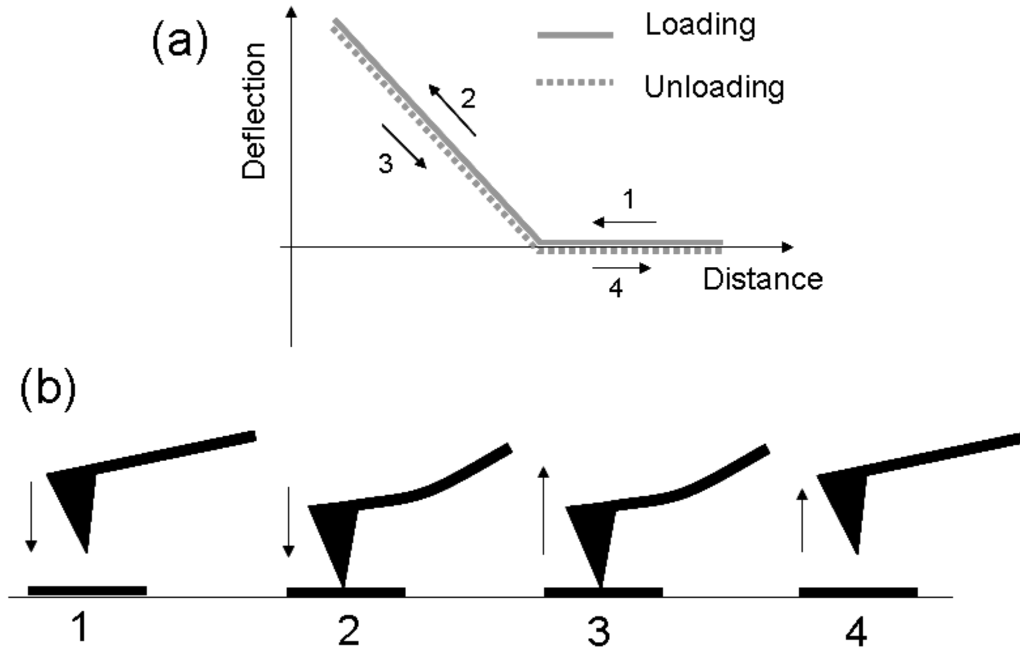

Figure 1-12: (a) Force curve in the absence of adhesion. (b) Schematic of the tip-sample positions corresponding to the regions of the force curve shown in (a), see the text above for details.

If a meniscus layer is present (which is usually the case for operation under ambient conditions), the behavior becomes more complex, this can be summarized in the following steps (assuming again the start position where the tip does not contact the surface): (1) tip approaches the surface, no deflection; (2) tip contacts the meniscus layer, the capillary force pulls down the tip into contact with the surface, and the cantilever bends downward causing a small negative deflection; (3) as the tip is lowered further, it experiences the repulsive contact force, the cantilever starts to bend upwards and deflection increases from the initial negative value to a positive value; (4) as the tip is moved up during unloading, the deflection decreases till the contact force becomes in equilibrium with the capillary force, and the deflection becomes zero; (5) as the tip keeps on retracting, the capillary force holds onto the tip, the cantilever bends downwards and the deflection is negative; (6) with further

retraction, the tip finally breaks free form the meniscus layer and sharply rebounds upwards, and deflection goes back to zero; (7) tip moves away, deflection remains zero. These steps are illustrated in Fig. 1-13 below.

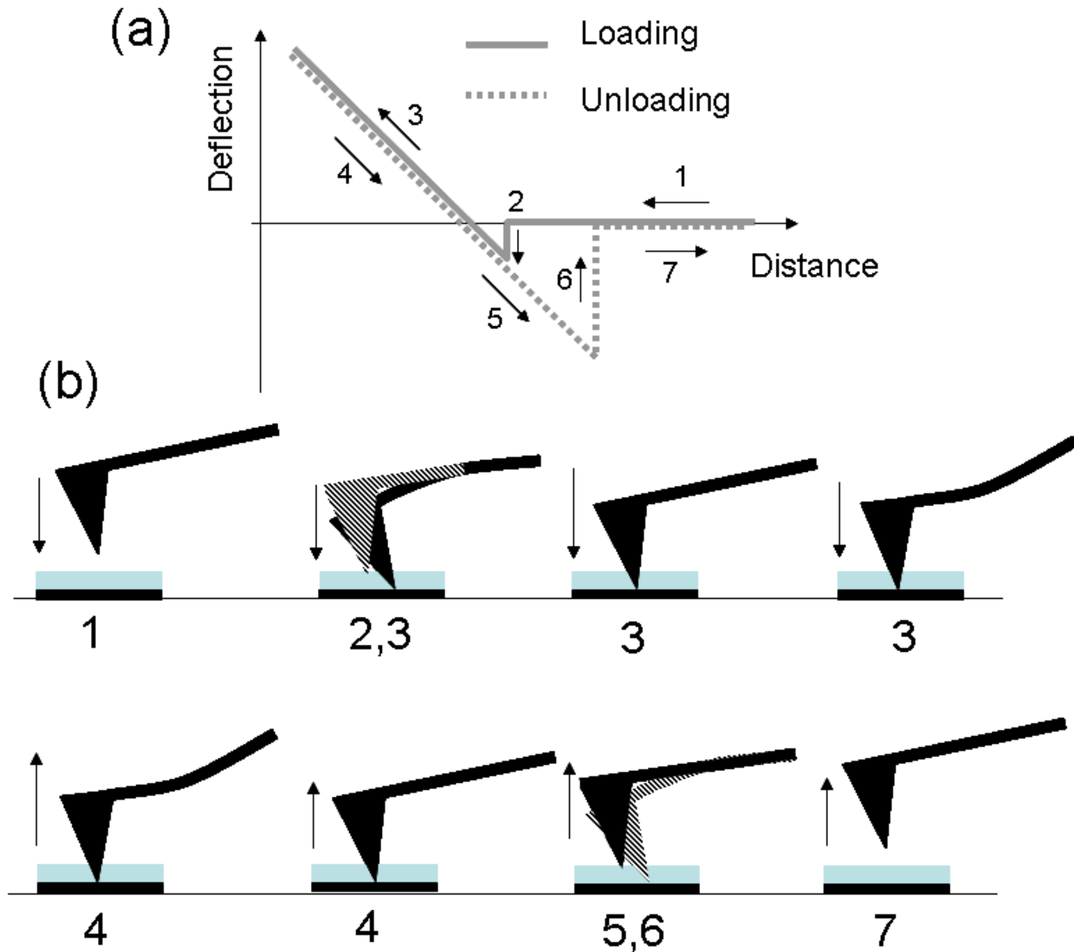

Figure 1-13: (a) Force curve in the presence of a meniscus layer. (b) Schematic of the tip-sample positions corresponding to the regions of the force curve shown in (a), the cyan rectangle above the sample surface represents the meniscus layer. See the text above for details.

I used force curves extensively in order to establish contact with carbon nanotubes using a conductive AFM cantilever. This will be discussed in detail in Chapter 3.

1.4 Review of previous experimental work

In carbon nanotube devices, the standard four-probe measurement technique to eliminate contact effects usually fails, mostly because of the invasiveness of the metallic voltage probes [43]. Many other techniques have been devised to study the intrinsic response of the nanotube channel. Some of these techniques involve using a conductive AFM cantilever as a local electrical contact, for instance to record resistance versus length measurements in contact mode [44], injecting current locally in AC mode [45, 46], or establishing a contact at selected positions in two [8, 33, 47], and three-probe [13, 48] configurations. AFM has also been employed in electrostatic force microscopy (EFM) to reveal the potential drop across nanotube devices [49], and in scanning gate microscopy to reveal the distribution of defects in the channel [49-52]. Other techniques include using non-invasive multiwalled carbon nanotubes voltage probes in a four probe configuration [53], studying multiple devices of various lengths all patterned on one long nanotube [24], studying telescopically extended multiwalled nanotubes [54], and studying a large number of devices that have different channel lengths built using different nanotubes [11, 55]. I will briefly discuss each of these techniques below.

For scanned probe techniques like conductive contact mode [44] and pulsed current injection in AC mode [45, 46], the main advantage is obtaining a quick image of the position-dependent conductance within the scanning range. However, the contact with the nanotubes is only transient and, as I established previously in Chapter 3, the current most likely does not reach the force-independent regime.

Attempting to solve this problem by using a larger force while scanning is potentially damaging to the nanotube and/or probe especially in the contact mode method. Additionally, because the technique relies on measurement of fast transient current pulses, the data may be influenced by the changing impedance as the nanotube channel length changes, and correcting for this effect may be difficult, since this impedance is not known independently. Therefore, I believe the data obtained from these methods should be viewed as qualitative. Such qualitative methods might be useful in studying large-area heterogeneous conductive networks like nanotube mats, where obtaining the overall conductance map is more important than transport measurements at specific points. An example of data obtained using the AC current injection method is shown in Fig. 1-14 below.

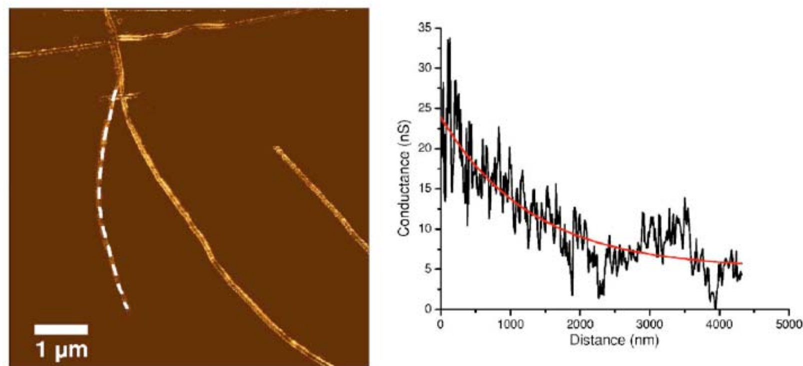

Figure 1-14: Conductance map and the corresponding conductance versus length data obtained using the AC current injection method, from Reference [46].

Multiwalled CNTs have been demonstrated to make minimally invasive voltage probes to single-walled CNTs [53]. However, this technique requires AFM manipulation in order to change the channel length, making this technique rather difficult and limited only to short (1-2 μm) channel lengths. For telescopic extension

of multiwalled nanotubes [54] the obtained data reflects both channel transport properties and tunneling between the walls which may also depend on length and it can be hard to separate the two.

The study of ensembles of nanotube devices can reveal important trends [11, 55], but the absence of detailed knowledge about contact resistance, and individual defects in each device makes the data useful only in a statistical sense, while explaining any deviation from the general trend becomes only a subject of speculation. Some of these disadvantages can be lifted by using other techniques alongside, like SGM or EFM [11]. The technique of building many devices of various lengths on one long nanotube [24] is quite similar, with the added advantage of having the same nanotube (i.e. same chirality) in all the devices; however it can still be subject to variations in contact resistance. Also, while it is reasonable to assume that the distribution of the more common point-like defects should be similar in the various segments, there is still the possibility of a rare strong defect occurring in at least one of the segments, thus altering the obtained trend. These two methods in general have one big advantage over AFM-based techniques, that they easily allow a larger range of manipulations to be performed on the samples like studying temperature dependence, or applying a large gate voltage. An example of the data obtained from many devices built on one long CNT is shown in Fig. 1-15 below.

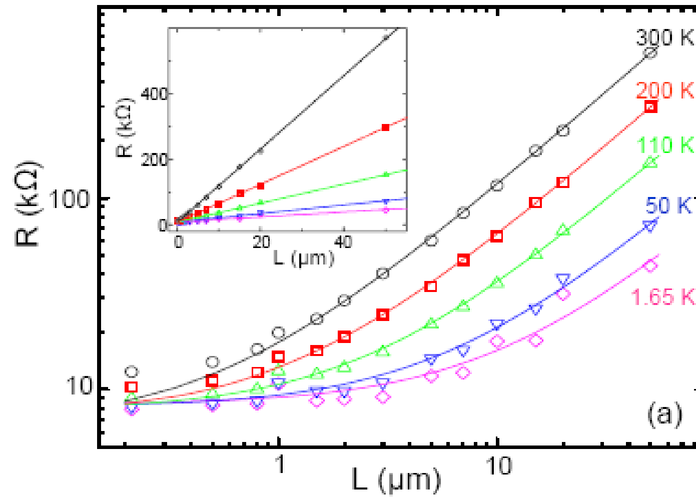

Figure 1-15: Resistance versus length data obtained from different length devices all patterned on one long nanotube. Inset is the same data on a linear scale. From Reference [24].

EFM reveals the potential distribution in the channel of a nanotube device by monitoring the amplitude of the cantilever oscillations as a small AC voltage is applied across the sample. SGM reveals the defect distribution in the channel of a nanotube device by observing the sensitivity of the current flow across the channel to local gating by an AFM cantilever [49]. This technique is rather qualitative, though some efforts [51, 56] have been made to extract quantitative data about the size of the defect potential barriers. Because of its local nature, it might be hard to reconcile the data obtained using this method with global transport properties across the channel determined by all the defects together. Examples of data obtained using these two methods are shown in Fig. 1-16 below.

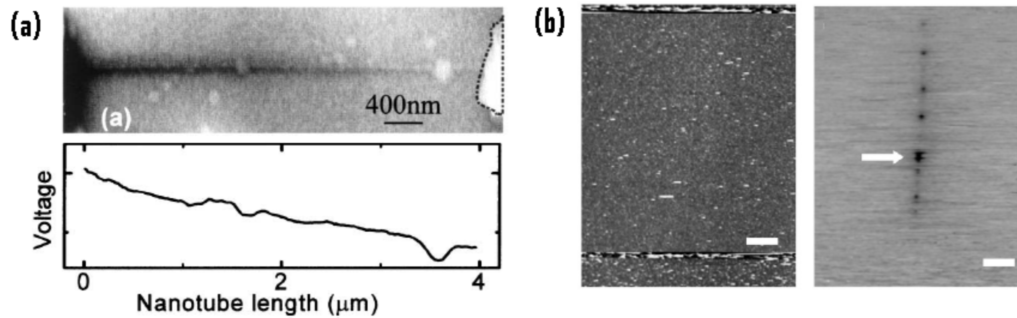

Figure 1-16: (a) EFM image and the corresponding EFM signal as a function of nanotube length, from Reference [49]. (b) Nanotube device and the corresponding SGM signal revealing the defect sites in the device, from Reference [52]. Scale bar in (b) is 2 μm.

Local contact to a CNT at select positions using a conductive AFM cantilever has been employed in two geometries. In the three-terminal mode [13, 48], two fixed electrodes are used to pass a current along the device, while a conductive AFM cantilever is used to sense the potential at each point. The advantage of this method is its insensitivity to the details of the probe-nanotube contact resistance; as long as it is much lower than the input impedance of the device used to record the potential. However if the contact with the cantilever causes some permanent change in the nanotube at the contact point, possibly in the form of contamination or by creating a defect, then this would affect any subsequent measurement. Also, it is unclear whether localization (evidenced by a non-linear dependence of resistance on length) can be detected using this method since localization is a property of the conductance of the whole system rather than a property of the potential distribution across the system. An example of the data obtained using this method is shown in Fig. 1-17 below.

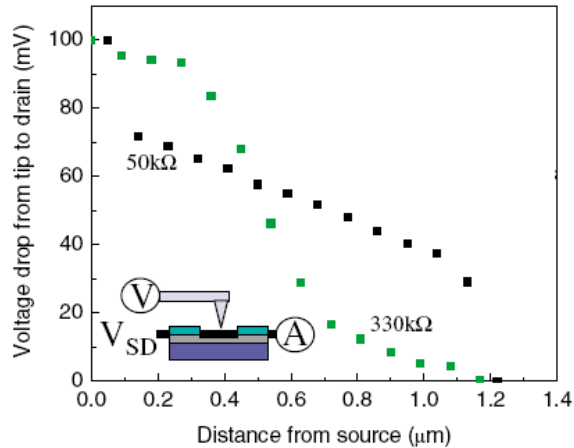

Figure 1-17: Profile of voltage drop along a nanotube device at two different gate voltages obtained using the three-terminal method, from Reference [48].

In the two-terminal mode [8, 33, 47], a single static electrode is used while the conductive AFM cantilever serves as a second movable electrode to obtain the current response of the channel at various distances away from the static electrode. This is the method I have adapted in the current work; in the next section I will explain the details of my measurement technique. The main advantage of this method is the straightforward interpretation of the data, and the main disadvantage is that the contact resistance between the nanotube and the cantilever might change every time the contact is established. As I demonstrated in Chapter 3, if the contact resistance is not taken properly into account, it could result in smearing out or even creating a false trend in the data. This may have been a problem in earlier studies [8, 33, 47, 57] ; hence the protocols for establishing a reproducible contact to the CNT discussed in Chapter 3 prompt a re-examination of the length-dependent resistance of CNTs. An example of the data obtained using this method is shown in Fig. 1-18 below.

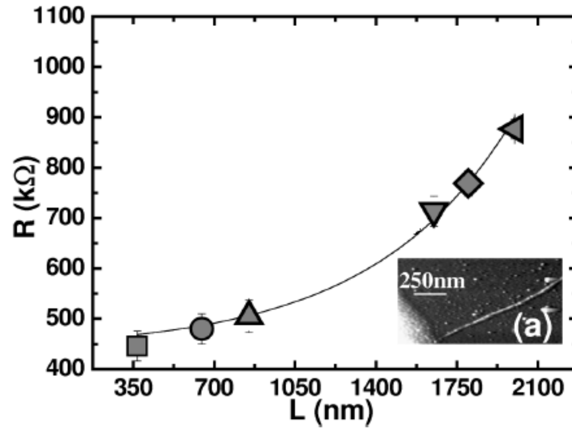

Figure 1-18: Resistance versus length along a carbon nanotube device obtained using the two-terminal method, from Reference [33].

There is some inconsistency in the previous work regarding the dependence of resistance on length in carbon nanotubes. While some work indicates a linear dependence [24, 48], others indicate a non-linear dependence [33, 46, 47, 54]. Understanding this is one of the main motivations of the current work.

In Chapter 2, I will describe the preparation of the carbon nanotube samples used in the current study, along with the AFM nanolithography procedure to perform length-dependent electrical transport measurements in a two-terminal configuration.

In Chapter 3, I will show experimental measurements concerning the characterization of the contact between a metal-coated AFM cantilever and carbon nanotubes. I will discuss the parameters controlling that problem, and a model that explains the observed behavior. I will use the results to establish a protocol for contact carbon nanotubes with a conducting AFM tip in order to produce a contact whose resistance is fairly reproducible and independent of contact force or bias voltage.

In Chapter 4, I will report length dependent electrical transport measurements for several semiconducting and metallic carbon nanotubes. I will discuss the observed behavior in terms of the interplay between contact effects, doping, disorder, and phonon scattering.

Chapter 5 is a separate unit from the first four chapters. There, I treat the problem of phase coherence time saturation in quasi one-dimensional metallic conductors at low temperatures. I begin by reviewing the problem, and this is followed by a description of the experimental setup. After that I will show my experimental results for the phase coherence time in quasi one-dimensional silver wires measured using both weak localization and universal conductance fluctuations, and comment on the observed behavior.

Chapter 2: Sample preparation and setup for performing local transport measurements on carbon nanotubes

This chapter describes various experimental aspects for performing local transport measurements on carbon nanotubes. I begin with a description of carbon nanotube sample preparation, followed by a description of the atomic force microscope (AFM) cantilevers used in the measurement. Finally I will describe the measurement setup employing an AFM, including the AFM nanolithography program used to obtain the measurements described in Chapters 3 and 4.

2.1 Sample preparation

Sample preparation involves first preparing carbon nanotubes on a SiO_2/Si substrate via chemical vapor deposition, and second preparation a fixed gold electrode by shadow evaporation. These two steps are described in detail below.

2.1.1 Chemical vapor deposition (CVD) of carbon nanotubes

The first step in fabricating the samples is growth of carbon nanotubes using chemical vapor deposition (CVD) [58-60]. In this method, metallic nanoparticles dispersed on the surface of the substrate catalyze the dissociation of carbon

containing gases (feedstock gases) at high temperatures; the resulting carbon dissolves into the nanoparticles and is extruded as carbon nanotubes.

The substrate used is heavily-doped Si with a 500 nm oxide layer. CVD is performed in a quartz tube oven, as is shown schematically in Fig. 2-1 below. More details of this CVD setup can be found in References [61, 62].

Two CVD recipes have been employed; the first follows closely that of Reference [58], the source of iron nanoparticles is a solution of ferritin (a biological protein complex containing ~4500 Fe atoms; commercially obtained from Atomate corporation) in DI water at a concentration of 200 μg/ml. The details of this recipe are as follows:

- Soak samples in ferritin solution at 4 ^{o}C overnight
- Rinse in DI water and blow dry
- Calcine in air for 5 min. at 800 ^{o}C (this removes the organic shell of ferritin, leaving Fe_2O_3 nanoparticles on the surface)
- Heat in oven to 900 ^{o}C
- Pass mixture of methane (200 sccm) and hydrogen (200 sccm) for 10 minutes (hydrogen reduces Fe_2O_3 nanoparticles into Fe nanoparticles, and methane is the feedstock gas)
- Cool down to room temperature in a flow of argon

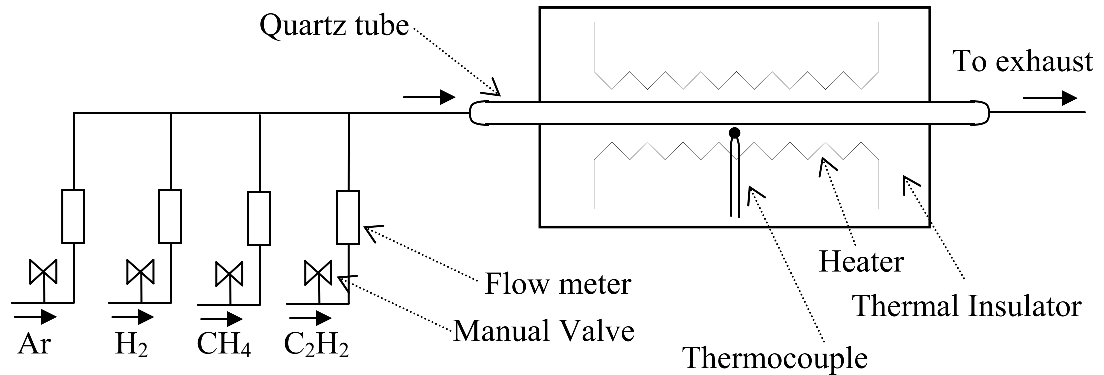

Figure 2-1: Details of the quartz tube furnace used for CVD growth of carbon nanotubes. The heater and the thermocouple are connected to a temperature controller (not shown).

The second recipe follows the catalyst preparation procedure of Reference [59] where the source of iron nanoparticles is a solution of ferric nitrate $Fe(NO_3)_3$ in isopropanol (typically a 20-10 μg/ml solution is used to get well dispersed nanotubes), the details of the recipe are as follows:

- Dip samples into ferric nitrate solution for about a minute
- Dip samples into hexanes for a few seconds (this deposits $Fe(NO_3)_3$ nanoparticles on the surface)
- Heat samples in oven to 850 ^{o}C under a flow of argon
- Turn off argon flow, and pass a mixture of 1900 sccm hydrogen, 1300 sccm methane, and 18 sccm ethylene for 10 minutes (hydrogen reduces $Fe(NO_3)_3$ nanoparticles into Fe nanoparticles, methane and ethylene are the feedstock gases)
- Cool down to room temperature in a flow of argon

After growth, the samples were characterized by taking a few AFM scans at random positions to determine the degree of dispersion of the nanotubes produced, and only samples with well separated nanotubes are selected. The typical diameter of the nanotubes grown using both recipes was around 2 nm.

2.1.2 Evaporation of fixed electrode

The metal selected for the contacts is gold. As will be discussed in detail in Chapter 4, gold has a high work function (5.1 eV), and has been reported before to form ohmic contacts to nanotubes [33, 48].

I used shadow masking and thermal evaporation to define a fixed gold electrode on the surface of the samples after nanotube growth. The second (movable) electrode is a gold-coated AFM cantilever as will be explained shortly. Shadow evaporation offers several advantages: (1) it is rather simple compared to lithography-based methods, it only requires coarse alignment of the mask such that the produced edge is normal to the direction of gas flow during nanotube growth, because the nanotubes tend to be oriented along that direction; (2) it keeps the nanotubes in their pristine as-grown state, the nanotubes never get coated with resist or exposed to chemicals during development or liftoff (however it have been recently shown [63], that acrylic-based resists which are commonly used in e-beam lithography can be completely cleaned off the surface of carbon nanotubes); (3) with the proper areal density of grown nanotubes (which is controlled by the dispersion of the catalyst), many devices can be obtained at once (however their positions are unknown, and they

need to be located using an AFM or an SEM); (4) because there is no liftoff step, gold can be evaporated directly onto the surface without a sticking layer (usually Cr or Ti) therefore there is no need for the annealing step [48] required in that case in order to improve the contact resistance.

I usually used either a thin glass slide (thickness ~ 0.25 mm), or the cleaved edge of a silicon wafer (thickness ~0.37 mm) as shadow masks. Both of these offered relatively straight, sharp edges (they had microscopic non-uniformities though). The selected mask was then directly held against the sample surface using a metallic clamp, this was done in order to reduce penumbra effects and therefore improve the sharpness of the edge of the evaporated film. The masked sample was then installed in a thermal evaporator and the desired thickness of gold (99.999 % pure) is deposited. After that the mask is gently removed. To prevent electrical shorts to the silicon backgate, the gold close to the edges of the sample is mechanically removed using a sharp wooden tip (with no sticking layer, the gold film easily peels off the SiO_2 surface). The sample is then fixed to a suitable holder and wire bonded, Fig. 2-2 below illustrates the various steps of sample fabrication.

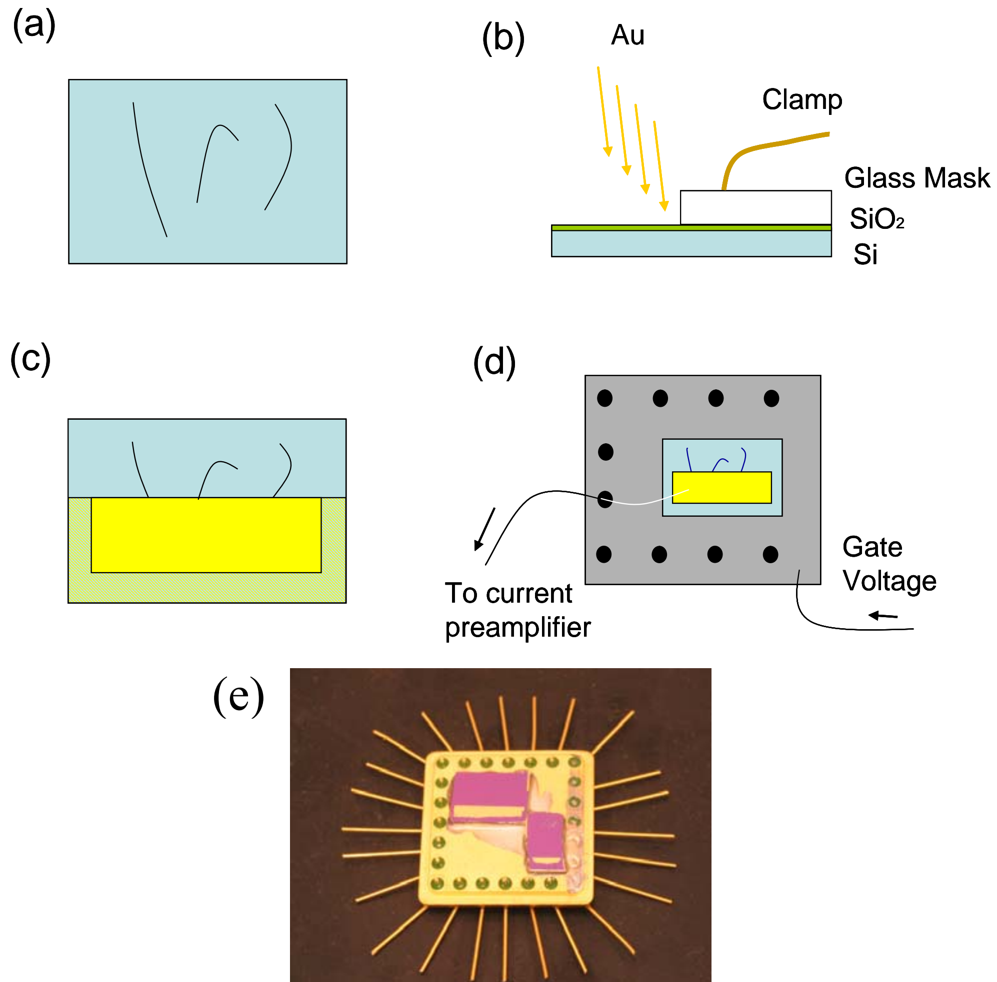

Figure 2-2: Illustrations of sample preparation steps. (a) CVD of carbon nanotubes; (b) shadow evaporation of fixed gold electrode; (c) mechanical removal of excess gold; (d) fixing to a suitable holder and wire bonding. A photograph of two finished samples bonded to a holder is shown in (e). The purple rectangles are the SiO_2/Si substrates, the small gold rectangles within purple rectangles are the fixed gold electrodes. The holder is about 20x20 mm.

The main disadvantage I found about the shadow-mask evaporation technique is the lack of sharpness of the gold edge produced. Close examination of the AFM scans near the fixed electrode revealed that while the electrode edge is sharply defined, it is followed by a thin long-decaying profile on the surface of SiO_2. Fig. 2-3

below shows the typical height profile obtained using the shadow mask evaporation method compared with an edge defined by e-beam lithography.

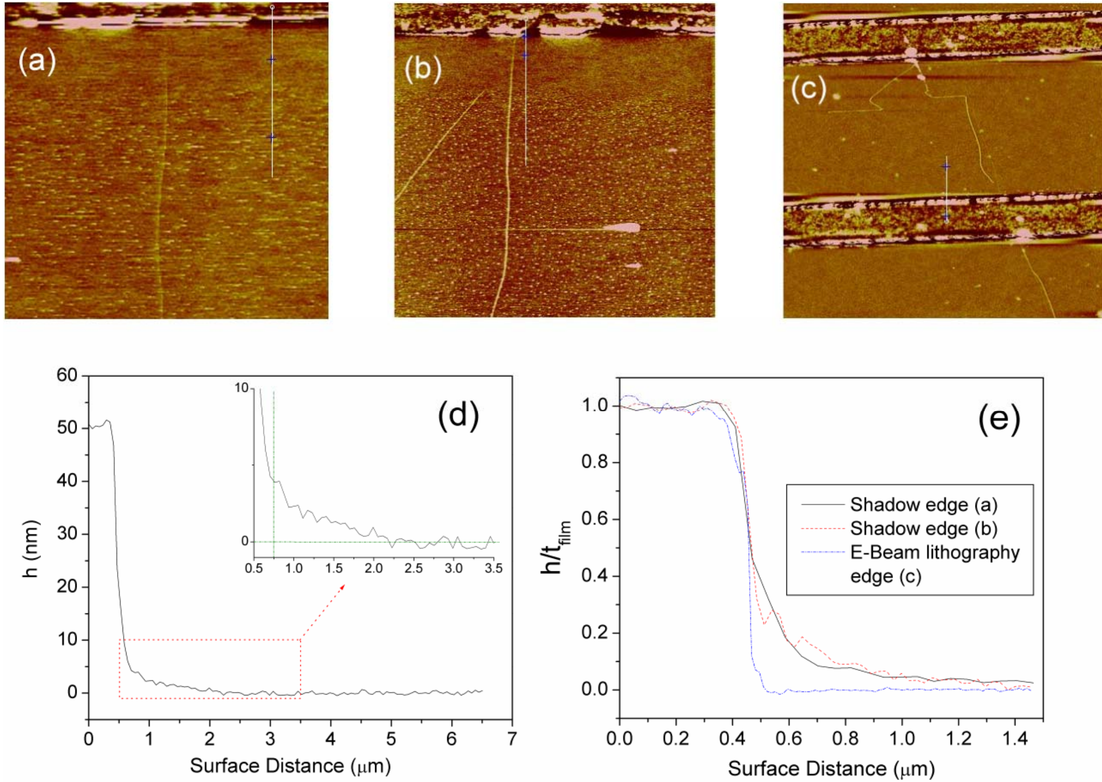

Figure 2-3: Comparison of shadow-evaporated edges and an edge defined by e-beam lithography; (a) and (b) show shadow-evaporated gold edges, images are 11.8x11.8 μm and 13.8x13.8 μm respectively; (c) shows gold lines defined by e-beam lithography (device courtesy of Y. F. Chen), images is 7.2x7.2 μm; (d) height profile across the shadow-evaporated edge shown in (a); (e) comparison of three sections (indicated by the white vertical lines) across the edges in (a), (b), and (c) the heights are normalized by the total thickness of the evaporated gold films.

The thickness of this long tail ranges roughly from 5 nm in the immediate vicinity of the electrode and decays into a thickness of less than 0.5 nm typically within a distance of 1.5-2 μm. This range of thickness is lower than the electrical percolation threshold for gold on SiO_2 which is about 16 nm [64] and therefore the gold film is not electrically conductive in the tail region, and consists of isolated

grains, or islands of metal. However, the presence of this extended tail of gold islands somewhat affects the transport properties of carbon nanotubes as will discussed in Chapter 4. For the rest of this work, this extended tail of gold islands will be referred to as the ‘gold island band’.

2.2 Cantilever preparation

Two types of cantilevers have been used for measurements, FESP and LTESP (both from Veeco instruments). FESP cantilevers have a nominal force constant of 2.8 N/m and will be referred to throughout this work as ‘soft cantilevers’. LTESP cantilevers have a nominal force constant of 48 N/m and will be referred to throughout this work as ‘hard cantilevers’. Both types have a nominal length of 225 μm, a tip (cone) height of 10-15 μm and are made of silicon.

In order to make the cantilevers conductive, the raw Si cantilevers are coated with gold using thermal evaporation. Because gold does not adhere well to silicon dioxide, a 50-60 nm thick layer of titanium was evaporated first on the cantilevers, followed by 60-90 nm of gold, this outer gold coating is what contacts the nanotubes. This composite metallic coating has proven to be quite durable, enduring hundreds of contacts to the sample surface before any significant erosion is observed (this will be discussed in detail in Chapters 3 and 4).

2.3 Measurement setup

2.3.1 Variables of the problem

The measurements are performed in a two-terminal field effect transistor (FET) configuration with one terminal being the fixed gold electrode, and the other being the movable metal coated cantilever.

Positioning the movable electrode (cantilever) requires three inputs to the measurement system. X and Y positions of the cantilever determine the point on the nanotube where the contact is made, which determines the length L of the nanotube channel. The Z position determines the deflection of the cantilever hence the contact force. The deflection is recorded using a photodetector monitoring a laser beam reflecting off the free end of the cantilever.

Two voltages bias the nanotube device, the drain voltage V_d (considering the fixed electrode as the grounded source) is applied to the conductive cantilever, the gate voltage V_g determines the depletion state of the device and is applied to the Si backgate. Both voltages determine the drain current I_d flowing through the channel, which passes through a current preamplifier whose voltage output is monitored.

All the above amount to five inputs to the system (X, Y, Z, V_g, and V_d) and three outputs (L, I_d and deflection). This is shown schematically in Fig. 2-4 below.

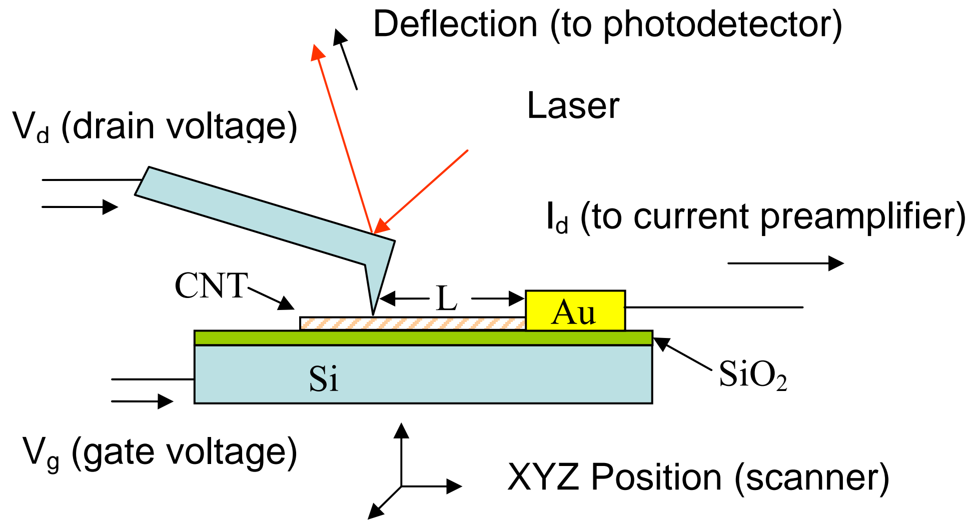

Figure 2-4: Schematic of the measurement system, X and Y positions of the scanner determine the channel length L, Z position determines the deflection (contact force), V_d and V_g determine the current through the channel I_d .

2.3.2 Instrumentation

The AFM used is a model Dimension 5000 from Veeco instruments, which is also equipped with a closed loop scanner (model NPXYZ100B from nPoint, Inc.) which offers high linearity and low hysteresis for positioning applications. The positioning commands of the scanner are sent through a USB connection. A data acquisition card (PCI-MIO-16XE-10 from National Instruments) provides V_{d} and V_{g} from digital to analog converters. It also monitors the deflection signal from the Dimension 5000 photodetector, and the voltage output from the current preamplifier (model 1211 from DL Instruments) through analog to digital converters. All the input/output signals mentioned above have a range of ±10 V. Figure 2-6 below shows a view of the AFM with the sample installed.

Both the USB positioning signal and the data acquisition card are controlled by a LabVIEW based nanolithography program that I designed for the purpose of obtaining local transport measurements in carbon nanotubes; this will be explained in detail in the next section.

2.3.3 Measurement procedure

As described before, the sample consists of nanotubes contacted on one end by the fixed gold electrode, and the other end by the gold coated cantilever which needs to be correctly positioned such that it contacts the nanotube somewhere between the free end and the fixed electrode. The first step is to perform AFM scans (in AC mode) near the edge of the fixed gold electrode (Fig. 2-5-c) at various positions, until a suitable nanotube is found. Then an AFM scan of suitable size (usually 35x35 μm) is recorded, which serves as a reference for the positions along the nanotube. At this point the nanolithography program can be started.

The measurement procedure begins by stopping the AFM scanning motion as well as stopping the AC vibrations of the cantilever, followed by moving the cantilever to the center of the frame, which serves as a reference for all consequent positioning commands. The previously recorded AFM image of the surface is imported into the nanolithography program as a position reference.

The main functions of this nanolithography program can be divided into two groups, the contact control group, and the sweeping/measurement group. The function of the contact control group of commands is to achieve and fine-tune the

contact between the conductive AFM cantilever and the nanotube. The function of the sweeping/measurement group is to study the response of the outputs (I_d and deflection) to a single input or a combination of inputs (Z position, V_g , V_d).

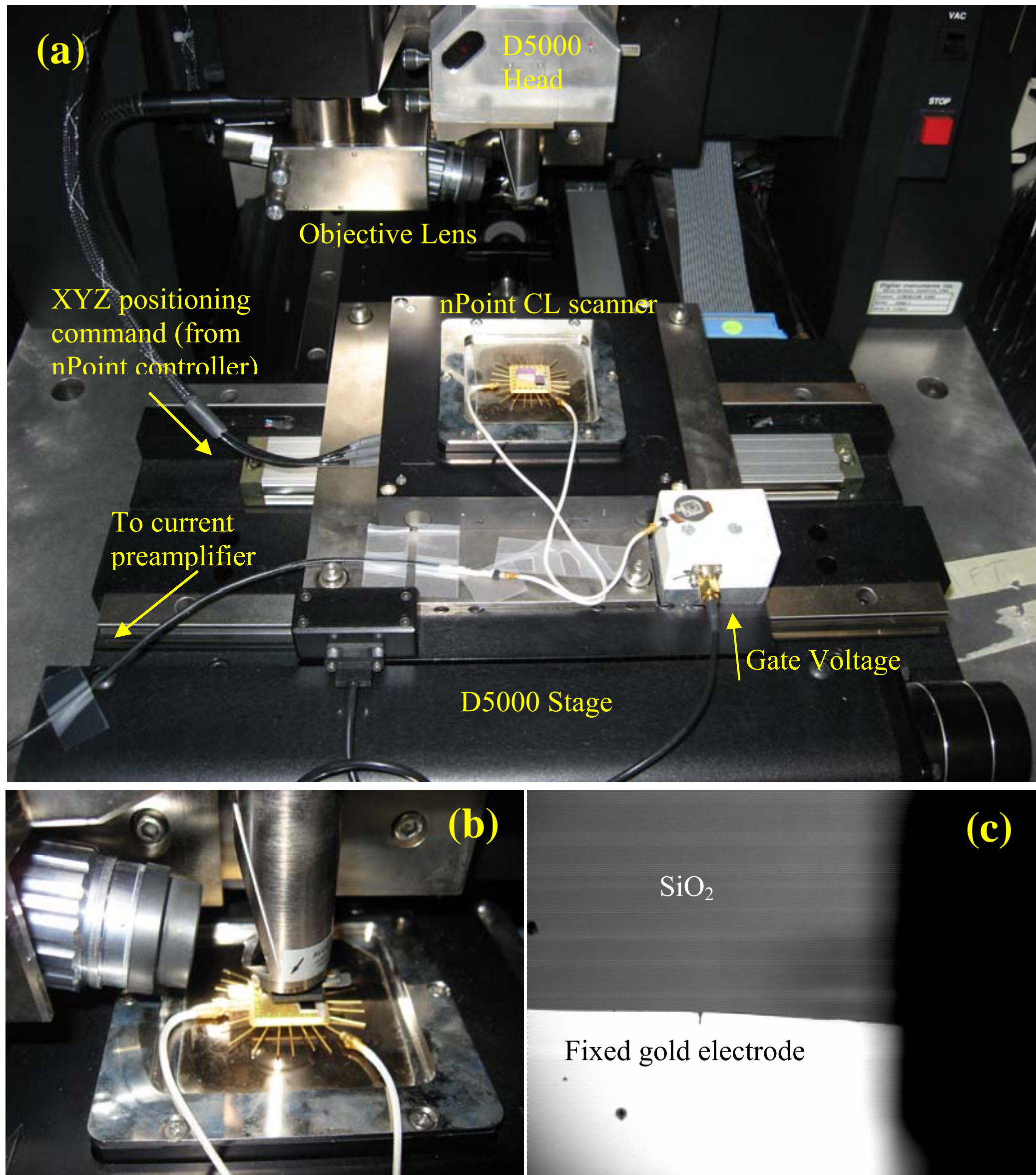

Figure 2-5: Photographs of the measurement setup. (a) General view, with the sample installed and the AFM head not engaged. (b) Detailed view of the sample with the AFM scanning head engaged. (c) View from the optical microscope of the AFM near the fixed gold electrode, the dark shadow to the right is the cantilever carrier, the cantilever itself is out of focus and hard to see.

The basic functions of the contact control group are detailed as follows:

(a) Set XY position

This function is used for coarse positioning of the cantilever in XY. These coarse contact positions are usually determined graphically using the imported AFM image of the surface mentioned above. Using this, the cantilever can be moved into the close proximity of the point along the nanotube where measurement is desired. The procedure is as follows:

- Move from old X position to new X position
- Wait for XY settling time
- Move from old Y position to new Y position
- Wait for XY settling time

The XY settling time (20 ms) is determined by the gain setting of the scanner's PID controller.

(b) Lower cantilever

This command lowers the cantilever until the deflection setpoint is achieved (the adjustment of the deflection setpoint will be discussed in Chapter 3). This is used to establish the contact between the cantilever and the carbon nanotubes. The procedure is as follows:

- Move cantilever down by increment δZ
- Wait for Z settling time
- Read deflection

- If deflection ≥ setpoint, then exit, else repeat

The Z settling time (10 ms) is determined by the gain setting of the scanner's PID controller; δZ is 2.5 nm by design; deflection and deflection setpoint are in volts, which can be converted into nanometers through the sensitivity of the AFM photodetector (10.85 V/μm in my system).

(c) Raise cantilever

This command is used to break the contact between the cantilever and the carbon nanotubes after the desired measurements have been taken. The procedure is as follows:

- Read old deflection
- Move cantilever up by increment δZ
- Wait for Z settling time
- Read new deflection
- If new deflection = old deflection, then go to next step, else repeat
- Move cantilever up by distance Z_{up}
- Wait for Z settling time
- Exit

The condition that the deflection is equal before and after moving up by δZ means the cantilever has just broken free from the surface (see Chapter 1), the additional distance Z_{up} (usually selected as 30-50 nm) is an added insurance.

(d) Search

The search function is used to find the exact position of contact; it starts with an initial guess for the contact site on the nanotube channel selected graphically on the previously recorded AFM image of the nanotube. The search radius (usually selected as 200-300 nm) is a neighborhood around the initial guess site. ΔXY is a suitable increment/decrement (usually 10-15 nm) in either X or Y depending on the orientation of the nanotube, drain current settling time is three times the rise time of the current preamplifier (3 or 10 ms were usually used). The procedure is as follows:

- Set XY position to search position
- Lower cantilever
- Wait for drain current settling time
- Read drain current
- If drain current ≥ contact criteria, then declare search success and exit
- New search position = current search position + ΔXY
- If new search position is out of search radius, then declare search failure and exit
- Raise cantilever, and repeat

The basic functions of the sweep/measurement group are detailed as follows:

(e) Sweep voltage

This generates a single sweep measurement of current vs. either V_d or V_g. The procedure is as follows:

- Start with voltage sweep beginning value
- Set voltage
- Wait for drain current settling time
- Record drain current
- Increment voltage
- If new voltage ≥ sweep end value, then display sweep, save data, and exit, else repeat from step #2

Examples of the output from this function will appear in Chapter 3, Chapter 4, and Appendix A.

(f) Sweep deflection

This generates a measurement of current vs. deflection on approaching and retracting the cantilever. Below is the procedure assuming the cantilever was initially raised above the surface; the opposite case requires some change in the order of commands but is more or less the same. The procedure is as follows:

- Move cantilever down by increment δZ
- Wait for Z settling time
- Wait for drain current settling time
- Read deflection and drain current
- If deflection ≥ setpoint, then go to next step, else repeat

- Read old deflection
- Move cantilever up by increment δZ
- Wait for Z settling time
- Wait for drain current settling time
- Read drain current and new deflection
- If new deflection = old deflection, then go to next step, else repeat from step #6
- Move cantilever up by distance Z_{up}
- Wait for Z settling time
- Exit

Examples of the output from this function will appear in Chapter 3.

(g) sweep deflection and voltage

The output of this function is a 2-D map $I_d(V, D)$ where V is either V_d or V_g and D is the deflection (contact force). Again, the procedure below assumes the cantilever was initially raised above the surface. The procedure is as follows:

- Move cantilever down by increment δZ
- Wait for Z settling time
- Sweep voltage
- Read deflection
- If deflection ≥ setpoint, then go to next step, else repeat
- Read old deflection

- Move cantilever up by increment δZ
- Wait for Z settling time
- Sweep voltage
- Read new deflection
- If new deflection = old deflection, then go to next step, else repeat from step #6
- Move cantilever up by distance Z_{up}
- Wait for Z settling time
- Exit

Examples of the output from this function will appear in Chapter 3

(h) Sweep V_g and V_d

The output of this function is a 2-D map $I_d(V_d, V_g)$, this type of map was rarely recorded since it requires a long time to record, i.e. a long time of contact between the cantilever and the nanotube, which increases the possibility of damage to either one or both of them. The procedure is as follows:

- Start with V_g sweep beginning value
- Set voltage (V_g)
- Wait for drain current settling time
- Sweep Voltage (V_d)
- Increment voltage (V_g)
- If new $V_g \geq V_g$ sweep end value, then save data, and exit, else repeat from step #2

Fig. 2-6 below shows an example of such a dual $I_d(V_d, V_g)$ sweep (this is provided here since this data type does not appear in any other chapter).

(i) Time series

In time series data, both deflection and I_d are recorded as a function of time, this type of data is useful in studying transient phenomena like charging or stability of the tip-nanotube contact. Examples of the output from this function will appear in Chapter 3 and Chapter 4.

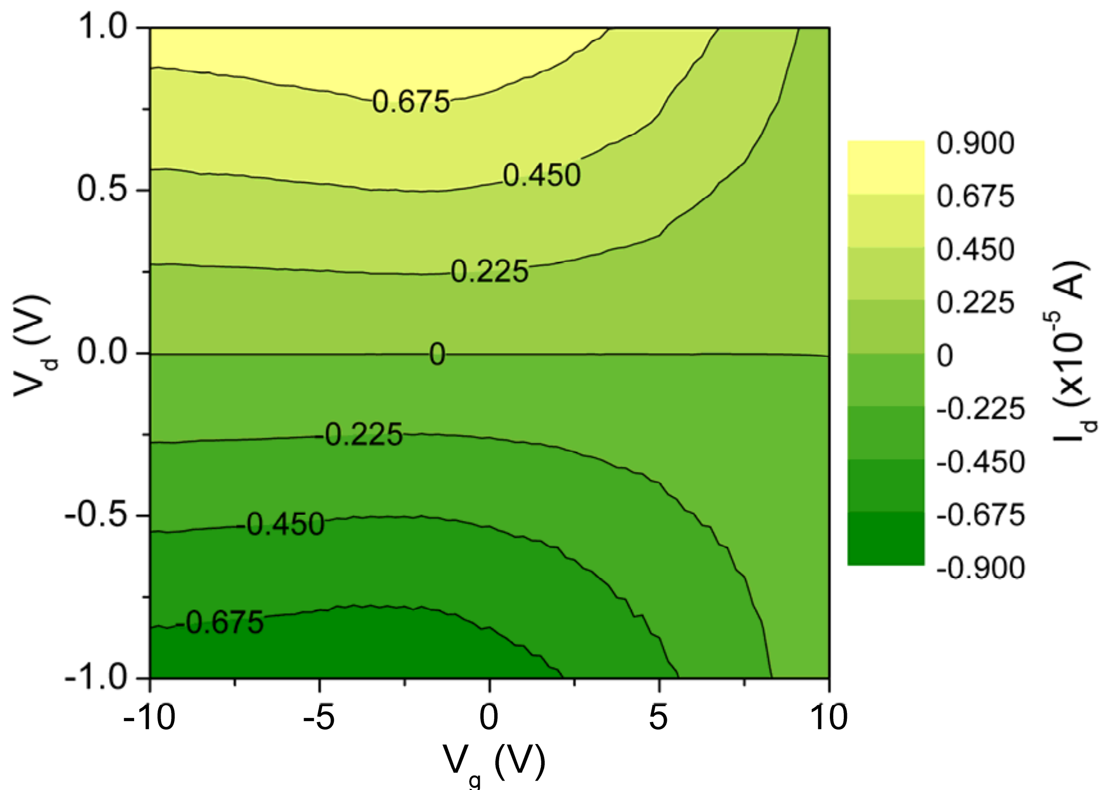

Figure 2-6: Constant current contour map of I_d as a function of both V_d and V_g on nanotube D2 (see Table (2-1)), about 22 μm away from the fixed electrode.

I used this nanolithography program to record local transport measurements on seven different nanotubes, Table (2-1) below summarizes their properties, a more detailed description of these will be presented in Chapter 4 and Appendix A.

Nanotube Name	Type	Diameter (nm)
D1	Semiconducting	2.1
D2	Metallic	2.2
D3	Semiconducting	3.0
D4	Metallic	4.1
D5	Semiconducting	1.9
D6	Metallic	4.1
D7	Metallic	2.0

Table (2-1): Brief description of the nanotubes measured in Chapters 3 and 4.

In Chapter 3 I will discuss the characterization of the electrical contact between metal coated AFM cantilevers and carbon nanotubes, and in Chapter 4 I will discuss the local transport measurements obtained for some of these nanotubes.

Chapter 3: Characterization of the electrical contact between a conductive AFM cantilever and a carbon nanotube

In order to successfully interpret local electrical transport data obtained using the moving electrode technique, it is important to characterize the contact between the conductive AFM cantilever and the CNT. While the moving electrode technique was used by several authors [8, 13, 33, 47, 48, 57], only a few attempts of characterization exist in the literature [57, 65]. In this chapter, I present a detailed study of the AFM cantilever-CNT electrical contact. I will show results for the behavior of the contact under different loading and positioning conditions, and an interpretation of these results in terms of electro-mechanical switching caused by lateral movement of the cantilever during loading, which explains well the major features observed experimentally.

3.1 Parameters of the contact

By performing resistance measurements in a two terminal configuration, one faces the usual problem of separating the desired resistance from any parasitic resistance in series with it. In the case of a carbon nanotube device, the desired resistance is that of the nanotube, and the parasitic resistance mainly comes from the contact resistance between the nanotube and the metallic electrodes. Other contributions possibly come from the input resistance of the current preamplifier used

and the resistance of the leads. In my measurement system the input resistance of the current preamplifier varied between 2-200 Ω for the current scales usually used, and the leads resistance was about 50 Ω, this was measured through contacting the cantilever to the fixed gold electrode (see Chapter 2). Thus the overall contribution of these two parasitic resistances amounts to about 50-250 Ω, which is much lower than the ideal contact resistance ($h/4e^2 \approx 6.5$ kΩ) of a metal-single walled CNT-metal structure. For the moving electrode technique, while the contact resistance between the nanotube and the static gold electrode is fixed, the contact resistance between the nanotube and the metal coated AFM cantilever will change every time the contact is established, which would cause an undesirable scatter in length-dependent transport data. Therefore, it is important to understand how to obtain the contact in a controlled and reproducible manner, and the variables that affect it.

I expect the cantilever-CNT contact resistance to depend on the parameters of both the nanotube and the cantilever. The parameters related to the metal coated AFM cantilever are its force constant, which determines the force exerted by the cantilever on the surface for a given deflection setpoint, and the coating metal which, in the case of semiconducting nanotubes, determines whether the electrical contact is of the ohmic or Schottky barrier type [2-4, 6, 7, 66]. The relevant parameters for the nanotube are its type, i.e. whether metallic or semiconducting, its diameter (which determines bandgap for a semiconducting nanotube), and its geometric orientation relative to the cantilever. From general considerations, I also expect the contact to depend on the lateral position of the tip apex relative to the nanotube. I will discuss the experimental evidence that these are the relevant parameters in the next section.

3.2 Conductance vs. load behavior

To investigate the behavior of the contact as a function of loading force, I used the search function of my nanolithography program (see Chapter 2) to locate a CNT, and then changed the lateral position of the cantilever by small steps of 2-6 nm. The purpose was to investigate whether there is an optimal combination of load and lateral position that would minimize the contact resistance between the cantilever and the nanotube. In the most common measurement geometry, the CNT orientation was normal to the long axis of the cantilever, and therefore the lateral position was adjusted in the X direction. This geometry, which I will term "horizontal profile", is shown in Fig. 3-1-a below.

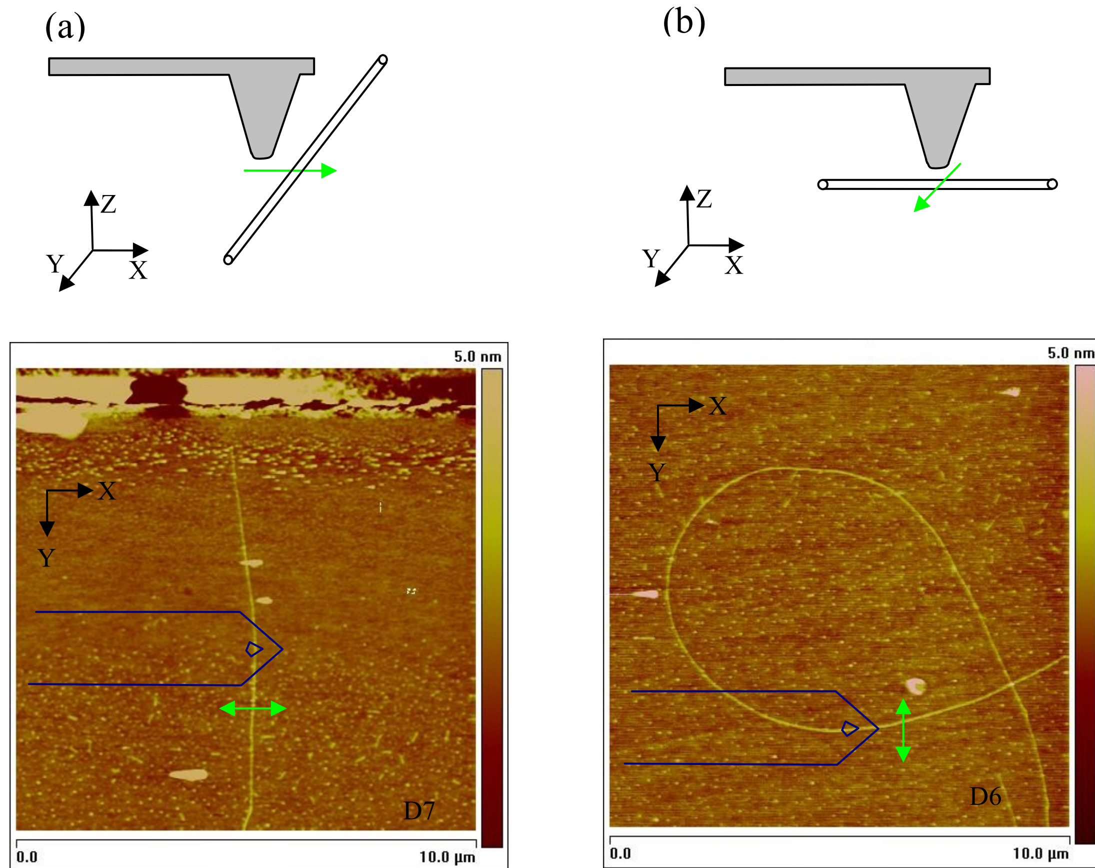

Figure 3-1: Illustration of the two measurement geometries. (a) “Horizontal profile” measurement geometry. The nanotube is oriented normal to the long axis of the cantilever thus the lateral position is adjusted in the X direction, (b) “Vertical profile” measurement geometry. The nanotube is oriented parallel to the long axis of the cantilever thus the lateral position is adjusted in the Y direction. Cantilever drawing is not to scale.

At the selected positions, I started a number of loading cycles. I recorded simultaneous readings of the Z displacement of the scanner, deflection of the cantilever, and current passing through the CNT device. In this geometry, I was able to observe three distinct types of behavior for these current-force curves; these are shown in Figs. 3-2-a through 3-2-c below, and deflection for the same loading cycles is shown in Fig. 3-2-e. Fig. 3-2-e indicates that after the mechanical contact between the cantilever and the surface is established (beyond $\Delta Z \approx 0.06$ µm), the deflection is

proportional to the Z-displacement, so ΔZ measures the tip-surface force. Therefore I refer to these curves as "current-force curves" though they are, strictly speaking, current-displacement curves.

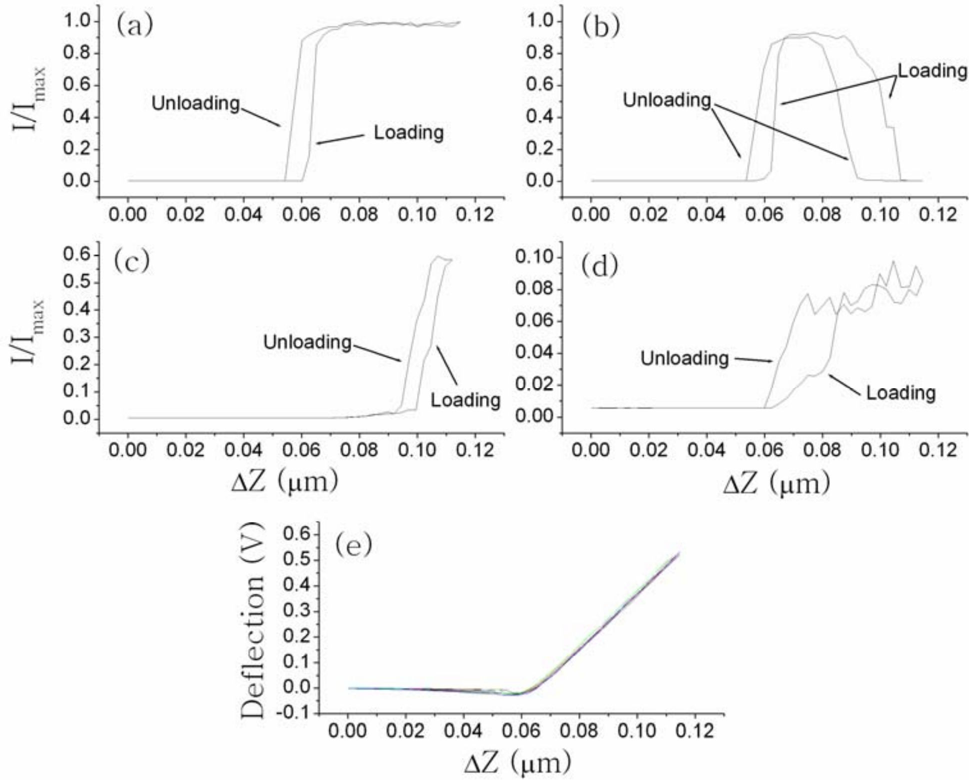

Figure 3-2: (a) to (d) Current-force curves of Types I, II, III, IV respectively. (e) Deflection corresponding to the four loading cycles. Data in (a-c) are taken at nearly the same point on nanotube D2 with different lateral positions (along the X axis) with I_{max} = 0.887 μA. Data in (d) are also taken on D2 at a different position with I_{max} = 0.816 μA. All Figures have V_d = 0.1 V, and V_g = 0.0 V.

In the current-force curves of Type I represented by Fig. 3-2-a; conduction through the CNT starts simultaneously with the mechanical contact ($\Delta Z \approx 0.06$ μm), and the current rises quickly with more loading, finally reaching a load independent value. In current-force curves of Type II, represented by Fig. 3-2-b, the contact starts similar to the Type I curves, but the current rises and then goes down quickly to zero

with more loading; the current may or may not reach its maximum value in the middle part. In current-force curves of Type III, represented by Fig 3-2-c, electrical conduction is delayed from mechanical contact, and then starts to behave like Type I with more loading.

Another extreme for the measurement geometry occurred when the CNT orientation was parallel to the long axis of the cantilever; in this case the lateral position was changed in the Y direction as is shown in Fig. 3-1-b. For this geometry, which I will term "vertical profile", current-force curves of Types II and III were mostly absent, and current-force curves of Type IV, represented by Fig. 3-2-d, emerged alongside Type I curves. In Type IV the electrical and mechanical contacts are simultaneous; however the contact resistance is high and the current generally fluctuates with further loading, and does not reach a saturation value.

The unloading portion of all these force sweeps is generally similar to the loading portion, with hysteresis caused by adhesion. I have observed these four types of behavior on all the nanotubes I studied, whether metallic or semiconducting, and independent of the cantilever force constant (typically 2.8 N/m for soft cantilevers, and 48 N/m for hard cantilevers), and contact type (Ohmic vs. Schottky). The type of behavior observed depended only on the geometry and lateral position of the cantilever. For example, Fig. 3-3 shows current-force curves of the Type I measured on nanotube D2 using both a hard and a soft cantilever, and Fig. 3-4 shows current-force curves of Type I measured using two different soft cantilevers on tube D3. One of these cantilevers was showing diode-like conduction through the CNT device, indicating a Schottky barrier contact between the tip and the nanotube [67]. This

probably happened due to poor gold coverage at the apex, leading to the contact being established by the titanium sticking layer underneath (see Chapter 2). Figs. 3-3 and 3-4 thus show that current-force curves of the Type I are independent of the cantilever type (hard vs. soft) and contact type (Ohmic vs. Schottky).

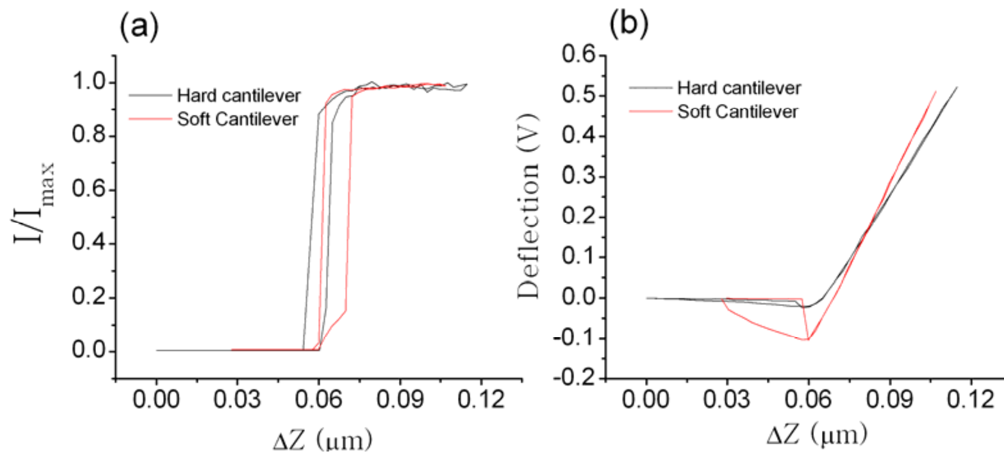

Figure 3-3: (a) Current response and (b) deflection response, for force curves of Type I measured on nanotube D2 (at two different positions) using a hard cantilever (black line) and a soft cantilever (red line). I_{max} = 0.89 μA for the hard cantilever case, and 0.587 μA for the soft cantilever case, V_d = 0.1 V, and V_g = 0.0 V for both.

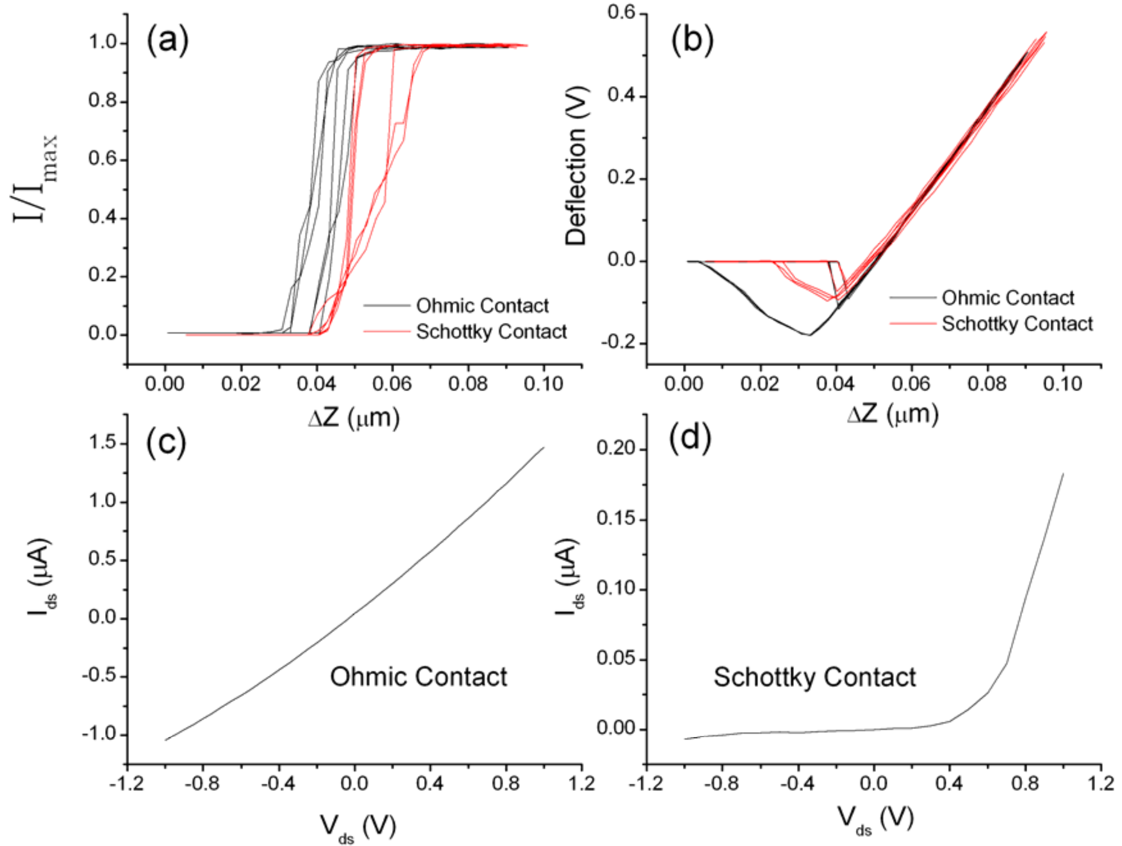

Figure 3-4: (a) Current response and (b) deflection response for force curves of Type I measured on nanotube D3 (at two different positions along the nanotube) under ohmic (black line) and Schottky barrier (red line) contact conditions. (c) and (d) show typical V_d sweeps for the two different contacts. Soft cantilevers have been used for both measurements, with $V_d = 0.5$ V, and $V_g = -5.0$ V. $I_{max} = 0.353$ μA for the ohmic case, and 0.416 μA for the Schottky case.

Of these four types, current-force curves of the Type I are the most operationally desirable for local transport measurements. The phase space for local transport results is a function of four parameters which are the drain voltage V_d, the gate voltage V_g, the length of the nanotube channel L, and the cantilever-CNT contact force F. By selecting a deflection setpoint that is higher than the threshold where current becomes independent of deflection (force), we can effectively reduce the phase space of the local transport results, from four dimensional, $G(V_d,V_g,L,F)$, into

three dimensional $G(V_d, V_g, L)$. Fig. 3-5 shows current-force curves of the Type I for seven different nanotubes, indicating that current-force curves Type I are generically obtainable, and are highly reproducible at least in the regime beyond the threshold.

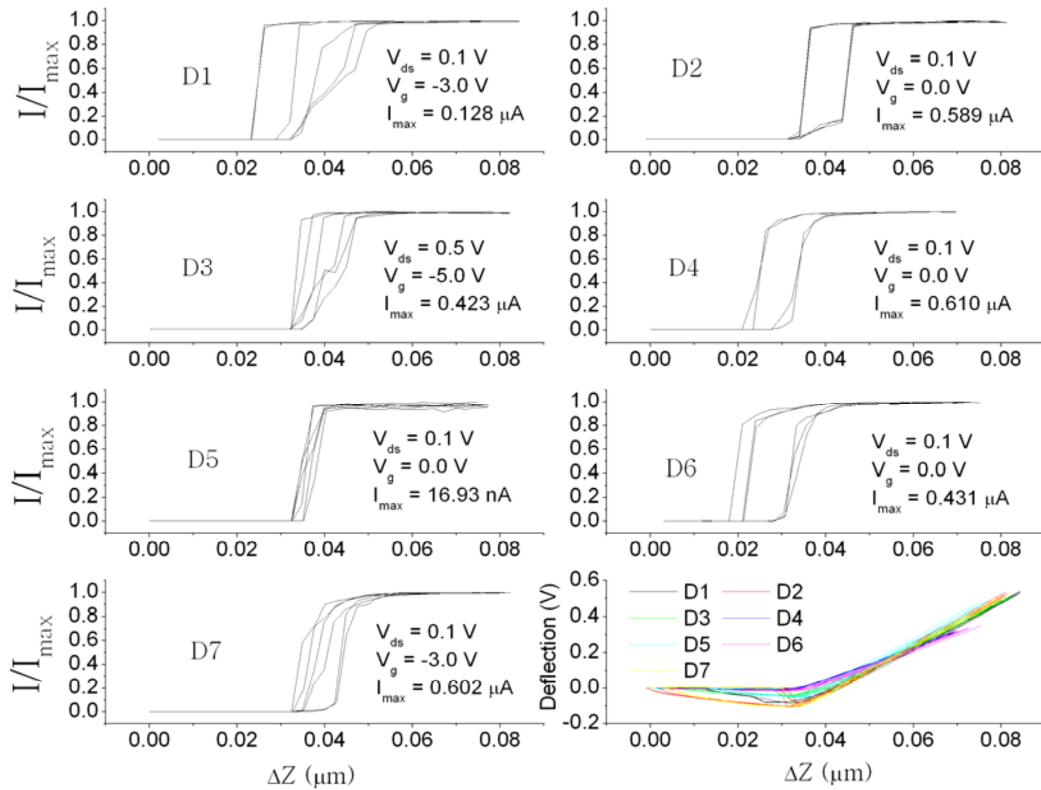

Figure 3-5: Current-force curves of Type I measured on seven different nanotubes; D1, D3, and D5 are semiconducting, the rest are metallic; D4 and D6 were measured using hard cantilevers, the rest using soft cantilevers. All the curves show three consecutive loading cycles except for that of D4 which shows two cycles only.

3.3 Conductance vs. both load and lateral position

In order to systematically study the occurrence of the four types of current-force curve behavior, I systematically collected current-force curves as a function of lateral

position (X position for horizontal profiles and Y position for vertical profiles). Initially I located the desired nanotube, and then moved the cantilever laterally in one direction, till the contact was entirely lost; then I started to move the cantilever back towards the nanotube in uniform increments of 2-6 nm, performing a single loading cycle at every point, till the contact is lost again. Note that the cantilever is moved uniformly in one direction, in order to avoid any effects from scanner hysteresis, or XY drift. I represent these curves as a 2-D map of the current passing through the device as a function of lateral position (X or Y position) and Z displacement of the scanner; these are shown in Fig. 3-6 below for nanotubes D2, D3, and D7. Current-force curves are vertical slices through these 2-D maps.

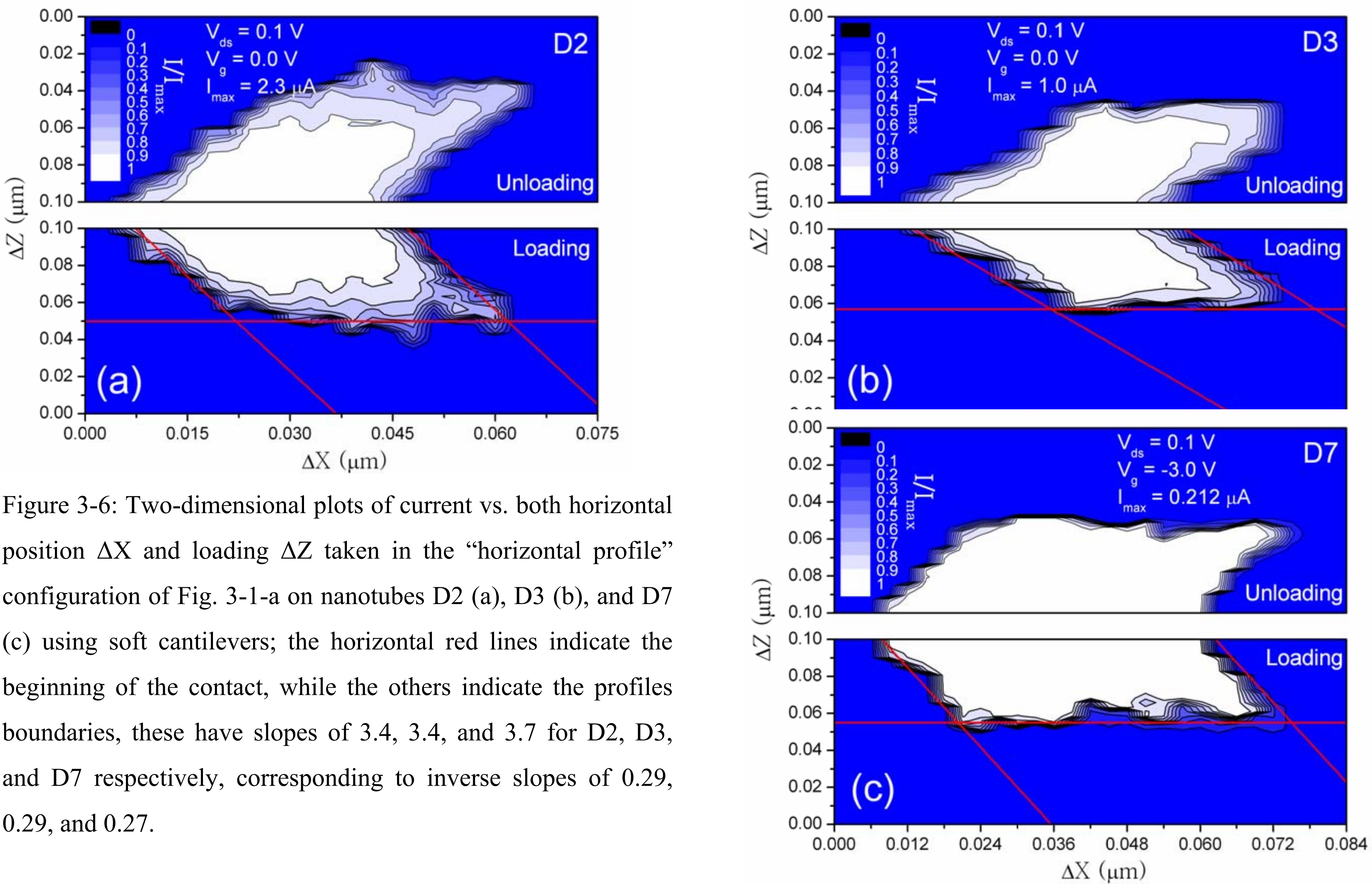

Figure 3-6: Two-dimensional plots of current vs. both horizontal position ΔX and loading ΔZ taken in the "horizontal profile" configuration of Fig. 3-1-a on nanotubes D2 (a), D3 (b), and D7 (c) using soft cantilevers; the horizontal red lines indicate the beginning of the contact, while the others indicate the profiles boundaries, these have slopes of 3.4, 3.4, and 3.7 for D2, D3, and D7 respectively, corresponding to inverse slopes of 0.29, 0.29, and 0.27.

All these measurements were taken using soft cantilevers, and all were oriented such that the nanotubes were normal to the long axis of the cantilever, therefore the lateral displacement was in the X direction, i.e. a " horizontal profile" (see Fig. 3-1-a).

The main features observed in horizontal profiles are: (1) the occurrence of the different types of current-force curves is not random, starting from low X values, initially we get curves of Type III, followed by Type I and then Type II respectively; (2) the maps consist of fast rising edges that surround a wide plateau, where the current through the contact is almost independent of the loading force; (3) this behavior is independent of the type of the nanotube, since these profiles look the same for D3 which is semiconducting, and both D6 and D2 which are metallic. I performed a similar measurement using hard cantilevers on tubes D2 and D6 as shown in Fig. 3-7 below. In general, the behavior in Fig. 3-7 can be seen to be similar around the edges of the pattern to that in Fig. 3-6, with two additional features, the presence of low conductance (i.e. high contact resistance) spots around the edges of the patterns (for example, at $\Delta X \sim 0.01$ μm in Fig. 3-7-a, and $\Delta X \sim 0.27$ μm in Fig. 3-7-b), and the presence of regions in the middle of the conductance plateau where the cantilever-CNT contact ceases to conduct altogether (at $\Delta X \sim 0.05$ μm in Fig. 3-7-a, and $\Delta X \sim 0.15$ μm in Fig. 3-7-b).

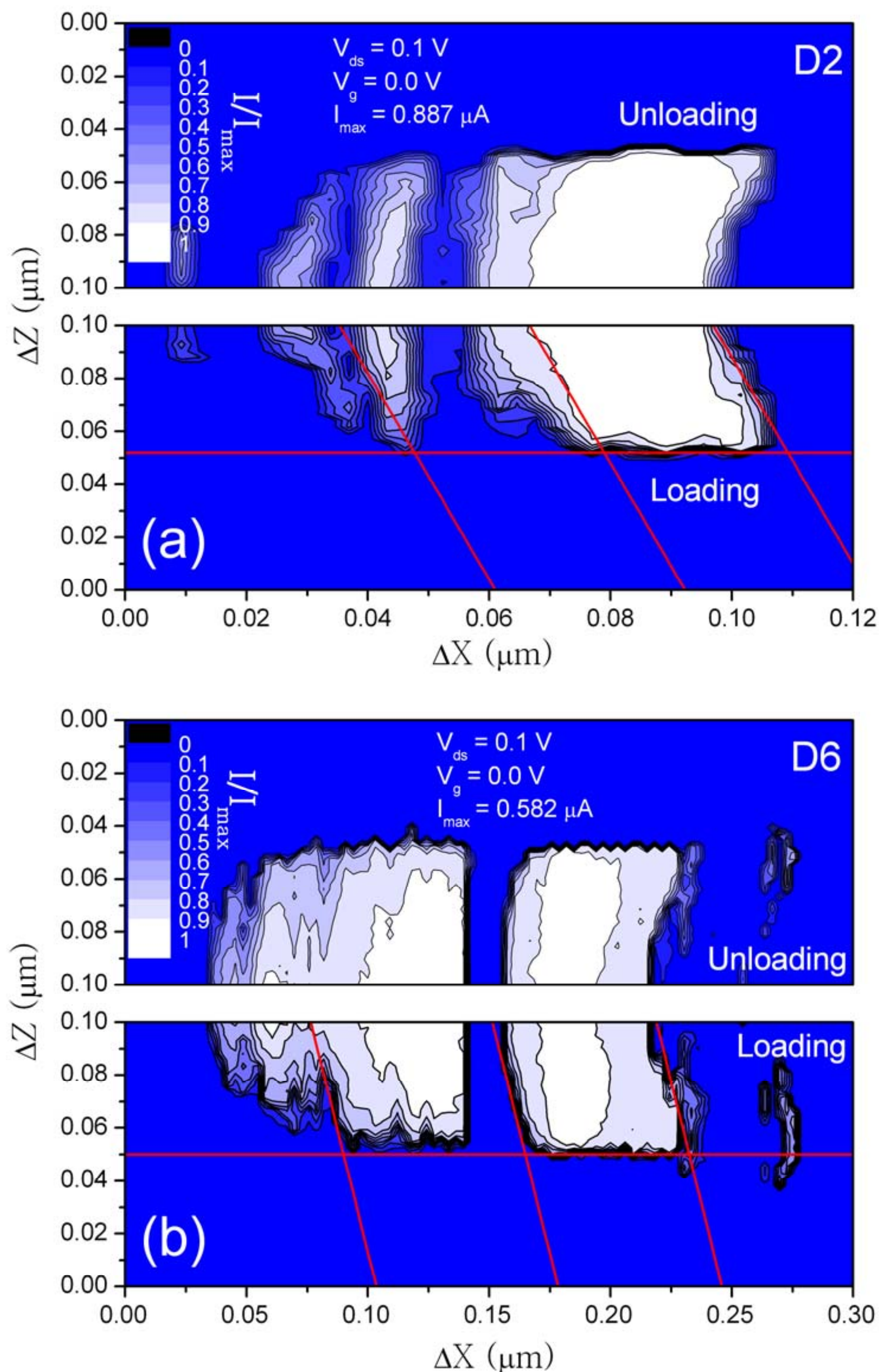

Figure 3-7: Two-dimensional plots of current vs. both horizontal position ΔX and loading ΔZ taken in the "horizontal profile" configuration of Fig. 3-1-a on nanotubes D2 (a), and D6 (b) using hard cantilevers; the horizontal red lines indicate the beginning of the contact, while the others indicate the profiles boundaries, slope for D2 is 3.7, and for D6 is 3.9 corresponding to inverse slopes of 0.27 and 0.26 respectively.

Looking at both Figures 3-6 and 3-7, we can see that the left edges of the plateaus, which correspond to Type III current-force curves, have almost the same slope as the right edges which correspond to Type II current-force curves, this possibly indicates a common origin for both, also the slopes of the edges of horizontal profiles taken on different nanotubes seem to be similar even for soft and hard cantilevers. The inverse of these slopes which I will name β, ranges roughly between 0.25 and 0.3; this implies a simple linear relation between Z displacement and X lateral displacement at the boundaries of the profile.

$$\Delta X = \beta \Delta Z \tag{3-1}$$

To study the orientation dependence of these profiles, I used nanotube D6 because it had a loop as is shown in Fig. 3-1-b; therefore it had different portions where the nanotube was parallel or perpendicular to the long axis of the cantilever. At these points, I collected force curves, with lateral motion being in the Y rather than X directions, i.e. a "vertical profile" (see Fig. 3-1-b). Fig. 3-8 shows two such profiles performed on D6 using two different hard cantilevers. While these maps also show wide plateaus with conductance mostly independent of loading force, the boundary shape is significantly different, with the beginning and the end of the plateau having almost vertical edges.

A model for the nanotube-tip contact which explains the behavior observed in horizontal profiles (Eqn. 3-1) and vertical profiles (nearly vertical edges of current maps) is presented below in section 3.5. For now, I note that for both types of

profiles, the presence of wide plateaus where the conductance is independent of load means that a correctly positioned cantilever would mostly produce force curves of Type I, which is most desirable.

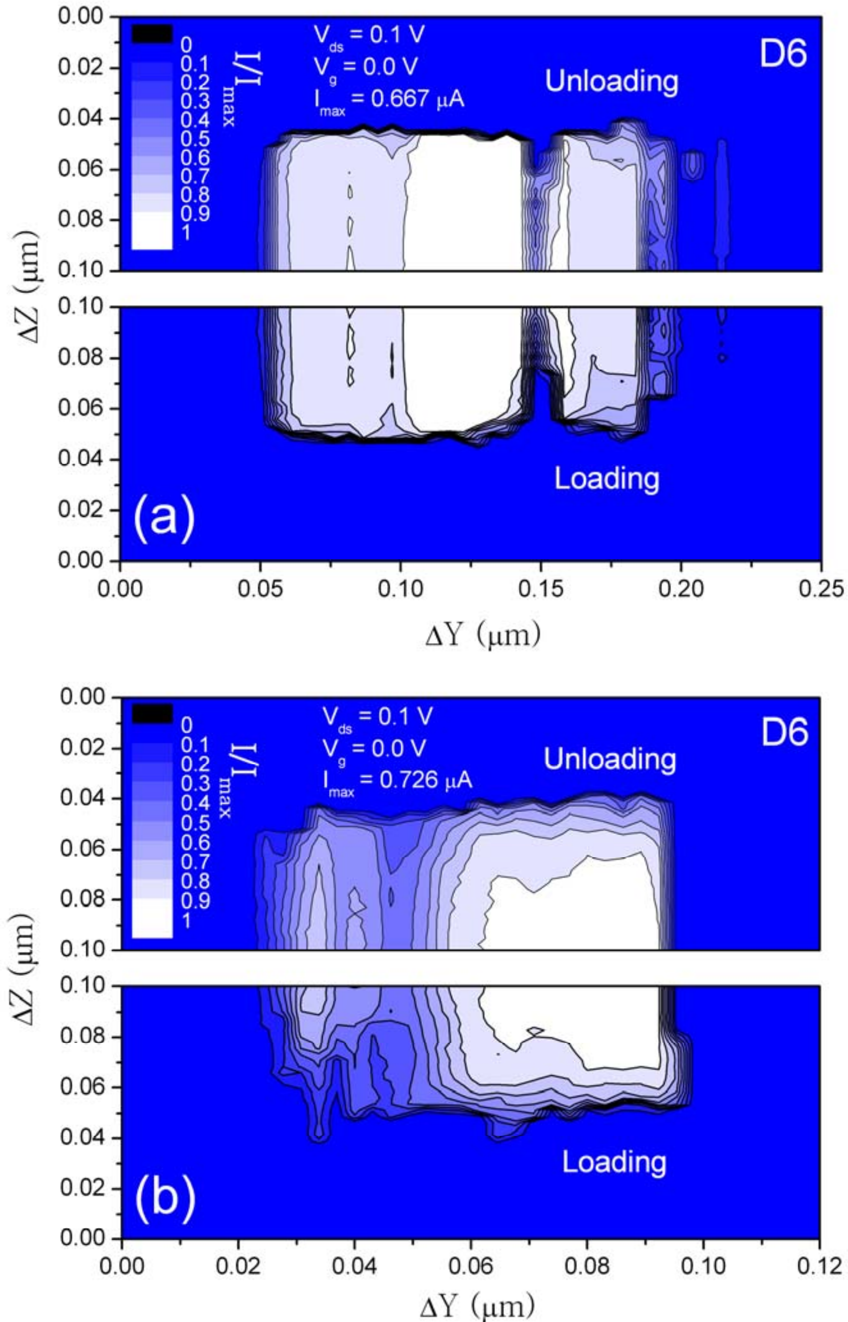

Figure 3-8: Two-dimensional plots of current vs. both vertical position ΔY and loading ΔZ taken in the "vertical profile" configuration of Fig. 3-1-b on nanotube D6 using two different hard cantilevers; notice the almost vertical boundaries.

3.4 Conductance vs. both load and bias conditions

Before I can justify the assertion in Section 3.1, that the four dimensional phase space of the local transport problem $G(V_d,V_g,L,F)$ can be reduced into a three dimensional one $G(V_d,V_g,L)$, I need to investigate the possibility of the presence of any hidden parametric relations between F (the contact force) and both V_d and V_g. To do so, first I contacted the nanotube; then I tuned the lateral position such that I got force curves of Type I, and then used the dual sweeping capability of my nanolithography program (see Chapter 2), the results are presented in the form of 2-D contour maps of constant drain current as a function of Z displacement and either V_d or V_g. I will first discuss the results for V_g; one remark is that, since both V_g sweeps and force curves are hysteretic, a full loading/sweeping cycle would produce four current maps; Figs. 3-9 and 3-10 show such maps for points on nanotubes D7 and D5 respectively.

The main feature I would like to emphasize in these maps is the shape of the constant current contours, which consist mainly of vertical and horizontal lines, with some fluctuations around the threshold region; this mostly indicates the absence of a hidden parametric relation between F and V_g, except maybe around the threshold. This behavior can be seen to be the same for the semiconducting nanotube D5, and the metallic nanotube D7.

Turing now to the relation between Z displacement and V_d. In most cases, unless V_d was swept to a high value beyond about ±(7-8) Volts, I did not observe much hysteresis in the current, therefore the dual sweep splits into only two maps corresponding to the loading and unloading portions of the force curve. Figs. 3-11 and 3-12 show such maps on tubes D3 and D7 respectively using soft cantilevers. For

these maps, we can see that while a well formed contact shows horizontal contour lines, therefore indicating the absence of a hidden relation between F and V_d , the contours near the threshold are not exactly vertical, they have some slope which could indicate the presence of a contact barrier.

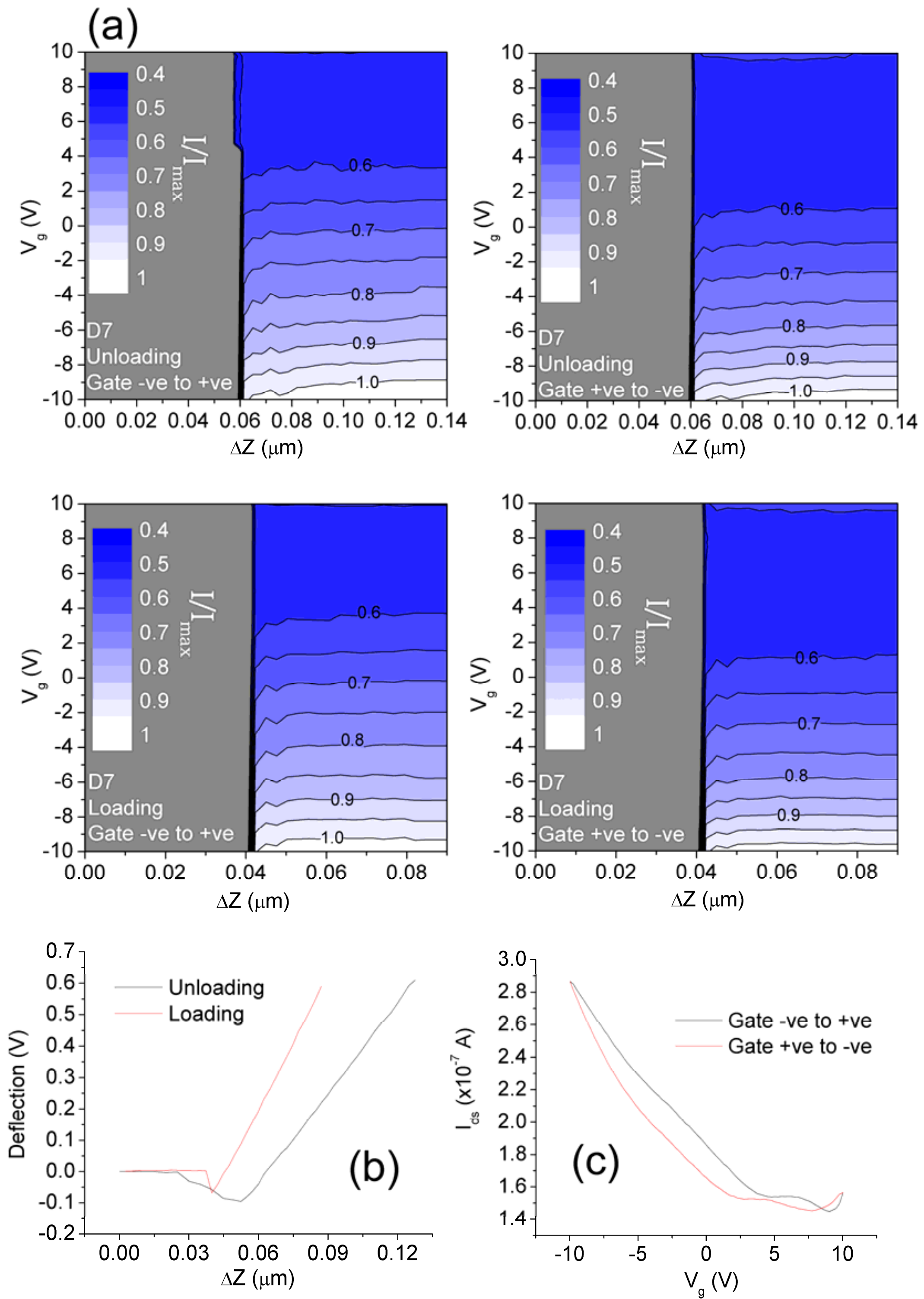

Figure 3-9: (a) Constant drain current contours as a function of both V_g and displacement ΔZ for metallic nanotube D7. (b) Deflection during the loading cycle. (c) A typical I_d versus V_g sweep beyond the contact threshold (ΔZ > 0.06 μm for unloading, and ΔZ > 0.04 μm for loading, below these the current is essentially zero). I_{max} = 0.288 μA, and V_d = 0.1 V for all maps.

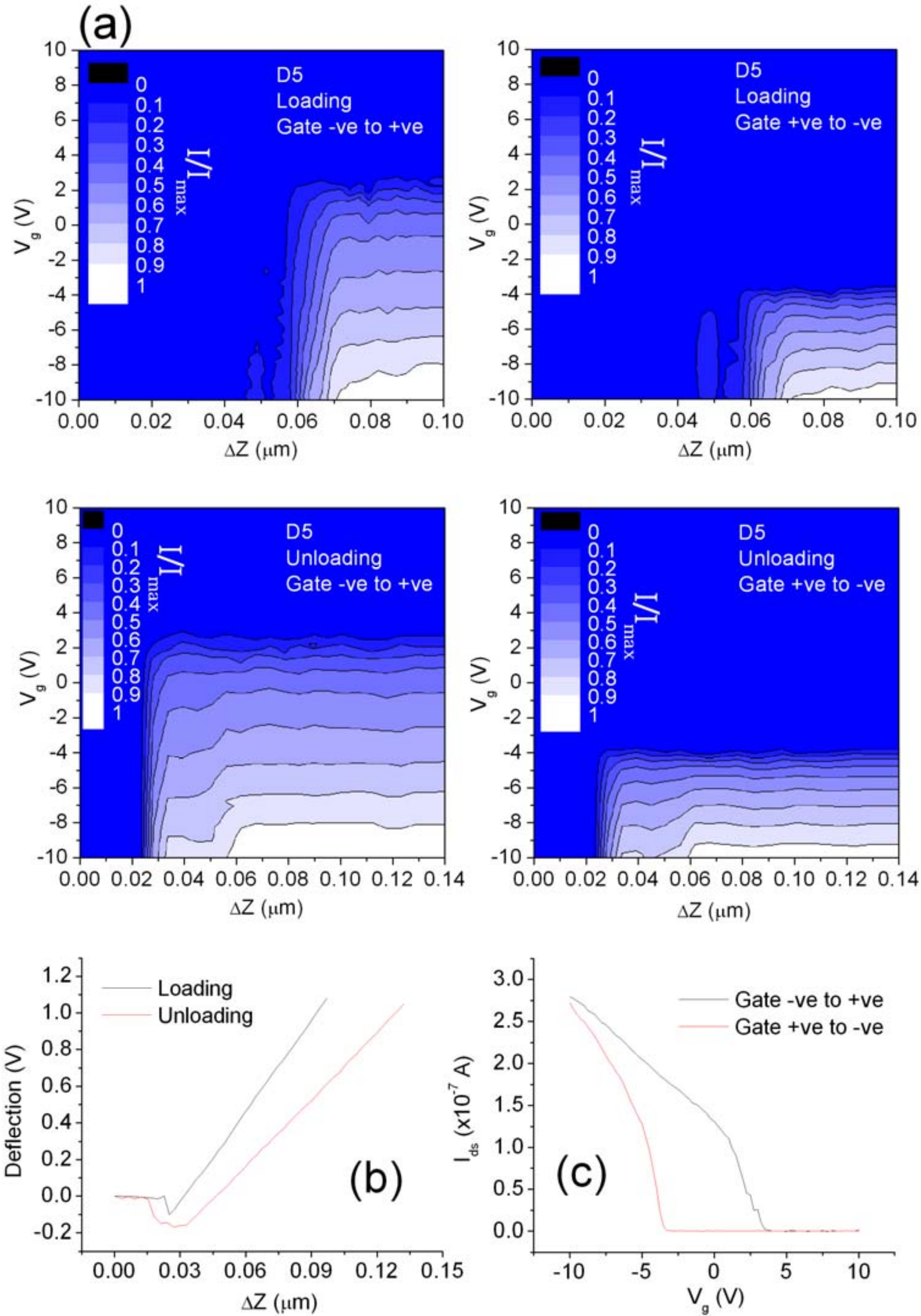

Figure 3-10: (a) Constant drain current contours as a function of both V_g and displacement ΔZ for semiconducting nanotube D5. (b) Deflection during the loading cycle. (c) A typical I_d versus V_g sweep beyond the contact threshold (ΔZ > 0.04 μm for unloading, and ΔZ > 0.07 μm for loading). I_{max} = 0.283 μA, and V_d = 0.1 V for all maps.

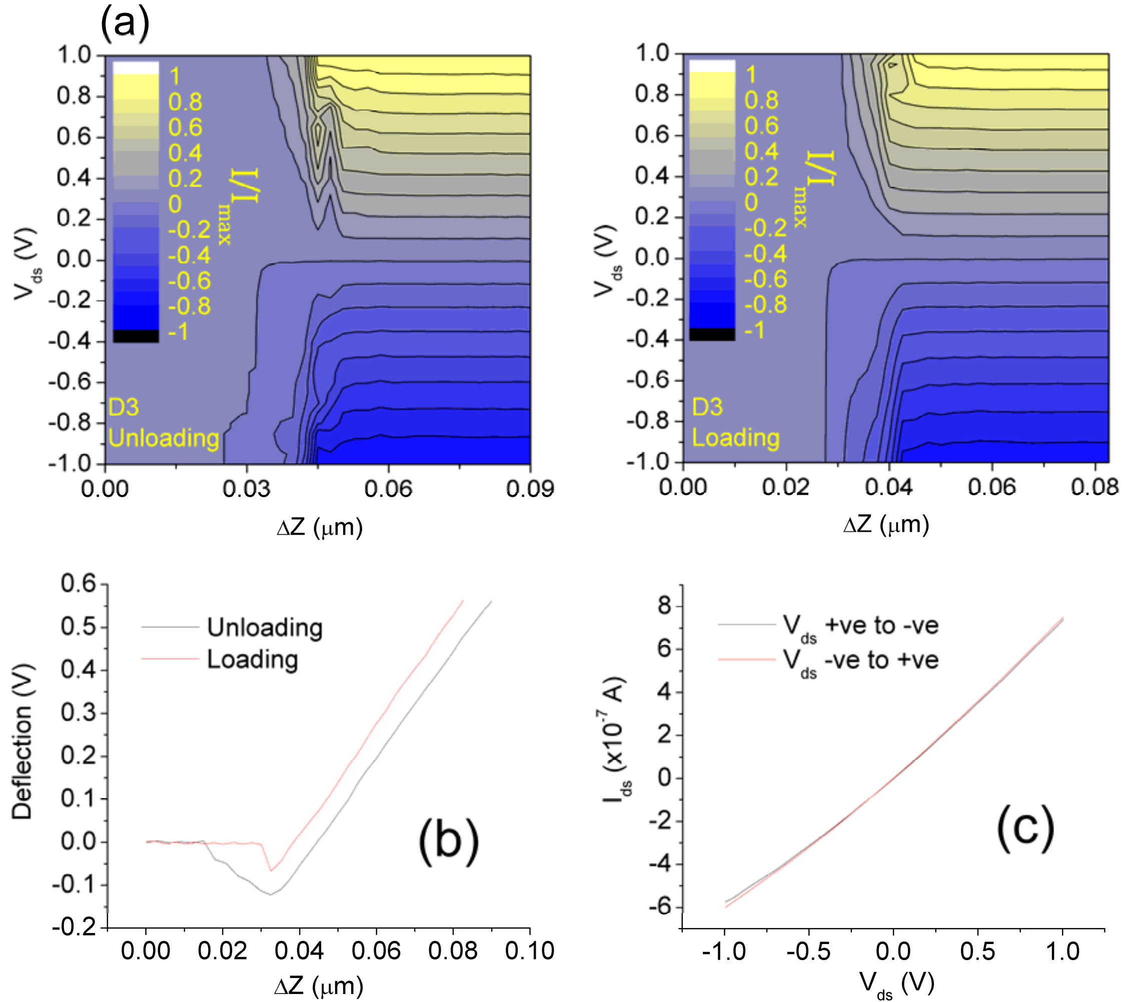

Figure 3-11: (a) Constant drain current contours as a function of both V_d and displacement ΔZ for semiconducting nanotube D3. (b) Deflection during the loading cycle. (c) A typical I_d versus V_d sweep beyond the contact threshold (ΔZ > 0.045 μm for both loading and unloading). I_{max} = 0.754 μA, and V_g = -2.5 V for all maps.

An important operational issue in these maps is, since sweeping the voltage was performed relatively slowly, the Z drift of the scanner contributed a little to the Z movement rate, thus creating some asymmetry between the loading and unloading portions of the force curve, in this case we can not calculate the loading force simply from the scanner displacement and need to use the deflection for that.

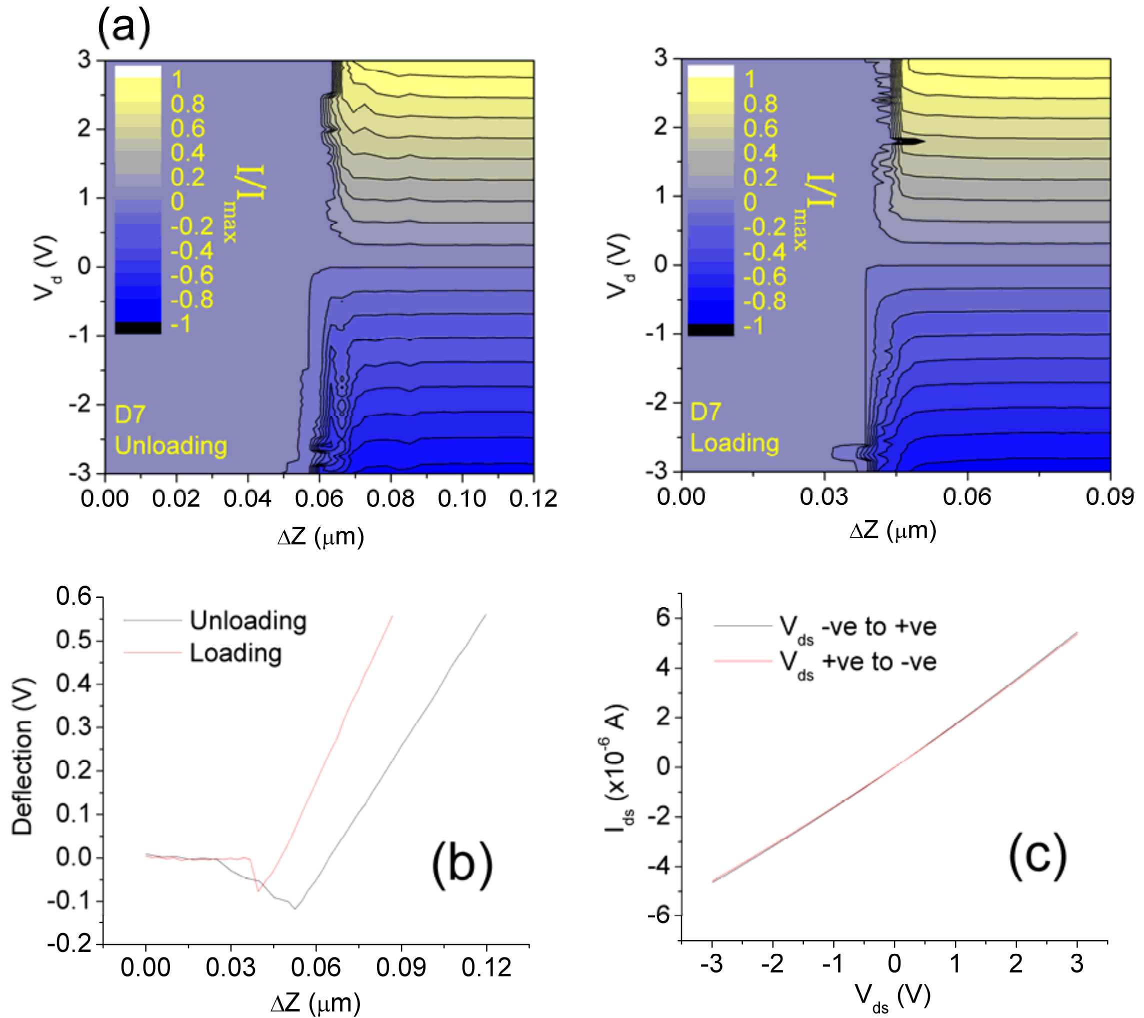

Figure 3-12: (a) Constant drain current contours as a function of both V_d and displacement ΔZ for metallic nanotube D7. (b) Deflection during the loading cycle. (c) A typical I_d versus V_d sweep beyond the contact threshold (ΔZ > 0.05 μm for loading and ΔZ > 0.07 μm for unloading). I_{max} = 5.47 μA, and V_g = 0.0 V for all maps.

3.4 Discussion

Recalling the basic difference between a movable and a fixed electrode, namely that a movable electrode exerts a variable force on the metal-nanotube contact; while a static electrode exerts a constant force on the nanotube due to van der

Waals interaction or chemical bonding between the electrode atoms and the nanotube, the question becomes whether the variation of the local stress at the tip-nanotube contact can actually explain the diverse switching behavior observed in the different types of current-force curves as reported in the previous section. It has been suggested [57] that contacting a carbon nanotube by a conductive AFM cantilever can cause radial deformation in the nanotube, which couples into the electronic properties of the nanotube at the contact spot, and this idea was used by the authors of Reference [57] to explain their experimental observation of non-monotonic force-current curves (which are mostly similar to Type II current-force curves reported here).

The coupling of radial deformation and electronic properties of nanotubes has been addressed in several theoretical works [68-72], where calculations show that semiconducting and metallic nanotubes respond in a different way to radial deformation, which should open a gap in metallic nanotubes, while it should narrow down the gap for semiconducting nanotubes [68-71]. In one work [72] it is also predicted that for metallic nanotubes beyond extreme pressures (800 GPa – 2 TPa), the nanotubes would collapse, causing the gap that initially opened to be closed again. Other calculations [73] predict that the radial deformation is not continuous, but there is a certain pressure threshold for a circular-to-oval transition which is diameter dependent. Also most of these works consider only radial deformation effects, while the combined effects of both radial deformation and contact to a metal (which is the case for nanotubes contacted by a metal-coated cantilever) have been rarely addressed [74, 75].

A primary observation from the data I presented in the previous section is that the behavior of contacts to the semiconducting nanotubes D1, D3, and D5, and that of contacts to the metallic nanotubes D2, D4, D6, and D7 was found to be similar in terms of their parametric dependence on contact force, lateral position, V_g, and V_d. This suggests that the proposed tip-induced radial deformation of the nanotubes can not be the factor modulating the current through the contacts, since they are expected theoretically to respond in very different ways to stress.

Of all the parameters initially expected to affect the electrical conduction through the CNT-cantilever contact, only the orientation of the nanotube and the lateral position of the cantilever seem to be relevant. In addition, I can make the following observations: First, the maximum value of current is highly reproducible for consecutive loading cycles as is evident from Fig. 3-5, this indicates that there is no permanent change in the nanotube at the contact area. Second, force curves of Type I seem to dominate the middle of both horizontal and vertical profiles, and the middle of the profiles is where one could expect the cantilever to be applying the maximum force to the nanotube. The other three current force curve types occur only as 'edge' situations, which occur when the lateral position of the cantilever is largely mismatched with the nanotube position. Therefore, if the assertion of the authors of Reference [57] that non-monotonic current-force curves (similar to Type II) are caused by the cantilever deforming the nanotube, then curves of Type II should have dominated the middle of the profiles rather than appearing only at the edge. Third, by comparing the shapes of the edges of horizontal profiles (which are dominated by Type II and Type III current-force curves) to those of vertical profiles (which are

dominated by Type IV current-force curves), one can see that this different behavior at the edges of the two geometries can not be induced through radial deformation, since the force at the edges can be expected to be nearly the same for both orientations, and this should have produced similar behavior. Fourth, the lack of a parametric correlation between the loading force and bias conditions discussed in section 3.4, and the indifference of this behavior to nanotube type also argue against a force-induced change in the local electronic structure at the contact.

In order to gain a deeper insight into the behavior of the contact as a function of contact force, I calculated the dimensionless quantity $\frac{1}{I(\Delta Z)}\frac{dI(\Delta Z)}{d(\Delta Z)}\delta Z = \frac{dI(\Delta Z)}{I(\Delta Z)}$ for current-force curves of Type I (δZ is the constant increment in ΔZ during loading/unloading, δZ = 2.5 nm in my system by design, also notice that $d(\Delta Z) = \delta Z$ since the data is stored in a discrete form). This quantity is not affected by the constant resistances in series with the tip-nanotube contact, which mainly come from the resistance of the nanotube channel and the contact resistance to the fixed electrode. In Fig. 3-13 below, I plot $dI(\Delta Z)/I(\Delta Z)$ as a function of ΔZ for current-force curves of five different nanotubes. Notice that ΔZ in Fig. 3-13 is measured from the point of onset of conduction. Since this point corresponds also to the onset of mechanical contact (for Type I); then ΔZ becomes a measure of force applied by the cantilever to the nanotube. The consistency observed among the different nanotubes, indicates that there is no dependence on nanotube type (metallic vs. semiconducting) and that this behavior of $dI(\Delta Z)/I(\Delta Z)$ is a general property of the tip-nanotube contact.

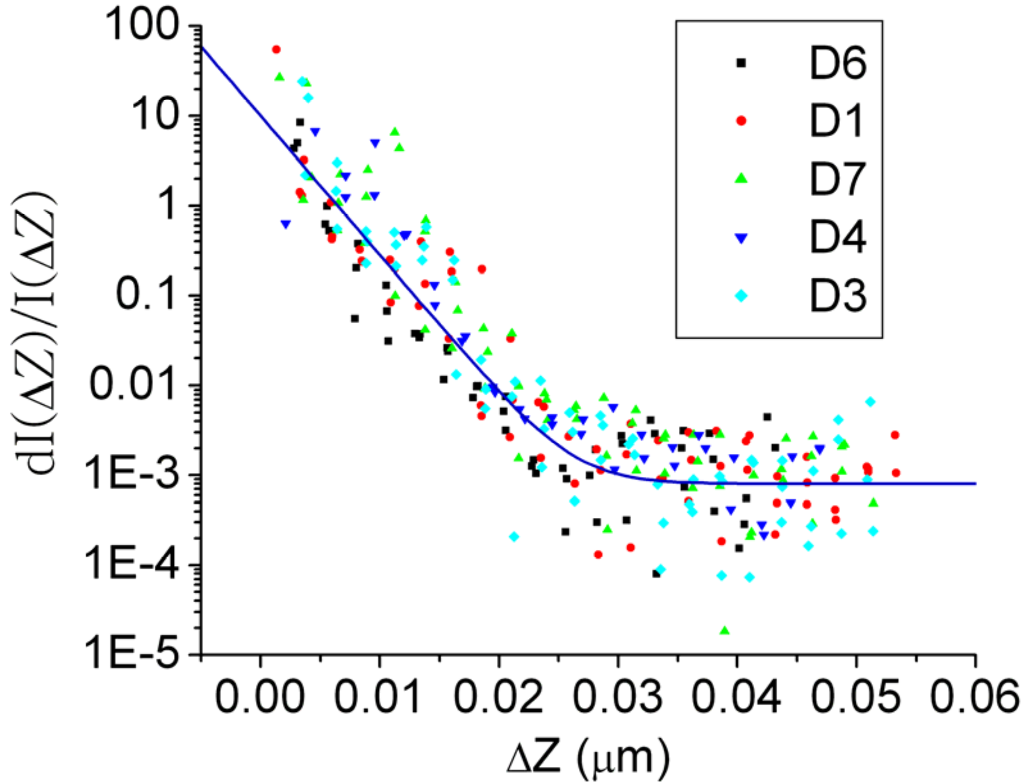

Figure 3-13: dI(ΔZ)/I(ΔZ) calculated from force curves of Type I for five different nanotubes during loading. The data is taken from Fig. 3-5 with the zero of ΔZ shifted to the onset of conduction (about 0.03 μm). The data shown is for loading only, unloading generally shows similar behavior. The thick blue curve is a guide to the eye in the form of Eq. (3-2), using $B = 10$, $A = 8\times10^{-4}$, and Z_0= 0.0028 μm.

Despite the large scatter in data, there is an obvious trend of an exponential decay that flattens near the end into the noise floor of the measurement (this mainly comes from the nanotube channel; I will discuss that in the next section). This behavior can be described by the phenomenological equation:

$$dI(\Delta Z)/I(\Delta Z) = A + Be^{-\Delta Z/Z_0} \qquad (3\text{-}2)$$

where A and B are dimensionless constants, and Z_0 is some characteristic Z displacement, this should actually be interpreted as a characteristic contact force,

since in this regime ΔZ is directly proportional to the contact force, *A* represents the current-normalized noise floor of the measurement. This exponential variation of $dI(\Delta Z)/I(\Delta Z)$ versus ΔZ possibly indicates the presence of some barrier at the cantilever-CNT contact, whose transparency is modulated by the contact force.

One last feature of the data in Fig 3-13 is that both soft cantilevers used on nanotubes D1, D7, and D3, and hard cantilevers used on nanotubes D4, and D6, seem to produce similar behavior in terms of the characteristic modulation displacement Z_0. If the modulation of the contact barrier depends on the local mechanical stress around the nanotube, then it must be that both types of cantilevers produce the same average level of stress despite the large difference between their nominal force constants (2.8 N/m for soft cantilevers, and 48 N/m for the hard ones). We can understand the reason for this, by recalling that the size of a metal coated tip apex is much larger than the typical diameter of a single walled carbon nanotube, and that due to the deformation of the metal at the apex when a force is applied, the apex does not have the usually assumed spheroid shape, it rather has a flat profile as is shown by the SEM images of used cantilevers in Fig. 3-14 below. Therefore as the tip lands on the nanotube, it is also touching the surface of the substrate, and this causes most of the force to be transferred directly to the substrate and very little is transmitted through the nanotube. Using this 'flat apex model' we can estimate the ratio between the average stresses around the nanotube for both types of cantilevers as:

$$P_H / P_S = \Delta Z_H k_H A_S / \Delta Z_S k_S A_H = \Delta Z_H k_H D_S^2 / \Delta Z_S k_S D_H^2 \qquad (3\text{-}3)$$

where P, k, A, D, and ΔZ correspond to stress, force constant, area, average diameter, and typically used Z displacement (i.e. deflection setpoint) respectively (as can be seen from Fig. 3-14, the cross sectional area of the apex is not circular, however assigning a diameter is a common way to estimate the size of the apex from AFM images). The diameter of a used hard cantilever is about 110 nm on the average as can be estimated from the width of the profiles in Figs. 3-7 and 3-8, and that of a soft cantilever is about 35 nm on the average as can be seen from Fig. 3-6. The typically used Z displacement was about 30 nm for hard cantilevers and 50 nm for soft cantilevers. Using these values in Equation (3-3) gives $P_H / P_S \sim 1$; therefore the stresses caused by both soft and hard cantilevers around a nanotube are almost equal, consistent with the predictions above. This may not be accidental; it is possible that deformation of the cantilever metallization occurs above a critical stress, thus producing a tip shape which reduces the stress to a maximum stress value which depends only on the tip metallization material. Using the parameters above that stress can be estimated to be ~ 150 MPa which is comparable to the values of yield strength between 65 to 220 MPa found for thin gold films [76] (these values were measured for tension stress though; shear stress is more relevant in the case of compression).

This flat apex model is in contrast with the often used Hertz contact model [57, 65] where the contact is modeled as that between a cylinder representing the nanotube and a sphere representing the tip apex, while assuming that the force is transmitted from the tip to the substrate entirely across the nanotube. Using this model ignores the yielding mechanics of the composite metallic coating covering the apex, and the details of the mechanical motion of the cantilever as it contacts the

surface (which will be discussed shortly). Also, asymmetries in cantilever manufacturing and installation, or the presence microscopic roughness of the apex/substrate, can activate the cantilever's twisting degree of freedom. All of these factors invalidate the assumption that the force is transmitted from the tip to the substrate entirely across the nanotube as is assumed in the Hertz model.

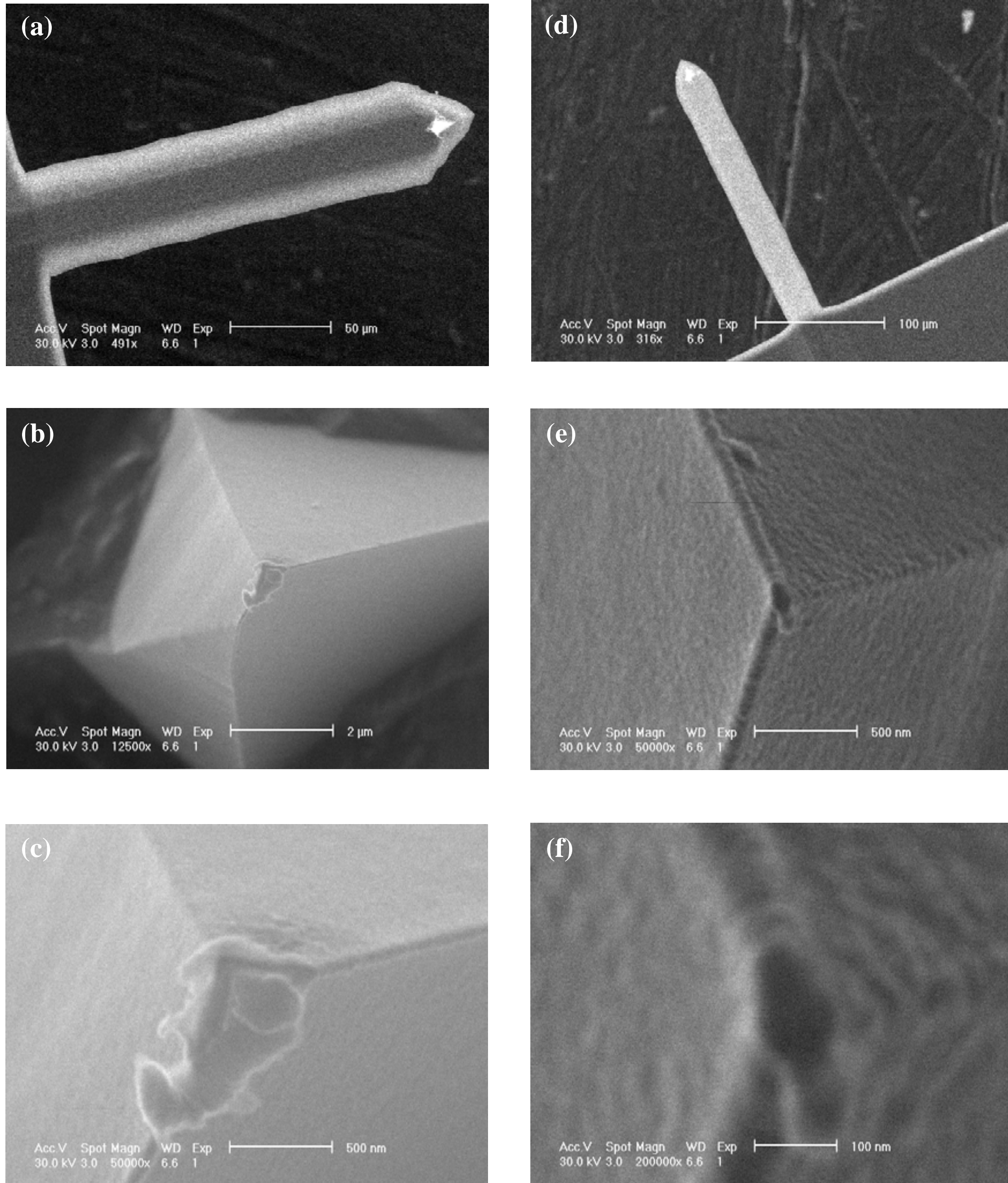

Figure 3-14: (a) to (c) SEM images of a hard cantilever at different magnifications showing the cantilever, cone, and apex; (d) to (f) the same for a soft cantilever.

The origin of the contact barrier which produces the exponential behavior in Fig. 3-13 is not clear. In my system the data is taken under ambient conditions, therefore the sample had an adsorbed water meniscus layer [6]. Also, before the

contacts to the nanotubes were made, the cantilever was used to image the surface in tapping mode, and therefore could have been contaminated by any residue on the surface. Both of these could cause the presence of a thin dielectric between the metal at the apex and the nanotube. However it is not clear that these mechanisms could produce the level of consistency seen in Figs. 3-13 and 3-3 for example, because the thickness and/or composition of such contamination layers can be expected to be highly variable between measurements even at different contact points along the same nanotube.

This barrier could also be associated with deformation of the gold film at the apex, with some stress needed to bring a certain number of gold grains into contact with the nanotube [77]. Also some theoretical calculations predict the presence of a tunnel barrier in the case of gold contacts to carbon nanotubes [74, 78], and a dependence of this barrier on the electrode-nanotube separation within atomic-scale distances [78, 79], where this tunnel barrier becomes smaller with a smaller metal-nanotube distance, which establishes a possible route for the modulation of the contact resistance through contact stress.

A final remark here is that, Fig. 3-13 shows only smooth, reversible changes; and as can be seen from Figs. 3-2 through 3-5 that electrical conduction (for force curves of Type I) starts simultaneously with the mechanical contact. Therefore there is no clear point that can be labeled as formation of a contact, or threshold. These should be understood only as figures of speech, with formation of contact meaning $dI(\Delta Z)/I(Z)$ reaching its noise-limited value; and threshold meaning the point

where the contact resistance becomes comparable to that of the nanotube device, thus resulting in a fast rise of the drain current.

One remaining task is to understand the reason for the switching behavior (i.e. current-force curves of Types II to IV) observed at the edges of profiles. Initially we should notice that the cantilever does not apply force to the surface like a piston. Depending of the local friction, the apex can acquire a parasitic lateral motion and slide on the surface [80-82], and also the cone (the pyramid at the end of the cantilever whose tip is the apex, see Fig. 3-14) rotates due to the change of the local slope at the end of the cantilever as known from beam bending theory [83]. These mechanical degrees of freedom could be responsible for the observed switching behavior through the tip sliding/rotating away, or towards the nanotube. I have considered two models corresponding to the two limits of strong and weak friction. In the first model, I considered that the static friction was strong enough to pin the apex on the surface. In that case the only allowed movement would be the rotation of the cone, and the switching behavior would come about from the apex rotating towards or away from the nanotube as is shown in Fig. 3-15 below.

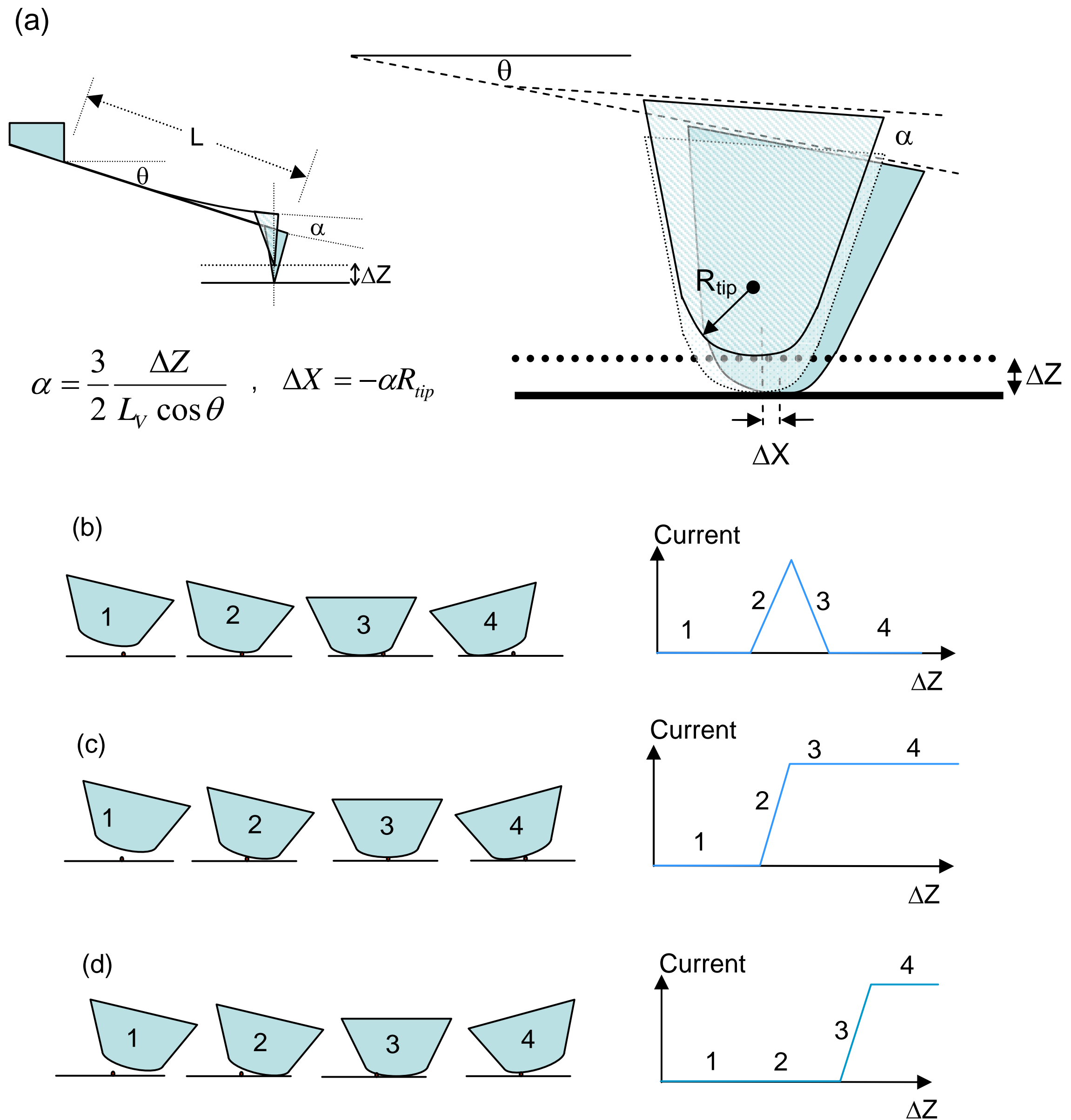

Figure 3-15: (a) Schematic of the pinned cantilever model. The qualitative explanations for force curves of Types II, I, and III are illustrated in (b-d) respectively.

This model predicts the relation between the Z displacement of the scanner and the lateral position as

$$\Delta X = \left(\frac{3}{2} \frac{R_{tip}}{L_V} \cos\theta \right) \Delta Z \qquad (3\text{-}4)$$

where R_{tip} is the radius of curvature of the apex (again this is to obtain a rough numerical value only, not that the apex is a spheroid), which can be roughly taken as about 17 nm for soft cantilevers and 55 nm for hard cantilevers; and θ is the mounting angle of the cantilever (about 12 degrees in my setup); L_V is the length of the cantilever, this is about 210 μm for both soft and hard cantilevers. It must be noticed that Eq. (3-4) is an upper limit, because the presence of friction actually modifies the above calculation for α, however the correction is always negative [81]. Comparing this to Eq. (3-1) we can easily see that the term between brackets is the profile boundary inverse slope β.

While this model can qualitatively describe the occurrence of the various types of force curves, it does not produce a correct quantitative description. The values of β predicted by Equation (3-4) are of order 0.001 at most for the typical values shown above. These are too small compared to the experimentally found values of 0.25-0.3 as I discussed in section 3.3 above. In addition, this model produces the wrong sign for the slope. Also according to Equation (3-4), there should be a noticeable difference in the slopes of profiles created by soft and hard cantilevers due to their different apex sizes, and this is not experimentally observed.

In the second model I considered, the static friction is not enough to hold the cantilever in place; therefore it slides freely on the surface. This model was initially developed in Reference [81] to account for this parasitic lateral motion in

nanoindentation experiments. In this case the switching is caused by the apex sliding toward/away from the nanotube as is shown in Fig. 3-16.

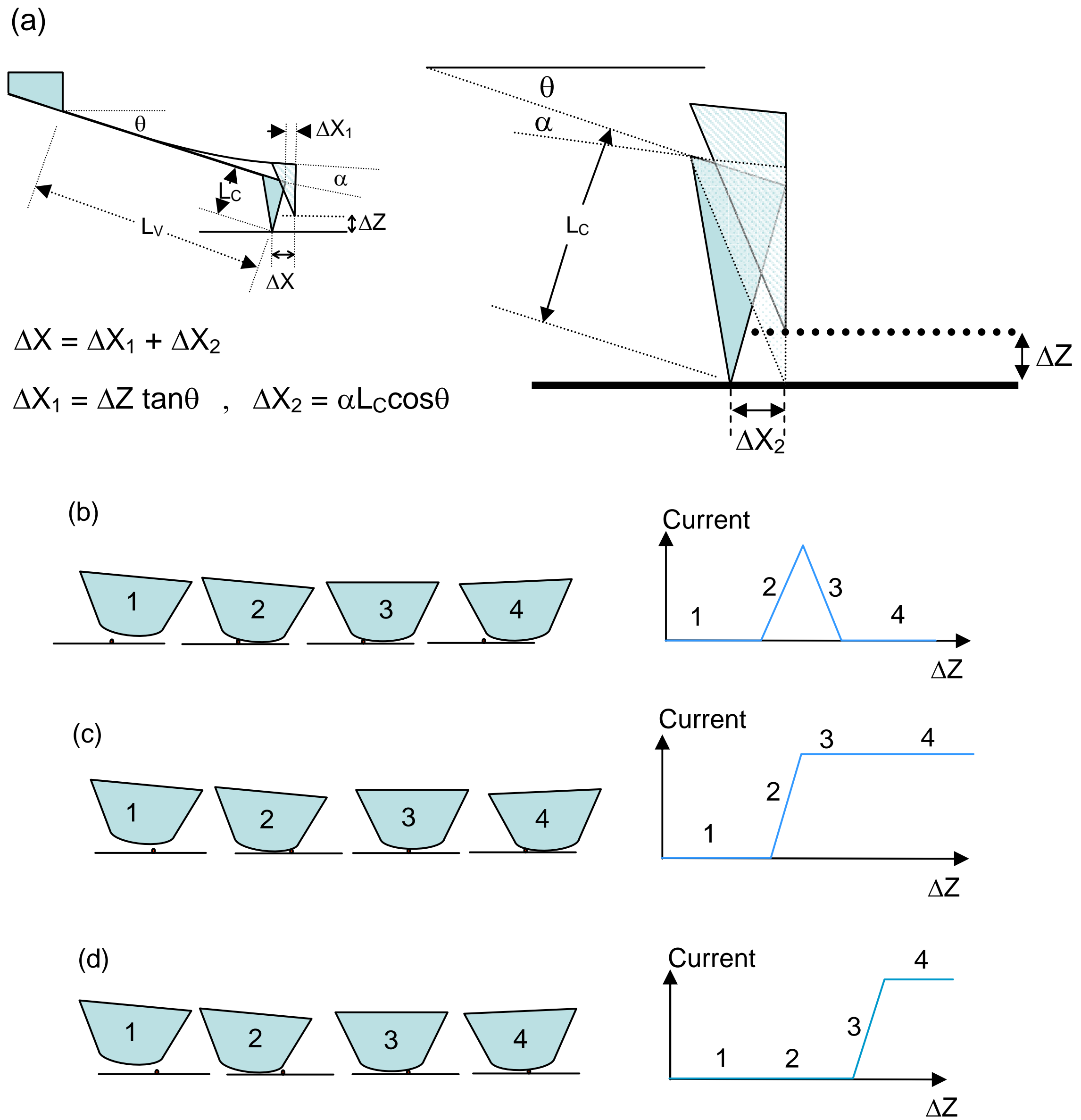

Figure 3-16: (a) Schematic of the sliding cantilever model (after Ref. [81]). The qualitative explanations for force curves of Types II, I, and III are illustrated in (b-d) respectively.

Following Reference [81] the relation between Z displacement and the lateral displacement is provided as:

$$\Delta X = \left(\tan\theta + \frac{3}{2}\frac{L_C}{L_V} \right)\Delta Z \qquad (3\text{-}5)$$

where L_C is the height of the cone, which is about 12 μm for both soft and hard cantilevers. Again, the term between brackets in Eq.(3-5) represents β, for typical parameters this would yield a value of about 0.3 in good agreement with the experimental values. Eqn. 3-5 also produces the correct sign for the slope, and is obviously dependent only on geometric parameters, which explains why both soft and hard cantilevers produce almost the same slopes.

This model also explains the boundary shapes of vertical profiles, in this case the cantilever slides along the nanotube, and the boundaries are defined by the edges of the apex as they begin to curve up, at these points the stress at the contact remains below the threshold stress, therefore the contact resistance remains high, thus producing force curves of Type IV.

The last comment concerns the comparison of the shapes of the horizontal profiles produced by soft and hard cantilevers as presented in Figs. 3-6, and 3-7; we saw there that hard cantilevers produced extra features in the form of weak conductance spots around the edges of the patterns, and there were regions in the middle of the conductance plateau where the cantilever-CNT contact ceased to conduct. These can be understood by comparing the SEM images (Figs. 3-14-c and 3-14-f) of the apexes of soft and hard cantilevers. Aside from the size, the metallization at the apex of the hard cantilever seems non-uniform with dangling edges. The non-uniformity explains the presence of regions where there is no conduction in the middle of the profiles as regions with poor or no metallization. The dangling edges

explain the weak conductance spots at the edges, as spurious contacts between these dangling edges and the nanotube. Similar features can also be observed in Fig. 3-8 of the vertical profiles since these were recorded using a hard cantilever as well.

3.5 Temporal stability of the contact

In addition to the force independence of the cantilever-nanotube contact, another important operational aspect is its temporal stability. In order to successfully perform local transport measurements, the contact should be stable for at least the typical drain or gate voltage sweeping time of 10-20 seconds. This is a system-dependent property, and can vary for the same system depending on many conditions such as electronic drift, or thermal expansion. These factors effectively appear as a drift in the position of the nanotube relative to the cantilever, which can possibly change a contact of Type I into one of the other less favorable edge types. This could happen either directly in the case of XY drift, or through the parasitic lateral motion in the case of Z drift.

In order to characterize the temporal stability of my system, I first located the desired nanotube, then fine tuned the lateral position to get a force curve of Type I, then I simultaneously recorded the deflection of the cantilever and the current through nanotube device using the time series capability of my nanolithography program. Two modes of operation are possible, for the first mode the deflection is actively kept constant, therefore eliminating the effect of Z drift. Because this deflection stabilization procedure was optimized to have a rather gentle, underdamped response,

it was rather slow, and only sparse data points could be taken with intervals ≥ 5 seconds. For the second mode the deflection is not controlled, and Z drift causes the deflection setpoint to change, in my system this drift was almost always in the direction that would increase the deflection, and had a typical value of 1-2 nm/s after several hours of operation. In this mode however, much smaller time intervals are possible.

Fig. 3-17 below shows the temporal stability of the current through several nanotubes taken under the constant deflection mode; we can notice that: (1) the current is stable within roughly 4% for times up to several minutes which is much longer than the typical voltage sweeping time of 10-20 seconds; (2) the major part of the variation has a relatively low frequency, therefore it is expected to have less effect on the relatively short voltage sweeps; (3) the deflection fluctuations are of order 0.01 V around the setpoint, and do not seem to correlate with the fluctuations of the current.

Fig. 3-18 below shows the temporal stability of the current through several nanotubes taken under the mode where the deflection is not stabilized. Other than the linear variation of the deflection due to Z drift, the behavior of the current and deflection fluctuations is similar to that of the constant deflection mode. Additionally, the fluctuations in current and deflection are uncorrelated. This is a direct consequence of the current independence of deflection well beyond the stress threshold as discussed in the previous section.

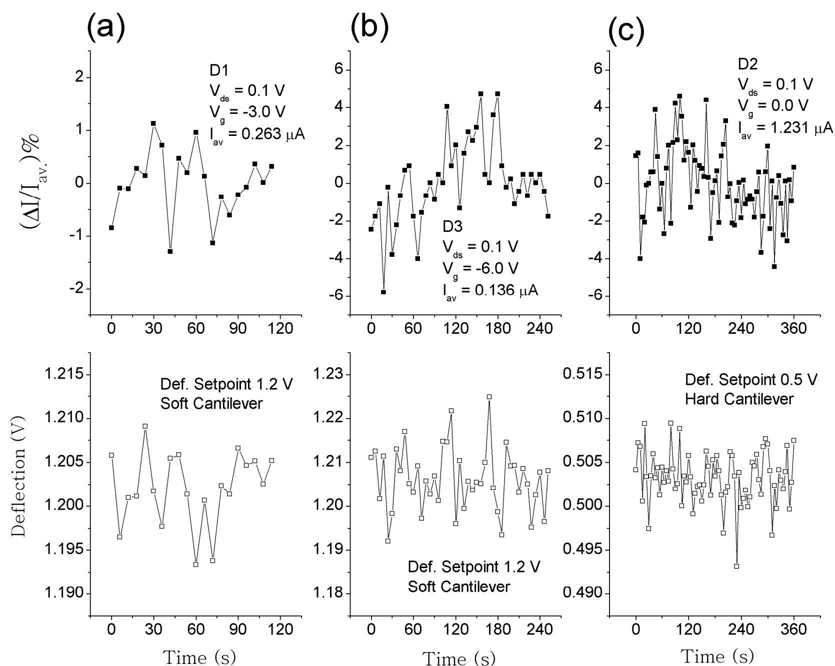

Figure 3-17: (a-c) Current (top) and deflection (bottom) versus time for tip-nanotube contacts to nanotube D1 (a), nanotube D3 (b), and nanotube D2 (c). Data are taken under constant deflection mode.

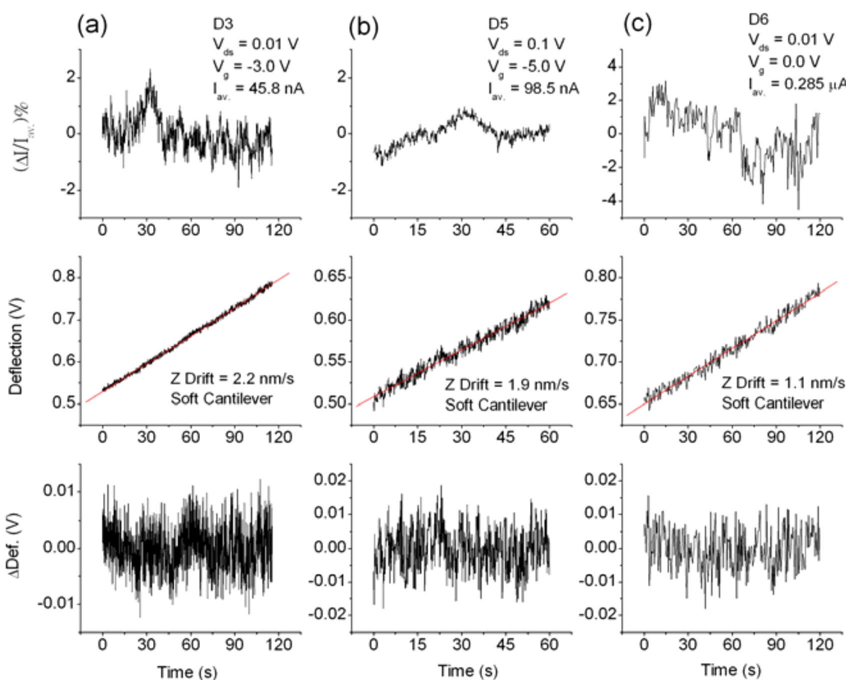

Figure 3-18: (a-c) Current (top), deflection (middle), and deflection fluctuations (bottom) for a tip-nanotube contact with nanotube D3 (a), nanotube D5 (b), and nanotube D6 (c). Data are taken without deflection stabilization; deflection fluctuations are the difference between the actual deflection and the linear fit.

In the above, the current is sensitive to resistance of the nanotube device as a whole, not just the tip-nanotube contact. Therefore the observed current fluctuations do not necessarily originate from the contact. In Fig. 3-19 below, I show the normalized noise power spectrum for the current through nanotube D2, which displays an obvious *1/f* like behavior. This *1/f* like character is not an artifact of the measurement system as is evident from Fig. 3-19-d showing the normalized noise power spectrum for current going through a 100 KΩ metal film resistor obtained using the same measurement setup, which exhibits much lower and only white noise for the same frequency range. Nanotubes are known to exhibit *1/f* noise and telegraph noise [84-89]. Considering this along with the lack of correlation between the current and deflection fluctuations, I conclude that it is more likely that these current fluctuations were caused by the nanotube channel rather than the cantilever-nanotube contact.

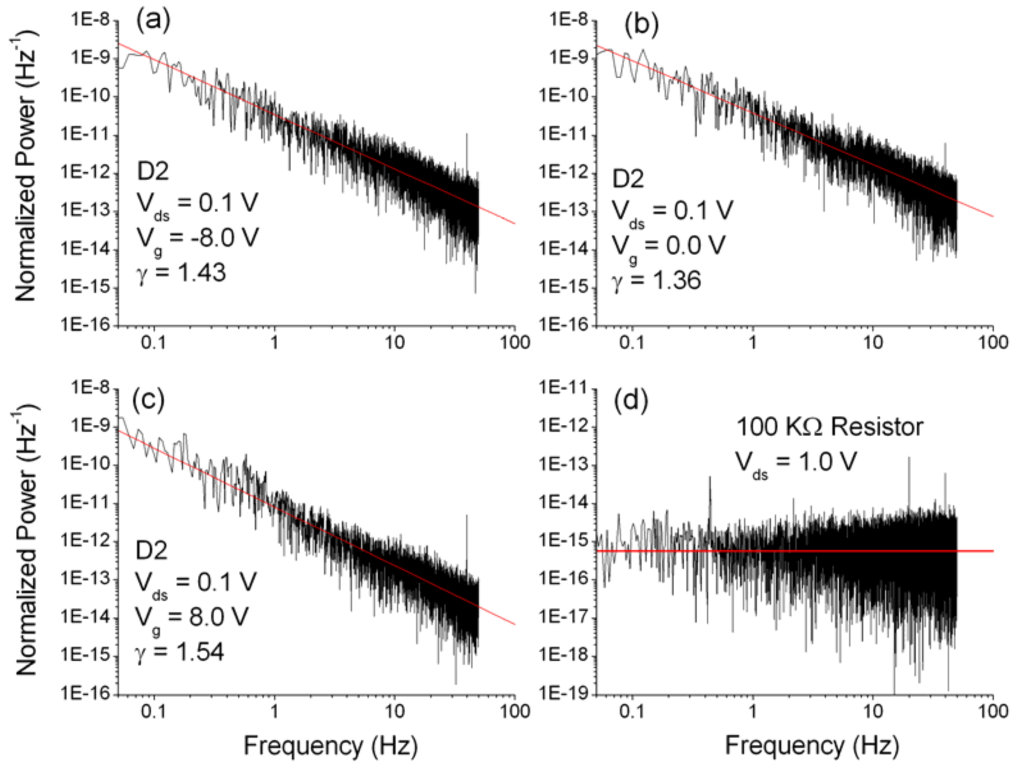

Figure 3-19: (a) to (c) Normalized noise power versus frequency of current measured in nanotube D2 at three gate voltages, the red lines are curve fits of the form A/f^{γ}, (d) Normalized noise power versus frequency of current measured through a dummy 100 KΩ resistor (notice the different vertical scale), the red line is a constant.

The exponent for the frequency dependence was found to be larger than one for this metallic nanotube (D2) and seems to be gate voltage dependent as well. This is in contrast with the exponent of approximately one usually found for semiconducting nanotubes [88, 89], however there are some reports in literature indicating exponents larger than one in metallic nanotubes [87], this also can be caused by the presence of a small component of telegraph noise [88].

The noise power of the deflection shows a different character as in shown in Fig. 3-20 below, for the cantilever in contact with the substrate surface and when it is free; in both cases the noise starts as $1/f$ until about 3 Hz and then flattens out into

white noise; it must be noticed here that these fluctuations are produced by the whole optical lever configuration including mainly the laser, the cantilever, and the photodetector with its associated electronic components. The initial *1/f* behavior is likely coming from the laser and the rest of the electronics, as the cantilever should exhibit only white noise in the frequency range studied, i.e. much lower than the cantilever resonant frequency. This different character of deflection noise from current noise is another confirmation of the lack of correlation between the two, which is consistent with the discussion above. There is some difference between the noise spectrum of the free and surface bound cantilevers in the form of additional peaks which could be associated with ambient mechanical noise coupled through the air table.

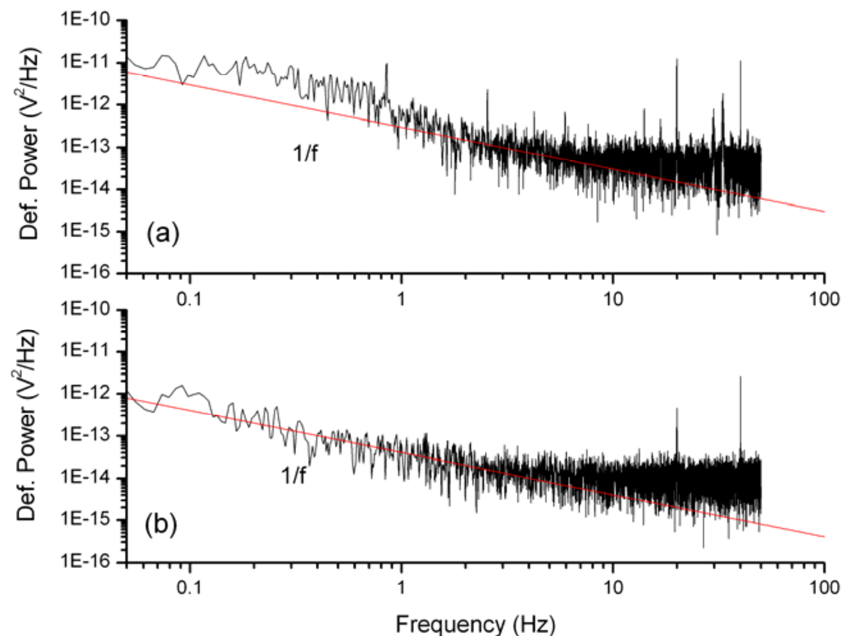

Figure 3-20: (a) Noise power versus frequency of deflection with the cantilever bound to the surface of the substrate. (b) Noise power versus frequency of deflection for a free cantilever.

3.6 Conclusions

It is possible to establish a good reproducible electrical contact between a conductive AFM cantilever and a carbon nanotube. For an optimized placement of the cantilever tip relative to the nanotube, the contact resistance is independent of the bias conditions, and independent of the contact force beyond a certain threshold force. Under certain conditions of tip placement relative to the nanotube, the contact resistance is a non-monotonic function of force. This "switching" behavior results from the parasitic lateral motion of the cantilever during loading, and is not, as has been assumed previously in the literature, due to radial deformation of the nanotube at the contact point.

My setup exhibits a good temporal stability of the contact, with contact times significantly longer than the typical drain or gate voltage sweeping times. The contact is stable in time to within the measurement limit imposed by $1/f$ noise from the carbon nanotube channel itself.

Chapter 4: Length dependent transport measurements of carbon nanotubes

This chapter describes the experimentally obtained resistance versus length results for one metallic and three semiconducting nanotubes. I begin with the experimental aspects and discuss the effects of contact resistance and charging on my measurements. This is followed by a detailed description of each of the nanotubes measured. I interpret the obtained $R(L)$ behavior in semiconducting nanotubes in terms of the long depletion lengths expected in one-dimensional conductors. The charge carriers remain delocalized in my measurement under all depletion conditions, and this is used to infer the relative roles of scattering by disorder and electron-phonon interaction.

4.1 Experimental procedure

As described previously in Chapter 2, my samples consist of sparse carbon nanotubes grown using chemical vapor deposition (CVD) on the surface of an oxidized silicon wafer, followed by the deposition of a single gold electrode using shadow evaporation. The fixed electrode is connected to the input of a current preamplifier and therefore is nearly at ground potential all the time. As in the usual FET terminology, I will consider the grounded fixed electrode as the source, the

metal-coated cantilever contacting the nanotube the drain, and the silicon under the oxide is the back gate.

Since the nanotubes grow randomly, their positions are not known before hand, thus the procedure starts with performing AFM scans (in AC mode) on the exposed silicon dioxide near the edge of the fixed electrode until a suitable nanotube that is in contact with the electrode is found.

The resistance measurements are performed starting at the free end of the nanotube and going towards the fixed electrode, this is done to account for the possibility that the cantilever contact with the nanotube can possibly cause contamination, defects, or even breaks at the contact point, thus affecting any subsequent measurement. When the free end is found, a scan of suitable size is recorded to serve as a reference for the positions along the nanotube, and then the nanolithography program used for measurements (see Chapter 2) is started.

For each measurement session, it is necessary to determine three parameters that are usually kept constant throughout the session. The first is the deflection setpoint, this should be set high enough for the current to reach a force independent value (for a Type I current-force curve) as mentioned previously in Chapter 3, so it should be a little higher than the contact force threshold, but not much higher in order to minimize the possibility of damage to the nanotube or the cantilever. The second parameter is a steady-state gate voltage, the gate voltage at which the drain voltage sweeps are recorded. For metallic nanotubes the steady-state gate voltage is usually set to zero since they are in an on-state for all gate voltages. For semiconducting nanotubes the steady-state gate voltage is usually set to a value sufficiently more

negative than their voltage threshold (I usually used a value between -3 to -5 Volts). The last parameter is a steady-state drain voltage; this is the drain voltage at which the gate sweeps are performed. The steady-state drain voltage should be high enough to obtain a good signal to noise ratio in the gate sweeps, but not so high to cause a nonlinear response at small channel lengths. This is checked by performing a drain voltage sweep that encompasses the desired steady state drain voltage and making sure the resulting drain current is within the linear response regime. The steady-state drain voltage was usually set between 0.1 and 0.5 Volts.

In the beginning of the run, the three parameters above are set to primary test values (usually 0.1 V for the drain voltage, -5 V for the gate voltage, and 0.5 V for the deflection setpoint). Then contact is attempted a few hundred nanometers beyond the free end of the nanotube using the search function of my nanolithography program. The test values are changed for each attempt until a primary contact is established. At this point it is possible to start recording current-force, gate voltage, and drain voltage sweeps, and the final values of the three parameters are selected according to the criteria above.

Now I will discuss the problem of the contact resistance. As my analysis in Chapter 3 indicates, when the deflection setpoint is set beyond the contact force threshold, the contact resistance becomes a function only of the lateral position of the cantilever relative to the nanotube, which controls the type of the current-force curve obtained. Therefore, a primary step to optimize the contact resistance is to adjust the lateral position of the cantilever such that Type I current-force curves are obtained (see Fig. 3-5). However this alone does not guarantee that the lowest possible contact

resistance has been obtained, since an eroded or contaminated cantilever can still show current-force curves of Type I, even while the contact resistance is quite high. The condition of the cantilever continuously changes in terms of both erosion and contamination throughout the measurement session, and a detailed study of the contact properties in the form of horizontal or vertical profiles (see Chapter 3) at each contact point is rather impractical. The practical solution is to sample the contact resistance at each point along the channel by changing the lateral position several times (usually 5-10 times) with a small step of 2-10 nm (This is of course done such that one remains mostly within the Type I plateau, confirmed by monitoring the current-force curve in real time on an oscilloscope). At each lateral position the desired gate and drain voltage sweeps are performed. The result is a set of transport data for each position along the CNT. The resistance values extracted from these data have scatter due to variations in contact resistance and also charging effects discussed below, therefore the resistance data is multiple-valued at each channel length. I assume that the lower envelope of the resistance best represents $R(L)$ of the CNT under a constant contact resistance. When the data is taken according to the recipe described above, the lower envelope usually has a low scatter and well bounded behavior. This is illustrated in Fig. 4-1 below, where I show the full resistance dataset for a 20 μm segment of nanotube D5. The smooth lower envelope is evident compared to the large scatter of the overall dataset. For the rest of this chapter, I will show only the lower envelopes of the datasets, unless otherwise is stated.

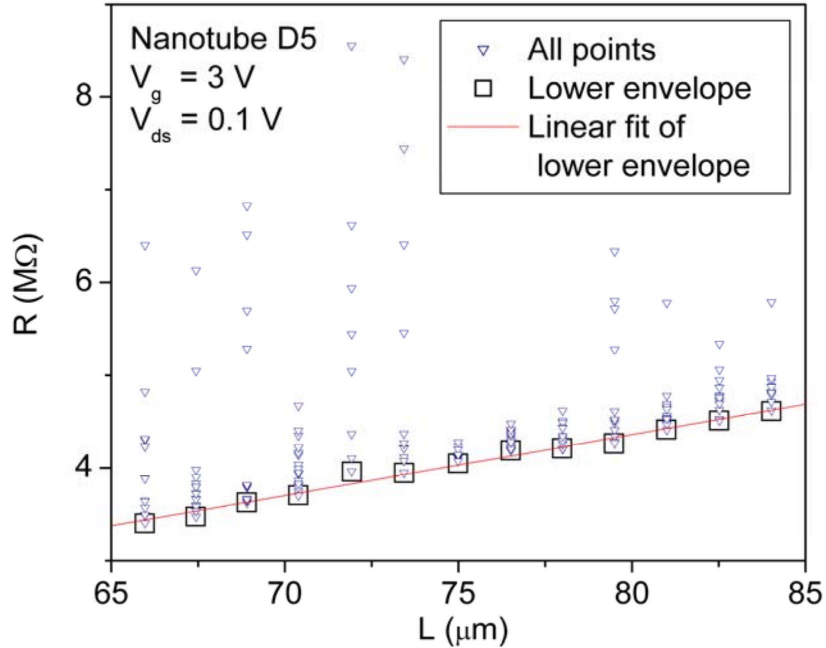

Figure 4-1: The full set of resistance values obtained for channel lengths between 65 and 85 μm on nanotube D5 illustrating a smooth lower envelope. The slope of the linear fit to the lower envelope is 65.54 KΩ/μm.

Other than the contact resistance, an important factor that contributes to scatter in the data is trapped charge. Sweeping the gate voltage can cause some of the charge traps either in the silicon dioxide [90, 91] or the water meniscus [92] to become populated. The trapped charges decay with a rather long time constant. Fig. 4-2 below shows the current through nanotubes D3 as a function of time right after performing a gate sweep. The similarity between the cases with the contact stabilized (i.e. deflection kept constant, see Chapter 3) and not stabilized (i.e. deflection changing due to Z drift, see Chapter 2) excludes this time dependence as a contact effect.

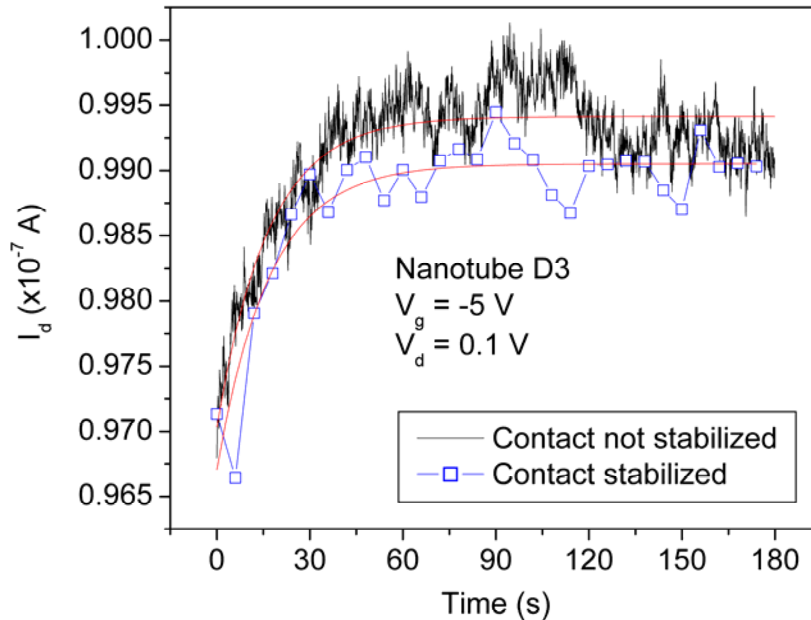

Figure 4-2: Two time series of the drain current of nanotube D3 at fixed gate and drain voltages directly after a gate sweep (-5 V to 10V, then 10 V to -10 V, and then -10 V to 5 V). Both time series are at the same point along the nanotube. The time constant for recovery of the current is about 16.8 seconds in both cases.

Trapped charge results in hysteresis in the gate-voltage dependence of the CNT conductance and this causes a shift in the threshold voltage between the various sweeps. The effect of hysteresis is minimized by considering gate-voltage sweeps with the same gate-voltage history, i.e. same sweep rate and sweep direction. In general, for a well behaved cantilever the combined effect of contact resistance and trapped charge on the overall measured resistance (when the nanotube is in the on-state) is about 5%, but it can get much larger for an eroded/contaminated cantilever (due to large variations in contact resistance) or near the threshold (where a threshold shift has a proportionally larger effect on conductance). Fig. 4-3 below shows several gate sweeps performed on nanotubes D1 and D5 at the same point. The cantilever used on D5 was well behaved as can be seen from the small variation in the on-state current, charging effects can be seen in the small shifts in the threshold and the

disconnection at -5 V after the cyclic sweeps. In contrast, the cantilever used on D1 is not well behaved (i.e. eroded or contaminated) as is evident from the large variation in the on-state current, the sweeps also show charging effects (this was a re-measurement of D1, the data pertaining to D1 in the results section below was taken using a well behaved cantilever).

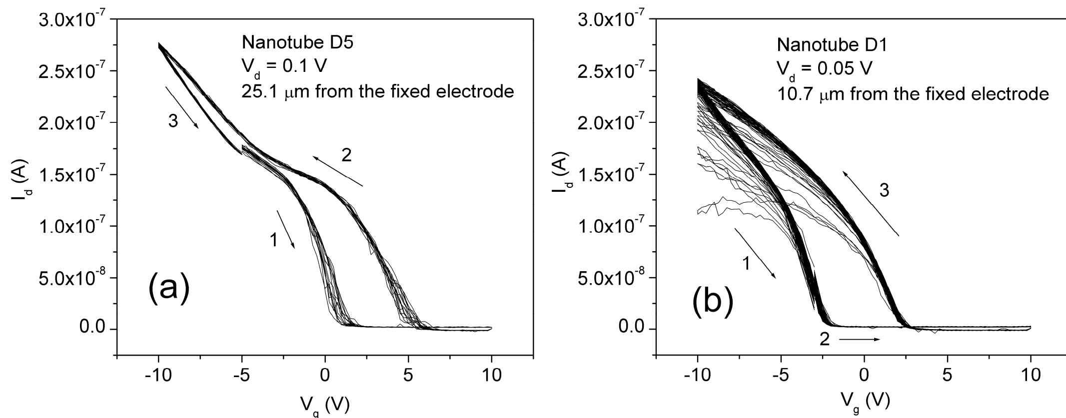

Figure 4-3: Effects of trapped charge and contact resistance on the measured drain current. (a) Several sequential drain current-gate voltage measurements of nanotube D5. The arrows indicate the gate sweeping direction; here the cantilever is well behaved (see text). (b) Several sequential drain current-gate voltage measurements of nanotube D1. Here the cantilever shows signs of erosion or contamination. The contact was broken and remade between the sweeps.

After the desired measurements are taken at the first point, another point is selected (usually 0.5 to 2 μm away) and the procedure is repeated, until the last point within the scan range is reached. Some of the long nanotubes did not fit in one scan (for resolution purposes, I usually used a scan size of 35 μm x 35 μm or lower). For such long nanotubes it was necessary to use several slightly overlapping scans. Then the data is stitched together with the guidance of common features in the overlapping regions of the images.

4.2 Results

I have used my setup to perform local transport measurements on seven different nanotubes, in this chapter I will discuss the results for a metallic nanotube D7, and three semiconducting nanotubes D1, D3, and D5. The results for nanotubes D2, D4, and D6 are briefly reported in Appendix A. I will first discuss the geometry and characteristics of each nanotube, then draw general conclusions from the data.

4.2.1 Nanotube D7

D7 is a metallic nanotube, the diameter is 2.0 ± 0.1 nm and the total length is 20.4 μm. The extension of the gold islands band at the edge of the macroscopic gold electrode (see Chapter 2) is about 1.3 μm. A full view of D7 is shown in Fig. 4-4 below.

Figure 4-4: An AFM topography scan of nanotube D7, the scan is 22x22 μm.

The resistance *R* versus length *L* results obtained at gate voltages from -10 V to 10 V are shown in Fig. 4-5-a, and for the three select gate voltages of -10 V, 0 V, and 10 V in Fig. 4-5-b below (notice the logarithmic scale in Fig. 4-5-a, and the linear scale in Fig. 4-5-b).

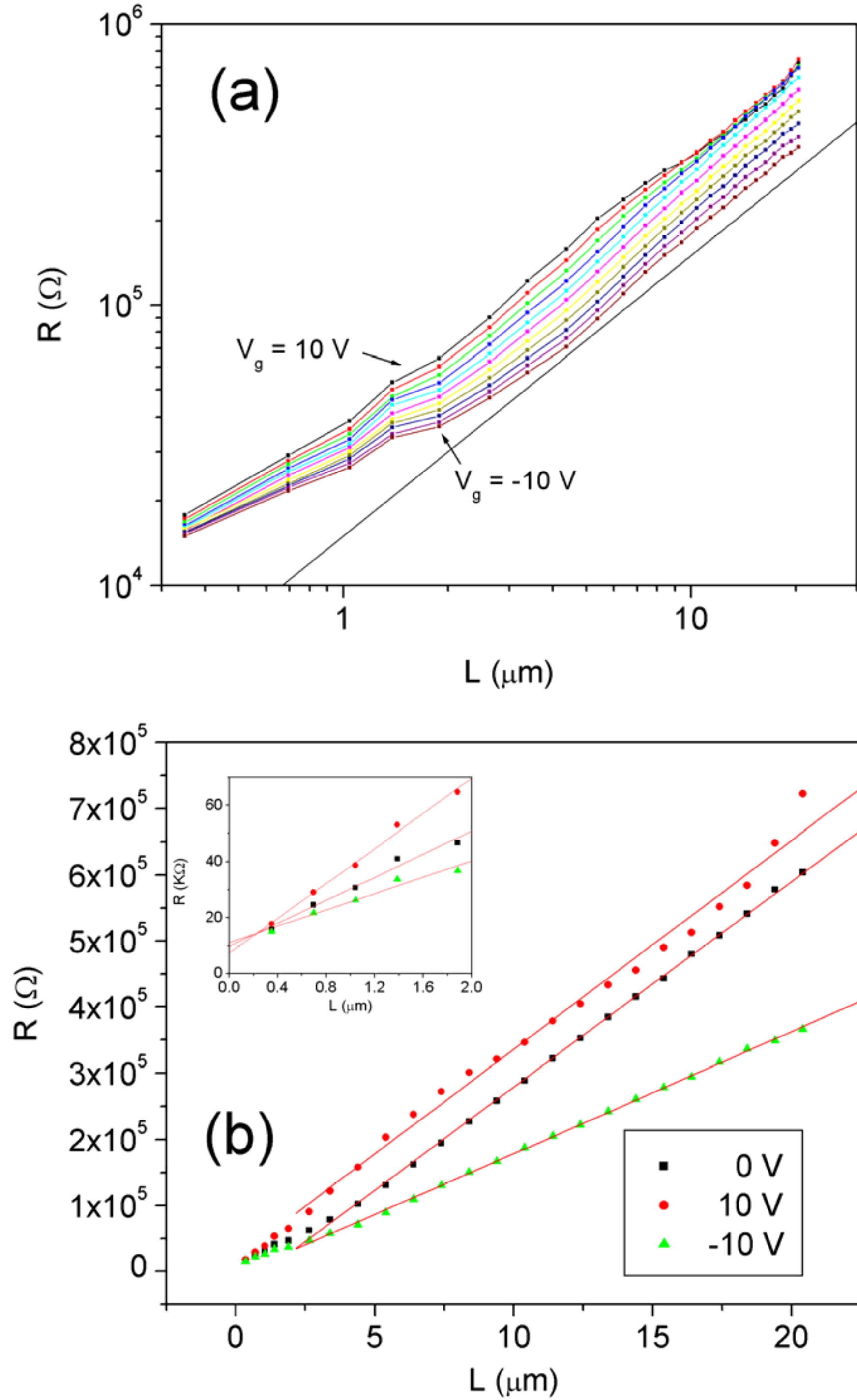

Figure 4-5: (a) Resistance versus channel length of nanotube D7 at various gate voltages between -10 V and 10 V in steps of 1 V, the thin black line is a proportional relationship (power-law slope of unity), (b) the same data at gate voltages of 0 V, -10 V, and 10 V only with linear fitting (excluding points below 2 μm), the inset shows the details for short channel lengths (the line fits here are not extensions of the lines in the main panel), V_d = 0.1 V for all the points.

The main features that could be observed are: (1) the overall behavior of *R(L)* is linear or close to linear, (2) for lengths roughly below 3 μm, *R*(*L*) has a somewhat lower slope than that of the overall linear trend for most gate voltages, with some other deviations developing near the free end of the nanotube for gate voltages near 10 V, (3) there is an observable kink in the data at about 1.4 μm, this is roughly the same as the border of the gold island band, (4) the contact resistance (as estimated from the zero length intercept) is about 10 KΩ, and has a rather weak dependence on the gate voltage; this is comparable to the theoretical limit of $1/(4e^2/h) \approx 6.5$ KΩ expected for a 1-D conductor with four conductance channels.

The generally linear behavior indicates diffusive transport. This has been reported in literature before for both metallic and semiconducting carbon nanotubes in their on-state [24]. Deviations from linearity could be phenomenologically related to qualitative changes in the behavior of the drain current versus gate voltage at various lengths as is shown in Fig. 4-6 below.

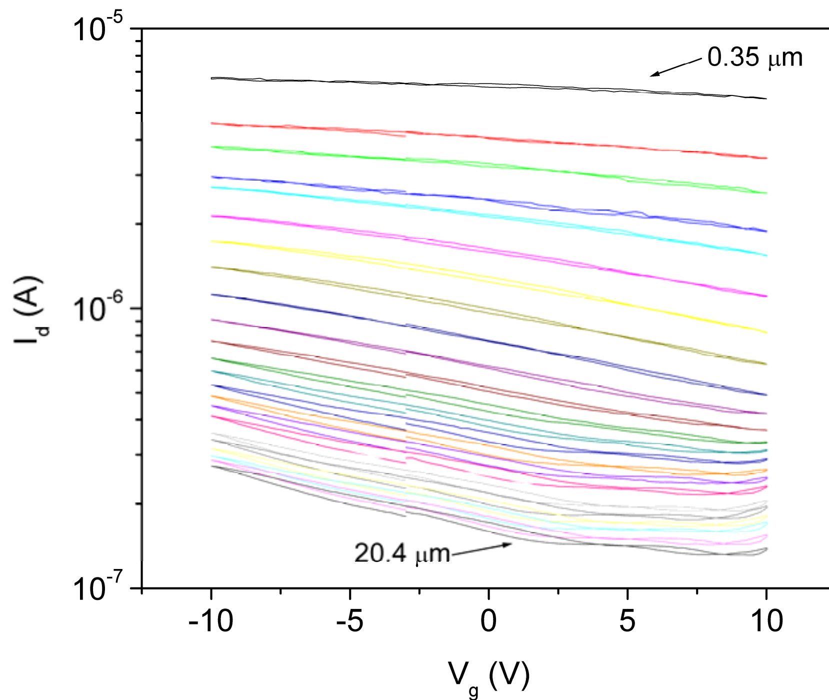

Figure 4-6: Drain current versus gate voltage sweeps at various lengths of nanotube D7. The top trace is at 0.35 μm, and the bottom one is at 20.4 μm away from the fixed electrode, $V_d = 0.1$ V for all the curves, average length step is 1 μm.

Metallic carbon nanotubes are expected to show current saturation at high drain voltages due to scattering by zone-boundary phonons, with the saturation value around 25 μA [14]. D7 does show such a tendency for current saturation at high bias as is shown in Fig. 4-7 below, however the current saturation value is about 70 μA. It is unclear if this indicates that D7 is possibly multiple walled rather than a single walled CNT.

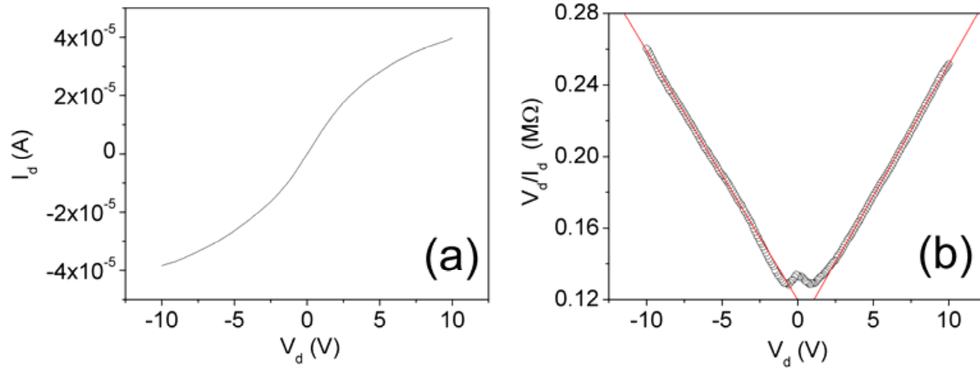

Figure 4-7: Current saturation in nanotube D7, (a) drain voltage sweep 2.8 μm away from the fixed electrode (V_g = 0 V), showing the tendency to saturation at high drain voltage values, (b) shows V_d/I_d , the red lines are linear fits for $|V_d| \geq 2.5$ V, the inverse slope of these lines [14] gives a current saturation value of about 70 μA.

4.2.2 Nanotube D1

D1 is a semiconducting nanotube, the diameter is 2.1 ± 0.1 nm, the total length is 26.1 μm. The extension of the gold islands band at the edge of the macroscopic gold electrode is about 2.7 μm. A full view of D1 is shown in Fig. 4-8 below.

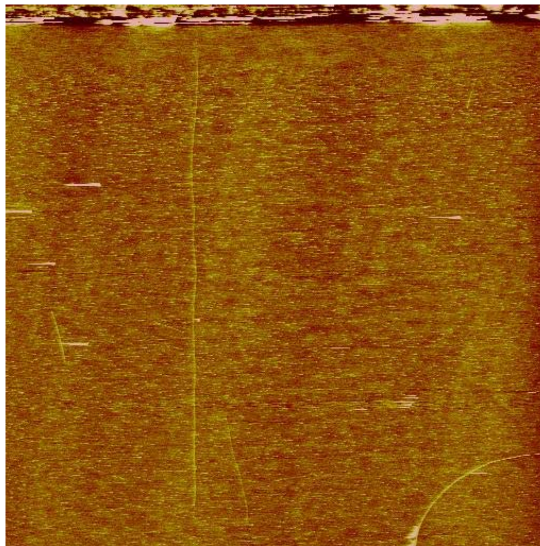

Figure 4-8: An AFM topography scan of nanotube D1, the scan is 30x30 μm.

The obtained $R(L)$ at gate voltages from -10 V to 9 V, are shown in Fig. 4-9-a (notice the logarithmic scale), and at a gate voltage of -10 V in Fig. 4-9-b below (notice the linear scale). The main features that could be observed are: (1) when the nanotube is in the on-state, $R(L)$ behavior is linear for lengths greater than about 3.5 μm, below that the resistance tends to be somewhat lower than the linear trend of the rest of the nanotube, (2) for the nanotube near its off-state, the linear behavior persists for lengths larger than roughly 8-9 μm, below that length there is a rapid decrease in resistance, there is also an observable kink in the trend at about 2.8 μm, (3) the contact resistance is about 10 KΩ, which is again close to the theoretical limit and is rather insensitive to the gate voltage.

The kinks in the resistance versus length behavior for both the on and near off-states can again be associated with the boundary of the gold islands band. The rapid drop in resistance in the intermediate length regime, roughly between 9 and 4 μm is associated with qualitative changes in the drain current versus gate voltage behavior as the channel length decreases. This is shown in Fig. 4-10 below, with the most pronounced features being a shift of the threshold voltage towards higher positive values, this results in the nanotube not being fully depleted even for V_g = +10 V at the shorter channel lengths.

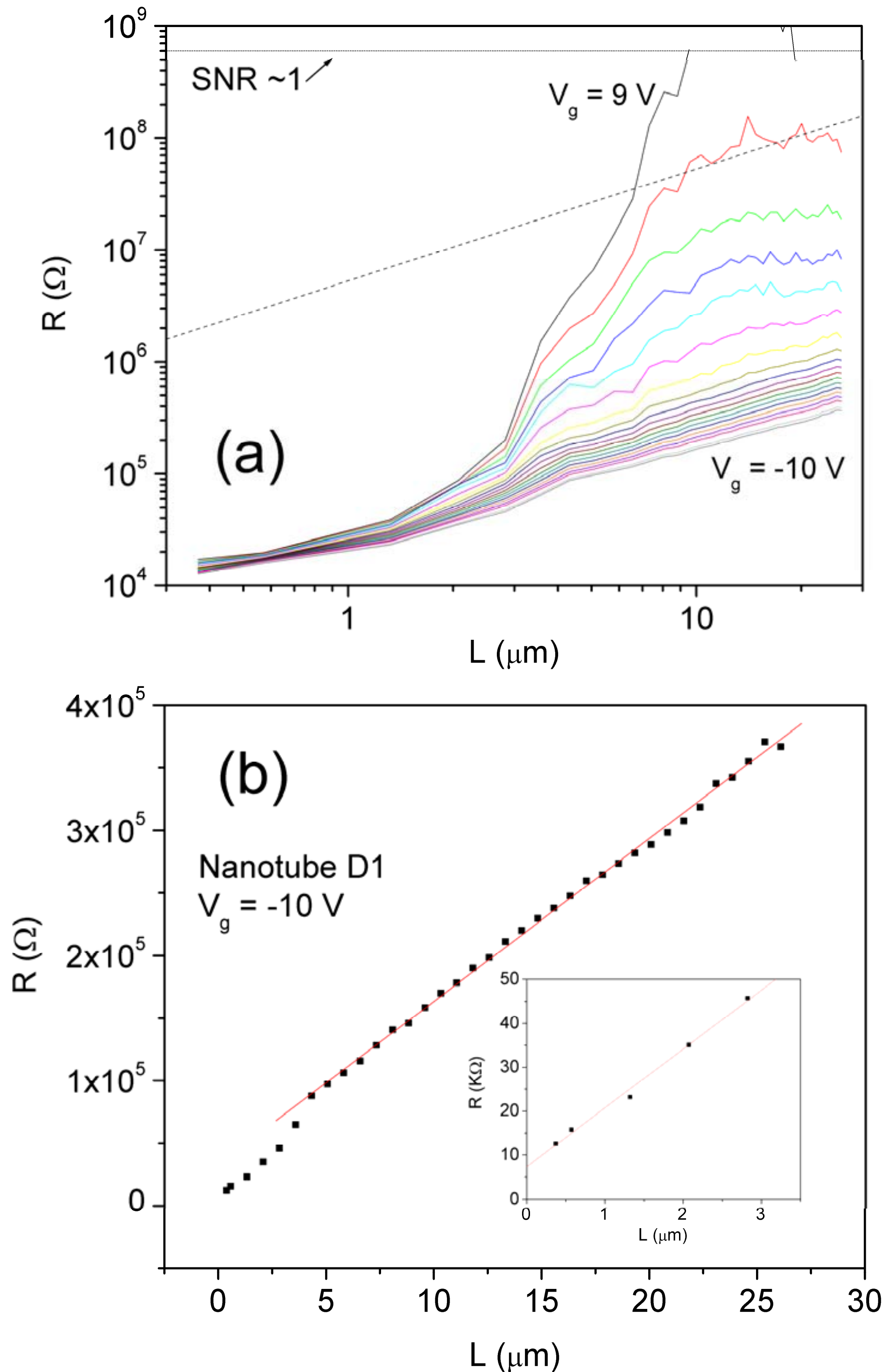

Figure 4-9: (a) Resistance versus length of nanotube D1 at various gate voltages between 9 V and -10 V in steps of 1 V, the thin black line is a proportional relationship (power-law slope of unity), (b) the same data at a gate voltage of -10 V, with linear fitting (excluding points below 4 μm), inset shows the details for short channel lengths (the line fit here is not an extension of the line in the main panel), V_d = 0.1 V for all curves.

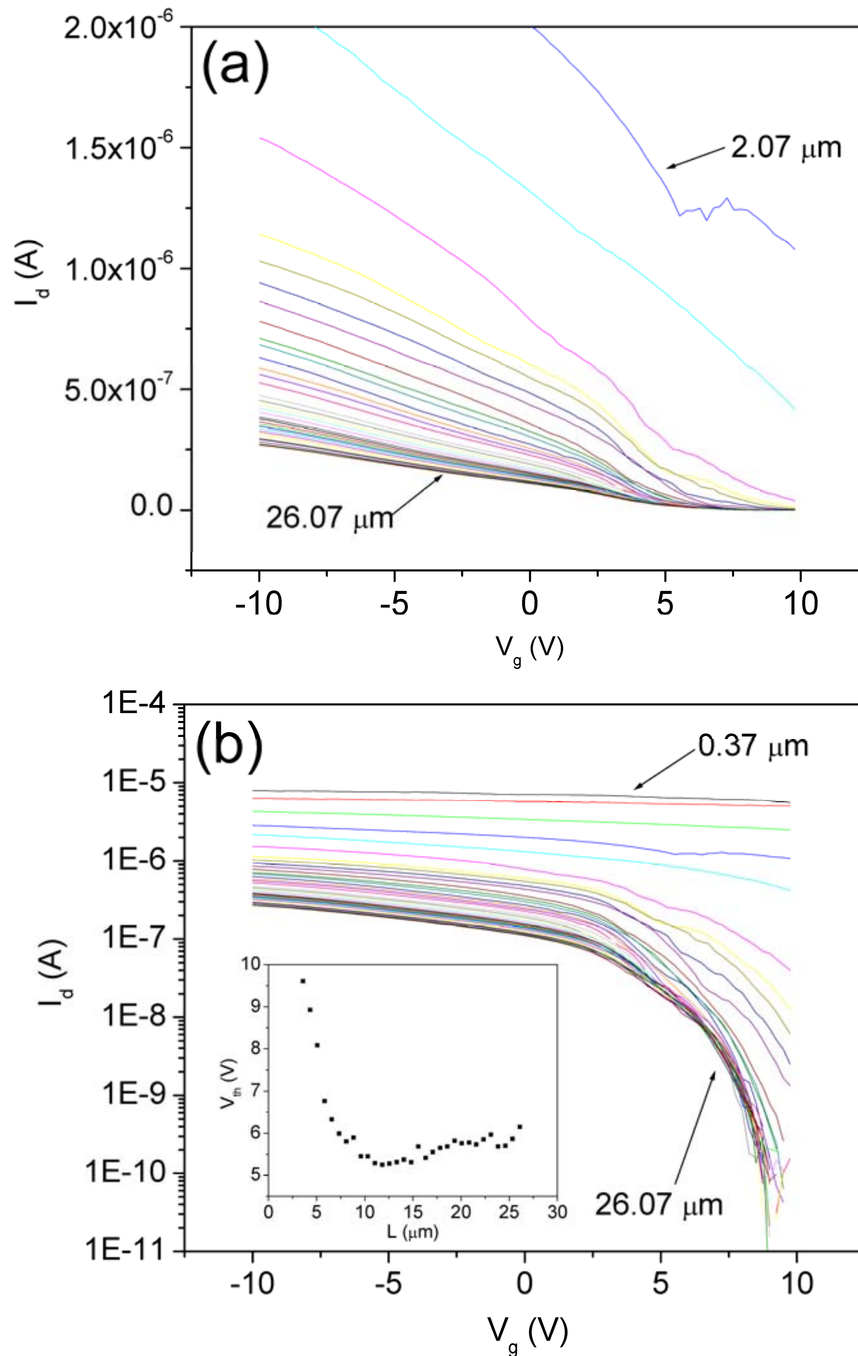

Figure 4-10: Drain current versus gate voltage sweeps at various lengths of nanotube D1 on a linear scale (a) and logarithmic scale (b). The drain voltage V_d = 0.1 V for all curves. The average step in length is 0.75 μm. In (a) the top trace is at 2.07 μm, and the bottom one is at 26.07 μm away from the fixed electrode. In (b) notice the top three traces (at channel lengths of 0.37, 0.57, and 1.32 μm top to bottom) not shown in (a). The inset shows the threshold voltage as a function of length.

4.2.3 Nanotube D5

D5 is a semiconducting nanotube, the diameter is 1.9 ± 0.2 nm, the total length is 130 μm, and the extension of the gold islands band at the edge of the macroscopic gold electrode is about 8 μm (this however can be divided into two regions of 'light coverage' roughly between 3 μm and 8 μm away from the electrode, and 'heavy coverage' for lengths less than 3 μm). Between 32.6-39.5 μm and 91.6-103.8 μm the nanotube had some contamination (this was an occasional problem with nanotubes grown from Ferritin catalyst), and therefore no measurements were taken there to prevent the contamination of the probe. A view showing most of D5 is shown in Fig. 4-11 below.

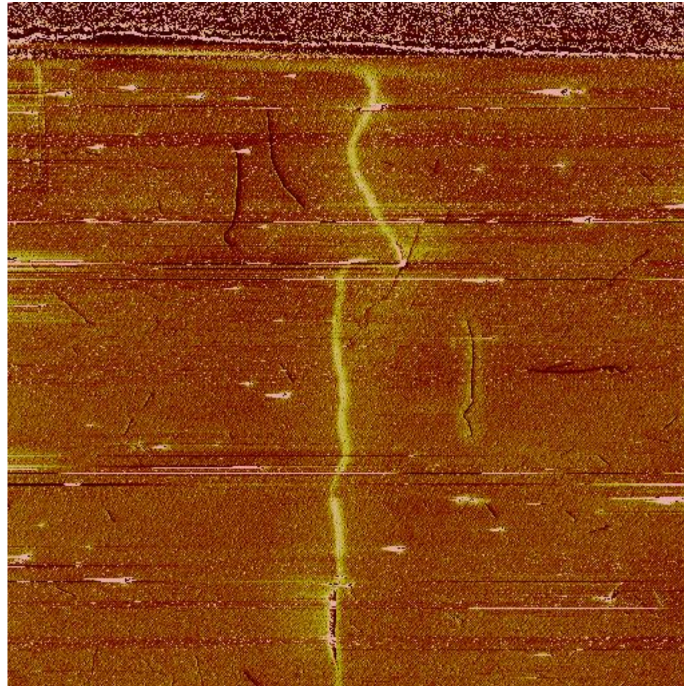

Figure 4-11: An AFM phase scan of nanotube D5, the scan is 100x100 μm, -4 V was applied to the gate in order to create a large phase contrast with the grounded nanotube, one of the contamination regions is clearly visible near the bottom.

The obtained resistance versus length results at gate voltages from -10 V to 9 V, are shown in Fig. 4-12-a (notice the logarithmic scale), and at the gate voltages of -10 V in Fig. 4-12-b below (notice the linear scale).

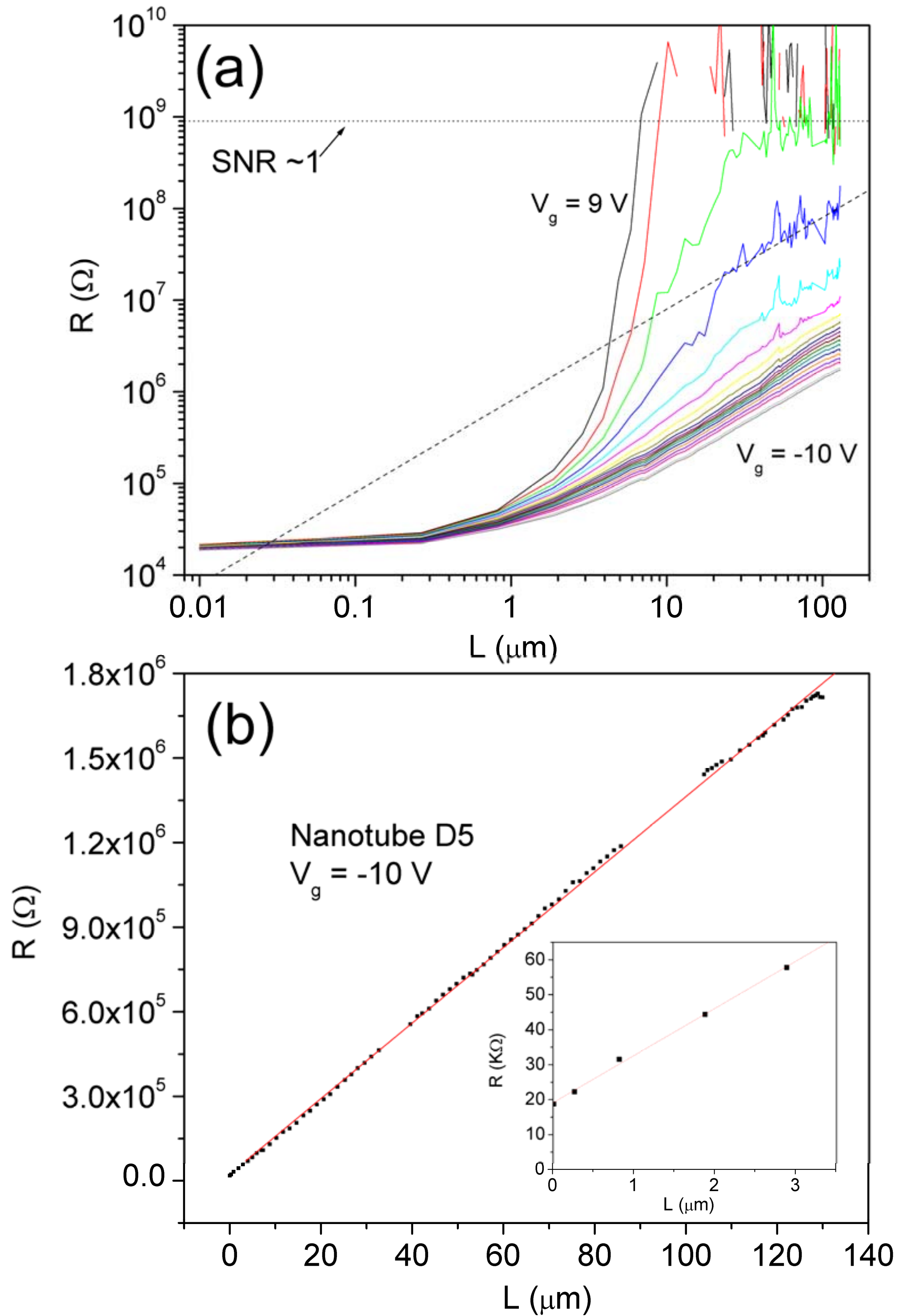

Figure 4-12: (a) Resistance versus length of nanotube D5 at various gate voltages between 9 V and -10 V in steps of 1 V. The thin black line is a proportional relationship (power-law slope of unity), (b) the same data at a gate voltage of -10 V, with linear fitting, the inset shows the details for short channel lengths, $V_d = 0.1$ V for all curves.

The presence of the contamination regions does not seem to affect the resistance since there is an apparent continuity across the gaps in the measurement. In general, the behavior can be seen to be qualitatively similar to that of D1, the length scales however are slightly different. For example, the region of rapid decrease in resistance when the nanotube approaches the off-state extends between about 20 μm down to 3 μm, below 3 μm (the beginning of the 'heavy coverage' zone in the gold islands band) the resistance tends to be less sensitive to the gate voltage. The drain current versus gate voltage for D5 is shown in Fig. 4-13 below, and it shows similar features to D1 in terms of the threshold shift and lack of full depletion at $V_g = +10$ V at the short length scales.

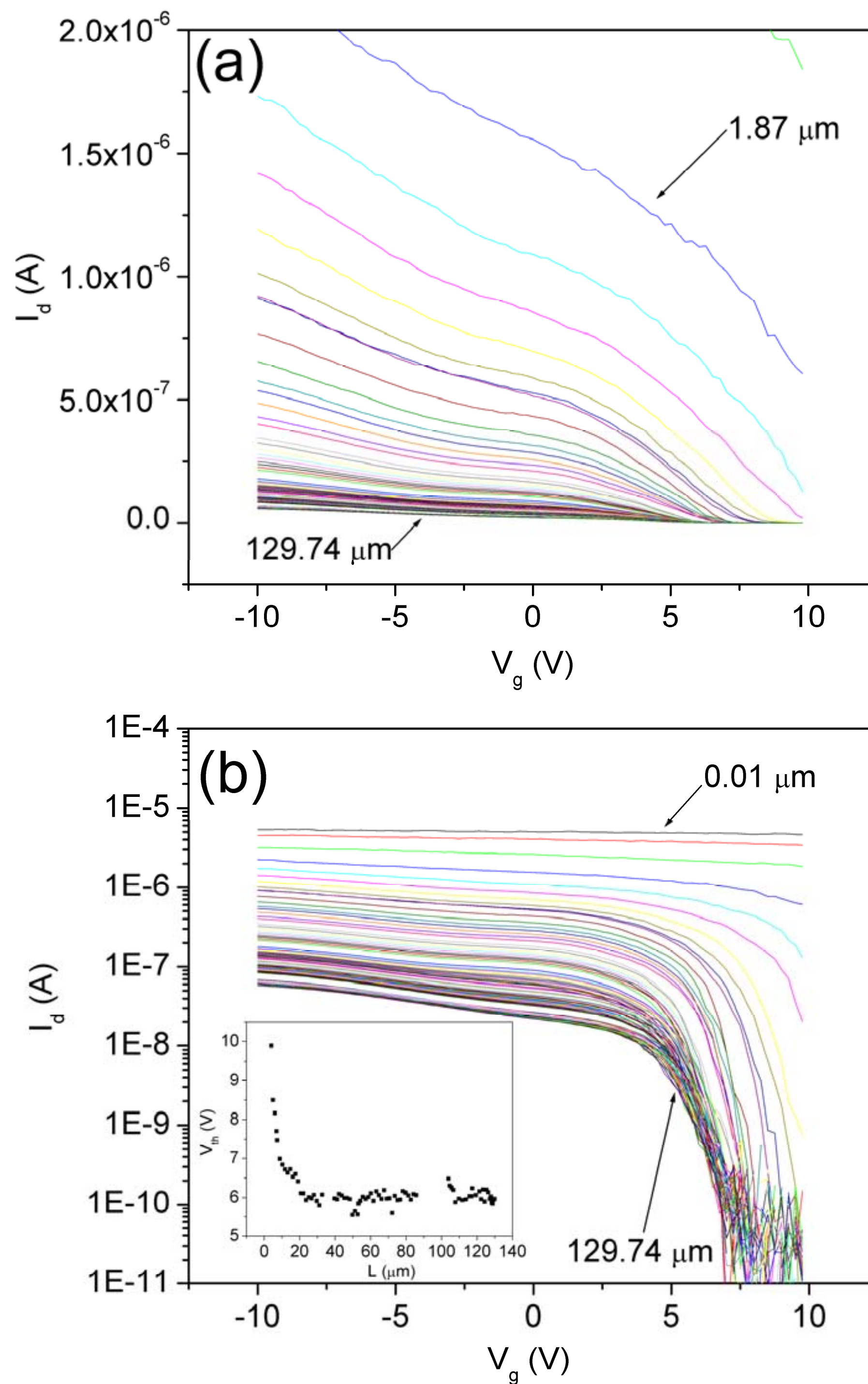

Figure 4-13: Drain current versus gate voltage sweeps at various lengths of nanotube D5 on a linear scale (a) and logarithmic scale (b). The drain voltage $V_d = 0.1$ V for all curves. The average step in length is 1.5 μm. The top trace in (a) is at 1.87 μm, and the bottom one is at 129.74 μm away from the fixed electrode. In (b) notice the top three traces (at channel lengths of 0.01, 0.27, and 0.82 μm top to bottom) not shown in (a). The inset in (b) shows the threshold voltage as a function of length.

4.2.4 Nanotube D3

D3 is a semiconducting nanotube. As I will show shortly, this nanotube contains two different segments separated by a junction. The diameter is 2.1 ± 0.1 nm near the end, and 3.0 ± 0.3 near the electrode side (this however was estimated from low resolution scans), the total length is about 104 μm, the last 17 μm at the free end were not measured due to the presence of contamination, the position of the suspected junction is about 34 μm away from the gold electrode, the extension of the gold islands band at the edge of the macroscopic gold electrode is 0.6 μm at most. A partial view of D3 is shown in Fig. 4-14 below.

Figure 4-14: An AFM topography scan of nanotube D3, the scan is 35x35 μm, the position of the junction (34 μm from the electrode) is indicated by the green circle.

Fig. 4-15 below shows the on-state resistance for the whole nanotube, it can be clearly seen that there is a sharp change in the slope around 34 μm away from the fixed electrode, in the AFM scan this position corresponds to a small kink that is indicated by the circle in Fig. 4-14 above.

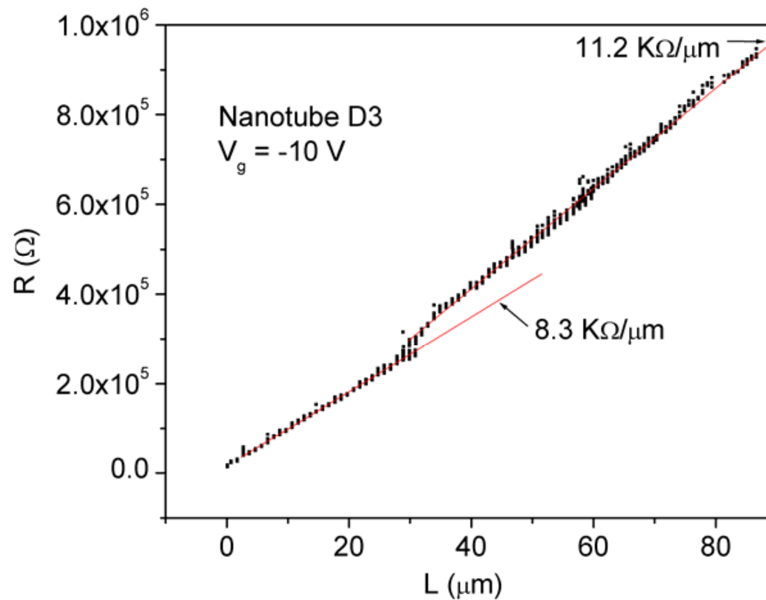

Figure 4-15: Resistance versus length for nanotube D3 at a gate voltage of -10 V (in this case all data points are shown, not just the lower envelope), V_d = 0.5 V. Red lines are linear fits to data point less than and greater than 34 μm; slopes correspond to resistivity of 8.3 KΩ/μm and 11.2 kΩ/μm, respectively.

By closely examining the drain current versus gate voltage response around that site, one can see a large reproducible change in the threshold voltage as is shown in Fig. 4-16-a below, this change causes the post-junction segment (relative to the fixed electrode) to turn off much faster than the pre-junction segment for gate voltages roughly between 1.5-4.5 V, this is shown in Fig. 4-16-b for a gate voltage of 3 V.

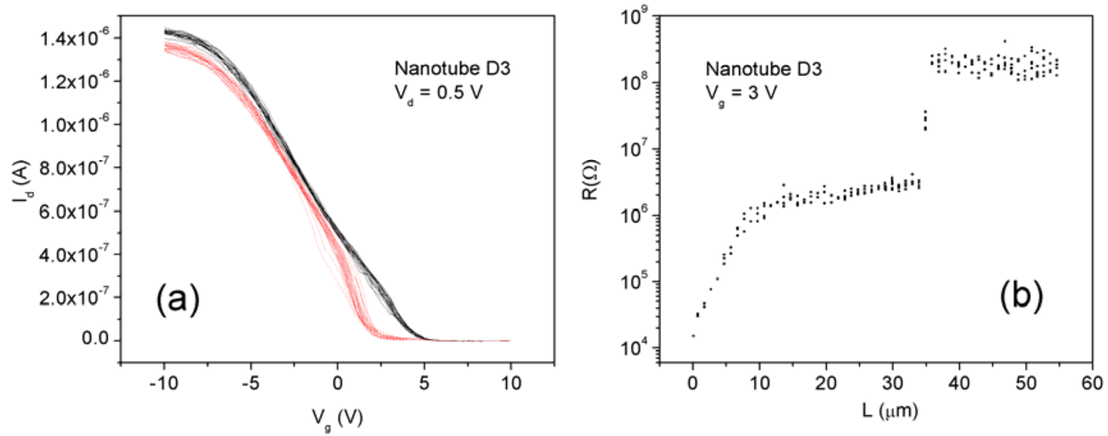

Figure 4-16: Change in behavior of nanotube D3 at 34 μm. (a) I_d vs. V_g sweeps for lengths smaller than 34 μm (red dotted traces) and larger than 34 μm (solid black traces) showing a large change in the threshold voltage. The curves correspond to data taken at points 1 μm apart. (b) $R(L)$ at V_g = 3 V showing the disconnection caused by the extraneous gate voltage dependence of the junction. V_d = 0.5 V for all data in (a) and (b). In (b) all data points are shown, not just the lower envelope.

All the above indicates a different nature of the pre- and post-junction segments. This junction can be an interface between two nanotubes of different chirality; another possibility is that the smaller diameter nanotube is actually continuous all the way with an extra wall added in the pre-junction segment. The resistivity ratio of the two segments is about 0.74 which is almost equal to the ratio of their diameters which is 0.7 ± 0.08. Such an inverse proportionality between the resistivity and the diameter is expected [11, 93] and observed for single walled carbon nanotubes [11]. The observation of this inverse relationship here supports the first model (that the junction is an interface between two nanotubes of different chirality), or indicates that the current is mostly carried by the outer shell in the second model (the smaller diameter nanotube is continuous with an extra wall added in the pre-junction segment), and thus this portion of the nanotube can still be treated as single walled.

Due to the extraneous gate dependence introduced by this junction in the post-junction region, I will analyze the length-dependent resistance of D3 only for the pre-junction segment in the following parts of this chapter. The resistance versus length as a function of gate voltage from -10 V to 9 V for the pre-defect segment is shown in Fig. 4-17 below.

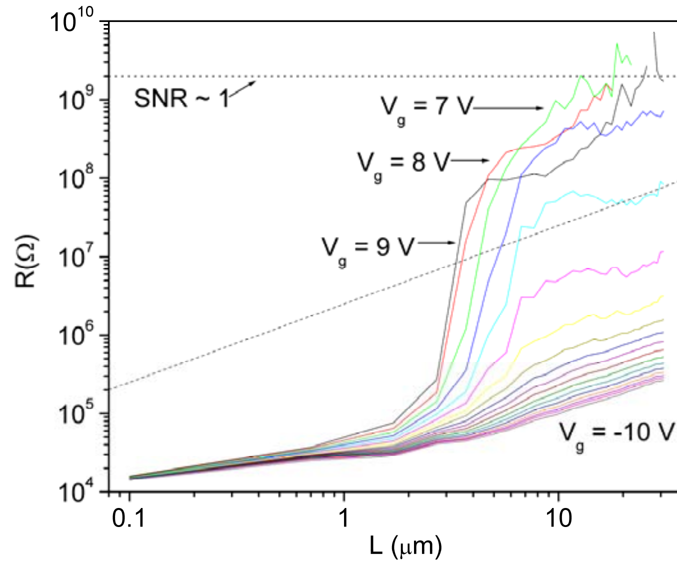

Figure 4-17: Resistance versus length of nanotube D3 at various gate voltages between 9 V and -10 V in steps of 1 V. The dotted black line is a proportional relationship (power-law slope of unity), $V_d = 0.5$ V for all curves.

The behavior can be seen to generally exhibit similar characteristics to those of D1, and D5. One significant difference though is that after some positive gate voltage (roughly between $V_g = 7$ V and $V_g = 8$ V), the resistance starts to drop. This can be seen in Fig. 4-17 above, where the trace for $V_g = 8$ V shows lower resistance than that for $V_g = 7$ V. This behavior can be understood from the drain current versus gate voltage shown in Fig. 4-18 below, as the onset of n-type conduction; that this is observable only for D3 and not D1 or D5, and is probably due to the fact that D3 has the largest diameter, and therefore the smallest bandgap [94].

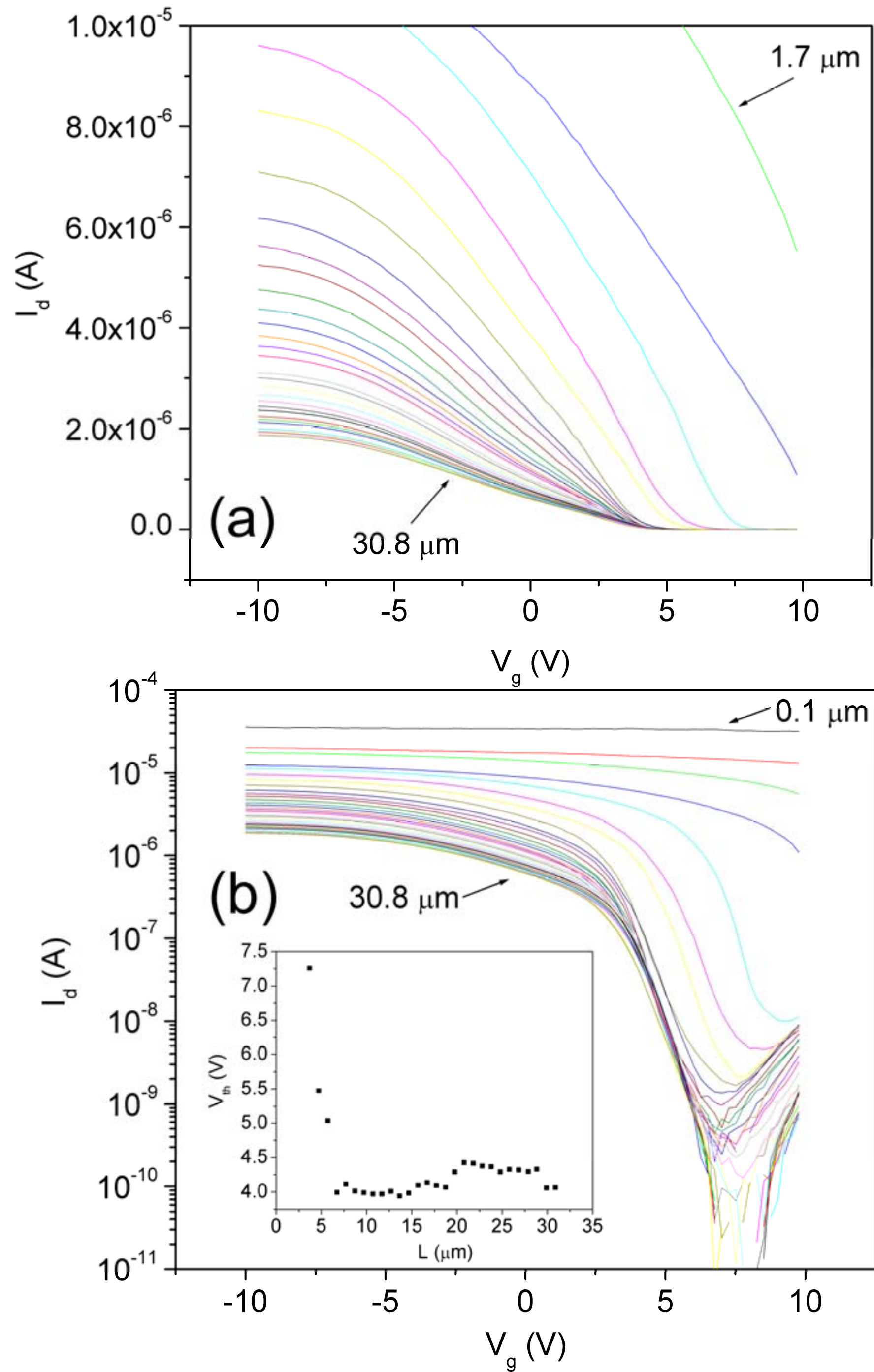

Figure 4-18: Drain current versus gate voltage sweeps at various lengths of nanotube D3 on a linear scale (a) and logarithmic scale (b). The drain voltage V_d = 0.5 V for all curves. The average step in length is 1 μm. In (a) the top trace is at 1.7 μm, and the bottom one is at 30.8 μm away from the fixed electrode. In (b) notice the top two traces (at channel lengths of 0.1, and 0.7 μm top to bottom) not shown in (a). The inset shows the threshold voltage at various lengths.

4.3 Discussion

The main features of the data presented above can be summarized as follows: (1) when a nanotube is on, the resistance versus length is linear for almost all the length; (2) when a nanotube is near the off state i.e. it is in an advanced depletion state, there exist two regions with different qualitative behavior, for channel lengths less than about 10 μm, the resistance rises quickly with increasing channel length in an almost exponential manner, then for longer channel lengths the resistance is linear; (3) this behavior at the advanced depletion state of the nanotube can be qualitatively associated with a shift in the threshold voltage which becomes more positive for shorter channel lengths; (4) for both the on and depleted cases, the resistance versus length is mostly continuous across the island band region with only a mild kink at the boundary of that region, followed by a trend of slightly lower resistance than the trend extrapolated from the rest of the nanotube unaffected by the islands band; (5) the contact resistance is higher than but close (within a factor of 2) to the theoretical limit expected for a single walled carbon nanotube, and is mostly insensitive to the gate voltage. In the following sections I will discuss the possible explanations of these features, and the conclusions that can be drawn about electronic transport in the nanotubes.

4.3.1 Contact resistance and contact type: Ohmic vs. Schottky

In my measurements nanotubes are contacted on one side by the fixed gold electrode (the source), and on the other side of the channel by the gold coated cantilever (the drain), therefore the contacting metal is gold on both sides. In general, a nanotube-metal junction can either be of the ohmic [6, 66] or Schottky barrier [2-4, 7] types. The type of contact depends on the work function of the contacting metal, since Fermi level pinning is thought to either be nonexistent or play an insignificant role in nanotube-metal junctions [95, 96]. The junction type also depends on the nanotube bandgap, and hence diameter of the contacted nanotube. Both experimental [6] and theoretical [96, 97] works show that for the same contacting metal, there exists a critical diameter below which the contact is of the Schottky barrier type, and above which the contact is of the ohmic type. These works indicate this critical diameter to be about 1.8 nm for nanotubes contacted by palladium.

For all three semiconducting CNTs studied (D1, D3, D5), I observed a low (within a factor of 2 from the theoretical limit) and gate voltage independent contact resistance. These observations are consistent with an ohmic contact, where the Schottky barrier model predicts a large modulation of the barrier by the gate voltage [2, 7]. Given that the work function of gold is similar to that of Palladium (about 5.1 eV), it is reasonable to expect an ohmic contact for these large diameter ($d > 1.9$ nm) nanotubes, whose diameters are larger than the critical diameter for an ohmic contact with palladium. Gold has also been reported before to form ohmic contacts to nanotubes [33, 48]. The high saturation drain current of 25 μA for short channel lengths at high negative drain voltages for D5 (which has the smallest diameter), is also indicative of the absence of a Schottky barrier [66].

Another measure that has been used [4, 6, 7, 23] to judge the type of the nanotube-metal junction is the subthreshold swing $S = (d \log_{10} I_d / dV_g)^{-1}$ where I_d is the drain current in the subthreshold region (this is roughly the region below $I_d = 10^{-8}$ A for D1 and D5, and $I_d = 10^{-7}$ A for D3, as shown in Figures 4-10-b, 4-13-b, and 4-18-b respectively). The determination of the threshold and subthreshold swing are illustrated in Fig. 4-19 below.

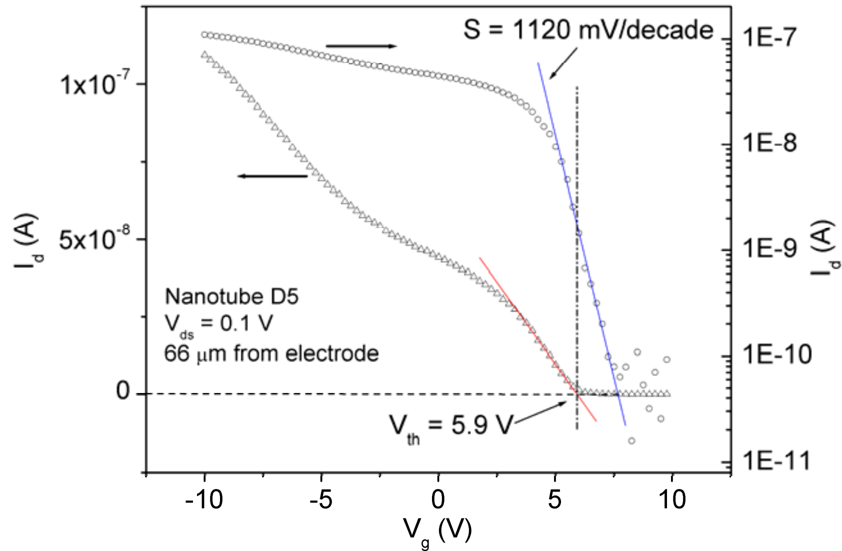

Figure 4-19: Determination of the threshold voltage V_{th} and the subthreshold swing S. The triangles and the circles represent the same I_d versus V_g data on linear (triangles) and logarithmic (circles) scales respectively. The threshold voltage is the point of linear extrapolation of $I_d(V_g)$ to zero (red line). The subthreshold swing is the inverse of the logarithmic slope of $I_d(V_g)$ in the subthreshold region (blue line).

Typical values of $S \sim$ 1000-2000 mV/decade are obtained for nanotubes with a Schottky barrier contact on thick dielectrics at room temperature [4, 7], and $S \sim 160$ mV/decade for ohmic contacts under the same conditions [66] which is close to the theoretically expected value of 60 mV/decade for MOSFETs at room temperature. In

the three semiconducting nanotubes I measured, *S* is of order 1000 mV/decade on the average which is consistent with expectations for a Schottky barrier contact.

It must be noticed however, that in most of the previous work cited above, the subthreshold swing was characterized for relatively short nanotubes ~ 1 μm. In one work on long nanotubes [23] the subthreshold swing was large (~800 mV/decade) at room temperature despite an ohmic contact. This was revealed by the temperature dependence of *S*, which did not become temperature independent upon cooling down as expected for Schottky barrier contacts [7]. This suggests that a study of the subthreshold swing as a function of channel length *S*(*L*) may shed light on some of the variability observed in the literature. Fig. 4-20 below shows *S*(*L*) for the three semiconducting nanotubes D1, D3, and D5. Surprisingly the subthreshold swing shows a trend of increasing linearly with channel length. This behavior is at odds with what is expected from the Schottky barrier model, which predicts a subthreshold swing that is independent of channel length [7]. It is also at odds with the conventional MOSFET model, where the subthreshold swing increases for shorter channel lengths due to the increase in depletion capacitance relative to the gate capacitance [98].

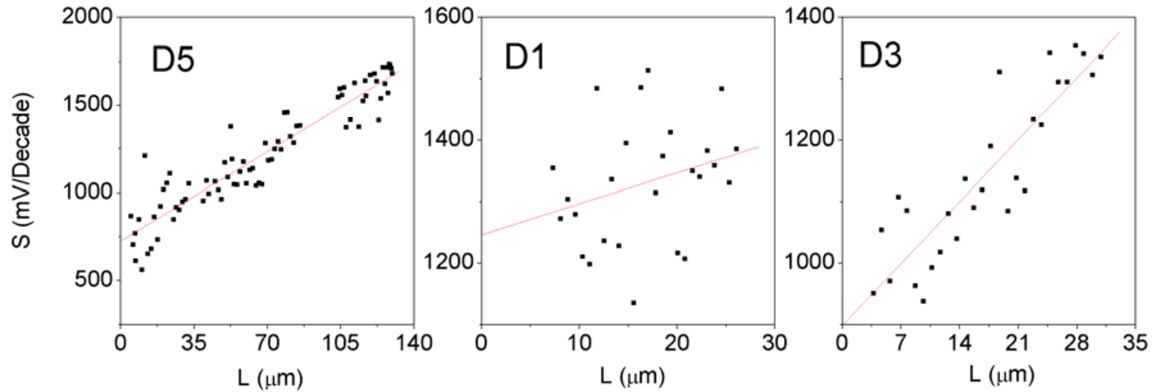

Figure 4-20: Subthreshold swing S versus channel length L for nanotubes D5, D1, and D3. Red lines are linear fits with slopes 7.3, 5.0, and 14.4 mV/decade/μm for D5, D1, and D3 respectively, the zero channel length intercepts are 730, 1250, 900 mV/decade for D5, D1, and D3 respectively.

However, here I can examine the length-dependent resistivity directly to determine whether the resistance in the subthreshold regime is in the bulk of the nanotube or in the contacts. As shown below in section 4.3.5, the nanotube channel resistivity itself is diverging in the subthreshold regime, and shows a similar subthreshold swing as that found by measuring I_d versus V_g at a single point. Hence I conclude that the semiconducting nanotubes studied here are bulk-switching devices i.e. channel resistance dominates over contact resistance for all V_g. This indicates that subthreshold swing alone is not a definitive indicator of Schottky barrier behavior.

While the length dependence of the subthreshold swing is not fully understood, I qualitatively attribute this behavior to an increasing role of charge traps (which have an associated interface capacitance) in the switching of nanotubes at longer channel lengths, i.e. the observed large subthreshold swing behavior is associated with a 'bulk switching' mechanism which is more significant in long channel nanotube devices in contrast to 'barrier switching' of the Schottky barrier model.

To conclude, the low contact resistance and near-independence of contact resistance on gate voltage are consistent with an ohmic contact between gold and the large diameter nanotubes studied here, which is consistent with previous theoretical and experimental studies. The CNTs studied here exhibit large subthreshold swings, normally associated with Schottky barrier contacts. However, the length-dependent resistance data indicate bulk-switching behavior, i.e. dominance of channel resistance over contact resistance in the subthreshold regime, consistent with ohmic contacts and in contrast with the Schottky-barrier model. The length dependence of the subthreshold swing is anomalous and not yet understood.

4.3.2 The effect of the islands band

As described in Chapter 2, the gold islands band at the edge of the shadow evaporated fixed electrode typically has a thickness of ~1 nm, and becomes slightly thicker (2-4 nm) for the last ~ 500 nm of nanotube length in the immediate vicinity of the electrode. These thicknesses are much smaller than the percolation threshold for electric conduction in gold films which is about ~16 nm [64], therefore this band is not conductive (I also verified this by directly contacting it with the cantilever a small distance ~ 50 nm sideways from the nanotubes, therefore these islands are not short-circuiting the nanotubes). The trend of having a slightly lower resistance in the portion of the nanotubes within the islands band region might be explained as a doping effect induced by charge transfer between the islands in touch with the nanotubes and the nanotubes themselves. This is consistent with the ohmic contact

between gold and nanotubes as discussed above. Gold has a higher work function (5.1 eV) than the nanotubes whose work function is about 4.66 eV independent of chirality for diameters larger than 1 nm [99, 100]. Therefore these gold islands should cause p-type doping of carbon nanotubes. Such p-type doping of carbon nanotubes by palladium (which has a similar work function to gold) clusters has been experimentally observed before [101]. It also must be noticed that the short channel lengths of a few microns that are affected by the presence of the islands band, are also influenced by electrostatic effects, which I will discuss in the next sections.

4.3.3 Electrostatic effects

The controlling action of the backgate on the electrochemical potential of the channel of a nanotube device depends on the capacitive coupling between the gate and the channel. This can be divided into three parts which are: the geometrical electrostatic capacitance, the quantum capacitance, and the depletion capacitance. These capacitances should be considered as capacitors in series (i.e. added in inverse) [102, 103].

For the geometrical electrostatic capacitance the nanotube is commonly considered as an infinite cylindrical conductor separated from the planar gate electrode by a dielectric slab, with vacuum above. In this case the capacitance per unit length is well approximated by the expression [104]:

$$C_g = 2\pi\varepsilon\varepsilon_0 / \ln(4t/d) \quad (4\text{-}1)$$

where C_g is the capacitance per unit length, ε is the average of the dielectric constants of the gate insulator and vacuum, t is the thickness of the gate insulator, and d is the diameter of the nanotube; in my measurements t = 500 nm and ε = (3.9 + 1)/2 = 2.45. For a typical nanotube diameter of 2 nm this expression yields C_g of 2.0×10^{-11} F/m.

In my measurements the channel length varies by at least two orders of magnitude. This raises a concern about the length scale at which C_g begins to deviate from the description above as an infinite cylinder. Qualitatively, this length scale should be largely determined by the spatial extension of the fringe fields from the electrodes. In other words, as the channel length becomes smaller more field lines from the gate end up at the source or drain instead of the channel, which effectively reduces the capacitive coupling between the gate and the channel.

It is important to understand the length scale at which this reduction of gate control begins to occur since this could provide an explanation for the change in the I_d versus V_g behavior between the long and short channel lengths (Figures 4-9, 4-12, and 4-18). In these terms, the gate begins to lose control at the short channel lengths and therefore a higher positive gate voltage is required to turn the nanotubes off which causes the threshold to shift. Numerical studies of electrostatics of nanowire transistors [105, 106] indicate that the effective range of parasitic capacitance between the gate and the electrodes is largely determined by the gate dielectric thickness and not by the dielectric constant. Therefore the range where the parasitic capacitance between the gate and the electrodes begins to affect the gate control of the channel should be of order $2t_{ox} = 1$ μm. This length scale is significantly lower than the length scale of ~10 μm below which there is a rapid drop in the resistance of

the nanotubes in a depleted state associated with the threshold shifting to higher positive values, therefore this effect of parasitic capacitance can not explain this phenomenon.

For a single walled carbon nanotube with one subband occupied, the quantum capacitance per unit length is of order $C_Q \sim 4e^2 / \pi\hbar v_F = 4\times10^{-10}$ F/m [102] which is much larger than the geometrical electrostatic capacitance, and since these two capacitances are in series, the quantum capacitance can be ignored. In general, the quantum capacitance is a function of the Fermi level position since $C_Q = e^2 g(E)$ where *g(E)* is the density of states. Therefore it should grow even bigger as the gate moves the Fermi level towards the Van Hove singularity at the valence band edge which corresponds to the high depletion state of the nanotube [107]. The depletion capacitance is due to the charge transfer process at the nanotube-metal junction which is discussed in the next section.

4.3.4 Depletion and charge transfer

In contrast to planar semiconductor-metal junctions where the depletion charge is confined to a limited depletion region of a few nanometers that is adjacent to the metal, the one dimensional depletion region at the nanotube-metal junction decays slowly with a long logarithmic charge transfer tail following the region of full depletion [27, 28]. The characteristic length of decay for this charge tail is exponentially dependent on the reciprocal of the doping fraction and therefore can

reach several microns under conditions of high depletion [27]. This behavior is phenomenologically consistent with the observed shift in the threshold voltage at short channel lengths. For channel lengths longer than twice the depletion region (once for each electrode), the threshold voltage would be determined by the position of the valence band in the middle region, which is unaffected by charge transfer from the electrodes. Thus the threshold remains constant at long lengths. As the channel length becomes shorter, the middle region becomes increasingly affected by the holes transferred from the electrodes, which cause the bands to bend down, and therefore a more positive gate voltage is needed to bring the Fermi level down to the edge of the valence band. Quantitatively, the characteristic length of the charge decay is given by [27]:

$$L_D = W^2 / R \qquad \text{(4-2-a)}$$

and

$$W = R \ \exp(\varepsilon\varepsilon_0 E_g / e^2 RNf) \quad W >> R \qquad \text{(4-2-b)}$$

where W can be taken as the distance from the junction where the Fermi level comes within $2k_B T$ from the band edge, R is the radius of the nanotube, ε is the dielectric constant of the gate insulator, E_g is the bandgap of the nanotube, N = 38.17 atom/nm^2 is the atomic areal density, and f is the doping fraction. The bandgap is related to the radius by [18]:

$$E_g = [0.35 \text{ eV.nm}]/R. \quad (4\text{-}3)$$

Combining these equations we obtain the doping fraction as:

$$f = [2.486\times 10^{-3} \text{ nm}^2]/R^2 \ln(L_D/R) \quad (4\text{-}4)$$

where the gate dielectric constant ε was taken as 2.45 to account for the absence of the dielectric above the nanotube (see the discussion above). The characteristic length L_D can experimentally be obtained from the threshold versus length data shown in the insets of Figures 4-10-b, 4-13-b, and 4-18-b, I empirically used an exponential fitting function $V_{th} = A + B\exp(L/L_{th})$ in order to extract the characteristic length scale L_{th} of the variation in the threshold voltage with channel length (these values are shown in Table (4-1) below). L_{th} should be equal to $2L_D$ since there is a depletion region for each electrode. Using Equation (4-4) the doping fraction can be calculated. If this doping fraction extracted from the voltage threshold versus channel length truly corresponds to the Fermi level approaching $2k_BT$ from the valence band, as is assumed above, then it should correlate with the thermal population of holes above the Fermi level in the same limit. This could be estimated from:

$$\sigma_{1D} = e\int D(E)f(E-E_F)dE = e(2\pi RNf_k) \quad (4\text{-}5)$$

where σ_{1D} is the linear charge density, $D(E)$ is the 1-D density of states, $f(E-E_f)$ is the Fermi function, and f_k is an equivalent doping fraction of the thermal population, the

integral is to be evaluated within $2k_BT$ from the valence band edge. The nanotube 1-D density of states (for one band) is given by [108]:

$$D(E) = \frac{4}{\pi \hbar v_{F,m}} \left(1 - \left(\frac{E_g}{2E} \right)^2 \right)^{-1/2} \qquad E > E_g/2 \tag{4-6}$$

where $v_{F,m} = 8 \times 10^5$ m/s is the Fermi velocity for a metallic nanotube, and the energy is measured relative to mid-gap. Substituting (4-6) into (4-5) we get the equivalent doping fraction f_k as:

$$f_k = \frac{2}{\pi^2 R N \hbar v_{F,m}} \int_{E_g/2}^{E_g/2+2k_BT} \frac{1}{\sqrt{1-(E_g/2E)^2}} \frac{1}{1+e^{(E-E_g/2)/k_BT}} dE \tag{4-7}$$

making the substitutions $\Lambda = E/k_BT$, and $\Psi = E_g/2k_BT$, this could be written as:

$$f_k = \frac{2k_BT}{\pi^2 R N \hbar v_{F,m}} \int_{\Psi}^{\Psi+2} \frac{1}{\sqrt{1-(\Psi/\Lambda)^2}} \frac{1}{1+e^{(\Lambda-\Psi)}} d\Lambda \tag{4-8}$$

using Equation (4-3), we get:

$$\Psi = \frac{[6.731\ nm]}{R} \tag{4-9}$$

at room temperature $k_B T = 0.026$ eV. Inserting the numerical values into Equation (4-8) we get:

$$f_k = \frac{[2.761\times10^{-4}\ nm]}{R}\int_{\Psi}^{\Psi+2}\frac{1}{\sqrt{1-(\Psi/\Lambda)^2}}\frac{1}{1+e^{(\Lambda-\Psi)}}d\Lambda \qquad (4\text{-}10)$$

using Equations (4-9) and (4-10), f_k can be numerically evaluated for a given nanotube radius R, the obtained values are shown in Table (4-1) below, and are compared with the values of f calculated from Equation (4-4).

Nanotube	R (nm)	$L_{th} = 2L_D$ (μm)	f	f_k	f/f_k
D5	0.95	4.320	3.564 x 10^{-4}	5.543 x 10^{-4}	0.643
D1	1.05	2.376	3.207 x 10^{-4}	4.793 x 10^{-4}	0.669
D3	1.50	1.374	1.803 x 10^{-4}	2.866 x 10^{-4}	0.629

Table (4-1): Comparison of charge transfer and thermal doping fractions, L_{th} is determined from fitting the threshold versus length data in Figures 4-9-b, 4-12-b, and 4-18-b to an exponential form (see text), f is determined from both R and L_{th} using Equation (4-4) and f_k is determined from R using Equations (4-9) and (4-10).

In essence, Table (4-1) compares the experimental doping fraction f, determined from the experimental variation of the threshold voltage with length, with the theoretical estimate f_k determined using the nanotube radius. We can see that f and f_k are very comparable in magnitude, and differ by a constant multiplicative factor of ~0.65. This could come about because the $2k_BT$ criterion is actually for W, which is shorter than L_D as can be seen from Equation (4-2-a). Therefore the charge transfer induced band bending is smaller at L_D than it is at W, and as the Fermi level

approaches $2k_BT$ from the valence band edge at W it should be within a smaller energy span from the valence band edge at L_D. This corresponds to a smaller upper limit of the integral in Equation (4-8) and therefore a smaller value of f.

I conclude that charge transfer from the electrode and the associated long depletion length in 1-D provides a reasonable explanation for the observed shift in threshold voltage with length. This length-dependent threshold voltage also explains the fast non-linear change in resistance versus length at shorter channel lengths under depletion conditions, now understood as a finite size effect of the depletion region.

The above results provide the first quantitative, transport-based evidence, for the extremely long depletion lengths that are predicted to be characteristic of one-dimensional semiconductors. These have also been recently observed qualitatively [29] using scanning photovoltage microscopy. In addition, my measurements point out that length-dependent resistance measurements of semiconducting carbon nanotubes require extremely long samples in order to observe the intrinsic behavior in a portion of the sample where the charge density is not varying i.e. a portion that is unaffected by charge transfer from the contacts.

4.3.5 Mean free path

As my results above show, the resistance versus length in the on-state is linear for most of the length of the nanotubes, and it remains linear for channel lengths larger than ~ 10 μm under depletion conditions. The resistivity at these length scales should be an intrinsic property of the nanotubes which is unaffected by contact

resistance or depletion. For a single walled nanotube the resistivity (resistance per unit length) ρ and the mean free path l_m are related by [10, 24]:

$$l_m = \left(\frac{4e^2}{h} \rho \right)^{-1} \qquad (4\text{-}11)$$

Fig. 4-21 below shows the resistivity versus gate voltage obtained from the linear portions of resistance versus length for nanotubes D1, D5, and D3 (these correspond to channel lengths larger than about 8 μm in Fig. 4-8 for D1, 20 μm in Fig. 4-11 for D5, and 7 μm in Fig. 4-17 for D3) along with the corresponding mean free paths calculated from Equation (4-11).

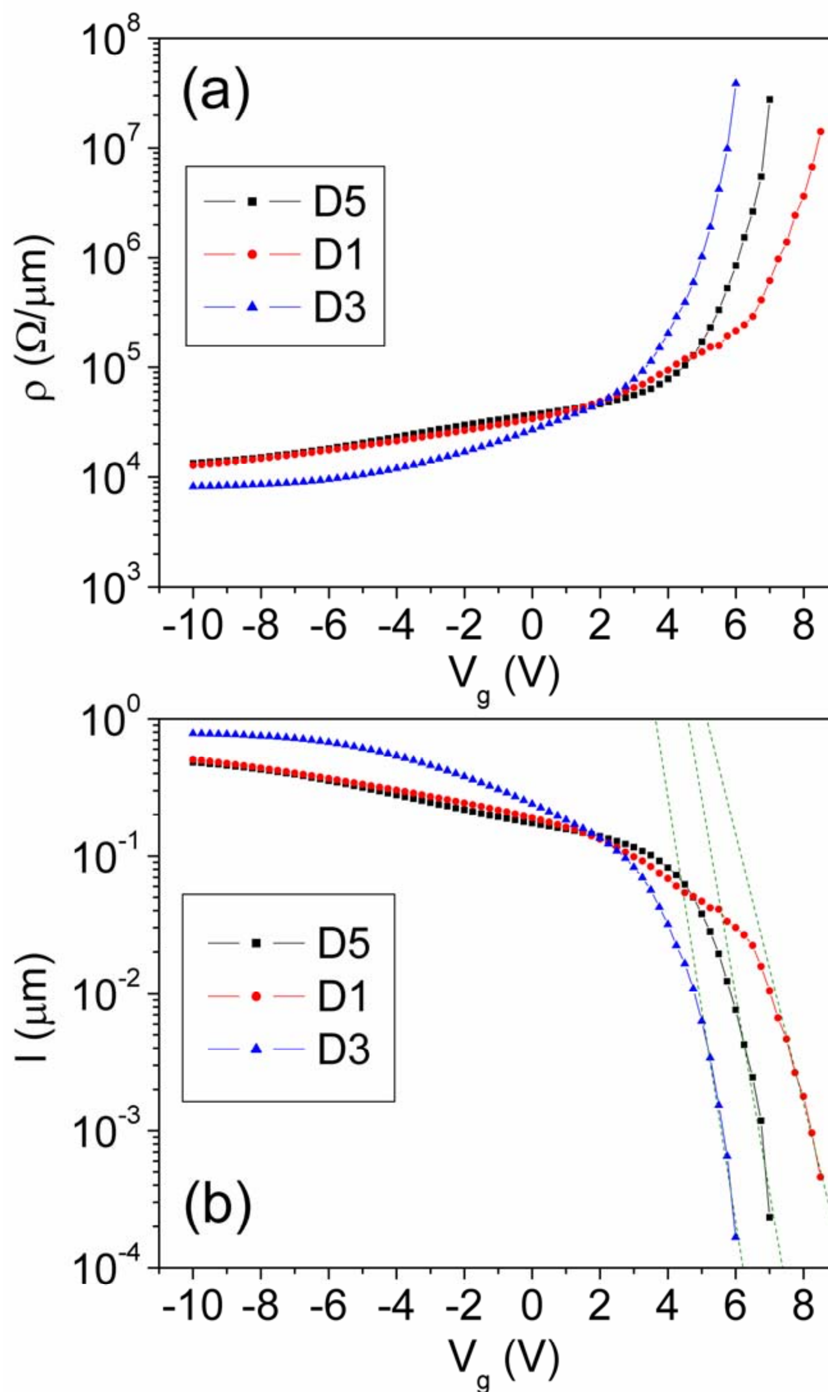

Figure 4-21: (a) Resistivity ρ and (b) mean free path l as a function of V_g for the three semiconducting nanotubes D5, D1, and D3. The dashed green lines in (b) are exponential fits to l in the subthreshold region corresponding to subthreshold swings of 700, 1020, and 650 mV/decade for D5, D1, and D3 respectively. Only p-type data is shown for D3.

We can observe that the resistivity increases with gate voltage, remaining within a factor of 10 from the minimum resistivity at -10 V for most of the range, however near the threshold it starts to diverge, reaching values that exceed 10^7 Ω/μm before the limit of my measurement sensitivity is reached. Notably, $R(L)$ is still linear at these high resistivity values, i.e. resistivity remains a meaningful concept. The corresponding mean free paths become very small (~ 0.46 nm for D1, 0.23 nm for D5, and 0.17 nm for D3) approaching the Ioffe-Regel limit $l \sim a$ where a is the inter-atomic spacing [109] (this is 0.144 nm for carbon-carbon bonds in graphite) .

For l near the threshold, one could assign a subthreshold swing $S_l = (d \log_{10} l / dV_g)^{-1}$. S_l should be an intrinsic property of the nanotube channel. The values obtained for S_l are 700, 1020, and 650 mV/decade for D5, D1, and D3 respectively. These can now be compared to the $S(L)$ values obtained from individual I_d versus V_g sweeps shown in Fig. 4-20 above (this can be done since $l \propto I_d$ for constant L and V_d). In particular, the above S_l values are similar to the values of S linearly extrapolated (from long channel lengths) to zero channel length, these are 730, 1250, 900 mV/decade for D5, D1, and D3 respectively. This indicates that the large observed values of the subthreshold swing are intrinsic to the nanotube channel, rather than an effect of the contacts, which confirms the conclusions in Section 4.3.1 that the contacts in my measurements are ohmic, and that switching in my devices is caused by the bulk of the nanotubes rather than at the contacts.

The persistence of diffusive transport near the off state of semiconducting carbon nanotubes at room temperature is rather different from their behavior at low temperatures, where electrostatic potential fluctuations due to disorder (structural

defects or charged impurities in the substrate), cause the nanotube to breakup into several segments with conduction caused by charge hopping between them, as evidenced by the observation of Coulomb blockade oscillations at low temperatures [10, 30-32, 110]. The same defects that cause such break up could still be active at room temperature as is inferred from scanning gate microscopy (SGM) measurements. However, it is clear from the linear $R(L)$ that the charge carriers in my measurements remained delocalized. This experimental fact can help reveal the different roles of scattering mechanisms near the band edge as I will discuss below.

At room temperature the dominant scattering mechanisms in carbon nanotubes are scattering by disorder and by phonons. In the low bias regime studied here, the main contribution to electron-phonon interaction comes from acoustic phonons [5, 12-14], with a possible contribution from optical phonons [111]. Both of these mechanisms are gate voltage dependent. The gate voltage dependence of disorder is revealed by both SGM [51] and scanning photovoltage microscopy [29]. The disorder sites usually have a stronger signature in these measurements under depletion conditions. This could come about because of the changes in the density of states caused by structural defects, or the generation of local depletion regions by charged impurities. A simple physical picture for this is the gate voltage modulating the height and width of local potential barriers at the disorder sites and therefore their transmission coefficients. The result would be a gate modulation of the elastic mean free path, becoming smaller upon approaching the threshold. For phonon scattering, the rate of scattering is proportional to the density of states by Fermi's golden rule [112], therefore as the Fermi level approaches the van Hove singularity at the edge of

the valence band (which is associated with the threshold as established in the previous section), both the electron-phonon scattering time and mean free path should quickly drop, which is confirmed by theoretical calculations [25, 113, 114]. Using Matthiessen's rule, the amplitude of the overall mean free path would be dominated by the shorter of the disorder scattering and phonon scattering mean free paths: $1/l = 1/l_{disorder} + 1/l_{ph}$ where l_{disorder} is the disorder scattering mean free path, and l_{ph} is the phonon scattering mean free path.

The interplay between these two mechanisms depends on the spatial distribution and strength of defects, and I consider two cases of strong and weak disorder. The first case is when the disorder generates strong enough barriers that transport is dominated by thermionic emission or thermally assisted tunneling [115] through these barriers. Then as the sample is cooled down the resistance should increase, being ultimately dominated by the heterogeneous localization caused by Coulomb blockade, with charges hopping between the segments defined by the barriers [10, 110]. For the second case, that is weak disorder, the transport would be dominated by phonon scattering, and upon cooling down the resistance should decrease, finally reaching a saturation value determined by disorder. In this case one might expect to observe Anderson-type homogeneous localization effects. Both of these types of temperature dependence have been reported for carbon nanotubes [24, 110]. However the localization effects observed in Reference [24] were anomalous and not of the Anderson type in terms of both the magnitude and temperature dependence of the presumed localization length. Both of these types of localization effects should lead to an exponential $R(L)$ behavior at sufficiently low temperature.

Like temperature, changing the gate voltage should also change the relative magnitudes of disorder and phonon scattering mean free paths. However in my measurements the transport seems to remain diffusive for all measurable resistances. The absence of any localization effects can then be used to understand the relative importance of the two scattering mechanisms near the threshold voltage.

Considering the strong disorder model, the absence of Coulomb blockade oscillations in I_d versus V_g data means that the thermal energy at room temperature k_BT = 26 meV is larger than the sum of the charging energy $E_C = e^2/2C_{Seg}$ and the single particle level spacing ΔE (see Chapter 1) of any segment that could form under depletion conditions. The capacitance of the segment C_{Seg} can be estimated as the sum of the capacitance to the gate and the capacitance between the segment and the leads (in this case the rest of the nanotube). The capacitance to the gate can be estimated from Equation (4-1), however this might not be very accurate if the segment length is much less than the oxide thickness (500 nm) as discussed before. Capacitance to the leads is ~ 0.3 aF as given in Reference [32]. For a nanotube with diameter d ~ 2 nm, E_{C} can be found to be:

$$E_C \approx \frac{[4\ eV.nm]}{15 + L_{Seg}} \tag{4-12}$$

where L_{Seg} is the segment length. The level spacing can be evaluated from the density of states (4-6), $\Delta E = 1/D(E)L_{Seg}$. Using the dispersion relation, this can be written in terms of the wave vector k as:

$$\Delta E(k) = \frac{\pi\hbar v_F}{4L_{Seg}}\left(1+\left(\frac{E_g}{2\hbar v_F k}\right)^2\right)^{-1/2} . \qquad (4\text{-}13)$$

At the energy span of concern near the top of the valence band, k becomes small $k \sim 2\pi / L_{Seg}$, therefore (4-13) can be written as:

$$\Delta E \approx \frac{(\pi\hbar v_F)^2}{E_g}\frac{1}{L_{Seg}^2} = \frac{[7.8\ eV.nm^2]}{L_{Seg}^2} \qquad (4\text{-}14)$$

using $\Delta E + E_C = k_B T$ along with Equations (4-12) and (4-12), I estimated the lower bound for the mean distance between disorder sites in my devices. This yields L_{Seg} ~ 140 nm under high depletion conditions, which is not far from the segment size of a 100 nm or more typically obtained from Coulomb blockade oscillations at low temperatures [10, 66]. It should be noticed here that this is mainly determined by the charging energy (4-12) and the contribution from the level spacing ΔE is almost negligible.

For the weak disorder model, the system would remain delocalized if the thermal energy is larger than the level spacing of the localized states, which can be evaluated similar to Equation (4-14) as:

$$\Delta E_L \approx [7.8\ \text{eV.nm}^2]/\xi^2 \qquad (4\text{-}15)$$

where ξ is the localization length. In one dimension the localization length is related to the mean free path as $\xi \approx N_{ch} l$ where N_{ch} is the number of spin-degenerate conductance channels [116]. Using $N_{ch} = 2$ for single walled carbon nanotubes, we get a minimum mean distance between defects of about 9 nm. Both of these estimates are at least one order of magnitude higher than the experimentally observed mean free paths in the turn off regime. Thus, from the lack of observable localization, I conclude that scattering by disorder is not the mechanism responsible for the fast drop of the mean free path in the turn off regime. This can now be understood as being due to the electron-phonon scattering rate becoming higher near the Van Hove singularity at the valence band edge.

For the on state it is hard to determine the relative contributions of these two mechanisms in the absence of data on temperature dependence. However we can notice a proportionality between the on state mean free paths and the diameters of the nanotubes (which is the same as the inverse proportionality between resistivity and diameters mentioned earlier in section 4.2.4), with $(l)_{ON} \approx 0.5$ μm for D1 and D5 whose diameters are ~ 2 nm, and $(l)_{ON} \approx 0.75$ μm for D3 whose diameter is 3 nm (see Fig. 4-21). Such a proportionality is expected for the case of electron-phonon interaction [11, 93], but is unlikely for scattering by disorder. For point disorder (atomic defects) on the nanotube, one could argue that the mean free path should be *inversely* proportional to the diameter of the nanotube: if the probability per unit surface area for a certain type of structural defect to form is P_D then for a nanotube of diameter d the linear density of defects would be $\pi N P_D d$ (assuming P_D is independent of curvature), therefore the average distance between defects is

$l_{disorder} = (\pi N P_D d)^{-1}$. This trend can somewhat be observed in the data of Reference [24] where the temperature dependence of the on-state mean free path for seven semiconducting nanotubes was studied. In that work the saturation mean free path at ~ 50 K (which is mainly due to disorder) can be seen to be longer for smaller diameter nanotubes. Therefore the proportionality between the diameters and the on state mean free paths might be taken as an indication that the electron-phonon interaction probably dominates this regime as well.

4.3.6 Mobility

From the resistivity data for D5, D1, and D3 (Fig. 4-21) I calculated the field effect mobility μ_{FE} as [23]:

$$\mu_{FE} = \frac{L}{C_g}\frac{\partial G}{\partial V_g} = \frac{1}{C_g}\frac{\partial (1/\rho)}{\partial V_g} \tag{4-16}$$

I evaluated C_g using Equation (4-1) using $\varepsilon = 2.45$ as discussed before. The field effect mobility data evaluated from Equation (4-16) are shown in Fig. 4-22 below.

The values of the peak mobility are 3840, 2280, and 5940 $cm^2/V.s$ for D5, D1, and D3 respectively. These values are in general agreement with some previously published data for nanotubes with similar diameters [11] but much lower than others [23]. The oscillatory functional dependence of μ_{FE} on V_g for D5 and D1 is rather unusual compared with the reported dependence in References [11, 23], but seems to

carry some resemblance with the calculations in Reference [93] where the effects of intersubband scattering by phonons are considered.

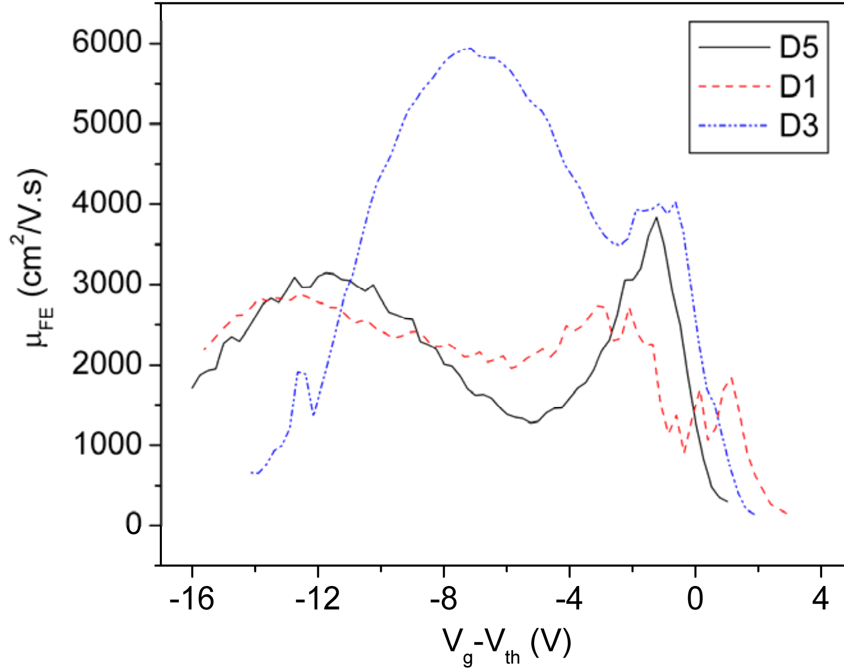

Figure 4-22: Field effect mobility for nanotubes D5, D1, and D3, calculated from the data in Fig. 4-21 and Equation (4-15), the average threshold voltages are 6.01, 5.63, and 4.16 V for D5, D1, and D3 respectively.

4.3.7 Comments on nanotube D7

As shown in Section 4.2.1 for the metallic nanotube D7, the behavior of the resistance versus length was linear in general, with only mild deviations from linearity at gate voltages close to 10 V. These deviations were traced back to the drain current versus gate voltage having some evolution with channel length (see Fig. 4-5). The origin of this evolution is not understood since in this case the nanotube always remains in the on state and therefore there is no depletion region (which was the

origin of the evolution in the drain current versus gate voltage in the semiconducting nanotubes D1, D3, and D5).

Fig. 4-23 below shows the resistivity and the corresponding mean free path calculated from Equation (4-11). It can be seen that the mean free path is somewhat low compared to the typically obtained mean free paths (>1 μm) in metallic carbon nanotubes at room temperature [5, 13, 24, 49], which might indicate a large disorder in this nanotube.

Due to the limited range of gate voltage available in my setup (-10 V to 10 V) it is hard to judge the nature of the plateau in drain current versus gate voltage which appears beyond $V_g \sim 5$ V for long channel lengths and gradually disappears for the short lengths (this is also reflected in Fig. 4-22).

The large value ~ 70 μA of the saturation current compared to the value of saturation current ~ 25 μA in single walled carbon nanotubes which is due to scattering by zone-boundary phonons [14], might suggest the presence of inner shells which actively carries current at least in the high bias regime. Unfortunately the other metallic nanotubes I studied (D4 and D6 see Appendix A) have large diameters (> 4) nm and possibly had multiple walls and also a different topology (both have loops) therefore they might not be suitable for a comparison. Further study of straight small diameter metallic nanotubes is needed before having a conclusion about the above issues.

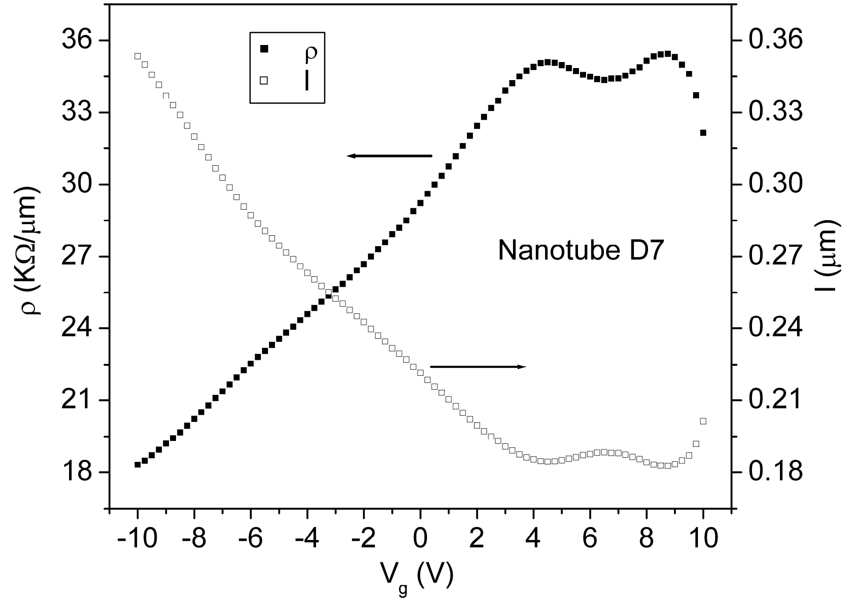

Figure 4-23: Resistivity and the corresponding mean free path as a function of gate voltage for the metallic nanotube D7, $V_d = 0.1$ V for all points.

4.3.8 The D3 junction

As discussed in section 4.2.4, nanotube D3 has two distinct segments of different diameter, which also show different resistivity and gate voltage dependence. I considered two models of this junction. In the first model the two segments are two nanotubes of different chirality separated by a molecular junction, and in the second model the presumed junction marks the beginning of an extra nanotube wall. Assuming that the first model is correct, and then using the drain current versus gate voltage response shown in Fig. 4-16-a, I calculated the transmission coefficient of the junction as a function of gate voltage as:

$$T_J = 1/((4e^2/h)R_J + 1) \qquad (4\text{-}17\text{-a})$$

And

$$R_J = R_{SJ} - R_{RJ} - R_{Seg} \quad (4\text{-}17\text{-}b)$$

where R_{SJ} is the post-junction resistance, R_{RJ} is the pre-junction resistance (both referenced to the fixed electrode), and R_{Seg} is the resistance of the segment containing the defect (1 μm in this case) which is estimated locally from other adjacent measurements. The calculated transmission coefficient is shown in Fig. 4-24 below. This calculation however, assumes only two transmission channels (i.e. a single-walled nanotube) and would need to be modified in the second model if current is carried by multiple nanotube shells. The rather high value (close to unity) of the transmission coefficient near the gate voltage of -10 V might be an indication that this is the case.

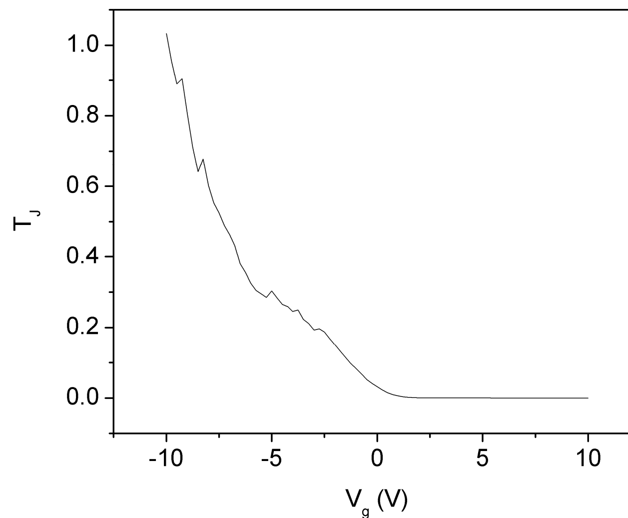

Figure 4-24: The transmission coefficient of the junction between the two segments of D3 calculated from the data in Fig. 4-16-a using Equations (4-16-a) and (4-16-b).

4.4 Conclusion

I performed resistance versus length measurements on several long carbon nanotubes using a metal-coated AFM cantilever to realize a movable metal contact. The gold-nanotube contact resistance (both at the fixed electrode and the AFM tip) is low, within a factor of two of the theoretical lower limit. The gold contact to the large diameter ($\geq$ 1.9 nm) semiconducting nanotubes studied here is ohmic, and switching occurs in the bulk. An apparent non-linear $R(L)$ in semiconducting nanotubes observed at shorter lengths is explained by the very long depletion lengths in one-dimensional semiconducting channels, and points out the importance of studying $R(L)$ in very long nanotubes. All nanotubes show linear resistance versus length for long lengths (> 10 μm) at all measured resistivities. I conclude that transport remains diffusive under all depletion conditions, which is attributed to both low disorder and high temperature. The dominant scattering mechanism is the electron-phonon interaction under all depletion conditions.

Chapter 5: Transport measurements in mesoscopic silver wires at low temperatures

5.1 Background

Mesoscopic physics is a subject that has been extensively studied for the last quarter century [117]. Among the various topics of mesoscopic physics, the subject of quantum corrections to conductivity occupies a special position, for it offers not only an elegant manifestation of quantum interference phenomena in solid state systems, but also a readily accessible experimental tool for measuring the phase coherence time and other scattering times governing the quantum transport in these systems [118, 119].

In a disordered conductor, the electron motion is basically diffusive with the electron being scattered along its path, mostly elastically by the static disorder potential. Occasionally, it suffers inelastic scattering through interaction with phonons, other electrons, and the energy or spin degrees of freedom of any dynamic defects or impurities. These represent an effective position- and time-dependent environment to which the electron is coupled.

The electron can move form one point to another along several paths with corresponding partial wave-functions. If for simplicity we consider only two paths, the appearance of a non-vanishing interference term in the superposition of these two partial wave-functions depends on the environment not being able to distinguish

between these two paths, i.e. there should be some degree of overlap between the environmental degrees of freedom coupled to these two paths, or equivalently, the probability distribution function of the relative phase between the two paths should be sufficiently narrow compared to 2π [120]. This leads to the conclusion that elastic scattering by the static disorder potential does not cause a loss of coherence between the paths, while most of the inelastic processes like electron-electron or electron-phonon scattering do cause such decoherence [119]. The effect of interactions on the evolution of the electron wave function therefore sets an average time scale and a corresponding average length scale over which an electron wave function keeps some degree of coherence. These are called the phase coherence time τ_ϕ and the phase coherence length L_ϕ. For a diffusive conductor these are related by $L_\phi = \sqrt{D\tau_\phi}$ where D is the diffusion constant.

As the temperature approaches zero, the dephasing rate is expected to vanish since both the phase space available for scattering and the density of excitations become smaller with lower temperature, thus causing τ_ϕ and L_ϕ to grow without limit. Assuming no magnetic scattering or dynamic defects exist, only the electron-electron and electron-phonon interactions would participate in dephasing. The electron-phonon interaction tends to be negligible below about 1-2 Kelvin in one- and two-dimensional samples, thus leaving the electron-electron interaction as the dominant decoherence mechanism. In these low-dimensional systems, the dephasing rate due to the electron-electron interaction is dominated by quasi-elastic scattering i.e. scattering with small energy transfers ($\Delta E << KT$), sometimes called Nyquist dephasing since it is equivalent to the scattering of an electron by the fluctuating

electric field (Nyquist noise) created by all the other electrons. The theoretically expected behavior of τ_ϕ as a function of temperature for a one dimensional wire due to this mechanism is [121, 122]

$$(\tau_\phi)_{e-e} = \left[\frac{8\hbar N_F V_W}{R(eKT)^2} \right]^{1/3} \tag{5-1}$$

where N_F is the density of states at the Fermi surface (for silver, $N_F = 1.03\times10^{47}\,J^{-1}.m^{-3}$), V_W is the volume of the wire, and R is the resistance of the wire.

5.2 The problem of τ_ϕ saturation

Measurements of τ_ϕ and L_ϕ by various experimental groups in various materials over the past twenty years have shown that they do not actually diverge as the temperature gets lower in the region where electron-electron interaction is dominant, but they tend to saturate at some temperature [123]. This phenomenon was not systematically studied until 1997 when it was extensively investigated by Mohanty and coworkers [124], and their work induced further theoretical and experimental investigations to find the origin of this contradiction with conventional theory. Three main lines of explanation have been proposed, as we will detail below.

5.2.1 Intrinsic decoherence

Intrinsic decoherence was first proposed by Mohanty, Jariwala and Webb (MJW) [124, 125] to explain their experimental results. Their basic idea was that even at zero temperature the zero-point fluctuations of the electron gas would cause a fluctuating electromagnetic field that couples to the electron being observed thus causing decoherence. The spectral density of this electromagnetic field is both temperature and frequency independent. Therefore, in order to get any physically meaningful quantities phenomenological frequency cutoffs have to be imposed. The lower cutoff was taken to be $\hbar D / L_{\phi}^{2}$ because frequencies less than $1/\tau_{\phi}$ do not contribute to dephasing and the upper limit was taken to be the classical electron energy $mV_{D}^{2}/2$, where V_D is the diffusion velocity. This leads to a finite value for τ_{ϕ} at zero temperature that is almost material independent and depends mainly on classical transport parameters. The temperature dependence of τ_{ϕ} was also obtained which they found to fit well to a large volume of experimental data [124, 125], and is given by

$$(\tau_{\phi})_{Intrinsic} = \tau_{0} \tanh\left\lfloor \alpha \pi^{2} \sqrt{\hbar / \tau_{0} KT} \right\rfloor \quad \text{(5-2-a)}$$

With

$$\tau_{0} = \left(\frac{4\pi\hbar^{2} L}{e^{2} d^{2} R m^{*} D^{3/2}} \right)^{2} \quad \text{(5-2-b)}$$

in the above, d is the classical dimensionality of the sample, m^* is the effective mass of the electron, and α is a constant of order unity. These formulae were also demonstrated to be usable for designing samples that have a specific saturation temperature [126]. Figure 5-1 below shows the typical saturation behavior of τ_ϕ reported by MJW in their gold samples. The parameters for these samples are shown in Table (5-1).

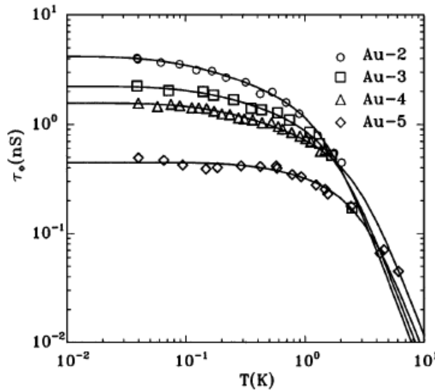

Figure 5-1: Temperature dependence of τ_ϕ for four gold wires, the solid lines are fits to Equation (5-2) with the addition of phonon scattering (adapted from Reference [124]).

This idea of intrinsic decoherence was further supported by more rigorous calculations by Golubev and Zaikin [127-131] who employed a non-perturbative approach that included the effect of zero-point fluctuations. This idea of intrinsic decoherence came under severe criticism conceptually [132, 133] with the main argument being that zero-point fluctuations of the electromagnetic field can not cause energy exchange and therefore can not cause decoherence. In addition, the non-perturbative approach of Golubev and Zaikin was also criticized [122, 134] as being mathematically erroneous. However, this controversy has not been settled [135] and

intrinsic decoherence cannot be ruled out as a possible explanation of the saturation of τ_ϕ on either theoretical or experimental grounds.

5.2.2 Decoherence by dilute magnetic impurities

A nominally 'pure' metallic sample still contains impurities at the PPM or sub PPM level and some of these could be magnetic. Magnetic impurities can cause dephasing through spin-flip scattering, whose rate is usually calculated from the Suhl-Nagaoka approximation for the Kondo effect [136, 137]:

$$\tau_{sf}^{-1} = \frac{c}{2\pi\hbar N_F} \frac{\pi^2 S(S+1)}{\pi^2 S(S+1) + \ln^2(T/T_K)} \tag{5-3}$$

Where c is impurity concentration, S is impurity spin, and T_K is the Kondo temperature corresponding to the particular host-impurity system.

It has been suggested, mainly by the Saclay and MSU groups [138-141], that magnetic impurities having a low Kondo temperature are the cause of saturation. This was inferred by comparing the phase coherence times in Au and Ag samples of similar classical transport parameters with different impurity levels ranging from 1 to 10 PPM. They found that in samples with nominal purity 6N (99.9999%) the phase coherence times were long and had a temperature dependence that is close to the theoretical estimate down to about 40 mK. In contrast, their samples with nominal purity 5N (99.999%), have shown a saturation of the phase coherence time below

roughly 1 K. This contrasting behavior is shown in Figure 5-2 with the sample parameters shown in Table (5-1). By using Suhl-Nagaoka approximation to calculate the spin flip scattering rate due to magnetic impurities, and assuming that the main impurity in their samples was Mn which has a Kondo temperature of about 40 mK in bulk Au and Ag, they estimated that a concentration level of about 0.13 PPM of Mn was sufficient to cause the observed saturation in the 5N samples.

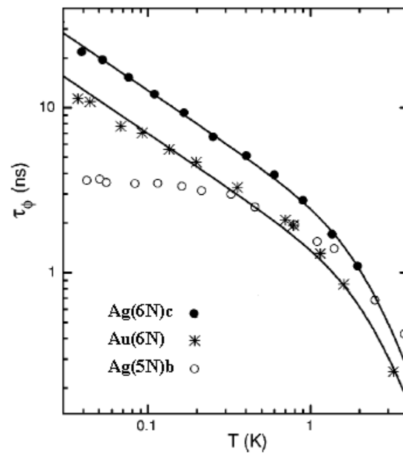

Figure 5-2: Phase coherence time versus temperature for samples made of 5N Ag, 6N Ag, and 6N Au, the solid lines are fits to Equation (5-1) with the addition of phonon scattering (adapted from Reference [138]).

The fact that magnetic impurities can cause dephasing through spin-flip scattering has been known for a long time. The question is whether this explanation can account for all the experimental observations concerning τ_ϕ saturation, and whether the Suhl-Nagaoka approximation employed by the Saclay and MSU groups does describe the reality about the behavior of magnetic impurities in mesoscopic devices. The answer to the first question is that this mechanism cannot be universal since saturation has been observed in systems where magnetic impurities do not usually play a role in transport such as semiconductors and 2-D electron gas

heterostructures [123]. In addition, saturation has also been observed in disordered Au wires placed in a magnetic field high enough to quench spin-flip scattering [142].

Sample	$R(K\Omega)$	$L(\mu m)$	$w(nm)$	$t(nm)$	$\rho(\Omega.nm)$	$D(cm^2/s)$	$l_e(nm)$	Ref.
Au-2	0.30	207	110	60	9.6	612	87.5	[124]
Au-3	1.44	155	100	35	32.6	120	25.8	[124]
Au-4	1.81	57.9	60	25	46.9	83.7	17.9	[124]
Au-5	3.62	18.9	190	40	1456	2.7	0.6	[124]
Ag(6N)c	1.44	400	105	55	20.8	185	38.9	[138]
Au(6N)	1.08	175	90	45	36.1	135	23.3	[138]
Ag(5N)b	1.31	270	90	65	28.4	135	28.5	[138]

Table (5-1): Parameters of the samples in Figure 5-1 and Figure 5-2 (adapted from Reference [124] and Reference [138]).

The second question is rather subtle. The problem of magnetic impurities in non-magnetic hosts involves a number of diverse phenomena such as the Kondo effect, the RKKY interaction, local spin fluctuations (LSF), and others. This problem is thought to be well understood in bulk systems [136, 143, 144], however some controversy arises when it comes to low dimensional systems [145]. These controversies have been a subject of extensive studies in the last two decades. The main topics that have been studied are the existence and possible explanations of a Kondo size effect, Kondo impurity-mediated energy exchange between electrons, and the interplay between the Kondo and the RKKY interaction.

Experimental and theoretical debates about the presence of a Kondo size effect [146-150], and its possible association with at least one of the sample dimensions being smaller than the size of the Kondo screening cloud (which was not found to be the case), led to the study of the behavior of Kondo impurities in a finite medium by Zawadowski and coworkers [151-155]. They theoretically predicted that

a spin-orbit induced magnetic anisotropy near the surfaces can effectively 'freeze' the spin *S* of impurities into a singlet if *S* is an integer or into a doublet of lowest energy if *S* is half an integer. This freezing is a function of both the distance from the surface and temperature, therefore making both the effective impurity spin and concentration a function of temperature. It must be noticed that the existence of the spin-orbit scattering by itself does not modify the Kondo effect [156], it is the combination of both spin-orbit and the finiteness of the medium that causes this freezing. This theory seems to be in good agreement with some of the experimental data [157-159], but is at odds with others [160]. The presence of surface roughness was found to enhance the surface-induced anisotropy and the splitting of the impurity spin energy levels [161, 162]. This makes the situation even more complex in realistic samples because of their granular structure.

An additional aspect that has been investigated in Kondo systems is the magnetic impurity mediated electron-electron interaction. Experiments measuring the non-equilibrium electron energy distribution function in disordered metallic wires using tunnel junctions [141, 163-165] have revealed an anomalous electron-electron interaction in some samples. This interaction was observed to be a function of the magnetic field leading to the assumption that the cause is dilute magnetic impurities. Theoretical calculations for S=1/2 impurities [166-168] have provided some quantitative agreement with these experiments. The concentrations of magnetic impurities inferred from these calculations, however, are about two orders of magnitude higher than the concentrations inferred from the weak localization measurements on samples with similar purity [163]. Similar calculations have been

done for higher S values, but this does not lift the aforementioned disagreement [169]. Another theoretically expected effect of medium finiteness is the Kondo temperature T_K and the exchange energy J becoming functions of position due to their dependence on the local density of states [170].

A consequence of the interaction between the conduction electrons and the local magnetic moment of an impurity is the existence of an oscillatory spin polarization cloud that decays rather slowly in distance, and therefore is able to mediate an indirect spin-spin interaction between impurities. This interaction is known as the Ruderman-Kittel-Kasyua-Yoshida (RKKY) interaction, this is the interaction responsible for the formation of a spin glass state. The RKKY interaction is always a factor that complicates the interpretation of experimental observations in dilute magnetic alloys using isolated impurity models [143]. Even samples which have a low concentration of magnetic impurities, and therefore a low spin glass temperature, can still show behavior that is reminiscent of this interaction. Part of the reason is that the average inter-impurity distance changes as the cube root of the impurity concentration, which is a rather slow function. Calculations have shown that the RKKY interaction is enhanced in low dimensional systems [171], and could create non-uniform magnetic states in thin films [172]. This could also cause the electron phase relaxation rate to be a non-monotonic function of temperature [173]. Experiments on Mg quench-condensed thin films with Fe impurities, and at temperatures much lower than the Kondo temperature of this system, have shown deviations from the Fermi liquid behavior expected in this temperature regime as the impurity spins should be fully shielded. These deviations were found to be dependent

on the impurity concentration and thus were attributed to inter-impurity interactions [174-176].

Disorder has been known to suppress the Kondo effect. This problem has been recently revisited theoretically [177, 178], and experimentally [150]. Disorder is also expected to affect some aspects of the RKKY interaction [179, 180]. Also, the effect of local spin fluctuations (LSF) on dephasing has been investigated experimentally [181]. That work has shown that LSF impurities cause a much weaker dephasing than Kondo impurities.

From this review it is clear that the problem is rather complex. This leads to the belief that the analysis of the experimental measurements in Reference [138] using Suhl-Nagaoka approximation is an over-simplification. This analysis assumes a single impurity species with a single T_K and S, and a temperature-independent effective impurity concentration, and as was shown above this might not be correct. It might be argued that these variations can be absorbed into an effective simple Kondo model. Indeed, this seems to be, at least qualitatively, the case in many experiments [137, 149, 150, 182-184]. However, it can be noticed that in all these experiments there was always a dominant impurity at the few PPM or above level. This means that in these experiments there was always a sufficient amount of effectively 'bulk' impurities to mask out any anomalies. Also notable is that even in these systems, the agreement with theory generally becomes worse below T_K , and this is indicated by the reported experimental difficulty in reaching the unitarity limit (complete screening of impurities' magnetic moments) [175, 183, 184]. This also invalidates the usage of Suhl-Nagaoka approximation, which assumes that the

unitarity limit should be reached if $T \ll T_K$. This suggests that this renormalization into a simple Kondo picture might not work well for high purity samples which do not have a dominant magnetic impurity, which is supported by a recent theoretical calculation [185], where the scattering rate by dilute magnetic impurities is found to be consistently lower than that predicted by the Suhl-Nagaoka approximation. The invalidity of Suhl-Nagaoka approximation in high purity samples might help to explain the excessively low estimates, in the order of 0.01 PPM, of magnetic impurity concentrations obtained in Reference [138] for 6N Au and Ag samples. Also, as mentioned before, estimates of magnetic impurity levels in 5N samples using the Suhl-Nagaoka approximation are two orders of magnitude lower than the corresponding estimates from the energy relaxation rates in similar samples [163]. Further, using S=1/2 for Mn impurities in Ag might not be correct since Mn in bulk Ag has S=5/2 [186], and attempting to explain this lower S value in terms of freezing out by surface anisotropy further invalidates the usage of Suhl-Nagaoka approximation as explained before. The choice in Reference [138] of Mn as an impurity for ion implantation in Ag could have been a poor choice since some evidence exists that the Ag-Mn system might not be an ideal Kondo system [187]. Also if S is larger than 1/2 complete shielding of the impurity spin is not possible even at zero temperature [188], which again invalidates using Suhl-Nagaoka approximation.

To conclude, magnetic impurities have an undeniable role in dephasing at low temperatures, and indeed they could be the cause of phase coherence time saturation

in some cases. However, a cautious assessment is needed before a proper judgment can be made about their role in a particular set of measurements.

5.2.3 Dephasing by coupling to two-level systems (TLS)

In a disordered solid, an atomic positional arrangement can arise where one or more atoms get trapped in a double well potential. Therefore, they can tunnel between the states localized at the minima of the wells through the middle barrier. The low energy excitations of such an arrangement can be approximated as a two level system (TLS). The distribution of the parameters describing these systems such as the tunneling rate and energy are assumed to be very broad. Further, TLS are assumed to couple to phonons and conduction electrons [189]. Two models have been proposed to account for dephasing by TLS. The first model calculates their effect through the closely related phenomenon of $1/f$ noise [190]. The second model describes them as two-channel Kondo impurities [191-193]. Both models agree that coupling to TLS could cause some extra dephasing, therefore saturation of the phase coherence time, for some limited temperature range. That extra dephasing vanishes as the temperature approaches zero. Only a few attempts have been made to fit experimental dephasing data to TLS theories [165]. In a recent experimental test [194] where Ag samples were ion implanted with a low dose of Ag^+ ions (which should increase the disorder and hence the density of TLS) no measurable effect on the scattering rates was found. It has been theoretically argued that dephasing by

TLS might be irrelevant for disordered metals in the usually investigated low temperature regime [195, 196].

5.2.4 Dephasing by external microwave noise

It has been suggested that external microwave noise is the cause of saturation [197, 198]. However, one experiment shows that when microwave radiation with frequency comparable to $1/\tau_\phi$ couples sufficient power into the samples to cause an observable dephasing, this is accompanied by an enhanced energy relaxation, and this effect has not been observed in most measurements [126]. However, there has been recent experimental work on this problem attempting to separate the effect of direct heating of the electron gas by microwave radiation from true dephasing by the electromagnetic field [199].

5.2.5 Other explanations

Other suggestions to account for the saturation include electron-phonon interaction in open systems [200], coherent inter-grain charge transfer [201], vacuum fluctuations of the electromagnetic field [201-203], quantum measurement effects [204], and spin-magnon interaction [205]. However, these propositions have attracted only a little experimental and theoretical attention, hence I mention them only for completeness.

5.3 Experimental procedure

In this work, I report on measurements of phase coherence time (length) in quasi 1-D silver wires. This was done through measuring the weak localization (WL) correction to conductivity which results from the coherent backscattering of time-reversed paths [118, 206, 207], and universal conductance fluctuations (UCF) correction which results from the statistical fluctuations in the averaging of the interference terms of non time-reversed paths over a region of order L_ϕ [119, 208, 209]. The application of a magnetic field adds an extra phase to wave functions. For time-reversed paths, the two paths acquire opposite phases, and increasing the field further increases their phase difference until their interference term, hence the WL correction, is quenched at some characteristic field. For a 1-D conductor, this field is of order $h/2eL_\phi w$, where w is the width of the wire. This is the field required to thread one-half of a flux quantum through a phase coherent area $L_\phi w$, thus causing a phase difference of 2π between the time-reversed trajectories. The WL correction appears as an enhancement of resistance at low magnetic field, or as a depression in the case of weak anti-localization caused by strong spin-orbit scattering. Fitting the low field magnetoresistance to the proper theoretical form provides L_ϕ and other scattering lengths as we will discuss later.

The phase change due to the magnetic field also affects the phases of non time-reversed paths, thus changing the ensemble average of their interference terms. As the field changes this ensemble average changes too. After some field span, the new ensemble of phases becomes statistically independent from the initial ensemble,

resulting in the appearance of UCF as reproducible sample-specific quasi-random fluctuations in the magneto-conductance which would have a correlation field B_C. This is approximately the field needed to thread a flux quantum through a phase coherent area thus changing the phase of each partial wave function by 2π. For 1-D samples, this field is given by $h/eL_\phi w$. This correlation field is obtained as the half-width of the autocorrelation function of conductance as I will discuss later. One important issue is whether the τ_ϕ values calculated from these two different measurements are identical. This has been a subject of debate [210-214]. At least it is agreed that both estimates should have the same order of magnitude and temperature dependence. However, this is not necessarily the case in a system that has magnetic impurities. In this situation, temperature dependence of the two dephasing times can be different since $(\tau_\phi)_{UCF}$ is calculated from the high field magnetoresistance and the high magnetic field would polarize the magnetic moments of the impurities, thus suppressing the spin-flip scattering. This offers a powerful method to determine whether the origin of saturation in a certain sample is magnetic or not. This method was used by Mohanty and Webb [142] who measured τ_ϕ from WL and high field UCF in quasi 1-D gold wires and were able to show that $(\tau_\phi)_{UCF}$ saturated down to 40 mK similar to $(\tau_\phi)_{WL}$, thus proving that the origin of τ_ϕ saturation in these samples is non-magnetic.

My samples are made of 99.9994% purity silver with the main impurity being Palladium, which is non-magnetic. Other elements could still exist in sub PPM levels. In the first step of sample fabrication, oxidized Si wafers are spin-coated with two layers of PMMA resist. The top layer has a higher molecular weight to help

create an undercut profile in the developed patterns, which improves the liftoff process. The resist is baked for about one hour at about 170 C. Then, using an SEM, e-beam lithography is used to pattern the image of the samples and contact pads on the resist. This is followed by development in a 3:1 IPA:MIBK mixture. The developed patterns are installed in a thermal evaporator used only for high purity gold and silver. Before evaporation, plasma etching is performed to improve the adhesion of silver to the SiO_2 surface. Silver is then evaporated at various rates ranging from 0.1 Å/s to 12 Å/s, and at residual pressures ranging from $1x10^{-6}$ Torr to about $5x10^{-5}$ Torr. The evaporated thickness is determined from a crystal monitor and is double-checked in a co-evaporated film using a surface profiler. The samples are then taken out and immersed in Acetone for lift-off. After that, the SEM is used to check for good samples. If any are found, the wafer is then covered with a thick layer of PMMA to protect the samples during dicing, which is done using a diamond tip dicer. The good samples are then extracted, fixed on a suitable holder, wire bonded, and checked for electrical continuity.

I encountered many problems in producing these samples. These problems mainly came from the extreme tendency of these ultrathin silver films to agglomerate even at moderate temperatures. Similar behavior have been reported in literature [215-218]. I had to give up baking the protective resist layer (used before dicing) since this caused breaks to develop in all samples examined. The thinnest samples (~20 nm) have shown agglomeration even at room temperature. These samples developed breaks within a few days at room temperature. This behavior is consistent with the observations about the thermal stability of thin silver films in Reference

[218]. The thicker samples displayed a linear increase in resistivity with time as shown in Figure 5-3 below, ultimately failing. Near their failure, the wires had a large (in the order of hundreds of kilo-Ohms), fluctuating resistance.

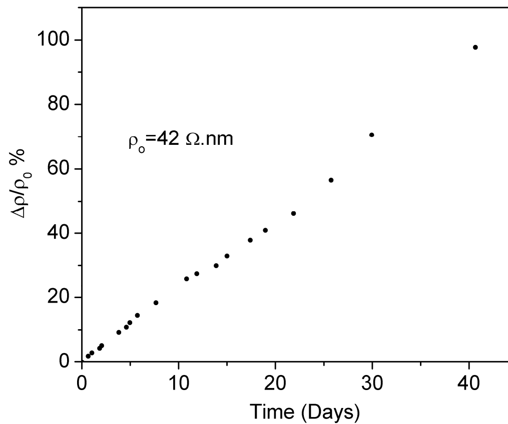

Figure 5-3: Resistivity of a silver nanowire exposed to air at room temperature as a function of time.

The increase in resistivity might be explained by agglomeration causing constrictions to form across the wire, or by the interaction of silver with sulfur compounds present in air forming inter-granular insulating layers. I believe both played a role. The assumption that the silver interaction with sulfur compounds increases the resistivity through forming inter-granular insulating layers, rather than through reducing the effective cross section of the wire, is based on the observation that passing a current for some time through samples near failure causes a reduction and stabilization of their resistance. Also, reduction of the cross section causes a non-linear change of resistance with time [219], in contrast to the nearly linear change observed. Thus, aged silver wires likely have a non-uniform structure with high resistivity spots or constrictions. These might dominate the transport and/or produce

local heating at low temperatures. I found that storing the samples in helium significantly reduced these changes. On one hand, this kept the samples away from the sulfur compounds in air, and on the other hand it possibly reduced the agglomeration which is enhanced in the presence of oxygen [216].

Another problem was my inability to control the resistivity of the samples through changing the evaporation parameters (rate, residual pressure). Obtaining samples with a diverse set of resistivity values is needed in order to test the validity of the theory of intrinsic decoherence. There, the expected behavior of τ_ϕ as a function of temperature is controlled by the value of τ_0, which in turn is controlled by the diffusion constant as seen from Equations (5-2-a), and (5-2-b). This insensitivity of the resistivity to evaporation parameters in silver is in contrast to gold where using this method, it is possible to change the resistivity of ultrathin gold wires by about one order of magnitude [64]. However it has been reported that highly disordered silver films could be produced under a much lower pressure and evaporation rate than what the evaporator I used could access [220]. Attempts to increase the resistivity of the wires through reducing their cross sectional area [64, 221] failed because of the instability of thin wires at room temperature mentioned above.

All the samples were patterned in the form of a meander, and connected to four 2-D contact pads through 1-D leads in order to perform four probe measurements. A typical sample geometry is shown in Figure 5-4. The length of the 1-D leads was always made to be longer than $3L_\phi$ in order to minimize non-local contributions to the measurements [119, 222-224]. Table (5-2) summarizes the properties of my samples.

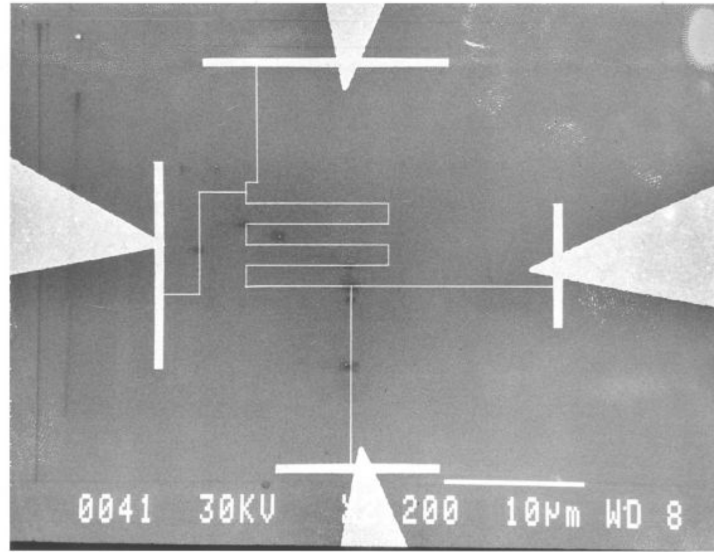

Figure 5-4: An example of a quasi 1-D metallic sample, the meander is 56.14 μm and the quasi 1-D leads are about 12.5 μm each.

Sample	$R(K\Omega)$	$L(\mu m)$	$w(nm)$	$t(nm)$	$\rho(\Omega.nm)$	$D(cm^2/s)$	$l_e(nm)$
S-1	1.88	246	75	43	24.6	153.5	32.8
S-2	1.41	56.14	39	30	29.4	128.7	27.6
S-3	0.26	26.1	70	45	31.3	120.5	25.8
S-4	0.105	26.1	95	61.5	23.5	160.9	34.5
S-5†	7.54	246	50	36	55.2	68.6	14.7
S-6	3.03	1130	80	91	19.5	193.7	41.5

Table (5-2): Samples properties, both resistance and resistivity are low temperature values, the diffusion constant D is calculated from $D = 1/e^2 N_F \rho$, and the elastic mean free path is calculated from l_e from $l_e = mv_F / \rho ne^2$ where v_F is the Fermi velocity 1.39×10^6 m/s , and n is the electronic density 6.1×10^{28} m^{-3}.

† This was an aged sample

The samples were installed in a dilution refrigerator with a base temperature of about 5 mK. Temperatures above about 100 mK were measured using a calibrated Germanium resistance thermometer (GRT). This was also used to calibrate an RF SQUID based magnetic susceptibility thermometer [225], then this calibration is extrapolated down to the base temperature. Both thermometers were fixed to the

mixing chamber. Sometimes, I used an un-calibrated Ruthenium oxide thermometer fixed in the sample cell as an indicator of thermal equilibrium. It is believed that Ruthenium oxide thermometers are not usable below about 20 mK due to saturation of the resistance [64]. However, I found that by using an ultra-low excitation current ~10 pA, the resistance did not actually saturate as is shown in Figure 5-5. Below 20 mK, the resistance changes roughly as a weak power of temperature; the previously observed saturation behavior may have been caused by excessive Joule heating due to an excitation current which was too large.

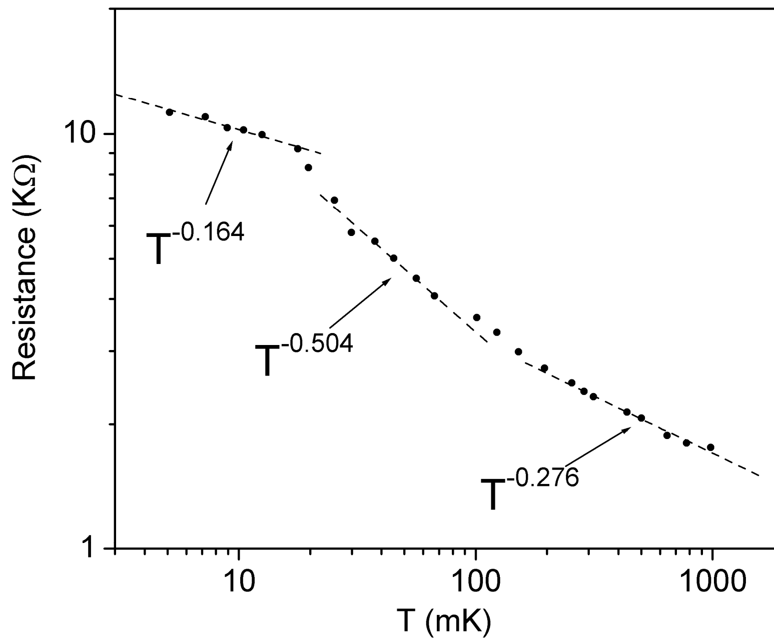

Figure 5-5: Resistance of Ruthenium oxide thermometer as a function of temperature, room temperature resistance is about 1 KΩ.

It must be noticed that the temperature indicated by the thermometers does not necessarily reflect the actual temperature of the electrons in the samples. Heating or loss of thermal contact between the electrons and the thermal bath can be indicated

only through any temperature-dependent effect measured in the sample itself. This is usually taken to be the electron-electron interaction correction to the conductivity, which I will discuss later. The refrigerator was equipped with an 8 Tesla superconducting magnet. For weak localization sweeps, the magnetic field was ramped between about $\pm$ 1500 Gauss in a period of 6-12 hours. For the UCF sweeps the field is ramped from zero to about 7.9 Tesla, then back to zero in a period of about 20 hours. The slow ramping allows more points to be averaged per field bin, thus a better signal to noise ratio is obtained. It also reduces the possibility of eddy current heating of the sample cell.

The WL and UCF corrections to the conductivity are rather small. In my samples, they correspond to a relative change of about 0.1% in resistance. The electrical measurements are done via lock-in amplifiers using two different configurations. In the 'direct' configuration shown schematically in Figure 5-6-a below, the excitation current is fed into the I^+ lead of the sample from the reference voltage output of the lock-in amplifier through a resistance much larger than the sample resistance, thus effectively converting it into a reference current output, and the I^- lead is grounded. The voltage difference across the sample measured between the V^+ and the V^- leads is fed into a differential pre-amplifier, and from there into the lock-in amplifier, which is internally referenced to the excitation frequency. I had some trouble with this configuration in the form of long-time period drifting of the output. These drifts were proportional to the input/output voltages of the lock-in amplifiers, and I could link them to variations in the ambient temperature.

The second configuration is a Wheatstone bridge configuration, where another branch with a constant resistor and a variable standard resistor were added to the previous configuration between the reference voltage output and the V^- lead in order to null the voltage drop across the classical resistance of the sample as is shown schematically in Figure 5-6-b below. This configuration reduces the input voltage to the lock-in amplifiers, consequently reducing the thermal drift voltage relative to the signal voltage, and offered another advantage by enabling the measurement to be performed at the highest possible sensitivity of the lock-in amplifiers without having to change the sensitivity as the samples' excitation currents are changed. However, for reasons that I do not understand, this configuration produced anomalous electron-electron interaction data. I believe this anomaly was a measurement artifact since the 'direct' configuration applied to the same samples, despite being smeared by the thermal drift of equipment, produced normal results. I did not observe any anomalies in the magnetoresistance data obtained using the bridge technique. The lock-in amplifiers were operated in the frequency range of 10-25 Hz. Care was taken to set the reference frequencies of the different amplifiers far apart compared to their bandwidths, ~1 Hz in this frequency range.

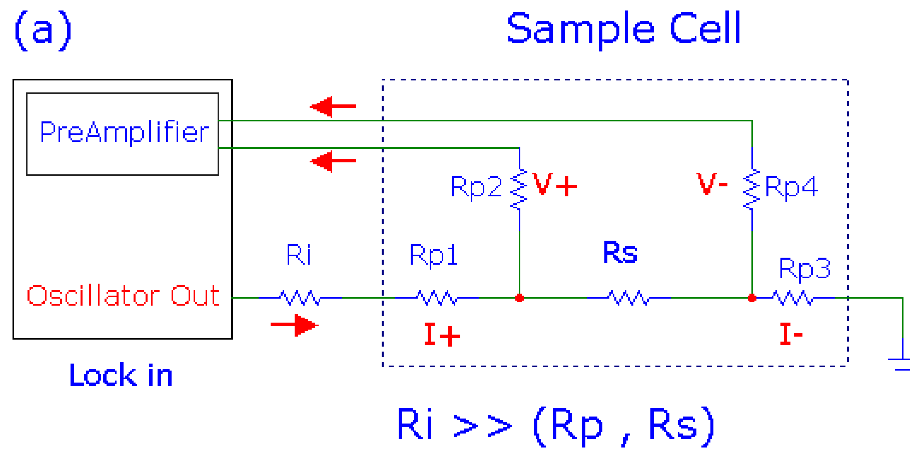

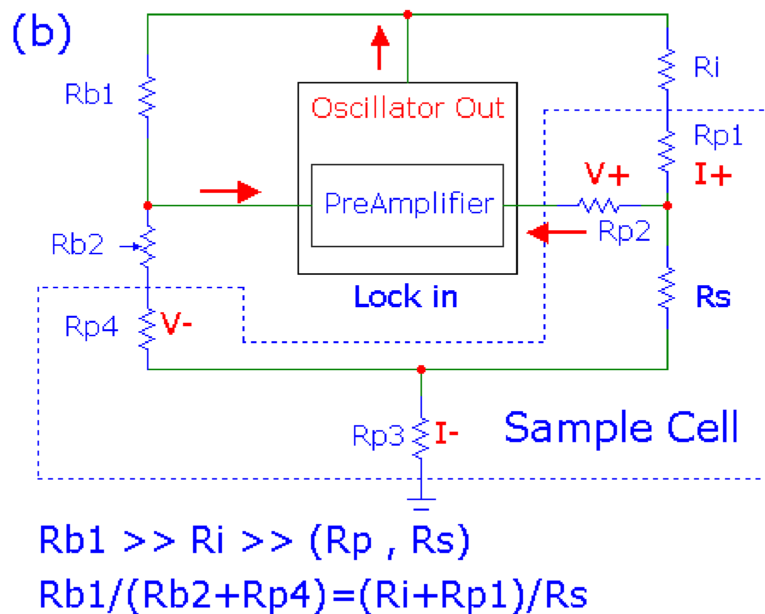

Figure 5-6: The two measurement configurations used. (a) The direct measurement configuration. Rp1 through Rp4 are 2 KΩ metal film protection resistors mounted in the sample cell, Rs is the sample resistance, and Ri is a large resistor to keep the excitation constant. (b) The bridge measurement configuration. Rb1 is a constant resistor, and Rb2 is a high precision variable resistor used to balance the bridge.

One important consideration in these measurements is the magnitude of the excitation current. A large voltage difference across the sample can directly heat the electron gas and reduce the quantum corrections. Meanwhile, a sufficiently large current is needed to obtain a good signal to noise ratio. One rule of thumb to avoid

heating is that the energy acquired by an electron from the electric field while passing across a phase coherent region, must be lower than the temperature i.e. $eV_{\phi} \leq KT$, where V_{ϕ} is the voltage drop per phase coherence length.

Experimental determination of the proper measurement current can be done by measuring the phase coherence length as a function of the excitation current and finding the value at which L_{ϕ} begins to drop. However, the presence of L_{ϕ} saturation complicates the direct interpretation of the results in terms of electron heating. At a current where L_{ϕ} is found to be current independent, the electrons could have been heated to a higher temperature still within the saturation region. Figure 5-7 shows the current test data for samples S-5 and S-6 at a temperature of about 7 mK. These samples (only briefly studied) showed L_{ϕ} saturation up to 1 K. For sample S-6 the criteria mentioned above gives a maximum current of 51 nA, yet L_{ϕ} seems to be current-independent up to double that value. On the other hand, sample S-5 where the maximum excitation current should be about 5.4 nA, shows heating at less than half this value. I interpret this as due to the existence of hot spots in this 'aged' silver wire. A detailed discussion of other measurement considerations in a similar system can be found in Reference [226].

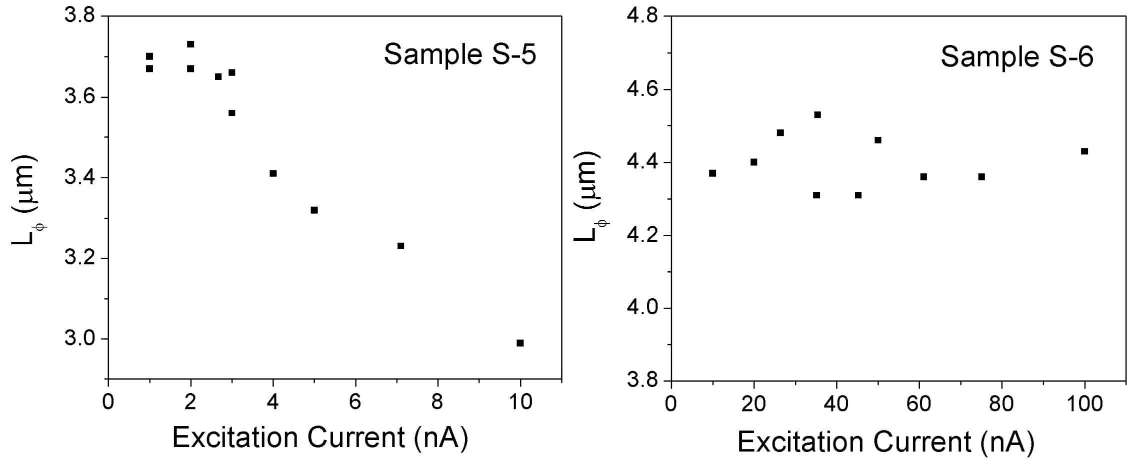

Figure 5-7: L_ϕ for samples S-5 and S-6 as a function of excitation current at 7 mK.

5.4 Results

5.4.1 Weak localization

Figure 5-8 below shows the low field magnetoresistance for samples S-1 to S-4 at 1 K (upper traces), and 220 mK (lower traces). All samples display positive magnetoresistance (weak anti-localization) as expected for silver, which has a considerable spin-orbit scattering. The data is fit to the theoretical form [226]:

$$\left(\frac{\Delta R}{R}\right)_{WL} = \frac{-e^2}{\pi\hbar}\frac{R}{L}\left[\frac{3}{2}(L_2^{-2}+L_B^{-2})^{-1/2} - \frac{1}{2}(L_1^{-2}+L_B^{-2})^{-1/2}\right] \qquad (5\text{-}4\text{-}a)$$

where

$$L_2^{-2} = L_\phi^{-2} + \frac{4}{3}L_{SO}^{-2} + \frac{2}{3}L_S^{-2}, \qquad (5\text{-}4\text{-}b)$$

$$L_1^{-2} = L_\phi^{-2} + 2L_S^{-2}, \qquad (5\text{-}4\text{-}c)$$

$$L_B = \frac{\sqrt{3}\hbar}{eBw}, \qquad (5\text{-}4\text{-}d)$$

and where L_{SO}, L_S, and L_B are the spin-orbit scattering length, spin-flip scattering length, and magnetic length respectively. In the actual fitting procedure, I added a constant term to account for offsets and a linear term to account for drifts. I fitted the traces for each sample to a constant value of L_{SO} since it is not a function of temperature. This constant value of L_{SO} is obtained from fitting the highest temperature trace (~ 2-4 K) where the UCF has diminished. It is a common belief that L_ϕ , L_{SO} , and L_S could all be obtained simultaneously from fitting to Equation (5-4-a) [123]. I do not believe that this is true since the actual fitting parameters obtained from Equation (5-4-a) are L_1 and L_2 . This makes the algebraic problem of solving for L_ϕ , L_{SO} , and L_S indeterminate. To get meaningful results, one of the three parameters must be fixed, and then the fitting determines the other two.

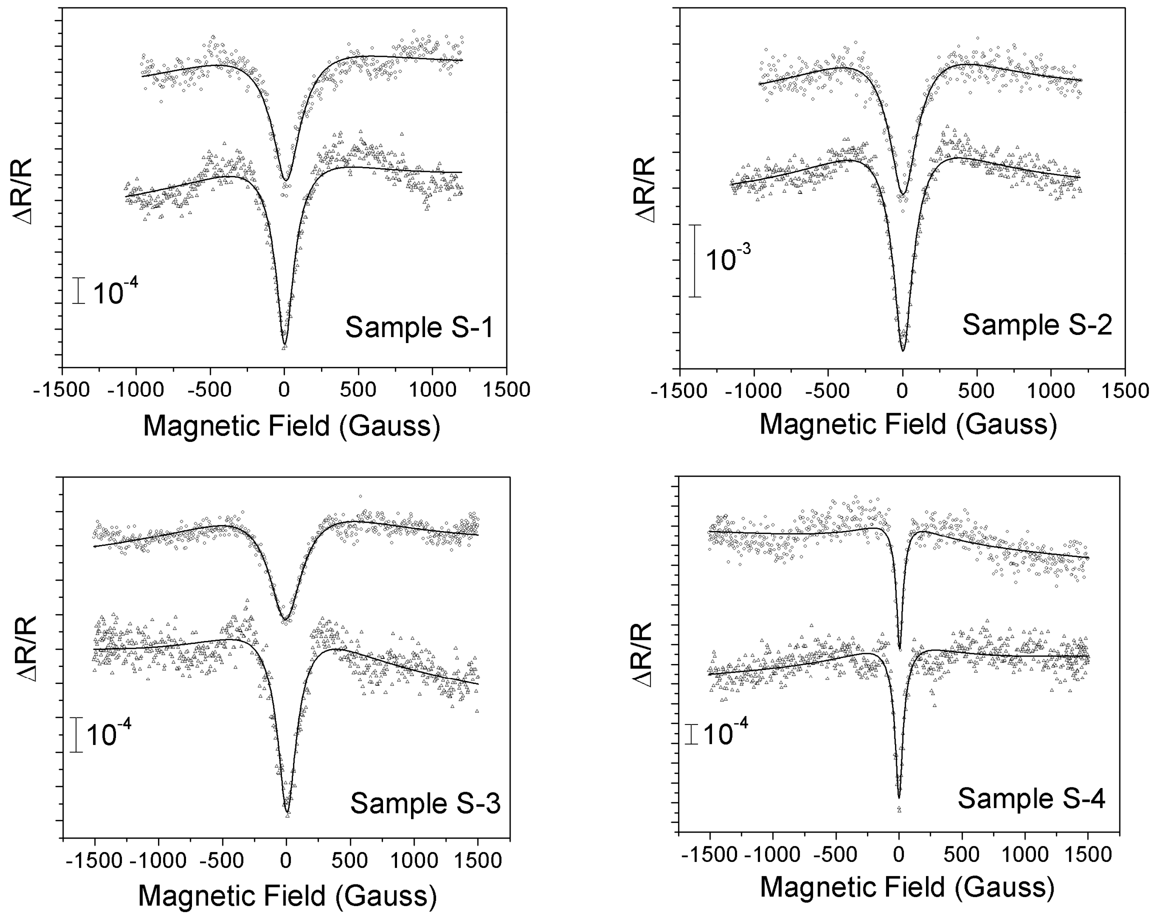

Figure 5-8: Low field magnetoresistance for samples S-1 to S-4 with fits to Equations (5-4), the spin-orbit scattering lengths are 0.447, 0.7, 0.33, and 0.645 μm for S-1 through S-4 respectively.

It might seem here that this problem is already solved by fixing L_{SO}, however for materials with strong spin-orbit scattering like gold and silver and in a high purity sample L_{SO} is usually about one order of magnitude lower than L_ϕ and L_S. Thus, the value of L_2 becomes rather insensitive to variations in L_ϕ and L_S, and we effectively get only one equation from L_1 to solve for L_ϕ and L_S. This means that we have to assume some value for L_S in order to obtain L_ϕ or vice versa. I initially assume that L_S is infinite, i.e. no magnetic scattering. Therefore, the values identified

experimentally as L_ϕ are actually the values of L_1. One last consideration is the width w which enters into the fitting through the magnetic length L_B . This is the physical width of the wire (assuming a rectangular cross section), so it must be constant. However, in fitting I usually left it as a free parameter. The reason for this is that Equation (5-4-a) is actually an approximate expression [122] . Therefore, allowing w to vary helps to absorb any small differences from the actual expression. Indeed, I found that doing this helps to improve the quality of fitting at the lower temperatures. Variations between w and the physical width of the wires as determined using the SEM were in the order of 20%. Figure 5-9 shows the experimental values of τ_ϕ for samples S-1 to S-4 as a function of temperature. I also show the theoretical predictions for dephasing by electron-electron interaction, calculated from Equation (5-1) with summary in Table (5-3), and intrinsic decoherence, calculated from Equations (5-2-a), and (5-2-b). These estimates should be smaller for temperatures roughly above 1 K due to the effect of electron-phonon interaction that I have not taken into account here.

Sample	$C_1\,(ns.K^{2/3})$	$C_2\,(\mu m.K^{1/3})$
S-1	2.06	5.62
S-2	0.99	3.57
S-3	1.92	4.98
S-4	3.12	7.09

Table (5-3): Theoretical coefficients for samples S-1 through S-4, calculated from Equation (5-1) for $(\tau_\phi)_{e-e} = C_1 T^{-2/3}$ and $(L_\phi)_{e-e} = C_2 T^{-1/3}$.

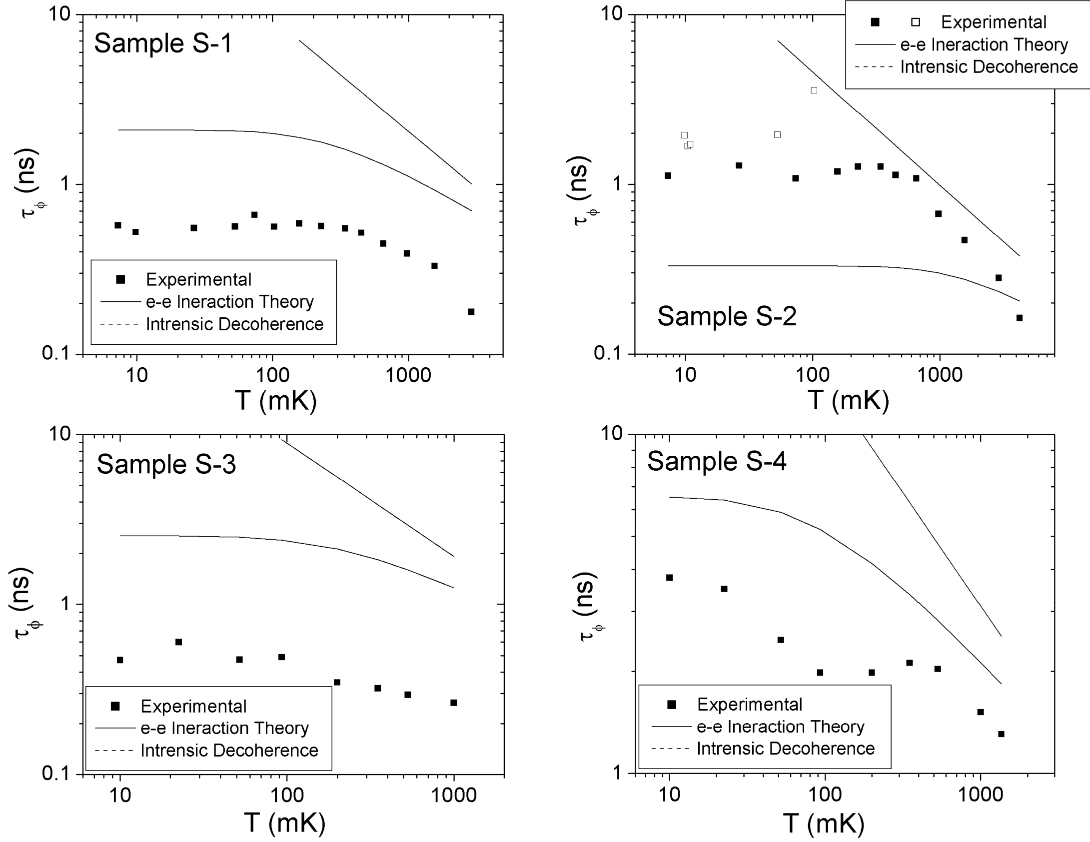

Figure 5-9: Experimentally measured τ_ϕ as a function of temperature for samples S-1 to S-4 along with the theoretical predictions from Equations (5-1) and (5-2).

Table (5-4) summarizes the experimental values of τ_ϕ and its theoretical estimates from both theories at 10 mK. Before commenting on the behavior of τ_ϕ in my samples, it might be important to discuss the error associated with these measurements. Variations between repeated measurements of L_ϕ are usually in the order of 3-4%, leading to variations in τ_ϕ of about 6-8% , and this should not lead to any significant alterations of the behavior displayed. It can be noticed that in all the samples τ_ϕ begins to saturate below about 600 mK and remains in saturation till the lowest measurement temperature of about 10 mK except for S-4. This sample shows some growth below about 100 mK then tends again to saturate at the lowest

temperatures. In addition, sample S-2 has shown some change of the τ_ϕ saturation value upon thermal cycling. Changing the temperature from about 7 mK to 4.2 K and back to 7 mK, τ_ϕ dropped from the higher values shown in Figure 5-8 using the open symbols, to lower stable values shown by the solid symbols. This effect was not observed in the other samples.

Sample	$(\tau_\phi)_{\text{Exp.}}$	$(\tau_\phi)_{\text{e-e}}$	$(\tau_\phi)_{\text{Intrinsic}}$
S-1	0.53	44.4	2.09
S-2	1.12	21.3	0.33
S-3	0.47	41.4	2.54
S-4	3.78	67.2	6.54

Table (5-4): Experimentally measured τ_ϕ at about 10 mK for samples S-1 to S-4 along with theoretical predictions from Equations (5-1) and (5-2), values are in nanoseconds.

Another feature is that the estimates for τ_ϕ from electron-electron interaction for all the samples are 1-2 orders of magnitude higher than the corresponding experimental measurements except for S-2. In this sample, the experimental and theoretical values for τ_ϕ roughly above 600 mK are rather close.

The estimates from intrinsic decoherence theory are one order of magnitude higher than the experimental values except for S-2. However, looking at Table (5-2) we can see that for this sample the value of the elastic mean free path is very close to the thickness, so the classical dimensionality *d* (which is actually a crossover function [64]) of this sample might have been closer to 2 than 3. Taking into account the extreme sensitivity of Equation (5-2-a) to this parameter ($\tau_0 \sim 1/d^7$ taking into account the dependence of the diffusion constant *D* on dimensionality), the difference

between the τ_0 estimates for 2 or 3 dimensions becomes large. For S-2, τ_0 becomes about 5.64 ns if d=2, which is higher than the measured values.

5.4.2 Electron-electron interaction

The electron-electron interaction causes a temperature-dependent correction to the resistance. In one dimensional samples this correction is proportional to $T^{-1/2}$ and is given by [122]:

$$\left(\frac{\Delta R}{R}\right)_{e-e} = -\frac{3\xi(3/2)}{\sqrt{2\pi}} R\left(\frac{e^2}{h}\right)\left(\frac{L_T}{L}\right) \tag{5-5}$$

where L_T is the thermal diffusion length $\sqrt{\hbar D/KT}$, and $\xi(x)$ is the Riemann Zeta function with $\xi(3/2) \approx 2.612$. As mentioned before, this correction is usually employed to probe the actual temperature of the electrons in the samples. To measure this correction, the voltage drop across the sample is monitored while the temperature of the refrigerator is ramped, while the magnetic field is set to a value high enough to quench the weak localization correction. These temperature ramps had to be sufficiently slow in order for the sample cell to have some degree of thermal equilibrium. This made the measurements susceptible to the thermal drifts of the amplifiers as explained before.

Figure 5-10 below shows $\Delta R/R$ versus $T^{-1/2}$ for samples S-1 through S-4. The temperature is changed between 80 mK and 220 mK for S-1 and S-2, and

between 50 mK and 400 mK for S-3 and S-4. All the samples were placed in a magnetic field of 6000 Gauss, which was sufficient to quench weak localization as is evident from Figure 5-7 above. In Table (5-5) I compare the theoretical expectations from Equation (5-5) with the experimental results from the slopes of the linear fits to the data in Figure 5-10. Despite the large fluctuations in these data due to thermal drift in the equipment, the agreement seems to be reasonable. This leads to the conclusion that down to 80 mK for S-1 and S-2, and down to 50 mK for S-3 and S-4, the samples were in good thermal contact with the ^{3}He bath.

Sample	$(C_3)_{Theoretical}$	$(C_3)_{Experimental}$
S-1	3.16x10^{-4}	2.17x10^{-4}
S-2	9.51x10^{-4}	6.07x10^{-4}
S-3	3.65x10^{-4}	2.96x10^{-4}
S-4	1.70x10^{-4}	1.86x10^{-4}

Table (5-5): Coefficients of $(\Delta R/R)_{e\text{-}e}=C_3T^{-1/2}$ for samples S-1 to S-4, the theoretical values are calculated from Equation (5-5), all values are in ($K^{1/2}$).

When the bridge technique was used to minimize the thermal drift (only for S-3 and S-4), the obtained results were anomalous. In this case, the correction increased with increasing temperature instead of decreasing. I believe this to be an artifact for two reasons: first, the direct configuration produced a rather normal response which is consistent with the expected theoretical behavior, and second, this anomalous response was (aside from an offset) identical for both samples. As I mentioned before, I do not understand the origin of this artifact.

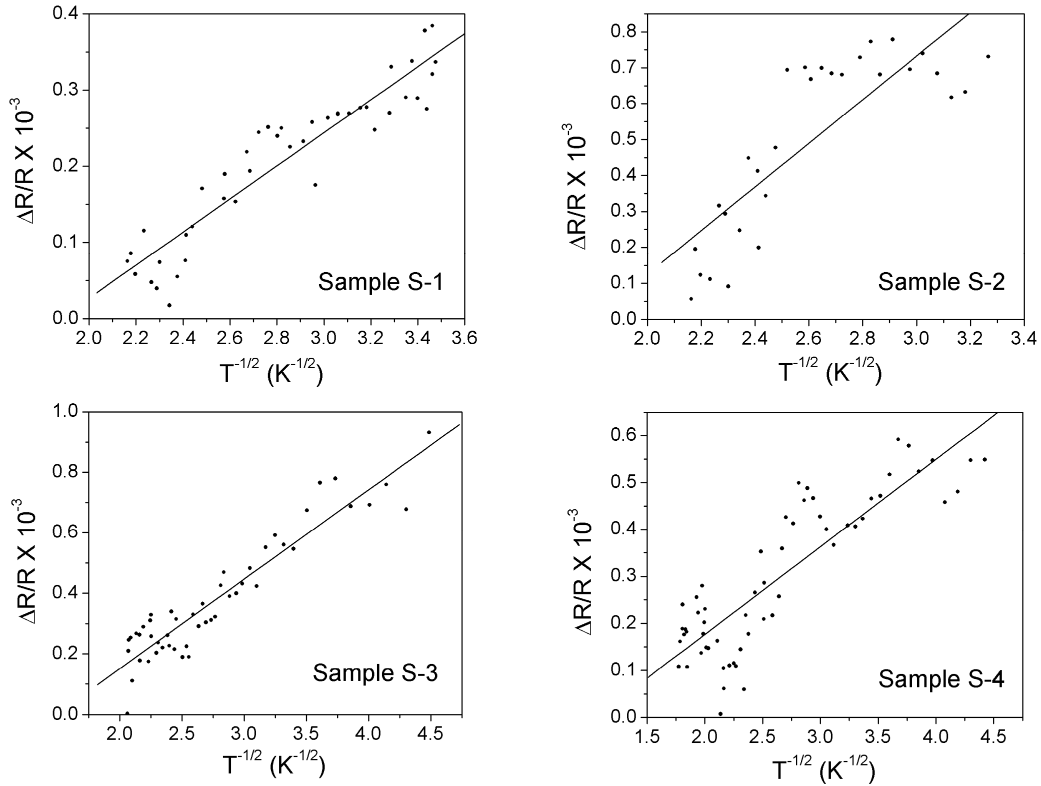

Figure 5-10: Electron-electron interaction data for samples S-1 to S-4. The slopes of the linear fits are shown in Table (5-5). The large fluctuations in the data are due to thermal drift in the equipment.

5.4.3 Universal conductance fluctuations (UCF)

Measurements of UCF were performed only for samples S-3 and S-4. These samples were specially made short enough to provide a reasonable UCF signal, but not too short such that the weak localization is not masked out by a much larger UCF signal. Figure (5-11-a) shows the conductance fluctuations of S-3 and S-4 at 99 mK for the up and down sweeps of the magnetic field. These traces are obtained after background subtraction in the form of a parabola, which accounts for the classical magnetoresistance and quasi-Hall [222] contributions plus an offset. The

reproducibility of the fluctuations is evident, indicating that they are indeed UCF rather than random noise.

Two quantities of interest are extracted from UCF traces. The first is the correlation field B_C obtained as the half width of the auto-correlation function of conductance traces $F(\Delta B) = < \Delta G(B)\Delta G(B+\Delta B) >$. The second is the root mean square (RMS) value of the fluctuations. Noise affects both measurements and needs to be subtracted out. To do so I recorded data at zero excitation current while sweeping the magnetic field, and from these data sets I got the RMS values of the voltage noise, which I assume to be current independent. The noise is subtracted using the formula $(\Delta G^2_{\mathrm{RMS}})_{\mathrm{UCF}} = (\Delta G^2_{\mathrm{RMS}})_{\mathrm{Total}} - (\Delta V^2_{\mathrm{RMS}})_{\mathrm{Noise}} / (IR^2)^2$.

Noise also increases peak value of the auto-correlation function at ΔB=0 (which is the mean square value of the fluctuations multiplied by the number N of data points), thus creating the so called 'noise peak' around ΔB=0. This peak has a finite width since the noise has some degree of correlation due to averaging. In order to determine the correct half width I did not use half the raw peak value $\frac{1}{2}(\Delta G_{\mathrm{RMS}})^2_{\mathrm{Total}} N$, but I rather used $\frac{1}{2}(\Delta G_{\mathrm{RMS}})^2_{\mathrm{UCF}} N$, which is the value after noise subtraction. The noise peak can actually dominate the auto-correlation function if the signal to noise ratio is low, and this can prevent the correct determination of the half width. This was mostly the case for my data below about 37 mK. Figure (5-11-b) shows the auto-correlation functions corresponding to the up field traces in Figure (5-11-a), both functions were normalized using their noise-subtracted peak values. The correlation field B_C is used to find L_ϕ from the equation [227]:

$$B_C = C\frac{(h/e)}{wL_\phi} \tag{5-6}$$

where the constant C ranges from 0.95 for $L_\phi >> L_T$ to 0.42 for $L_\phi << L_T$. For both S-3 and S-4 at the lowest temperature of about 22 mK, L_T is about 2.3 μm, which is still lower than L_ϕ of about 3.7 μm at the same temperature. Therefore, the value of C=0.95 can be used in these calculations. In designing the samples I made them rather wide such as to have a low B_C . This was done in order to have a sufficient number of fluctuation cycles within the limited range of magnetic field available. This came at the expense of lowering the resistance, thus leading to a lower signal to noise ratio. The RMS value of the UCF in 1-D samples is expected theoretically to follow the form [142]:

$$(\Delta G_{\mathrm{UCF}})_{\mathrm{RMS}} = \sqrt{\frac{8}{3\pi}}\left(\frac{e^2}{h}\right)\left(\frac{L_\phi}{L}\right)^{3/2}\left(\frac{L_T}{L_\phi}\right) \tag{5-7}$$

This formula is valid in the limit of strong spin-orbit interaction defined as $L_\phi = 3L_{SO}$ [228], and in the limit $L_\phi >> L_T$ [227], both conditions are satisfied in my samples. Another condition for the validity of Equation (5-6) is that k_BT must be higher than the Thouless energy $E_C = \hbar D / L_\phi^2$. For my samples, this corresponds to about 8 mK, which is lower than our lowest measurement temperature of about 22 mK.

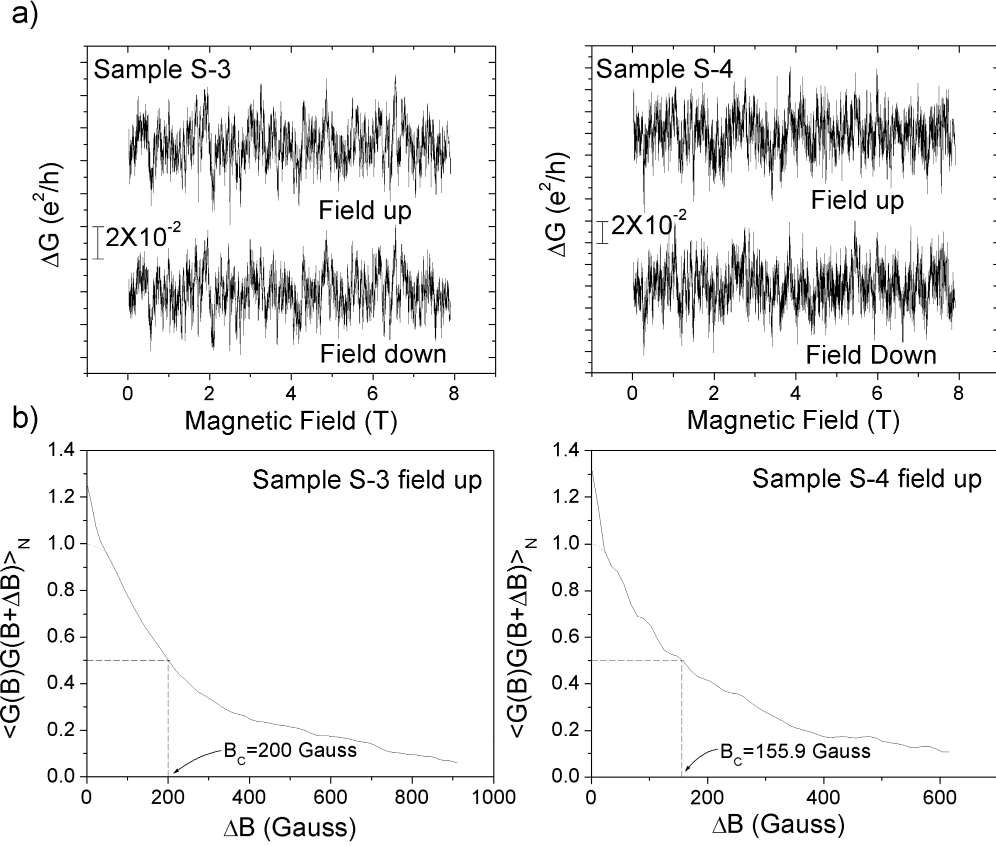

Figure 5-11: UCF traces for samples S-3 and S-4 at 99 mK and auto-correlation functions for the field up traces.

Figure 5-12 shows the value of L_ϕ calculated from the correlation fields of UCF traces as a function of temperature between 430 mK and 37 mK. In contrast to L_ϕ as found from weak localization, $(L_\phi)_{UCF}$ shows temperature dependence. The different temperature dependence for $(L_\phi)_{UCF}$ (determined at high magnetic field) and L_ϕ (determined at low magnetic field) is an indication of the presence of magnetic impurities in the samples (see previous discussion). The exponents that deduced from the linear fits to the data on a double logarithmic scale as shown in Figure (5-12-a), are smaller than the theoretically expected value of -⅓ . The exponents obtained are about -0.18 for both S-3 and S-4. However, given the scatter in the data, and the

density of points, it is difficult to decide whether this represents a real deviation from theory. In Figure (5-12-b) I plot L_{ϕ} as a function of $T^{-1/3}$ and the slopes of the linear fits are shown in Table (5-6). These values are clearly smaller than the corresponding ones in Table (5-3). As I mentioned before, it is not necessary that $(L_{\phi})_{WL}$ and $(L_{\phi})_{UCF}$ be identical.

Sample	$(C_2)_{\text{Corr. Field}}$ $(\mu m.K^{1/3})$	$(C_2)_{\text{RMS}}$ $(\mu m.K^{1/3})$
S-3	0.81	1.04
S-4	0.82	1.30

Table (5-6): Theoretical coefficients for $(L_{\phi})_{UCF} = C_2 T^{-1/3}$ from the correlation field and RMS data.

Figure 5-13 shows the temperature dependence of the RMS value of UCF for S-3 and S-4 between 430 mK and 22 mK. The data displays the expected behavior of growth with lowering temperature. On a double logarithmic plot as shown in Figure 5-13-a, the linear fits give temperature exponents of -0.49 for S-3, and -0.45 for S-4. Both exponents are lower than the expected theoretical value of -⅔ obtained by inserting the temperature dependence of L_{ϕ} into Equation (5-7). Again, these differences in exponents might not be significant.

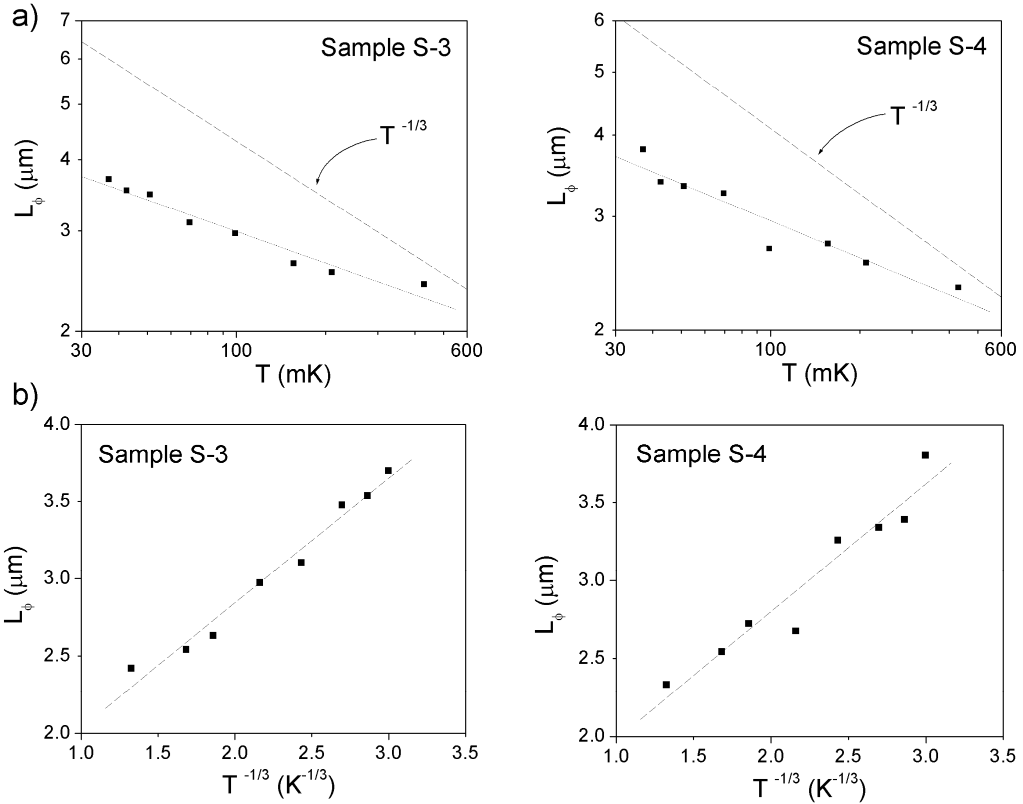

Figure 5-12: $(L_\phi)_{UCF}$ for samples S-3 and S-4 as a function of temperature, calculated from Equation (5-5). The exponents of the line fits in (a) are about -0.18, and the slopes of the line fits in (b) are shown in Table (5-6).

In Figure (5-13-b) I plot the RMS value as a function of $T^{-2/3}$. By comparing the slopes of the linear fits to the calculated slopes from Equation (5-7), assuming $L_\phi = C_2 T^{-1/3}$, from these I deduced the values of the constant C_2 shown in the right column of Table (5-6), and we can see that they are in reasonable agreement with the same values calculated from the correlation fields. Another way to see the agreement with theory is to rewrite Equation (5-7) in the from

$$(\Delta G_{\mathrm{UCF}})_{\mathrm{RMS}} L_\varphi^{-1/2} = \sqrt{\frac{8}{3\pi}}\left(\frac{e^2}{h}\right)\sqrt{\frac{\hbar D}{KL^3}} \quad T^{-1/2} \tag{5-8}$$

Then, using the values of L_ϕ obtained from the correlation fields; I plot the left hand side of Equation (5-8) as a function of $T^{-1/2}$ and obtain the experimental values of the slopes. The theoretical values can be calculated using the data in Table (5-2). I show this comparison in Table (5-7) and the agreement is reasonable. The growth of the RMS value down to 22 mK can be used as another indication of good thermal contact between the samples and the ^{3}He bath, which supports our electron-electron interaction measurements for samples S-3 and S-4.

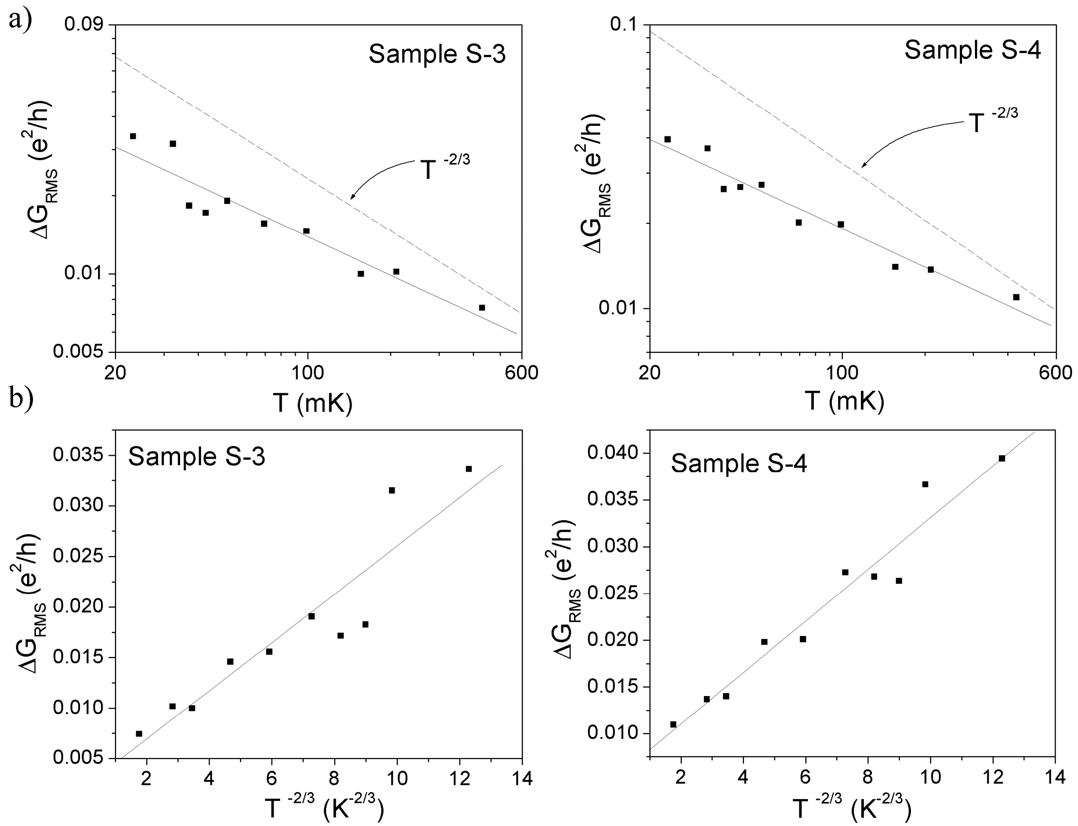

Figure 5-13: ΔG_{RMS} as a function of temperature for samples S-3 and S-4. The exponents of the line fits in (a) are -0.49 for S-3 and -0.45 for S-4, and the slopes of the line fits in (b) are shown in Table (5-7).

Since magnetic impurities are apparently the cause of saturation in $(\tau_\phi)_{WL}$, we might go back and calculate the residual dephasing rate due to mechanisms other than the electron-electron interaction, these are the electron-phonon interaction and the spin-flip scattering due to magnetic impurities. Using Equation (5-4-c), we get $1/\tau_R = (1/\tau_\phi)_{Exp.} - (1/\tau_\phi)_{e-e}$, where $1/\tau_R = 1/\tau_{e-ph} + 2/\tau_{sf}$ is the residual dephasing rate, the results of this calculation are shown in Figure (5-14).

Sample	$(C_5)_{Experimental}$	$(C_5)_{Theoretical}$
S-3	0.0424	0.0663
S-4	0.0423	0.0766

Table (5-7): Coefficients for $\Delta G_{RMS}[(L_\phi)_{CorrField}]^{-1/2} = C_5 T^{-1/2}$ for samples S-3 and S-4, units are $(\frac{e^2}{h}.\mu m^{-1/2}.K^{1/2})$

The increase in $1/\tau_R$ above about 600 mK can be attributed to the electron-phonon interaction. Below this temperature, the electron-phonon scattering rate, which drops as T^3, quickly dies out and the residual dephasing rate can be attributed to spin-flip scattering only.

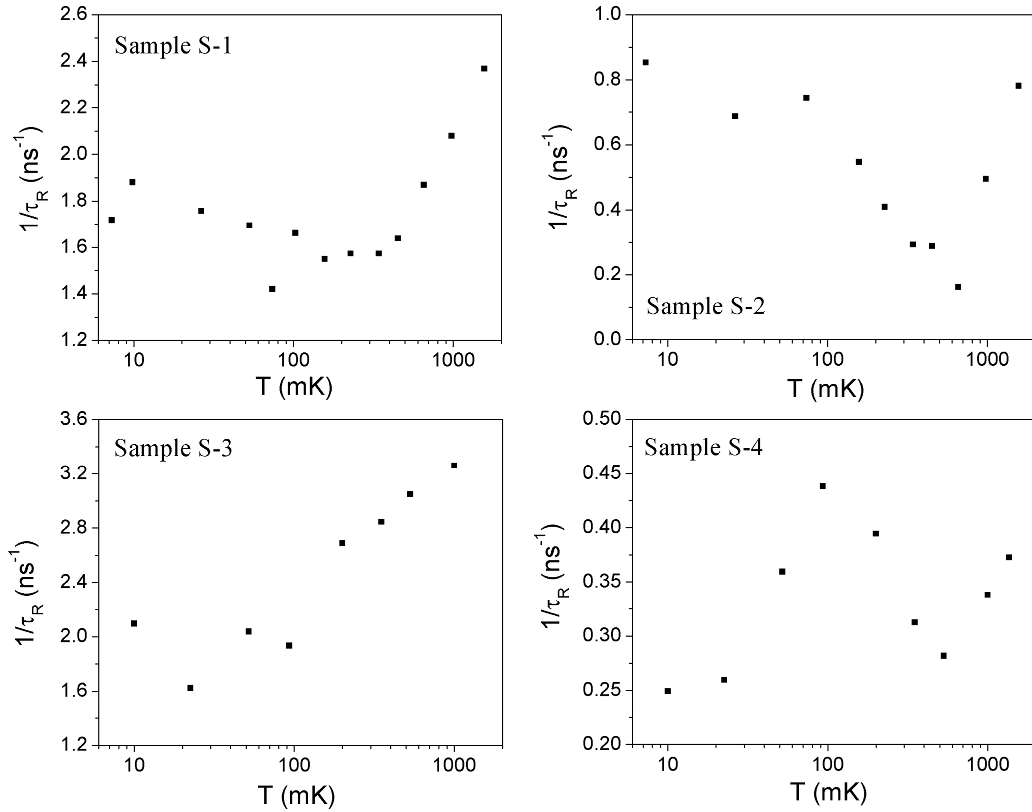

Figure 5-14: Residual scattering rate versus temperature for samples S-1 to S-4.

The diverse behavior of the magnetic scattering rate in the four samples is surprising since all of them were made out of the same silver assay, and therefore should have a similar content of magnetic impurities. I notice that only in sample S-4 the magnetic scattering rate shows a clear maximum around 100 mK, which for conventional Kondo behavior is identified with T_K. For the other samples, it is rather difficult to identify such a feature, and this is not consistent with conventional Kondo behavior. I also did not observe any sign indicating the presence of a species with a Kondo temperature in the proximity of 40 mK, in contrast to the beliefs of the authors of Reference [138]. I take all this as an indication supporting the previous discussion that samples with no dominant magnetic impurity cannot be described using Suhl-

Nagaoka approximation, and that a more realistic model is needed for the proper description of magnetic impurities in high purity mesoscopic samples. The presence of magnetic impurities might help explain the changes in the value of τ_ϕ in sample S-2 upon thermal cycling in terms of the presence of frozen spins that are freed as the temperature rises. This freezing can possibly happen through the surface anisotropy mechanism mentioned before because sample S-2 has the smallest lateral dimensions of all the samples. I believe that the concentration of magnetic impurities in my samples was rather low because I have not seen any obvious hysteresis in the magnetoresistance traces. I also have not seen any growth of the fluctuations' RMS value as a function of magnetic field, which in the presence of magnetic impurities, should display a magnetic field dependence [188]. Finally, it has been claimed [229], in an attempt to explain the saturation of $(L_\phi)_{UCF}$ observed in Reference [142], that the measurement of L_ϕ through UCF might not be sensitive enough to differentiate between a weak temperature dependence and true saturation. I believe my measurements clearly refute this claim since my UCF data in general had a lower signal to noise ratio than the corresponding measurements in Reference [142], and therefore these measurements do indicate the possibility of τ_ϕ saturation in the absence of any role by magnetic impurities.

5.5 Conclusion

Measurements of L_ϕ (or τ_ϕ) using both weak localization and UCF in the same sample offer a powerful method to differentiate between magnetic and non-magnetic

origins of saturation. In my measurements, I found that the phase coherence times in silver wires, obtained from weak localization, saturated roughly at temperatures below 600 mK, while the phase coherence times obtained from high magnetic field UCF grew as a power law down to 37 mK, thus concluding that the saturation of phase coherence time obtained from weak localization is due to the presence of dilute magnetic impurities. I also see possible signs indicating unconventional behavior of magnetic impurities in my samples. I conclude that comparison of temperature dependence of weak localization and UCF dephasing rates in the same sample is a powerful and unambiguous means of determining whether saturation of the dephasing time is due to magnetic impurities. These findings, considered along with the literature review in the beginning of this chapter, call for a more rigorous analysis of the role played by dilute magnetic impurities in mesoscopic samples.

Appendix A: Measurements of other carbon nanotubes

This appendix contains a description of the three carbon nanotubes D2, D4, and D6, these nanotubes were mainly used to obtain force data.

A.1 Nanotube D2

D2 is a metallic nanotube, the diameter is 2.2 ± 0.2 nm, and total length is about 45 μm. The last 12 microns from the free end side had some contamination and therefore I did not perform measurements in that part. The extension of the gold islands band at the edge of the macroscopic gold electrode is about 0.5 μm. Another nanotube intersects D2 about 4.1 μm away from the gold electrode, and that nanotube also contacts the gold electrode. That other nanotube is semiconducting as I verified that by directly contacting it. A partial view of D2 is shown in Fig. A-1 below. Typical I_d versus V_g and I_d versus V_d sweeps on D2 are shown in Fig. A-2 below.

Figure A-1: An AFM topography scan of nanotube D2. The scan size is 22x22 μm. The cut in the nanotube near the bottom of the frame accidentally happened during the measurement. The other nanotube intersecting D2 is visible near the top.

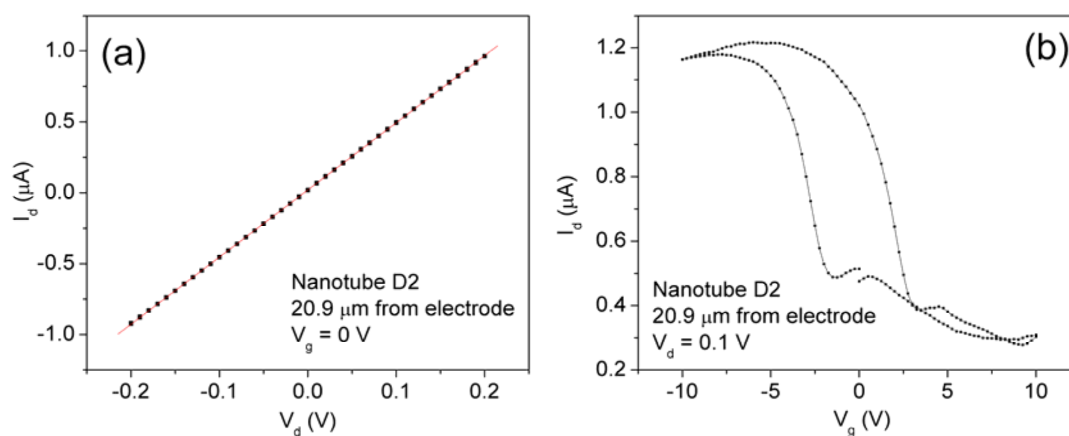

Figure A-2: Typical V_g and V_d sweeps on nanotube D2, (a) An I_d versus V_d sweep, the red line is a linear fit with slope 4.7 μS, (b) An I_d versus V_g sweep.

A.2 Nanotube D4

D4 is a metallic carbon nanotube, the diameter is 4.1 ± 0.2 nm. This nanotube has a naturally formed loop. The distance from the gold pad to the loop junction is 32.6 μm, and the part that makes up the loop has a length of 21.2 μm, this is followed by straight part that is 37.8 μm. Another nanotube (was not examined) intersects D4 about 1.5 μm away from the fixed electrode. A partial view of D4 is shown in Fig. A-3 below. Typical I_d versus V_g and I_d versus V_d sweeps on D4 are shown in Fig. A-4 below.

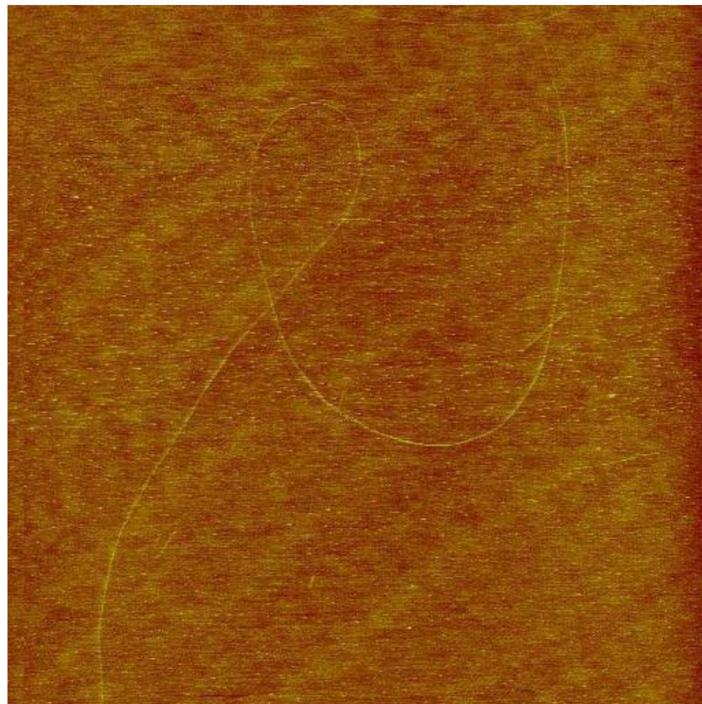

Figure A-3: An AFM topography scan of nanotube D4, the scan size is 30x30 μm, the other nanotube intersecting D4 is visible near the top. The edge of the fixed electrode is not visible but should be immediately above the top of the image.

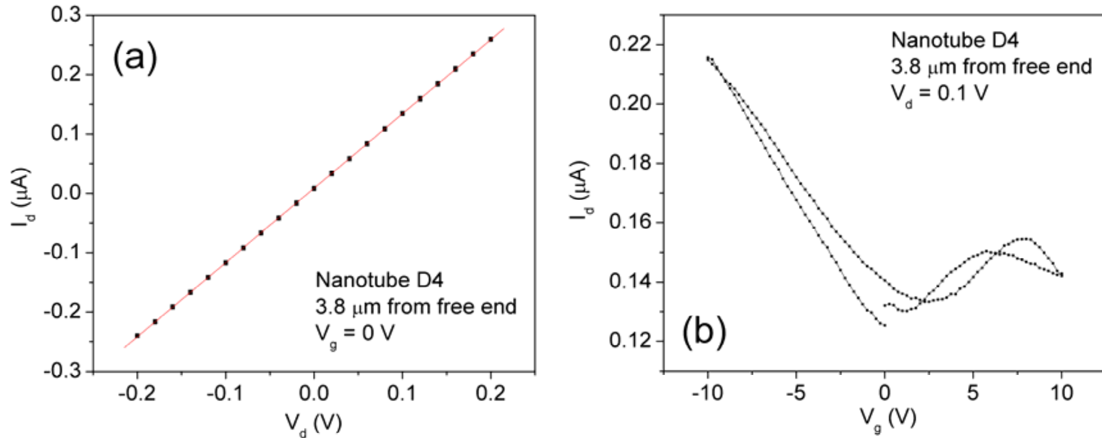

Figure A-4: Typical V_g and V_d sweeps on nanotube D4, (a) An I_d versus V_d sweep, the red line is a linear fit with slope 1.3 μS, (b) An I_d versus V_g sweep.

A.3 Nanotube D6

D6 is a metallic carbon nanotube. The diameter is 4.0 ± 0.4 nm. This nanotube has a naturally formed loop. The distance from the gold pad to the loop junction is 17.8 μm, and the part that makes up the loop has a length of 20.7 μm, this is followed by straight part that is 32.9 μm. A partial view of D6 is shown in Fig. A-5 below. Typical I_d versus V_g and I_d versus V_d sweeps on D4 are shown in Fig. A-6 below.

Figure A-5: An AFM phase scan of nanotube D6, the scan size is 25x25 μm.

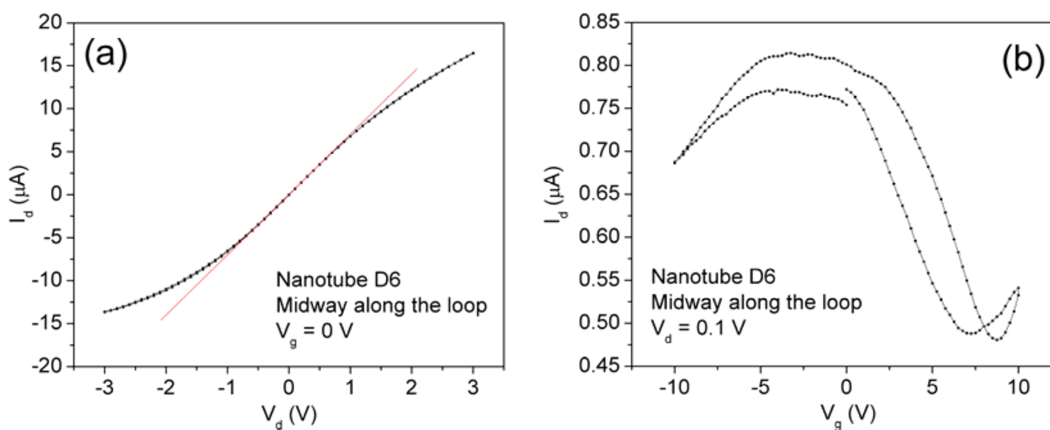

Figure A-6: Typical V_g and V_d sweeps on nanotube D6, (a) An I_d versus V_d sweep (notice the large V_d range), the red line is a linear fit for $|V_d| \le 0.5\,\text{V}$ only , with slope 7.0 μS, (b) An I_d versus V_g sweep.

Nanotubes which have loops (D4 and D6) were used to study the orientation dependence of the cantilever-nanotube contact (see Chapter 3).

Bibliography

[1] S. Iijima, "Helical microtubules of graphitic carbon," *Nature*, vol. 354, pp. 56-58, 1991.

[2] R. Martel, V. Derycke, C. Lavoie, J. Appenzeller, K. K. Chan, J. Tersoff, and P. Avouris, "Ambipolar Electrical Transport in Semiconducting Single-Wall Carbon Nanotubes," *Physical Review Letters*, vol. 87, pp. 256805, 2001.

[3] S. Heinze, J. Tersoff, R. Martel, V. Derycke, J. Appenzeller, and P. Avouris, "Carbon Nanotubes as Schottky Barrier Transistors," *Physical Review Letters*, vol. 89, pp. 106801, 2002.

[4] S. Heinze, M. Radosavljevic, J. Tersoff, and P. Avouris, "Unexpected scaling of the performance of carbon nanotube Schottky-barrier transistors," *Physical Review B*, vol. 68, pp. 235418, 2003.

[5] D. Mann, A. Javey, J. Kong, Q. Wang, and H. Dai, "Ballistic Transport in Metallic Nanotubes with Reliable Pd Ohmic Contacts," *Nano Lett.*, vol. 3, pp. 1541-1544, 2003.

[6] W. Kim, A. Javey, R. Tu, J. Cao, Q. Wang, and H. Dai, "Electrical contacts to carbon nanotubes down to 1 nm in diameter," *Applied Physics Letters*, vol. 87, pp. 173101-3, 2005.

[7] J. Appenzeller, J. Knoch, V. Derycke, R. Martel, S. Wind, and P. Avouris, "Field-Modulated Carrier Transport in Carbon Nanotube Transistors," *Physical Review Letters*, vol. 89, pp. 126801, 2002.

[8] C. Gomez-Navarro, P. J. D. Pablo, J. Gomez-Herrero, B. Biel, F. J. Garcia-Vidal, A. Rubio, and F. Flores, "Tuning the conductance of single-walled carbon nanotubes by ion irradiation in the Anderson localization regime," *Nat Mater*, vol. 4, pp. 534-539, 2005.

[9] Z. O. Yun Sung Woo, G. Vertesy, L. P. Biro, Siegmar Roth, "Effect of Ar irradiation on the behaviour of carbon nanotube transistor," *physica status solidi (b)*, vol. 243, pp. 3390-3393, 2006.

[10] P. L. McEuen, M. Bockrath, D. H. Cobden, Y.-G. Yoon, and S. G. Louie, "Disorder, Pseudospins, and Backscattering in Carbon Nanotubes," *Physical Review Letters*, vol. 83, pp. 5098, 1999.

[11] X. Zhou, J.-Y. Park, S. Huang, J. Liu, and P. L. McEuen, "Band Structure, Phonon Scattering, and the Performance Limit of Single-Walled Carbon Nanotube Transistors," *Physical Review Letters*, vol. 95, pp. 146805-4, 2005.

[12] A. Javey, J. Guo, M. Paulsson, Q. Wang, D. Mann, M. Lundstrom, and H. Dai, "High-Field Quasiballistic Transport in Short Carbon Nanotubes," *Physical Review Letters*, vol. 92, pp. 106804, 2004.

[13] J. Y. Park, S. Rosenblatt, Y. Yaish, V. Sazonova, H. Ustunel, S. Braig, T. A. Arias, P. W. Brouwer, and P. L. McEuen, "Electron-Phonon Scattering in Metallic Single-Walled Carbon Nanotubes," *Nano Lett.*, vol. 4, pp. 517-520, 2004.

[14] Z. Yao, C. L. Kane, and C. Dekker, "High-Field Electrical Transport in Single-Wall Carbon Nanotubes," *Physical Review Letters*, vol. 84, pp. 2941, 2000.

[15] M. Bockrath, D. H. Cobden, J. Lu, A. G. Rinzler, R. E. Smalley, L. Balents, and P. L. McEuen, "Luttinger-liquid behaviour in carbon nanotubes," *Nature*, vol. 397, pp. 598-601, 1999.

[16] Z. Yao, H. W. C. Postma, L. Balents, and C. Dekker, "Carbon nanotube intramolecular junctions," *Nature*, vol. 402, pp. 273-276, 1999.

[17] P. R. Wallace, "The Band Theory of Graphite," *Physical Review*, vol. 71, pp. 622, 1947.

[18] R. Saito, M. Dresselhaus, and G. Dresselhaus, *Physical Properties of Carbon Nanotubes* World Scientific Publishing Company, 1998.

[19] F. Ducastelle, X. Blase, J. M. Bonard, J. C. Charlier, and P. Petit, "Electronic Structure," in *Understanding Carbon Nanotubes*: Springer, 2006, pp. 199-276.

[20] J.-C. Charlier, X. Blase, and S. Roche, "Electronic and transport properties of nanotubes," *Reviews of Modern Physics*, vol. 79, pp. 677-56, 2007.

[21] J. C. Charlier, P. Eklund, J. Zhu, and A. Ferrari, "Electron and Phonon Properties of Graphene: Their Relationship with Carbon Nanotubes," in *Carbon Nanotubes*: Springer, 2008, pp. 673-709.

[22] M. P. Anantram and F. Leonard, "Physics of carbon nanotube electronic devices," *Reports on Progress in Physics*, vol. 69, pp. 507-561, 2006.

[23] T. Durkop, S. A. Getty, E. Cobas, and M. S. Fuhrer, "Extraordinary Mobility in Semiconducting Carbon Nanotubes," *Nano Lett.*, vol. 4, pp. 35-39, 2004.

[24] M. S. Purewal, B. H. Hong, A. Ravi, B. Chandra, J. Hone, and P. Kim, "Scaling of Resistance and Electron Mean Free Path of Single-Walled Carbon Nanotubes," *Physical Review Letters*, vol. 98, pp. 186808-4, 2007.

[25] V. Perebeinos, J. Tersoff, and P. Avouris, "Electron-Phonon Interaction and Transport in Semiconducting Carbon Nanotubes," *Physical Review Letters*, vol. 94, pp. 086802-4, 2005.

[26] Y.-F. Chen and M. S. Fuhrer, "Electric-Field-Dependent Charge-Carrier Velocity in Semiconducting Carbon Nanotubes," *Physical Review Letters*, vol. 95, pp. 236803-4, 2005.

[27] F. Léonard and J. Tersoff, "Novel Length Scales in Nanotube Devices," *Physical Review Letters*, vol. 83, pp. 5174, 1999.

[28] A. A. Odintsov, "Schottky Barriers in Carbon Nanotube Heterojunctions," *Physical Review Letters*, vol. 85, pp. 150, 2000.

[29] M. Freitag, J. C. Tsang, A. Bol, D. Yuan, J. Liu, and P. Avouris, "Imaging of the Schottky Barriers and Charge Depletion in Carbon Nanotube Transistors," *Nano Lett.*, vol. 7, pp. 2037-2042, 2007.

[30] M. Bockrath, D. H. Cobden, P. L. McEuen, N. G. Chopra, A. Zettl, A. Thess, and R. E. Smalley, "Single-Electron Transport in Ropes of Carbon Nanotubes," *Science*, vol. 275, pp. 1922-1925, 1997.

[31] S. J. Tans, M. H. Devoret, H. Dai, A. Thess, R. E. Smalley, L. J. Geerligs, and C. Dekker, "Individual single-wall carbon nanotubes as quantum wires," *Nature*, vol. 386, pp. 474-477, 1997.

[32] H. W. C. Postma, T. Teepen, Z. Yao, M. Grifoni, and C. Dekker, "Carbon Nanotube Single-Electron Transistors at Room Temperature," *Science*, vol. 293, pp. 76-79, 2001.

[33] P. J. de Pablo, C. Gómez-Navarro, J. Colchero, P. A. Serena, J. Gómez-Herrero, and A. M. Baró, "Nonlinear Resistance versus Length in Single-Walled Carbon Nanotubes," *Physical Review Letters*, vol. 88, pp. 036804, 2002.

[34] S. Datta, *Electronic Transport in Mesoscopic Systems*: Cambridge University Press, 1995.

[35] S. Roche, E. Akkermans, O. Chauvet, F. Hekking, R. Martel, J. P. Issi, G. Montambaux, and P. Poncharal, "Transport Properties," in *Understanding Carbon Nanotubes*: Springer, 2006, pp. 335-437.

[36] H. van Houten, C. W. J. Beenakker, and A. A. M. Staring, "Coulomb-Blockade Oscillations in Semiconductor Nanostructures," in *Single Charge Tunneling*, H. Grabert and M. H. Devoret, Eds. New York: Plenum, 1992.

[37] M. A. Kastner, "The single electron transistor and artificial atoms," *Annalen der Physik*, vol. 9, pp. 885-894, 2000.

[38] G. Binnig, C. F. Quate, and C. Gerber, "Atomic Force Microscope," *Physical Review Letters*, vol. 56, pp. 930, 1986.

[39] G. Meyer and N. M. Amer, "Novel optical approach to atomic force microscopy," *Applied Physics Letters*, vol. 53, pp. 1045-1047, 1988.

[40] O. Stukalov, C. A. Murray, A. Jacina, and J. R. Dutcher, "Relative humidity control for atomic force microscopes," *Review of Scientific Instruments*, vol. 77, pp. 033704-6, 2006.

[41] E. Dokou, L. Zhang, and M. A. Barteau, "Comparison of atomic force microscopy imaging methods and roughness determinations for a highly polished quartz surface," *Journal of Vacuum Science & Technology B: Microelectronics and Nanometer Structures*, vol. 20, pp. 2183-2186, 2002.

[42] L. Zitzler, S. Herminghaus, and F. Mugele, "Capillary forces in tapping mode atomic force microscopy," *Physical Review B*, vol. 66, pp. 155436, 2002.

[43] T. Kanbara, T. Takenobu, T. Takahashi, Y. Iwasa, K. Tsukagoshi, Y. Aoyagi, and H. Kataura, "Contact resistance modulation in carbon nanotube devices investigated by four-probe experiments," *Applied Physics Letters*, vol. 88, pp. 053118-3, 2006.

[44] H. Dai, E. W. Wong, and C. M. Lieber, "Probing Electrical Transport in Nanomaterials: Conductivity of Individual Carbon Nanotubes," *Science*, vol. 272, pp. 523-526, 1996.

[45] M. Stadermann, S. J. Papadakis, M. R. Falvo, J. Novak, E. Snow, Q. Fu, J. Liu, Y. Fridman, J. J. Boland, R. Superfine, and S. Washburn, "Nanoscale study of conduction through carbon nanotube networks," *Physical Review B*, vol. 69, pp. 201402, 2004.

[46] M. Stadermann, S. J. Papadakis, M. R. Falvo, Q. Fu, J. Liu, Y. Fridman, J. J. Boland, R. Superfine, and S. Washburn, "Exponential decay of local conductance in single-wall carbon nanotubes," *Physical Review B (Condensed Matter and Materials Physics)*, vol. 72, pp. 245406-4, 2005.

[47] P. Sundqvist, F. J. Garcia-Vidal, F. Flores, M. Moreno-Moreno, C. Gomez-Navarro, J. S. Bunch, and J. Gomez-Herrero, "Voltage and Length-Dependent Phase Diagram of the Electronic Transport in Carbon Nanotubes," *Nano Lett.*, vol. 7, pp. 2568-2573, 2007.

[48] Y. Yaish, J. Y. Park, S. Rosenblatt, V. Sazonova, M. Brink, and P. L. McEuen, "Electrical Nanoprobing of Semiconducting Carbon Nanotubes Using an Atomic Force Microscope," *Physical Review Letters*, vol. 92, pp. 046401, 2004.

[49] A. Bachtold, M. S. Fuhrer, S. Plyasunov, M. Forero, E. H. Anderson, A. Zettl, and P. L. McEuen, "Scanned Probe Microscopy of Electronic Transport in Carbon Nanotubes," *Physical Review Letters*, vol. 84, pp. 6082, 2000.

[50] M. Bockrath, W. Liang, D. Bozovic, J. H. Hafner, C. M. Lieber, M. Tinkham, and H. Park, "Resonant Electron Scattering by Defects in Single-Walled Carbon Nanotubes," *Science*, vol. 291, pp. 283-285, 2001.

[51] M. Freitag, A. T. Johnson, S. V. Kalinin, and D. A. Bonnell, "Role of Single Defects in Electronic Transport through Carbon Nanotube Field-Effect Transistors," *Physical Review Letters*, vol. 89, pp. 216801, 2002.

[52] Y. Kim, Y. M. Oh, J .Y. Park, and S. J. Kahng, "Mapping potential landscapes of semiconducting carbon nanotubes with scanning gate microscopy," *Nanotechnology*, vol. 18, pp. 475712, 2007.

[53] B. Gao, Y. F. Chen, M. S. Fuhrer, D. C. Glattli, and A. Bachtold, "Four-Point Resistance of Individual Single-Wall Carbon Nanotubes," *Physical Review Letters*, vol. 95, pp. 196802-4, 2005.

[54] J. Cumings and A. Zettl, "Localization and Nonlinear Resistance in Telescopically Extended Nanotubes," *Physical Review Letters*, vol. 93, pp. 086801, 2004.

[55] S. Li, Z. Yu, C. Rutherglen, and P. J. Burke, "Electrical Properties of 0.4 cm Long Single-Walled Carbon Nanotubes," *Nano Lett.*, vol. 4, pp. 2003-2007, 2004.

[56] V. Meunier, S. V. Kalinin, J. Shin, A. P. Baddorf, and R. J. Harrison, "Quantitative Analysis of Electronic Properties of Carbon Nanotubes by Scanning Probe Microscopy: From Atomic to Mesoscopic Length Scales," *Physical Review Letters*, vol. 93, pp. 246801, 2004.

[57] C. Gomez-Navarro, J. J. Saenz, and J. Gomez-Herrero, "Conductance Oscillations in Squashed Carbon Nanotubes," *Physical Review Letters*, vol. 96, pp. 076803-4, 2006.

[58] Y. Li, W. Kim, Y. Zhang, M. Rolandi, D. Wang, and H. Dai, "Growth of Single-Walled Carbon Nanotubes from Discrete Catalytic Nanoparticles of Various Sizes," *J. Phys. Chem. B*, vol. 105, pp. 11424-11431, 2001.

[59] J. H. Hafner, C. L. Cheung, T. H. Oosterkamp, and C. M. Lieber, "High-Yield Assembly of Individual Single-Walled Carbon Nanotube Tips for Scanning Probe Microscopies," *J. Phys. Chem. B*, vol. 105, pp. 743-746, 2001.

[60] W. Kim, H. C. Choi, M. Shim, Y. Li, D. Wang, and H. Dai, "Synthesis of Ultralong and High Percentage of Semiconducting Single-walled Carbon Nanotubes," *Nano Lett.*, vol. 2, pp. 703-708, 2002.

[61] T. Durkop, "Electronic Properties of Carbon Nanotubes studied in Field-Effect Transistor Geometries," vol. Ph.D. thesis: University of Maryland, 2004.

[62] T. Brintlinger, "Carbon Nanotube Electronics: Growth, Imaging and Electronic Properties," vol. Ph.D. thesis: University of Maryland, 2005.

[63] M. Ishigami, J. H. Chen, W. G. Cullen, M. S. Fuhrer, and E. D. Williams, "Atomic Structure of Graphene on SiO2," *Nano Lett.*, vol. 7, pp. 1643-1648, 2007.

[64] R. A. Webb, *Personal communication.*

[65] T. Nishio, Y. Miyato, K. Kobayashi, K. Matsushige, and H. Yamada, "Piezoresistive properties of carbon nanotubes under radial force investigated by atomic force microscopy," *Applied Physics Letters*, vol. 92, pp. 063117-3, 2008.

[66] A. Javey, J. Guo, Q. Wang, M. Lundstrom, and H. Dai, "Ballistic carbon nanotube field-effect transistors," *Nature*, vol. 424, pp. 654-657, 2003.

[67] H. M. Manohara, E. W. Wong, E. Schlecht, B. D. Hunt, and P. H. Siegel, "Carbon Nanotube Schottky Diodes Using Ti-Schottky and Pt-Ohmic Contacts for High Frequency Applications," *Nano Lett.*, vol. 5, pp. 1469-1474, 2005.

[68] C.-J. Park, Y.-H. Kim, and K. J. Chang, "Band-gap modification by radial deformation in carbon nanotubes," *Physical Review B*, vol. 60, pp. 10656, 1999.

[69] C. Kilic, S. Ciraci, O. Gülseren, and T. Yildirim, "Variable and reversible quantum structures on a single carbon nanotube," *Physical Review B*, vol. 62, pp. R16345, 2000.

[70] O. Gülseren, T. Yildirim, S. Ciraci, and C. Kilic, "Reversible band-gap engineering in carbon nanotubes by radial deformation," *Physical Review B*, vol. 65, pp. 155410, 2002.

[71] Y. Umeno, T. Kitamura, and A. Kushima, "Theoretical analysis on electronic properties of zigzag-type single-walled carbon nanotubes under radial deformation," *Computational Materials Science*, vol. 30, pp. 283-287, 2004.

[72] H. Mehrez, A. Svizhenko, M. P. Anantram, M. Elstner, and T. Frauenheim, "Analysis of band-gap formation in squashed armchair carbon nanotubes," *Physical Review B (Condensed Matter and Materials Physics)*, vol. 71, pp. 155421-7, 2005.

[73] M. Hasegawa and K. Nishidate, "Radial deformation and stability of single-wall carbon nanotubes under hydrostatic pressure," *Physical Review B (Condensed Matter and Materials Physics)*, vol. 74, pp. 115401-10, 2006.

[74] S. Dag, O. Gulseren, S. Ciraci, and T. Yildirim, "Electronic structure of the contact between carbon nanotube and metal electrodes," *Applied Physics Letters*, vol. 83, pp. 3180-3182, 2003.

[75] N. Park, D. Kang, S. Hong, and S. Han, "Pressure-dependent Schottky barrier at the metal-nanotube contact," *Applied Physics Letters*, vol. 87, pp. 013112-3, 2005.

[76] H. D. Espinosa, B. C. Prorok, and B. Peng, "Plasticity size effects in free-standing submicron polycrystalline FCC films subjected to pure tension," *Journal of the Mechanics and Physics of Solids*, vol. 52, pp. 667-689, 2004.

[77] S.-H. Ke, W. Yang, and H. U. Baranger, "Nanotube-metal junctions: 2- and 3-terminal electrical transport," *The Journal of Chemical Physics*, vol. 124, pp. 181102-5, 2006.

[78] B. Shan and K. Cho, "Ab initio study of Schottky barriers at metal-nanotube contacts," *Physical Review B*, vol. 70, pp. 233405, 2004.

[79] I. Deretzis and A. L. Magna, "Role of contact bonding on electronic transport in metal–carbon nanotube–metal systems," *Nanotechnology*, vol. 17, pp. 5063-5072, 2006.

[80] J. H. Hoh and A. Engel, "Friction effects on force measurements with an atomic force microscope," *Langmuir*, vol. 9, pp. 3310-3312, 1993.

[81] L. Huang, C. Meyer, and C. Prater, "Eliminating Lateral Forces During AFM Indentation," *Journal of Physics: Conference Series*, vol. 61, pp. 805-809, 2007.

[82] R. J. Cannara, M. J. Brukman, and R. W. Carpick, "Cantilever tilt compensation for variable-load atomic force microscopy," *Review of Scientific Instruments*, vol. 76, pp. 053706-6, 2005.

[83] J. E. Shigley, *Theory of machines*. New York: McGraw Hill, 1961.

[84] P. G. Collins, M. S. Fuhrer, and A. Zettl, "1/f noise in carbon nanotubes," *Applied Physics Letters*, vol. 76, pp. 894-896, 2000.

[85] F. Liu, M. Bao, K. L. Wang, X. Liu, C. Li, and C. Zhou, "Determination of the Small Band Gap of Carbon Nanotubes Using the Ambipolar Random Telegraph Signal," *Nano Lett.*, vol. 5, pp. 1333-1336, 2005.

[86] F. Liu, K. L. Wang, C. Li, and C. Zhou, "Study of Random Telegraph Signals in Single-Walled Carbon Nanotube Field Effect Transistors," *Nanotechnology, IEEE Transactions on*, vol. 5, pp. 441-445, 2006.

[87] S. Reza, Q. T. Huynh, G. Bosman, J. Sippel-Oakley, and A. G. Rinzler, "1/f noise in metallic and semiconducting carbon nanotubes," *Journal of Applied Physics*, vol. 100, pp. 094318-5, 2006.

[88] M. Ishigami, J. H. Chen, E. D. Williams, D. Tobias, Y. F. Chen, and M. S. Fuhrer, "Hooge's constant for carbon nanotube field effect transistors," *Applied Physics Letters*, vol. 88, pp. 203116-3, 2006.

[89] J. Appenzeller, L. Yu-Ming, J. Knoch, C. Zhihong, and P. Avouris, "1/f Noise in Carbon Nanotube Devices—On the Impact of Contacts and Device Geometry," *Nanotechnology, IEEE Transactions on*, vol. 6, pp. 368-373, 2007.

[90] M. S. Fuhrer, B. M. Kim, T. Durkop, and T. Brintlinger, "High-Mobility Nanotube Transistor Memory," *Nano Lett.*, vol. 2, pp. 755-759, 2002.

[91] M. Radosavljevic, M. Freitag, K. V. Thadani, and A. T. Johnson, "Nonvolatile Molecular Memory Elements Based on Ambipolar Nanotube Field Effect Transistors," *Nano Lett.*, vol. 2, pp. 761-764, 2002.

[92] W. Kim, A. Javey, O. Vermesh, Q. Wang, Y. Li, and H. Dai, "Hysteresis Caused by Water Molecules in Carbon Nanotube Field-Effect Transistors," *Nano Lett.*, vol. 3, pp. 193-198, 2003.

[93] G. Pennington, N. Goldsman, A. Akturk, and A. E. Wickenden, "Deformation potential carrier-phonon scattering in semiconducting carbon nanotube transistors," *Applied Physics Letters*, vol. 90, pp. 062110-3, 2007.

[94] A. Javey, M. Shim, and H. Dai, "Electrical properties and devices of large-diameter single-walled carbon nanotubes," *Applied Physics Letters*, vol. 80, pp. 1064-1066, 2002.

[95] F. Léonard and J. Tersoff, "Role of Fermi-Level Pinning in Nanotube Schottky Diodes," *Physical Review Letters*, vol. 84, pp. 4693, 2000.

[96] F. Leonard and D. A. Stewart, "Properties of short channel ballistic carbon nanotube transistors with ohmic contacts," *Nanotechnology*, vol. 17, pp. 4699-4705, 2006.

[97] F. Leonard and A. A. Talin, "Size-Dependent Effects on Electrical Contacts to Nanotubes and Nanowires," *Physical Review Letters*, vol. 97, pp. 026804-4, 2006.

[98] C. Fiegna, H. Iwai, T. Wada, M. Saito, E. Sangiorgi, and B. Ricco, "Scaling the MOS transistor below 0.1 um: methodology, device structures, and technology requirements," *Electron Devices, IEEE Transactions on*, vol. 41, pp. 941-951, 1994.

[99] S. Suzuki, Y. Watanabe, Y. Homma, S.-y. Fukuba, S. Heun, and A. Locatelli, "Work functions of individual single-walled carbon nanotubes," *Applied Physics Letters*, vol. 85, pp. 127-129, 2004.

[100] B. Shan and K. Cho, "First Principles Study of Work Functions of Single Wall Carbon Nanotubes," *Physical Review Letters*, vol. 94, pp. 236602-4, 2005.

[101] B.-K. Kim, N. Park, P. S. Na, H.-M. So, J.-J. Kim, H. Kim, K.-J. Kong, H. Chang, B.-H. Ryu, Y. Choi, and J.-O. Lee, "The effect of metal cluster coatings on carbon nanotubes," *Nanotechnology*, vol. 17, pp. 496-500, 2006.

[102] S. Rosenblatt, Y. Yaish, J. Park, J. Gore, V. Sazonova, and P. L. McEuen, "High Performance Electrolyte Gated Carbon Nanotube Transistors," *Nano Lett.*, vol. 2, pp. 869-872, 2002.

[103] J. P. Colinge and C. A. Colinge, *Physics of semiconductor devices*. Boston: Kluwer Academic Publishers, 2002.

[104] B. M. Kim, T. Brintlinger, E. Cobas, M. S. Fuhrer, H. Zheng, Z. Yu, R. Droopad, J. Ramdani, and K. Eisenbeiser, "High-performance carbon nanotube transistors on SrTiO[sub 3]/Si substrates," *Applied Physics Letters*, vol. 84, pp. 1946-1948, 2004.

[105] G. Jing, W. Jing, E. Polizzi, S. Datta, and M. Lundstrom, "Electrostatics of nanowire transistors," *Nanotechnology, IEEE Transactions on*, vol. 2, pp. 329-334, 2003.

[106] N. Neophytou, G. Jing, and M. S. Lundstrom, "Three-dimensional electrostatic effects of carbon nanotube transistors," *Nanotechnology, IEEE Transactions on*, vol. 5, pp. 385-392, 2006.

[107] D. L. John, L. C. Castro, and D. L. Pulfrey, "Quantum capacitance in nanoscale device modeling," *Journal of Applied Physics*, vol. 96, pp. 5180-5184, 2004.

[108] M. Biercuk, S. Ilani, C. Marcus, and P. McEuen, "Electrical Transport in Single-Wall Carbon Nanotubes," in *Carbon Nanotubes*: Springer, 2008, pp. 455-493.

[109] M. Gurvitch, "Ioffe-Regel criterion and resistivity of metals," *Physical Review B*, vol. 24, pp. 7404, 1981.

[110] B. Gao, D. C. Glattli, B. Placais, and A. Bachtold, "Cotunneling and one-dimensional localization in individual disordered single-wall carbon nanotubes: Temperature dependence of the intrinsic resistance," *Physical Review B (Condensed Matter and Materials Physics)*, vol. 74, pp. 085410-5, 2006.

[111] E. Pop, D. A. Mann, K. E. Goodson, and H. Dai, "Electrical and thermal transport in metallic single-wall carbon nanotubes on insulating substrates," *Journal of Applied Physics*, vol. 101, pp. 093710-10, 2007.

[112] M. Lundstrom, *Fundamentals of carrier transport*, Second ed: Cambridge University Press, 2000.

[113] G. Pennington and N. Goldsman, "Semiclassical transport and phonon scattering of electrons in semiconducting carbon nanotubes," *Physical Review B*, vol. 68, pp. 045426, 2003.

[114] S. Roche, J. Jiang, F. Triozon, and R. Saito, "Conductance and coherence lengths in disordered carbon nanotubes: Role of lattice defects and phonon vibrations," *Physical Review B (Condensed Matter and Materials Physics)*, vol. 72, pp. 113410-4, 2005.

[115] J. Appenzeller, M. Radosavljevic, J. Knoch, and P. Avouris, "Tunneling Versus Thermionic Emission in One-Dimensional Semiconductors," *Physical Review Letters*, vol. 92, pp. 048301, 2004.

[116] C. W. J. Beenakker, "Random-matrix theory of quantum transport," *Reviews of Modern Physics*, vol. 69, pp. 731, 1997.

[117] Y. Imry, *Introduction to Mesoscopic Physics*: Oxford University Press, 1997.

[118] J. Rammer, *Quantum Transport Theory*: Perseus Books, 1998.

[119] S. Washburn and R. A. Webb, "Quantum transport in small disordered samples from the diffusive to the ballistic regime," in *Reports on Progress in Physics*, vol. 55. UK, 1992, pp. 1311-1383.

[120] A. Stern, Y. Aharonov, and Y. Imry, "Phase uncertainty and loss of interference: a general picture," *Physical Review A (Atomic, Molecular, and Optical Physics)*, vol. 41, pp. 3436-3448, 1990.

[121] B. L. Altshuler, A. G. Aronov, and D. E. Khmelnitsky, "Effects of electron-electron collisions with small energy transfers on quantum localisation," in *Journal of Physics C (Solid State Physics)*, vol. 15. UK, 1982, pp. 7367-7386.

[122] I. L. Aleiner, B. L. Altshuler, and M. E. Gershenson, "Interaction effects and phase relaxation in disordered systems," in *Waves in Random Media*, vol. 9. UK: IOP Publishing, 1999, pp. 201-239.

[123] J. J. Lin and J. P. Bird, "Recent experimental studies of electron dephasing in metal and semiconductor mesoscopic structures," in *Journal of Physics: Condensed Matter*, vol. 14. UK: IOP Publishing, 2002, pp. R501-96.

[124] P. Mohanty, E. M. Q. Jariwala, and R. A. Webb, "Intrinsic Decoherence in Mesoscopic Systems," *Physical Review Letters*, vol. 78, pp. 3366-3369, 1997.

[125] P. Mohanty and R. A. Webb, "Decoherence and quantum fluctuations," *Physical Review B (Condensed Matter)*, vol. 55, pp. R13452-R13455, 1997.

[126] R. A. Webb, P.Mohanty, E. M. Q. Jariwala, T. R. Stevenson, and A. G. Zharikov, "Decoherence in Mesoscopic Systems," in *Quantum Coherence and Decoherence*, Y. A. Ono and K. Fujikawa, Eds.: Elsevier, 1999.

[127] D. S. Golubev and A. D. Zaikin, "Quantum Decoherence in Disordered Mesoscopic Systems," *Physical Review Letters*, vol. 81, pp. 1074-1077, 1998.

[128] D. S. Golubev and A. D. Zaikin, "Quantum decoherence and weak localization at low temperatures," *Physical Review B (Condensed Matter and Materials Physics)*, vol. 59, pp. 9195-9213, 1999.

[129] D. S. Golubev and A. D. Zaikin, "Interactions and weak localization: Perturbation theory and beyond," *Physical Review B (Condensed Matter and Materials Physics)*, vol. 62, pp. 14061-14098, 2000.

[130] A. D. Zaikin and D. S. Golubev, "Interaction and quantum decoherence in disordered conductors," *Physica B*, vol. 280, pp. 453-457, 2000.

[131] D. S. Golubev and A. D. Zaikin, "Low temperature decoherence by electron-electron interactions: role of quantum fluctuations," in *Journal of Low Temperature Physics*, vol. 132. USA: Kluwer Academic/Plenum Publishers, 2003, pp. 11-38.

[132] T. R. Kirkpatrick and D. Belitz, "Absence of electron dephasing at zero temperature," *Physical Review B (Condensed Matter and Materials Physics)*, vol. 65, pp. 195123, 2002.

[133] D. Cohen and Y. Imry, "Dephasing at low temperatures," *Physical Review B (Condensed Matter and Materials Physics)*, vol. 59, pp. 11143-11146, 1999.

[134] I. L. Aleiner, B. L. Altshuler, and M. G. Vavilov, "Absence of zero-temperature dephasing by electron-electron interaction," in *Journal of Low Temperature Physics*, vol. 126. USA: Kluwer Academic/Plenum Publishers, 2002, pp. 1377-1384.

[135] S. Bandopadhyay and D. Cohen, "Renormalization of the dephasing by zero point fluctuations," *Physical Review B (Condensed Matter and Materials Physics)*, vol. 77, pp. 155438-8, 2008.

[136] G. Gruner and A. Zawadowski, "Magnetic impurities in non-magnetic metals," in *Reports on Progress in Physics*, vol. 37. UK, 1974, pp. 1497-1583.

[137] C. V. Haesendonck, J. Vranken, and Y. Bruynseraede, "Resonant Kondo scattering of weakly localized electrons," *Physical Review Letters*, vol. 58, pp. 1968-1971, 1987.

[138] F. Pierre, A. B. Gougam, A. Anthore, H. Pothier, D. Esteve, and N. O. Birge, "Dephasing of electrons in mesoscopic metal wires," *Physical Review B (Condensed Matter and Materials Physics)*, vol. 68, pp. 085413, 2003.

[139] F. Pierre and N. O. Birge, "Dephasing by Extremely Dilute Magnetic Impurities Revealed by Aharonov-Bohm Oscillations," *Physical Review Letters*, vol. 89, pp. 206804, 2002.

[140] A. B. Gougam, F. Pierre, H. Pothier, D. Esteve, and N. O. Birge, "Comparison of energy and phase relaxation in metallic wires," *Journal of Low Temperature Physics*, vol. 118, pp. 447-456, 2000.

[141] F. Pierre, H. Pothier, D. Esteve, M. H. Devoret, A. B. Gougam, and N. O. Birge, "Probing interactions in mesoscopic gold wires," *Kondo Effect and Dephasing in Low-Dimensional Metallic Systems. Proceedings of the NATO Advanced Research Workshop*, pp. 119-132, 2001.

[142] P. Mohanty and R. A. Webb, "High-Field Measurements of Electron Decoherence Time in Metallic Nanowires: Switching off Magnetic Impurity Spins," *Physical Review Letters*, vol. 91, pp. 066604, 2003.

[143] A. E. Bell and A. D. Caplin, "Dilute transition metal alloys and the Kondo problem," in *Contemporary Physics*, vol. 16. UK, 1975, pp. 375-394.

[144] A. C. Hewson, *The Kondo Problem to Heavy Fermions*: Cambridge University Press, 1993.

[145] V. Chandrasekhar, C. V. Haesendonck, and A. Zawadowski, "Kondo Effect and Dephasing in Low-Dimensional Metallic Systems," Kluwer Academic Publishers, 2001.

[146] G. Chen and N. Giordano, "Thickness dependence of the Kondo effect in AuFe films," *Physical Review Letters*, vol. 66, pp. 209-211, 1991.

[147] G. Bergmann, "Critical size of small particles for the development of resonances," *Physical Review Letters*, vol. 67, pp. 2545-2548, 1991.

[148] M. A. Blachly and N. Giordano, "Kondo effect in one-dimensional Au(Fe)," *Physical Review B (Condensed Matter)*, vol. 46, pp. 2951-2957, 1992.

[149] V. Chandrasekhar, P. Santhanam, N. A. Penebre, R. A. Webb, H. Vloeberghs, C. V. Haesendonck, and Y. Bruynseraede, "Absence of size dependence of the Kondo resistivity," *Physical Review Letters*, vol. 72, pp. 2053-2056, 1994.

[150] M. A. Blachly and N. Giordano, "Kondo effect in systems of reduced dimensionality," *Physical Review B (Condensed Matter)*, vol. 51, pp. 12537-12550, 1995.

[151] O. Ujsaghy, A. Zawadowski, and B. L. Gyorffy, "Spin-orbit-induced magnetic anisotropy for impurities in metallic samples of reduced dimensions: Finite size dependence in the Kondo effect," *Physical Review Letters*, vol. 76, pp. 2378-2381, 1996.

[152] O. Ujsaghy and A. Zawadowski, "Spin-orbit-induced magnetic anisotropy for impurities in metallic samples. I. Surface anisotropy," *Physical Review B (Condensed Matter and Materials Physics)*, vol. 57, pp. 11598-11608, 1998.

[153] O. Ujsaghy and A. Zawadowski, "Spin-orbit-induced magnetic anisotropy for impurities in metallic samples. II. Finite-size dependence in the Kondo resistivity," *Physical Review B (Condensed Matter and Materials Physics)*, vol. 57, pp. 11609-11622, 1998.

[154] O. Ujsaghy and A. Zawadowski, "Spin-orbit-induced Kondo size effect in thin films with 5/2-spin impurities," *Physical Review B (Condensed Matter and Materials Physics)*, vol. 60, pp. 10602-10605, 1999.

[155] L. Borda and A. Zawadowski, "Theory of magnetoresistance in films of dilute magnetic alloys," *Physical Review B (Condensed Matter and Materials Physics)*, vol. 61, pp. 3570-3578, 2000.

[156] Y. Meir and N. S. Wingreen, "Spin-orbit scattering and the Kondo effect," *Physical Review B (Condensed Matter)*, vol. 50, pp. 4947-4950, 1994.

[157] N. Giordano, "Magnetoresistance of small Kondo systems," *Physical Review B (Condensed Matter)*, vol. 53, pp. 2487-2491, 1996.

[158] N. Giordano and T. M. Jacobs, "Substrate dependence of Kondo and local moment physics in thin metal films," *Journal of Applied Physics*, vol. 87, pp. 6079-6082, 2000.

[159] T. M. Jacobs and N. Giordano, "Kondo behavior of multilayers: Local-moment physics near surfaces," *Physical Review B (Condensed Matter and Materials Physics)*, vol. 62, pp. 14145-14148, 2000.

[160] N. Giordano and T. M. Jacobs, "Kondo effect in small metal systems," *Physica B*, vol. 280, pp. 434-437, 2000.

[161] V. M. Fomin, V. N. Gladilin, J. T. Devreese, C. Van Haesendonck, and G. Neuttiens, "Inhomogeneous splitting of impurity-spin energy levels in mesoscopic wires," in *Solid State Communications*, vol. 106. USA: Elsevier, 1998, pp. 293-297.

[162] E. Seynaeve, K. Temst, F. G. Aliev, C. V. Haesendonck, V. N. Gladilin, V. M. Fomin, and J. T. Devreese, "Impurity Spin Magnetization of Thin Fe Doped Au Films," *Physical Review Letters*, vol. 85, pp. 2593-2596, 2000.

[163] A. Anthore, F. Pierre, H. Pothier, and D. Esteve, "Magnetic-Field-Dependent Quasiparticle Energy Relaxation in Mesoscopic Wires," *Physical Review Letters*, vol. 90, pp. 076806, 2003.

[164] A. Anthore, F. Pierre, H. Pothier, D. Esteve, and M. H. Devoret, "Influence of Magnetic Field on Effective Electron-Electron Interactions in a Copper Wire," *cond-mat/0109297*, 2001.

[165] F. Pierre, H. Pothier, D. Esteve, and M. H. Devoret, "Energy redistribution between quasiparticles in mesoscopic silver wires," *Journal of Low Temperature Physics*, vol. 118, pp. 437-445, 2000.

[166] A. Kaminski and L. I. Glazman, "Electron Energy Relaxation in the Presence of Magnetic Impurities," *Physical Review Letters*, vol. 86, pp. 2400-2403, 2001.

[167] G. Goppert and H. Grabert, "Nonequilibrium electron distribution in the presence of Kondo impurities," *Physical Review B (Condensed Matter and Materials Physics)*, vol. 64, pp. 033301, 2001.

[168] G. Goppert, Y. M. Galperin, B. L. Altshuler, and H. Grabert, "Magnetic-field effects in energy relaxation mediated by Kondo impurities in mesoscopic wires," *Physical Review B (Condensed Matter and Materials Physics)*, vol. 66, pp. 195328, 2002.

[169] G. Goppert and H. Grabert, "Inelastic electron relaxation rates caused by spin-M/2 Kondo impurities," *Physical Review B (Condensed Matter and Materials Physics)*, vol. 68, pp. 193301, 2003.

[170] A. Crepieux and C. Lacroix, "Distribution of Kondo temperatures in a thin film," *Physical Review B (Condensed Matter and Materials Physics)*, vol. 61, pp. 6785-6789, 2000.

[171] G. Bergmann, W. Shieh, and M. Huberman, "Ruderman-Kittel-Kasuya-Yosida interaction in thin wires," *Physical Review B (Condensed Matter)*, vol. 46, pp. 8607-8609, 1992.

[172] A. Crepieux and C. Lacroix, "Competition between Kondo effect and RKKY interaction in a thin film," *Physical Review B (Condensed Matter and Materials Physics)*, vol. 59, pp. 13824-13828, 1999.

[173] M. G. Vavilov, L. I. Glazman, and A. I. Larkin, "Electron transport and energy relaxation in dilute magnetic alloys," *Physical Review B (Condensed Matter and Materials Physics)*, vol. 68, pp. 075119, 2003.

[174] G. Bergmann, "Magnetic screening of Fe impurities in Mg," *Physical Review Letters*, vol. 57, pp. 1460-1463, 1986.

[175] G. Bergmann, "Low-temperature behavior of Kondo impurities and check of the Fermi-liquid model," *Physical Review Letters*, vol. 58, pp. 1236-1239, 1987.

[176] R. P. Peters, G. Bergmann, and R. M. Mueller, "Quenching of interacting moments and anomalous Fermi-liquid behavior in disordered Kondo alloys at low temperatures," *Physical Review Letters*, vol. 60, pp. 1093-1096, 1988.

[177] V. Dobrosavljevic, T. R. Kirkpatrick, and B. G. Kotliar, "Kondo effect in disordered systems," *Physical Review Letters*, vol. 69, pp. 1113-1116, 1992.

[178] I. Martin, Y. Wan, and P. Phillips, "Size Dependence in the Disordered Kondo Problem," *Physical Review Letters*, vol. 78, pp. 114-117, 1997.

[179] A. Jagannathan, E. Abrahams, and M. J. Stephen, "Magnetic exchange in disordered metals," *Physical Review B (Condensed Matter)*, vol. 37, pp. 436-441, 1988.

[180] A. Jagannathan, "Backscattering and linear response in a disordered metal," *Physical Review B (Condensed Matter)*, vol. 40, pp. 5980-5984, 1989.

[181] G. Bergmann and H. Beckmann, "Identification of local spin fluctuations by weak localization," *Physical Review B (Condensed Matter)*, vol. 52, pp. R15687-90, 1995.

[182] R. P. Peters, G. Bergmann, and R. M. Mueller, "Kondo maximum of magnetic scattering," *Physical Review Letters*, vol. 58, pp. 1964-1967, 1987.

[183] P. Mohanty and R. A. Webb, "Low Temperature Anomaly in Mesoscopic Kondo Wires," *Physical Review Letters*, vol. 84, pp. 4481-4484, 2000.

[184] F. Schopfer, C. Bauerle, W. Rabaud, and L. Saminadayar, "Anomalous Temperature Dependence of the Dephasing Time in Mesoscopic Kondo Wires," *Physical Review Letters*, vol. 90, pp. 056801, 2003.

[185] T. Micklitz, A. Altland, T. A. Costi, and A. Rosch, "Universal Dephasing Rate due to Diluted Kondo Impurities," *Physical Review Letters*, vol. 96, pp. 226601-4, 2006.

[186] D. Jha and M. H. Jericho, "Low-Temperature Transport Properties of Dilute Silver-Manganese Alloys," *Physical Review B*, vol. 3, pp. 147, 1971.

[187] D. v. d. Marel, C. Westra, G. A. Sawatzky, and F. U. Hillebrecht, "Electronic structure of Mn impurities in noble metals," *Physical Review B (Condensed Matter)*, vol. 31, pp. 1936-1949, 1985.

[188] M. G. Vavilov and L. I. Glazman, "Conductance of mesoscopic systems with magnetic impurities," *Physical Review B (Condensed Matter and Materials Physics)*, vol. 67, pp. 115310, 2003.

[189] P. Esquinazi, "Tunneling Systems in Amorphous and Crystalline Solids," Springer, 1998.

[190] Y. Imry, H. Fukuyama, and P. Schwab, "Low-temperature dephasing in disordered conductors: the effect of "1/f" fluctuations," in *Europhysics Letters*, vol. 47. France: Eur. Phys. Soc. by EDP Sciences and Soc. Italiana Fisica, 1999, pp. 608-614.

[191] D. L. Cox and A. Zawadowski, "Exotic Kondo effects in metals: magnetic ions in a crystalline electric field and tunnelling centres," in *Advances in Physics*, vol. 47. UK: Taylor & Francis, 1998, pp. 599-942.

[192] A. Zawadowski, J. v. Delft, and D. C. Ralph, "Dephasing in Metals by Two-Level Systems in the 2-Channel Kondo Regime," *Physical Review Letters*, vol. 83, pp. 2632-2635, 1999.

[193] V. V. Afonin, J. Bergli, Y. M. Galperin, V. L. Gurevich, and V. I. Kozub, "Possible weak temperature dependence of electron dephasing," *Physical Review B (Condensed Matter and Materials Physics)*, vol. 66, pp. 165326, 2002.

[194] T. Capron, Y. Niimi, F. Mallet, Y. Baines, D. Mailly, F.-Y. Lo, A. Melnikov, A. D. Wieck, L. Saminadayar, and C. Bauerle, "Low-temperature dephasing in irradiated metallic wires," *Physical Review B (Condensed Matter and Materials Physics)*, vol. 77, pp. 033102-4, 2008.

[195] I. L. Aleiner, B. L. Altshuler, and Y. M. Galperin, "Experimental tests for the relevance of two-level systems for electron dephasing," *Physical Review B (Condensed Matter and Materials Physics)*, vol. 63, pp. 201401, 2001.

[196] I. L. Aleiner, B. L. Altshuler, Y. M. Galperin, and T. A. Shutenko, "Kondo Temperature for the Two-Channel Kondo Models of Tunneling Centers," *Physical Review Letters*, vol. 86, pp. 2629-2632, 2001.

[197] B. L. Altshuler, M. E. Gershenson, and I. L. Aleiner, "Phase relaxation of electrons in disordered conductors," *Physica E*, vol. 3, pp. 58-68, 1998.

[198] Y. B. Khavin, M. E. Gershenson, and A. L. Bogdanov, "Decoherence and the Thouless Crossover in One-Dimensional Conductors," *Physical Review Letters*, vol. 81, pp. 1066-1069, 1998.

[199] J. Wei, S. Pereverzev, and M. E. Gershenson, "Microwave-Induced Dephasing in One-Dimensional Metal Wires," *Physical Review Letters*, vol. 96, pp. 086801-4, 2006.

[200] K. Houshangpour and K. Maschke, "Phase coherence in mesoscopic systems at low temperatures," *Physical Review B (Condensed Matter and Materials Physics)*, vol. 59, pp. 4615-4617, 1999.

[201] G. Y. Wu, "Zero-temperature dephasing of conduction electrons in polycrystalline impure metals," *Physical Review B (Condensed Matter and Materials Physics)*, vol. 66, pp. 041102, 2002.

[202] X. R. Wang, G. Xiong, and S.-D. Wang, "Dephasing of conduction electrons due to zero-point fluctuation," *Physical Review B (Condensed Matter and Materials Physics)*, vol. 61, pp. R5090-R5092, 2000.

[203] X. R. Wang, G. Xiong, and S.-D. Wang, "Reply to ``Comment on `Dephasing of conduction electrons due to zero-point fluctuation' "," *Physical Review B (Condensed Matter and Materials Physics)*, vol. 64, pp. 117302, 2001.

[204] J. C. Flores, "Phase-coherence time saturation in mesoscopic systems: Wave-function collapse," *Physical Review B (Condensed Matter and Materials Physics)*, vol. 62, pp. R16291-R16293, 2000.

[205] M. Frasca, "Saturation of dephasing time in mesoscopic devices produced by a ferromagnetic state," *Physical Review B (Condensed Matter and Materials Physics)*, vol. 68, pp. 193413, 2003.

[206] P. A. Lee and T. V. Ramakrishnan, "Disordered electronic systems," in *Reviews of Modern Physics*, vol. 57. USA, 1985, pp. 287-337.

[207] G. Bergmann, "Physical interpretation of weak localization: A time-of-flight experiment with conduction electrons," *Physical Review B (Condensed Matter)*, vol. 28, pp. 2914-2920, 1983.

[208] P. A. Lee and A. D. Stone, "Universal conductance fluctuations in metals," *Physical Review Letters*, vol. 55, pp. 1622-1625, 1985.

[209] P. A. Lee, A. D. Stone, and H. Fukuyama, "Universal conductance fluctuations in metals: Effects of finite temperature, interactions, and magnetic field," *Physical Review B (Condensed Matter)*, vol. 35, pp. 1039-1070, 1987.

[210] P. McConville and N. O. Birge, "Weak localization, universal conductance fluctuations, and 1/f noise in Ag," *Physical Review B (Condensed Matter)*, vol. 47, pp. 16667-16670, 1993.

[211] Y. M. Blanter, "Electron-electron scattering rate in disordered mesoscopic systems," *Physical Review B (Condensed Matter)*, vol. 54, pp. 12807-12819, 1996.

[212] D. Hoadley, P. McConville, and N. O. Birge, "Experimental comparison of the phase-breaking lengths in weak localization and universal conductance fluctuations," *Physical Review B (Condensed Matter and Materials Physics)*, vol. 60, pp. 5617-5625, 1999.

[213] I. L. Aleiner and Y. M. Blanter, "Inelastic scattering time for conductance fluctuations," *Physical Review B (Condensed Matter and Materials Physics)*, vol. 65, pp. 115317, 2002.

[214] A. Trionfi, S. Lee, and D. Natelson, "Electronic coherence in metals: Comparing weak localization and time-dependent conductance fluctuations," *Physical Review B (Condensed Matter and Materials Physics)*, vol. 70, pp. 041304, 2004.

[215] S. K. Sharma and J. Spitz, "Hillock growth and agglomeration in thin silver films," in *Thin Solid Films*, vol. 61. Switzerland, 1979, pp. L13-15.

[216] S. K. Sharma and J. Spitz, "Hillock formation hole growth and agglomeration in thin silver films," in *Thin Solid Films*, vol. 65. Switzerland, 1980, pp. 339-350.

[217] K. Sieradzki, K. Bailey, and T. L. Alford, "Agglomeration and percolation conductivity," in *Applied Physics Letters*, vol. 79. USA: AIP, 2001, pp. 3401-3403.

[218] H. C. Kim, T. L. Alford, and D. R. Allee, "Thickness dependence on the thermal stability of silver thin films," in *Applied Physics Letters*, vol. 81. USA: AIP, 2002, pp. 4287-4289.

[219] J. Vranken, C. V. Haesendonck, and Y. Bruynseraede, "Enhanced magnetic surface scattering of weakly localized electrons," *Physical Review B (Condensed Matter)*, vol. 37, pp. 8502-8505, 1988.

[220] S. B. Arnason, S. P. Herschfield, and A. F. Hebard, "Bad Metals Made with Good-Metal Components," *Physical Review Letters*, vol. 81, pp. 3936-3939, 1998.

[221] C. Durkan and M. E. Welland, "Size effects in the electrical resistivity of polycrystalline nanowires," *Physical Review B (Condensed Matter and Materials Physics)*, vol. 61, pp. 14215-14218, 2000.

[222] A. Benoit, C. P. Umbach, R. B. Laibowitz, and R. A. Webb, "Length-independent voltage fluctuations in small devices," *Physical Review Letters*, vol. 58, pp. 2343-2346, 1987.

[223] H. Haucke, S. Washburn, A. D. Benoit, C. P. Umbach, and R. A. Webb, "Universal scaling of nonlocal and local resistance fluctuations in small wires," *Physical Review B (Condensed Matter)*, vol. 41, pp. 12454-12461, 1990.

[224] V. Chandrasekhar, P. Santhanam, and D. E. Prober, "Weak localization and conductance fluctuations in complex mesoscopic geometries," *Physical Review B (Condensed Matter)*, vol. 44, pp. 11203-11220, 1991.

[225] R. P. Giffard, R. A. Webb, and J. C. Wheatley, "Principles and methods of low-frequency electric and magnetic measurements using an rf-biased point-contact superconducting device," in *Journal of Low Temperature Physics*, vol. 6. USA, 1972, pp. 533-610.

[226] P. Mohanty, "Measurement of Decoherence: An Approach," in *Physics*. College Park: University of Maryland, 1998.

[227] C. W. J. Beenakker and H. v. Houten, "Flux-cancellation effect on narrow-channel magnetoresistance fluctuations," *Physical Review B (Condensed Matter)*, vol. 37, pp. 6544-6546, 1988.

[228] V. Chandrasekhar, P. Santhanam, and D. E. Prober, "Effect of spin-orbit and spin-flip scattering on conductance fluctuations," *Physical Review B (Condensed Matter)*, vol. 42, pp. 6823-6826, 1990.

[229] N. O. Birge and F. Pierre, "Electron Dephasing in Mesoscopic Metal Wires," *cond-mat/0401182*, 2004.